

NNT : 2016SACLX042

THÈSE DE DOCTORAT
DE
L'UNIVERSITÉ PARIS-SACLAY
PRÉPARÉE À
L'ÉCOLE POLYTECHNIQUE

ÉCOLE DOCTORALE N°579

Sciences mécaniques et énergétiques, matériaux et géosciences

Spécialité de doctorat : Mécanique des solides

Par

Monsieur Zepeng MA

**A New Strategy for Fatigue Analysis in Presence of
General Multiaxial Time Varying Loadings**

Thèse présentée et soutenue à Palaiseau, le 18 décembre 2017

Composition du Jury :

M. Franck MOREL	Professeur, LAMPA ENSAM, Angers	Rapporteur
M. Nicolas SAINTIER	Professeur, Arts et Métiers ParisTech	Rapporteur
M. Eric CHARKALUK	Professeur, École Polytechnique	Examinateur
M. Georges CAILLETAUD	Professeur, Mines ParisTech	Examinateur
Mme Ida RAOULT	Ingénieur de recherche, PSA	Examinaterice
M. Patrick LE TALLEC	Professeur, École Polytechnique	Directeur de thèse
M. Habibou MAITOURNAM	Professeur, ENSTA ParisTech	Co-encadrant

“The whole of science is nothing more than a refinement of everyday thinking.”

Albert Einstein

Acknowledgements

My thanks go to Prof. P. Le Tallec, dear supervisor of the thesis. I thank him for having assured the scientific quality in this work and for having also entrusted to me the responsibilities of my scientific productions. I will not repeat what was said on the day of the defense, but thanks to him I discovered France and polytechnique, a landscape that I once know little and far away. I could not have imagined having a better advisor and mentor for my Ph.D. studies.

I would like to thank Prof. H. Maitournam for helping me, at the crucial time of my thesis, to analyze the problems presented in this work.

I would then like to thank all the members of the jury for their work.

I take this opportunity to say thanks to Mme.Ida Haoult for her advice on the technical support and experiments issued by CETIM.

This thesis would not have been possible without the generous support from the Chaire PSA and the Laboratoire de Mécanique des Solides of Ecole Polytechnique to whom I express my profound gratitude.

I would like to thank my parents for all their love and encouragement that have overcome the barriers of the time difference and geographical distance for the past three years.

Finally, I would like to thank all those whom I met and whom I did not have a chance to say thank you.

Contents

Acknowledgements	v
List of Figures	xiii
List of Tables	xvi
1 Introduction	1
1.1 General introduction	1
2 Fatigue life calculation methods	5
2.1 Basquin curve	6
2.2 Basic fatigue criteria	7
2.3 Calculation method without cycle counting	21
3 Space gradient effects	29
3.1 Introduction	30
3.2 A first gradient approach	31
3.3 Optimized Crossland Criterion formulation	33
3.4 Optimized Papadopoulos Criterion formulation	34
3.5 Optimized Dang Van Criterion formulation	36
3.6 Calibration of the criteria	36
3.7 Discussion	46
3.8 Conclusion and perspectives	47
4 Time varying load : the standard approach	49
4.1 The notion of damage in fatigue	50
4.2 Verification method of Chaboche law	59
4.3 Chaboche law containing different criteria	60
4.4 Numerical testing on different loading patterns	60
4.5 Cycle Counting Method	66
5 Handling general loadings	73
5.1 Multiscale energy dissipation approach	73
5.2 Kinematic Hardening Models	75
5.3 Mean stress effect in local model	76
5.4 Weakening scales and yield function	79
5.5 Construction of an energy based fatigue approach	81
5.6 Nonlinearity of damage accumulation	83
5.7 Numerical strategy	89

5.8 Validation on recovery tests	98
5.9 Identification strategy	111
6 Numerical implementation and validation	115
6.1 Experimental verification	115
6.2 Experimental validation of the model on aluminum 6082 T6	121
6.3 Experimental validation of the model on 30NCD16 steel	126
6.4 Experimental validation of the model on SM45C steel	129
6.5 Experimental validation of the model on 10 HNAP steel	135
6.6 Conclusions	148
7 General conclusions	149
References	153
Appendices	161
.1 DETAILED EXPLOITATION	161
.2 MATLAB CODE LISTING	165

List of Figures

2.1	Idealized S-N curve for high cycle fatigue.	6
2.2	Elastic adaptation at the two scales (Dang Van [1999])	10
2.3	Material plane Δ passing through point O of a body and its associated (n, l, r) frame(Papadopoulos [1993]).	12
2.4	Algorithm of fatigue life determination with use of the energy parameter in the critical plane under biaxial random tension-compression (Łagoda et al. [1999]).	15
2.5	Finding the appropriate state for an affine load path A-B(Koutiri [2011]).	20
2.6	Path of the macroscopic shear stress \underline{C} acting on a material plane Δ and the corresponding path of the macroscopic resolved shear stress \underline{T} acting on an easy glide direction (Morel [2000]).	23
2.7	(a) Yield limit evolutions and (b) damage evolution in the three behavior phases (hardening, saturation and softening) when a cyclic loading is applied (Morel [2000]).	23
2.8	Different paths of loading in the plane and corresponding values of the phase-difference coefficient H (Morel [2000]). For a proportional loading, H is equal to $\sqrt{\pi}$. In the case of a particular circular path, H reaches the maximum value $\sqrt{2\pi}$ (Figure 2.8). The linear path and the circular one lead to two bounds of the coefficient H	24
2.9	block sequence tests (bending/bending+torsion/torsion) performed on a mild steel XC18.	26
3.1	Constant moment bending fatigue limit data: (a) constant radius R; (b) constant length L (Results of Pogoretskii [1966], represented by Weber [1999]).	30
3.2	Schematic representation of the nominal fatigue limit (ellipse arc) for two different tests: the arc is larger in the case of bending-torsion (presence of stress gradient) than in tension-compression.	31
3.3	Material plane Δ passing through point O of a body and its associated (n, l, r) frame.	34
3.4	4-point bending test (Papadopoulos and Panoskaltsis [1996])	37
3.5	Cantilever bending test (Papadopoulos and Panoskaltsis [1996])	39
3.6	Fatigue limits with gradient effect for different radii (Massonnet [1955]).	40
3.7	Fatigue limits with gradient effect for different radii (Moore and Morkovin [1944]).	40
3.8	Fatigue limits with gradient effect for different radii (Pogoretskii [1966]).	41
3.9	Fatigue limits with gradient effect for different radii (Papadopoulos and Panoskaltsis [1996]).	41
3.10	Fully reversed combined bending-twisting fatigue limit data (Findley et al. [1956], Papadopoulos and Panoskaltsis [1996]) compared with updated values computed with gradient effects using Eq.(3.6.34), Eq.(3.6.35), Eq.(3.6.36), Eq.(3.6.37) and Eq.(3.6.38) with $l_g = 2.5 \text{ mm}$. In absence of gradient effect, we would get the inner gray ellipse corresponding to classical Crossland criterion.	46
4.1	Linear accumulation of damage with linear evolution	51

4.2	Damage with nonlinear evolution and linear accumulation, where high then low stress loading sequence leads to the same fatigue life.	51
4.3	Damage with nonlinear evolution and nonlinear accumulation, where high stress and low stress follow different damage evolution curve. This leads to differences into the summation of fatigue life proportion between different loading sequences.	52
4.4	Damage accumulation in terms of N in constant loading condition, with D and N are related by the evolution equation (4.1.12)	55
4.5	Influence of function α in fatigue damage versus fatigue life ratio ($\gamma = 0.1$)	57
4.6	Influence of function γ in a plot of damage versus fatigue life ratio with $\alpha = 0.8$	58
4.7	$A_{II} - N_F$ curve in rotation at $r=0.1$	61
4.8	Two-stress level loading in pure rotation at $r=0.1$. The lower curve displays the relative proportion of cycles in high-low sequence, the upper curve displays the same information in a low-high sequence	62
4.9	$A_{II} - N_F$ curve in 4-point bending at $y=3$	63
4.10	Two-stress level loading in 4-point bending at $y=3$. The lower curve displays the relative proportion of cycles in high-low sequence, the upper curve displays the same information in a low-high sequence	64
4.11	$A_{II} - N_F$ curve in rotative bending at $r=3$	64
4.12	Two-stress level loading in rotative bending at $r=0.5$. The lower curve displays the relative proportion of cycles in high-low sequence, the upper curve displays the same information in a low-high sequence	65
4.13	Complex Cyclic Loading	67
4.14	Reorder to Start from Absolute Maximum (retrieved from “How to Calculate Fatigue Life When The Load History Is Complex”, February 13, 2015, author: Michael Bak, https://caeai.com/blog/how-calculate-fatigue-life-when-load-history-complex)	68
4.15	Imagine Filling with Water and Extract Stress Range and Mean Stress (retrieved from “How to Calculate Fatigue Life When The Load History Is Complex”, February 13, 2015, author: Michael Bak, https://caeai.com/blog/how-calculate-fatigue-life-when-load-history-complex)	68
4.16	Drain Water Starting at Lowest Valley and Repeat Cycle Extraction (retrieved from “How to Calculate Fatigue Life When The Load History Is Complex”, February 13, 2015, author: Michael Bak, https://caeai.com/blog/how-calculate-fatigue-life-when-load-history-complex)	68
4.17	Rainflow counting method demonstration	69
4.18	One million normally distributed random stresses around -100MPa	69
4.19	Amplitudes distribution extracted from Figure 4.18	70
4.20	Mean stresses distribution extracted from Figure 4.18	70
4.21	Rainflow matrix extracted from Figure 4.18	71
5.1	Kinematic hardening: a) uniaxial stress-strain diagram, b) evolution of the yield surface in the biaxial stress plane	75
5.2	Haigh diagram showing test data points for the effect of mean stress, and the Gerber, modified Goodman and Soderberg relations.	78
5.3	Weakening scales s probability distribution curve when $\beta = 1.5$	79
5.4	Weakening scales s probability distribution curve when $\beta = 5$	80
5.5	Illustration of uniaxial cyclic load with microscopic plastic dissipation at scale s	82
5.6	The relation between \tilde{D} and D when $\gamma = 2$	84

5.7	High to low and low to high loading sequence comparison in 4-point bending($F_{low} = 5000N, F_{high} = 30000N, Radius = 0.2m, \Sigma_u = 1.67E8$), with the proposed damage accumulation law (Eq.(5.6.5)) induced equation Eq.(5.6.10) and Chaboche type α (Eq.(5.6.7)) containing Crossland criterion	87
5.8	The evolution of α in bending and torsion with $\Sigma_y = 1080 \text{ MPa}, \Sigma_{bending} = \Sigma_{torsion} = 500 \text{ MPa}, a = 0.3$ and 200 time steps in one cycle	92
5.9	Comparing numerical strategy with optimal time steps in one cycle with the old one, in this way the number of steps in unit cycle is reduced from 400 to 35, meaning a cost reduction factor of 0.0875 (with $\Delta\alpha = 0.05, a = 0.4, \lambda = 0.1, \Sigma_y = 230 \text{ MPa}, \Sigma_{bending} = 225 \text{ MPa}$)	92
5.10	S-N curve of bending test on 30NCD16 steel using numerical and analytical method (Eq.(5.7.15)) with different time steps. Data are those of table.5.1	94
5.11	S-N curve using analytical and numerical results with optimal time steps methods ($\beta = 1.1, a = 0.01, \Delta\alpha = 2E - 5$ in unit cycle), yielding 200 full time steps reduced to 197 optimal time steps	96
5.12	S-N curve using analytical and numerical results with optimal time steps methods ($\beta = 1.1, a = 0.01, \Delta\alpha = 1E - 5$ in unit cycle), yielding 200 full time steps reduced to 199 optimal time steps	96
5.13	Relative error $\left(\frac{NF_{opt} - NF_{analytical}}{NF_{analytical}} \right)$ between analytical and numerical results with optimal time steps methods ($\beta = 1.1, a = 0.01, \Delta\alpha = 2 \times 10^{-5}$ in unit cycle) .	97
5.14	Relative error $\left(\frac{NF_{opt} - NF_{analytical}}{NF_{analytical}} \right)$ between analytical and numerical results with optimal time steps methods ($\beta = 1.1, a = 0.01, \Delta\alpha = 1 \times 10^{-5}$ in unit cycle) .	97
5.15	Microscopic $(\underline{S} - \underline{b})_{trial}$ and $(\underline{S} - \underline{b})$ evolution with time under different weakening scales ($s_3 = 1.21$ and $s_{10} = 1.13$) in sinusoidal load with zero mean stress	98
5.16	Microscopic $(\underline{S} - \underline{b})_{trial}$ and $(\underline{S} - \underline{b})$ evolution with time under different weakening scales ($s_3 = 1.21$ and $s_{10} = 1.13$) in sinusoidal load with mean stress=300 MPa	99
5.17	Validation of dissipated energy in all scales with analytical (method 3) and numerical method (method 1) with $\beta = 1.1, \Sigma = 0.85\sigma_y$. The time evolution of α does not play a role in the dissipation calculation which is normal since α does not enter in the dissipation calculation	99
5.18	Validation of dissipated energy in all scales with analytical and numerical method(enlarge- ment of Figure 5.17)	100
5.19	Dissipated energy accumulation through time with different methods, there are 100 time steps in unit cycle	100
5.20	Dissipated energy accumulation through time with of 3 methods(enlarge- ment of Figure 5.19)	101
5.21	Relative difference $\frac{W_{analytical} - W_{numerical}}{W_{analytical}}$ between analytical energy loss and nu- merical one with α varying with time of Figure 5.19	101
5.22	Damage evolution with time under sinusoidal load with different methods, there are 100 time steps in unit cycle($\beta = 1.1, \Sigma = 0.85\sigma_y$)	102
5.23	Damage evolution with time under sinusoidal load with two different methods(enlarge- ment of Figure 5.22)	102
5.24	Relative difference $\frac{D_{analytical} - D_{numerical}}{D_{analytical}}$ evolution with time of Figure 5.22	103
5.25	Validation of dissipated energy in all scales with analytical and numerical method with $\beta = 5, \Sigma = 0.4\sigma_y$	103

5.26 Validation of dissipated energy in all scales with analytical and numerical method with $\beta = 5$, $\Sigma = 0.8\sigma_y$	104
5.27 Damage evolution with time under sinusoidal load with $\beta = 5$, $\Sigma = 0.4\sigma_y$. In such a severe loading and with extreme non-linearity, the simple Chaboche like formula with frozen α departs from the outcome of the full numerical model	104
5.28 Damage evolution with time under sinusoidal load with $\beta = 5$, $\Sigma = 0.8\sigma_y$	105
5.29 Two level sequence effect. By comparing the vertical figures we can see high stress gives high $(1 - \alpha)$ value which causes fast damage accumulation speed. The evolution of $(1 - \alpha)$ is highly nonlinear and follows the value of stress at each time step.	107
5.30 Fatigue life of random loading dispersion	108
5.31 Major damage effect using different magnification power of Eq.(5.8.1) on sequence effect. Here high stress is 1 MPa and low stress is 0.8 MPa. We see that using a large power f in Eq.(5.8.1) induces a stronger sequence effect.	109
5.32 $(1-\alpha)$ term which stands for the load intensity evolution, both with and without the magnification power f	110
6.1 Complex loading of a car suspension arm (data from PSA tests)	116
6.2 Specimen geometry for fatigue tests of AW-6106 T6 aluminum (sample given by PSA)	116
6.3 Random loading history on BATCH_A_06 of AW-6106 T6 aluminum (see Tab.6.2)	117
6.4 Comparison between experimental and numerical results of 1D cyclic and random loading on aluminum fatigue tests by CETIM with constant α from the first row of Tab.6.7	120
6.5 Comparison between experimental and numerical results of 1D cyclic and random loading on aluminum fatigue tests by Cetim with load dependent α . Coefficients data are given in the second row of Tab.6.7	120
6.6 Specimen geometry for fatigue tests of aluminum 6082 T6 (dimension in millimeters), from Susmel and Petrone [2003]	121
6.7 The loading path and loading waveform of multiaxial corrosion fatigue (stress control) (a) loading path of proportional and non-proportional, (b) loading waveform of proportional loading, (c) loading waveform of non-proportion (Huang et al. [2017])	124
6.8 The 90° out-of-phase loading path has been found to produce the largest degree of non-proportional hardening (EFA).	124
6.9 Calibration on on 6082 T6 aluminum (Susmel and Petrone [2003]). Comparison between experimental results and our model used with coefficients given in Tab.6.11. We obtain a good correlation in bending and torsion tests. The out of phase test are not satisfactory in these batches: P32BT8, P41BT15, P36BT11.	125
6.10 Calibration on 30NCD16 (DUBAR [1992]). We can observe that the bending-torsion experimental values are largely dispersed	128
6.11 Calibration on 30NCD16 (DUBAR [1992]). In figure (c) test 29 (same N_F with test 30 but with smaller $\sigma_{x,m}$) and test 32 (2-D with large mean stress) from Tab.6.15 are more dispersed. The numerical tests are carried out using the coefficients of Tab.6.16	128
6.12 Fatigue curves on SM45C steel by Lee [2013]	130
6.13 Calibration on SM45C	133
6.14 Calibration on SM45C. The numerical tests are carried out using the coefficients of Tab.6.22	134
6.15 Bending-torsion fatigue tests on cylindrical specimens (Carpinteri et al. [2003])	136
6.16 Bending-torsion fatigue tests on cylindrical specimens (Carpinteri et al. [2003])	137
6.17 Multiaxial random loading sequence	138

6.18 S_a of bending tests with mean stress on 10HNAP	140
6.19 $Hydro_{+-}$ of bending tests with mean stress on 10HNAP	141
6.20 Bending and torsion test on 10HNAP steel($R=-1$). Data are presented in Tab.6.30 and 6.31. The torsion best fit and the bending numerical results(optimal time step of method 2 deduced in Chapter 5) are obtained with the coefficients of Tab.6.28	142
6.21 Wöhler tensile curves for various mean stress values. Data are presented in Tab.6.25 and results are obtained with the coefficients of Tab.6.28	143
6.22 Calibration on 10HNAP steel, bending and torsion tests on 10HNAP($R=-1$). Data are presented in Tab.6.30 and 6.31 and results obtained with the coefficients of Tab.6.28 .	144
6.23 Calibration on 10HNAP steel, bending tests with various mean stress on 10HNAP, data from Tab.6.25 and results obtained with the coefficients of Tab.6.28. For the case of $\sigma_m = 300$ MPa, the macroscopic maximum stress is greater than yield limit, which does not match our assumption that the material stays in elastic regime macroscopically (section 5.4.1).	145
6.24 Random bending-torsion 2D tests on 10HNAP, data from Tab.6.26 and Jabbado [2006]. Results are obtained with the coefficients of Tab.6.29 ($\alpha_M = \pi/8$ and $r = 0.2$)	146
6.25 Random bending-torsion 2D tests on 10HNAP, data from Tab.6.27 and Jabbado [2006]. Results are obtained with the coefficients of Tab.6.29 ($\alpha_M = \pi/4$ and $r = 0.5$)	147

List of Tables

3.1	Length scales of different materials	42
4.1	α induced sequence effect parameter η value with different criteria in pure rotation	62
4.2	α induced sequence effect parameter η value with different criteria in bending	63
4.3	α induced sequence effect parameter η value with different criteria in rotative bending	63
5.1	Material parameters in a simple cyclic load	98
5.2	Parameters concerned	112
5.3	Example of parameters sensitivity at cyclic loading of BATCH_A_02 on AW-6106 T6 aluminum (table.6.2)	113
6.1	Material parameters of AW-6106 T6 aluminum	116
6.2	Fatigue tests result on AW-6106 T6 aluminum, test data provided by CETIM	117
6.3	Proportion of stress above different thresholds with $\Sigma_y=230\text{MPa}$, test data provided by CETIM on AW-6106 T6 aluminum.	118
6.4	Parameters sensitivity at random loading of ep05 on AW-6106 T6 aluminum	118
6.5	Parameters sensitivity at cyclic loading of ep02 on AW-6106 T6 aluminum	119
6.6	Parameters sensitivity at random loading of ep05 on AW-6106 T6 aluminum	119
6.7	The parameters in 1D cyclic and random loading on AW-6106 T6 aluminum fatigue tests by Cetim	119
6.8	Mechanical and dynamic characteristics of aluminum 6082 T6 (Susmel and Petrone [2003])	121
6.9	Simple bending and torsion tests ($R = -1$), data from Susmel and Petrone [2003]	122
6.10	In-phase and out-of-phase bending-torsion tests ($R = -1$), data from Susmel and Petrone [2003]	123
6.11	Parameter identification of AL6082T6 steel	123
6.12	Mechanical and dynamic characteristics of 30NCD16 steel DUBAR [1992]	126
6.13	30NCD16 steel fully reversed bending tests DUBAR [1992]	126
6.14	30NCD16 steel fully reversed torsion tests (DUBAR [1992])	127
6.15	30NCD16 steel bending-torsion tests (DUBAR [1992])	127
6.16	Parameter identification of 30NCD16 steel	127
6.17	Chemical composition of SM45C steel	129
6.18	Mechanical and dynamic characteristics of SM45C steel	129
6.19	SM45C steel fully reversed bending tests(extracted from Lee [2013])	131
6.20	SM45 steel fully reversed torsion tests(extracted from Lee [2013])	131
6.21	Effect of mean bending stress on out-of-phase(90°) fatigue of SM45C steel (Lee [2013])	132
6.22	Parameter identification of SM45C steel	132
6.23	Chemical composition of 10 HNAP steel, data from Bedkowski [1994]	135
6.24	Mechanical characteristics of steel 10 HNAP, data from Bedkowski [1994]	135
6.25	Experimental results of tensile tests for various values of σ_m , data from VIDAL	136

6.26	Fatigue results under variable loads for $\alpha' = \pi/8$ and $r = f(\tau_{xy})/f(\sigma_{xx}) = 0.2$. . .	137
6.27	Fatigue results under variable loads for $\alpha' = \pi/4$ and $r = f(\tau_{xy})/f(\sigma_{xx}) = 0.5$. . .	138
6.28	Model parameters for 10HNAP steel	138
6.29	Model parameters for 10HNAP steel (random loading)	139
6.30	Constant amplitude bending tests performed on 10HNAP steel, data from VIDAL . .	139
6.31	Constant amplitude torsion tests performed on 10HNAP steel, data from VIDAL . .	139

Dedicated to the ones who supported me

Nomenclature

Σ_{max}	maximum stress during the loading cycles
S_{max}	maximum deviatoric stress during the loading cycles
σ_m	mean stress
σ_H	hydrostatic stress
σ_{-1}	fatigue limit for fully reversed condition
s_{-1}	tensile fatigue limit for $R = -1$
b	back stress
σ_y	macroscopic yield stress
N	current number of cycles
N_F	number of cycles to failure
\dot{p}	accumulated plastic strain rate given as $\sqrt{\frac{2}{3}} \dot{\varepsilon}_p $
D	damage variable
σ_a	stress amplitude
σ_u	ultimate tensile stress
$\langle \rangle$	Macaulay bracket symbol which keeps the positive value and set negative value to zero
\dot{w}	energy dissipation rate at a certain scale
\dot{W}	energy dissipation rate at all scales
W_{cyc}	dissipated energy per cycle
$\dot{\varepsilon}_p$	rate of effective plastic strain
\ddot{p}	accumulated plastic strain rate given as $\sqrt{\frac{2}{3}} \dot{\varepsilon}_p $
E	Young's modulus
$k = 500 \sim 800 MPa$	hardening parameter
β	weakening scales distribution exponent
γ	material parameter from Chaboche law
α	characterizes non-linearity of damage accumulation
a	material parameter from Chaboche law
$\lambda = 0 \sim 3$	hydrostatic pressure sensitivity
$\underline{\underline{S}} = dev \dot{\underline{\underline{\Sigma}}}$	deviatoric part of the stress tensor
$A_{II} = \tau_{oct,a} = \sqrt{\frac{1}{3}J_{2,a}}$	the amplitude of octahedral shear stress
$\dot{\varepsilon}_p$	rate of effective plastic strain
W_0	reference density of damage energy
J_2	The second principal invariant of the stress deviatoric tensor
$\sigma_{VM} = \sqrt{3J_2}$	Von Mises stress

1

Introduction

Contents

2.1	Basquin curve	6
2.2	Basic fatigue criteria	7
2.2.1	Criteria based on stress	8
2.2.2	Criteria based on energy	13
2.2.3	Criteria based on plasticity-damage coupling	18
2.3	Calculation method without cycle counting	21
2.3.1	Morel's method	21

1.1 General introduction

The fatigue of metallic structures subjected to cyclic stresses is a phenomenon which is traditionally studied at two levels. The fatigue is respectively qualified "low cycle" or "high cycle" if the load causing the rupture is applied during a relatively small or a large number of cycles. In turn, "high cycle fatigue" is divided in two domains: "limited endurance" where we speak of the finite lifetime regime and "unlimited endurance" where the structure can support a number of cycles theoretically infinite without breaking.

The threshold value dividing low- and high-cycle fatigue is somewhat arbitrary, but is generally based on the raw materials behavior at the micro-structural level in response to the applied stresses. Low cycle failures typically involve significant plastic deformation. An example would be reversed 90° bending of a paper clip. Gross plastic deformation will take place on the first bend, but failure will not occur until approximately 20 cycles. Plastic deformation does play a role in high cycle fatigue; however, the plastic deformation is very localized and not necessarily discernible by a macroscopic evaluation of the component. Most metals with a body centered cubic crystal structure have a characteristic response to cyclic stresses. These materials have a threshold stress limit below which fatigue cracks will not initiate. This threshold stress value is often referred to as the endurance limit. In steels, the life associated with this behavior is generally accepted to be 2×10^6 cycles (Stone [2012]). In other words, if a given stress state does not induce a fatigue failure within the first 2×10^6 cycles, future

failure of the component is considered unlikely. For spring applications, a more realistic threshold life value would be 2×10^7 cycles ([Stone \[2012\]](#)). Metals with a face center cubic crystal structure (e.g. aluminum, austenitic stainless steels, copper, etc.) do not typically have an endurance limit. For these materials, fatigue life continues to increase as stress levels decrease; however, a threshold limit is not typically reached below which infinite life can be expected.

1.1.1 Industrial background and motivation

The search for the best performance at the best cost in mechanics and transport leads to increasingly severe conditions of use of the mechanical components. Fatigue failures are widely studied because it accounts for 90% of all service failures due to mechanical causes ([Sohar \[2011\]](#)). Fatigue failures occur when metal is subjected to a repetitive or fluctuating stress and will fail at a stress much lower than its tensile strength and the process happens without any plastic deformation (no warning).

These practical problems can lead to the emergence of fatigue for very high level of stress gradient for small scale or complex geometric structures and non-constant multiaxial loading history. For these so-called "extreme" stresses, the mechanisms of damage as well as fatigue resistance levels are mostly unknown. This poses an important problem during the design phase since, on the one hand, the existing endurance criteria struggle to account for behavior for this type of loading, and on the other hand, the fatigue data that would allow to identify a model adapted to this problem are almost non-existent.

On the other hand, the mechanical components are generally of complex nature undergoing complex loads. Manufacturers are looking for a model of lifetime of their components, which is simple to use, great applicability to metallic materials and which treats almost all cases of possible loads. In the domain of limited endurance, very few criteria are proposed. At present, none of them can be used in design offices, and does not fully meet the demand for a tool to predictive lifetime. Indeed, most of the existing approaches rely on methods of counting cycles, whose extension to the case of multiaxial stresses turns out to be difficult or even impossible because of the difficulty of extracting and defining cycles.

Previous work carried out in collaboration with the PSA company indicates that the criteria of multi-axial endurance used for fatigue design (Papadopoulos model and Dang Van's criterion) struggle to account effectively for these very individuals ([Koutiri \[2011\]](#)). It therefore seems essential to characterize the mechanisms damage of this type of loading and to implement a modeling able to reflect these particular fatigue conditions.

The aim of this thesis is thus to establish a deterministic model of lifetime on metal structures working in limited endurance in high cycle fatigue, which handles almost all load cases (with constant and variable amplitudes) without recourse to cycle counting.

This thesis work is part of a regional project of "Chaire André Citroën"; one of whose objectives is to develop teaching by encouraging initiatives in the automotive sector and confronting students with typical technological innovations and major scientific challenges. The aim of this work is to study the fatigue-related criteria with a large number of cycles, taking into account the effects of variation in time or space. Three contributions were developed:

- Extension of the fatigue criteria to take into account the gradient effect.
- Development and testing of nonlinear accumulation methods of damage.
- Implementation of a strategy for measuring fatigue through a multi-scale analysis of the dissipated energy, thus enabling three-dimensional and complex states of charge to be treated and avoiding the notion of loading cycle.

The study presented in this report focuses more particularly on the last theme, with, as will be seen, a particular emphasis on the effect of micro-structural heterogeneities on fatigue.

The approach for solving the problem posed has four main stages:

- Proposing a strategy to decouple the effects of stress gradient and size effect.
- Review of the existing description of the non-linearity of damage accumulation and history dependent sequence effects.
- Construction of a model of fatigue behavior that accounts for the effects of microscopic plasticity as well as damage accumulation and history sequencing effects.
- Numerical simulation with such a model both on cyclic loading conditions and on random loading history.

1.1.2 Context and background

The fatigue of materials with many cycles is one of the phenomena that can lead to rupture of machine parts or structures in operation. Its progressive character masked until sudden breakage does not allow easy prediction of the durability of the structure.

The main factors influencing the fatigue resistance of materials are numerous (loading mode, temperature, micro-structural heterogeneities, residual stresses ...), making it a complex phenomenon to study. A lot of work has been done in the goal of better understanding the influence of these different factors. One of the main parameters influential, repeatedly studied, is the damage mechanism of the time varying stress.

Numerous experimental observations made on metallic materials have shown that the damage mechanisms operating in fatigue with large number of cycles and leading to breakup are of two categories. In a first step known as the priming step, micro-plasticity mechanisms, generally operating around heterogeneities specific to the material (inclusions, porosities, etc.), are the origin of the appearance of micro-cracks. If the load level is high enough, these cracks increase and cross a number of micro-structural barriers (e.g. grain boundaries). When the crack has reached a size sufficiently large in relation to the microstructure that the plasticized zone, a second phase intervenes where it propagates according to, the laws of fracture mechanics.

Two types of very distinct approaches are often used to model these mechanisms. The first concerns priming and mainly uses the framework of the mechanics of the micro-plasticity considered to be the main cause of onset of a crack. The second uses the fracture mechanics framework to estimate the number of cycles necessary for the propagation of a pre-existing crack ([Koutiri \[2011\]](#)).

In our work we concentrate on the first phase and consider the mechanisms related to the stochastic distribution of pre-existing micro-cracks at different scales which undergo strong plastic yielding in cyclic load history. The number of cycles to failure is determined from the plastic shakedown cycle occurring at these microscales.

1.1.3 Outline of the work

The bibliographical study conducted in the first part of this thesis ([Chapter 2](#)) aims to overview the basic multiaxial fatigue criteria and the physical basis of their origin. Models using the elastic shakedown concept, plasticity / damage on the mesoscopic scale as well as energy are compared. We will show that some loading effects are correctly reflected, however for others, the predictions are very different from one approach to another.

The second part ([Chapter 3](#)) is devoted to the extension of some classic high cycle fatigue (HCF) criteria in order to take into account a sensitivity of the criteria to stress spatial variations, and second to compare the performances of the extensions through several experimental fatigue tests. The gradient beneficial effect on bending-torsion in comparison with tension-compression is presented. Mechanisms of different approaches are compared and a more practical and simple expression is proposed taking into account the gradient of the stress amplitude and the maximum hydrostatic stress.

The generalization of the approach to other multiaxial fatigue criteria is also proposed. The proposition is then tested and applied to different simple situations such as cantilever rotative bending. The relative errors between the exact solutions and the experimental data are estimated. Biaxial bending-torsion tests are also simulated to demonstrate the capabilities of the approach.

The non-linearity of damage accumulation in fatigue is discussed in the third part (Chapter 4). The objective of this section is to review and use the development life model that takes into account the presence of complex variations of the load cycle. We focus on Chaboche damage accumulation law in case of multiaxial high cycle fatigue. Heuristic formulations with different multiaxial fatigue criteria have been proposed and will be briefly reviewed.

Chapter 5 then considers the problem of handling complex time histories in multiaxial loading. Cycle counting method to compare the effect of variable amplitude load histories to fatigue data and curves obtained with simple constant amplitude load cycles is presented, together with different approaches and limitations for handling multiaxial loading.

From this context, we then develop our new model. It is based on a priori given simplified probabilistic description of local material weak points. At each such point, a local plastic model with kinematic hardening is introduced, with a given distribution $p(s)$ of yield weakening factors. To take into account a dependence of the macroscopic fatigue behavior to the hydrostatic stress, the yield limit at each local point is supposed to depend on this macroscopic hydrostatic stress. The model will then suppose that the fatigue accumulation depends on the energy which is dissipated by plasticity of all these points during the loading history. This energy through all scales s will be combined with the nonlinear damage accumulation laws of chapter 4 to produce a simplified “multiscale” model of microscopic damage evolution.

The sixth chapter of the document deals with the numerical implementation of our method and its validation on different experimental results. Instead of doing the integration directly which can be difficult for complex loading, the Gaussian Quadrature rule with Legendre points is used to give the value of local dissipated energy rate. Cyclic and random tests on aluminum alloy used for automobile suspension arm is calibrated with our model. Then in the last chapter a multidimensional application is performed showing the capability of prediction on fatigue life of different material and loading patterns.

2

Fatigue life calculation methods

Contents

3.1	Introduction	30
3.2	A first gradient approach	31
3.2.1	General formulation	31
3.2.2	The classical Crossland criterion	32
3.2.3	Formulation of Crossland criterion with gradient effect	33
3.3	Optimized Crossland Criterion formulation	33
3.4	Optimized Papadopoulos Criterion formulation	34
3.5	Optimized Dang Van Criterion formulation	36
3.6	Calibration of the criteria	36
3.6.1	Fully reversed 4-point bending and rotating cantilever bending fatigue tests	36
3.6.2	Bending-torsion fatigue tests	42
3.7	Discussion	46
3.8	Conclusion and perspectives	47

To obtain a better knowledge of the impact of different types of stresses and mechanism of energy dissipation in high cycle fatigue(HCF), many researchers have carried out tests often difficult to implement and to control. From the data obtained and sometimes from the observations of the associated mechanisms, they have developed models that account more or less faithfully for the experiment. The approaches used are quite varied, but since the field of fatigue that interests us (HCF) is often governed by crack initiation, we make the choice in this chapter to treat only models established in the framework of continuum mechanics. It will therefore be a question of the state of the art of the most successful existing models but above all we will try to compare the predictions obtained when dealing with the equivalent stress and energy dissipation. This study will make it possible to reveal the great variety of the predictions obtained and to direct our work towards a better understanding of the behavior for the loads appearing the most problematic.

2.1 Basquin curve

Stress-Life Diagram (S-N Diagram)

The basis of the Stress-Life method is the Wohler S-N diagram. The S-N diagram plots nominal stress amplitude S versus cycles to failure N . There are numerous testing procedures to generate the required data for a proper S-N diagram. S-N test data are usually displayed on a log-log plot, with the actual S-N line representing the mean of the data from several tests.

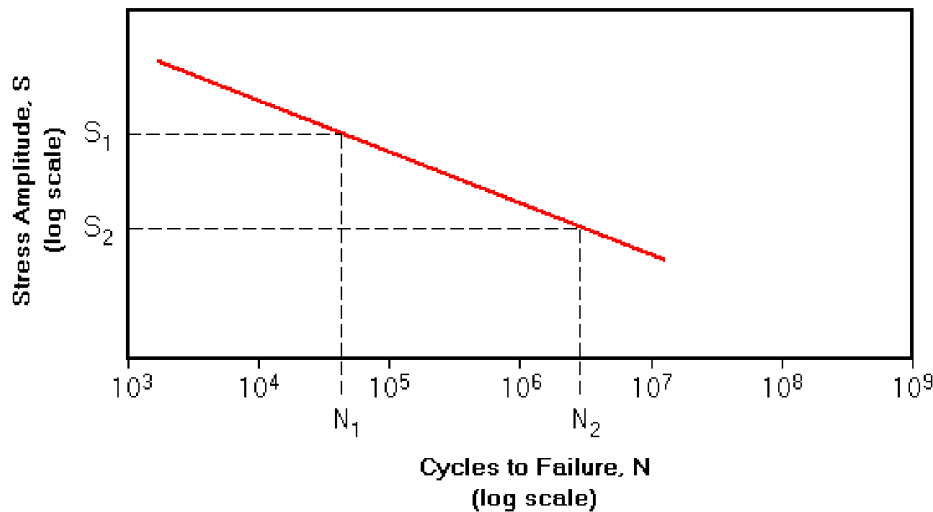


Figure 2.1 – Idealized S-N curve for high cycle fatigue.

Certain materials have a fatigue limit or endurance limit which represents a stress level below which the material does not fail and can be cycled infinitely. If the applied stress level is below the endurance limit of the material, the structure is said to have an infinite life. This is characteristic of steel and titanium in benign environmental conditions. A typical S-N curve corresponding to this type of material is shown in Figure 2.1.

Many non-ferrous metals and alloys, such as aluminum, magnesium, and copper alloys, do not exhibit well-defined endurance limits. These materials instead display a continuously decreasing S-N response. In such cases a fatigue strength S_f for a given number of cycles must be specified. An effective endurance limit for these materials is sometimes defined as the stress that causes failure at 1×10^8 or 5×10^8 loading cycles.

The concept of an endurance limit is then used in infinite-life or safe stress designs. The possibility of infinite cycling is due to interstitial elements (such as carbon or nitrogen in iron) that pin dislocations, thus preventing the slip mechanism that leads to the formation of microcracks. Care must be taken when using an endurance limit in design applications because infinite cycling potentiality can disappear due to:

- Periodic overloads (unpin dislocations)
- Corrosive environments (due to fatigue corrosion interaction)
- High temperatures (mobilize dislocations)

The endurance limit by itself is not a true property of a material, since other significant influences such as surface finish cannot be entirely eliminated. However, a test values (S'_e) obtained from polished specimens provide a baseline to which other factors can be applied. Influences that can then affect the endurance limit include:

- Surface Finish

- Temperature
- Stress Concentration
- Notch Sensitivity
- Size
- Environment

Power Relationship

When plotted on a log-log scale, an S-N curve can be approximated by a straight line as shown in Figure 2.1. Basquin's equation is a power law relationship as Eq.(2.1.1) which describes the linear relationship between the applied stress cycles (S) in the y-axis and the number of cycles to failure in the x-axis plotted on a log-log scale.

$$N = BS^{\frac{1}{b}} \quad (2.1.1)$$

To calculate the slope of the Basquin equation from two significant curve points, we need to solve the system of equations:

$$N_1 = N_2 \left(\frac{S_1}{S_2} \right)^{\frac{1}{b}},$$

yielding

$$b = \frac{\log S_1 - \log S_2}{\log N_1 - \log N_2},$$

where b is the slope of the line. Then the coefficient B in Eq.(2.1.1) is given by

$$B = N_1 S_1^{-\frac{1}{b}} = N_2 S_2^{-\frac{1}{b}},$$

with S_1 denoting the stress range value of the considered test.

For the constant B , in industry the stress range value (from the maximum cyclic stress to the minimum cyclic stress) is often considered. If the stress values of the S-N curve are given as alternating stresses (which is the common practice), multiply these stresses by 2 to calculate the constant B (stress range = 2* alternating stress, assuming a zero mean stress and full reversal of the cyclic load). If the S-N curve data are given in stress range values, apply them directly in the equation for estimating the constant B .

The power relationship is only valid for fatigue lives that are on the design line. For ferrous metals this range is from 1×10^3 to 1×10^6 cycles. For non-ferrous metals, this range is from 1×10^3 to 5×10^8 cycles.

Basquin curves are quite simple but how can we apply them to more complex loadings?

This limitation is at the origin of the development of more detailed criteria to be described in the next section.

2.2 Basic fatigue criteria

This bibliographic chapter reviews different methods to calculate the lifetime of multiaxial high cycle fatigue. In fact, the difficulty of defining the equivalent stress in situations with multiaxial loading and variable amplitude loading reveals the necessity of study these methods. These criteria allows to determine whether the stress trajectory in the stress space leads to the failure of the points concerned.

Papadopoulos suggested, in particular, to group families of fatigue criteria into four categories:

- Criteria based on strain
- Criteria based on stress

- Criteria based on energy
- Criteria based on plasticity-damage coupling.

Generally, the criteria developed in strain and sometimes in energy are adapted to the oligocyclic fatigue where the tests are often carried out with imposed strain. Approaches in stress and sometimes in energy, as well as those based on the coupling of plasticity and damage which have begun to emerge in recent years are being applied in the domain of endurance. Therefore, we will focus on the last three categories and analyze the different approaches.

2.2.1 Criteria based on stress

Three types of approach can be distinguished:

- Critical Plan Approaches
- Approaches based on stress invariants
- The criteria based on mean stress in an elementary volume

For simplicity and to avoid too costly identification procedures of fatigue data, criteria are often expressed using two parameters to characterize the local load. The first relates generally to a shear stress (on a plane or on average over an elementary volume) while the second reflects the normal stress effects (mean and amplitude) through the hydrostatic stress or the normal stress. The criteria using the hydrostatic stress are the most numerous ([Crossland \[1956\]](#), [Sines \[1959\]](#), [Morel \[1998\]](#), [Thu \[2008\]](#)). The micro-macro approach applied to the field of endurance was born with the work of ([Dang Van \[1973\]](#)), and since it has been used many times, including by ([Papadopoulos \[1993\]](#)) to take better account of loading path effects.

Many fatigue limit criteria can thus be written as:

$$f(\tau) + g(\sigma) \leq 0 \quad (2.2.1)$$

where f and g are given functions of the shear stress τ and of the normal stress σ respectively, as applied to different interfaces within the material.

The normal and shear stress acting on the material planes and used in Eq.(2.2.1) are sometimes defined from a critical plane ([Findley \[1959a\]](#)), or through integration at every plane of an elementary volume ([Liu and Zenner \[1993\]](#)). [Thu \[2008\]](#) proposes, in particular, a probabilistic approach based on this type of integration.

Crossland Criterion

Using traditional fatigue criteria, a near hyperbolic relationship between stress and fatigue life is assumed, with an asymptotic limit defined as the endurance stress. To predict this asymptotic limit, the Crossland Criterion is probably the most widely known. Crossland proposed that the second invariant of the deviatoric stress tensor and the hydrostatic pressure are the variables governing the endurance limit.

The classical Crossland criterion defines the fatigue limit of metallic specimens subjected to multi-axial in-phase cyclic stress ([Crossland \[1956\]](#)) :

$$f(\sqrt{J_{2,a}}, P_{max}) = \tau_{eq} + aP_{max} - b \leq 0 \quad (2.2.2)$$

where $\tau_{eq} = \sqrt{J_{2,a}}$ measures the amplitude of variation of the second invariant of the deviatoric stress and P_{max} is the maximum hydrostatic stress observed during a loading cycle. If

$f(\sqrt{J_{2,a}}, P_{max})$ is negative or null, there is no damage. If $f(\sqrt{J_{2,a}}, P_{max})$ is positive, there is likely to be damage and hence limited endurance. The physical constants a and b are material constants that needs to be determined experimentally. The amplitude of the square root of the second invariant of the stress deviator can be defined, in general case, as the radius of the smallest hypersphere of the deviatoric stress path (Papadopoulos et al. [1997]):

$$\sqrt{J_{2,a}} = \frac{1}{\sqrt{2}} \min_{\underline{S}_1} \left\{ \max_t \left((\underline{S}(t) - \underline{\underline{S}}_1) : (\underline{S}(t) - \underline{\underline{S}}_1) \right) \right\}. \quad (2.2.3)$$

Recall that the deviatoric stress \underline{S} associated to a stress tensor $\underline{\underline{\sigma}}$ is defined by

$$\underline{S} = \underline{\underline{\sigma}} - \frac{1}{3} (tr \underline{\underline{\sigma}}) \underline{\underline{1}}. \quad (2.2.4)$$

The maximum value that the hydrostatic stress reaches during the loading cycle is on the other hand:

$$P_{max} = \max_t \left\{ \frac{1}{3} tr(\underline{\underline{\sigma}}(t)) \right\}. \quad (2.2.5)$$

For a proportional cyclic loading, if one introduces the two extreme stress tensors $\underline{\underline{\sigma}}^A$ and $\underline{\underline{\sigma}}^B$ observed during the loading path, together with the stress amplitude

$$\underline{\underline{\Delta\sigma}} = \underline{\underline{\sigma}}^B - \underline{\underline{\sigma}}^A \quad (2.2.6)$$

and its deviatoric part $\underline{\underline{\Delta s}}$, the variation of the second invariant of the stress deviator reduces to

$$\begin{aligned} \sqrt{J_{2,a}} &= \frac{1}{2\sqrt{2}} \max_t \sqrt{\underline{\underline{\Delta s}} : \underline{\underline{\Delta s}}} \\ &= \frac{1}{2\sqrt{2}} \max_t \sqrt{(\Delta s_{11}^2 + \Delta s_{22}^2 + \Delta s_{33}^2 + 2\Delta s_{12}^2 + 2\Delta s_{13}^2 + 2\Delta s_{23}^2)}. \end{aligned} \quad (2.2.7)$$

The physical constants a and b can be related to the limit t_{-1} of endurance in alternate pure shear with

$$P_{max} = 0, \quad \underline{\underline{\Delta s}} = \begin{pmatrix} 0 & 2t & 0 \\ 2t & 0 & 0 \\ 0 & 0 & 0 \end{pmatrix}$$

and to the limit f_{-1} of endurance in alternate pure traction and compression where there is

$$P_{max} = \frac{1}{3}f, \quad \underline{\underline{\Delta s}} = \begin{pmatrix} \frac{4}{3}f & 0 & 0 \\ 0 & -\frac{2}{3}f & 0 \\ 0 & 0 & -\frac{2}{3}f \end{pmatrix}$$

by

$$a = \frac{(t_{-1} - \frac{f_{-1}}{\sqrt{3}})}{\frac{f_{-1}}{3}}, \quad b = t_{-1}. \quad (2.2.8)$$

Thus the classical Crossland criterion can be written as:

$$\sqrt{J_{2,a}} + aP_{max} - b \leq 0. \quad (2.2.9)$$

with a and b given by Eq.(2.2.8).

Dang Van Criterion

In multiaxial fatigue with large number of cycles, the important role of local plasticity on the appearance of a fatigue limit is widely accepted and fully justifies the use of a multi-scale approach.

Among the existing approaches, one of the most known and used is that of [Dang Van \[1999\]](#). This criterion is used in particular in the design of certain automotive structures at PSA and Renault. The criterion ([Dang Van et al. \[1986\]](#)) belongs to the family of critical plane type approaches. The main physical basis of this criterion focuses on the theory of elastic adaptation at two scales, mesoscopic and macroscopic. The macroscopic behavior of the material often remains elastic, only a grain oriented unfavorably undergoes plastic deformation. The author states the following hypothesis: "The multiscale approach is settled on the assumption that under high cycle fatigue loading, a structure will not be fractured by fatigue if an elastic shakedown is reached at the macroscopic scale as well as at mesoscopic scale." ([Dang Van \[1999\]](#)). The approach developed first is to describe the plasticity across the grain, assuming a yield criterion. The yield criterion is the law of Schmid with a linear isotropic hardening. The author then search the elastic adaptation formula and defines a fatigue test locally as shown in Figure 2.2 (Δ represents the tensor defining the orientation of the sliding system, γ is the plastic slip and τ is the amplitude of shear stress on the defined plan). Finally, a micro to

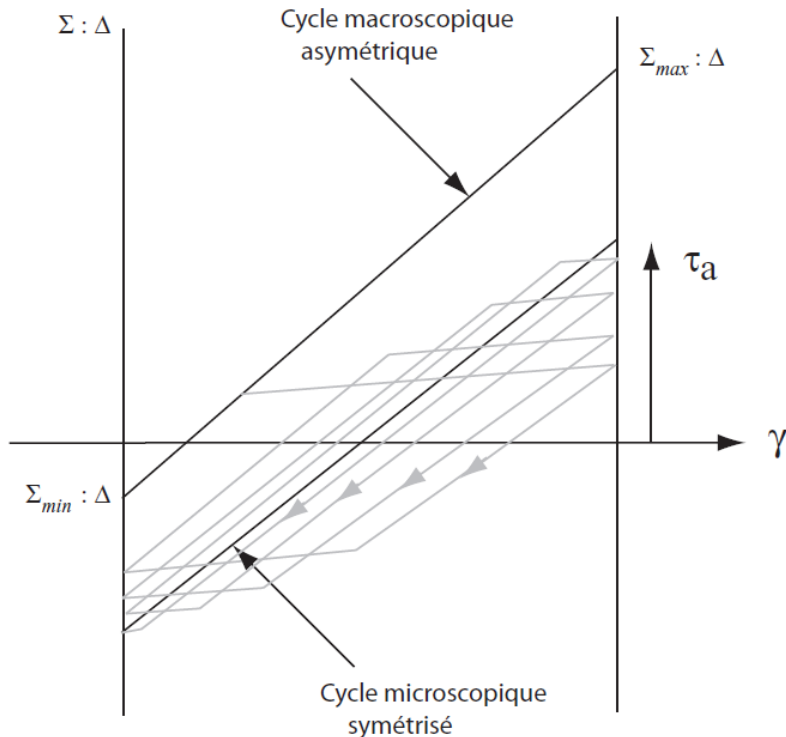


Figure 2.2 – Elastic adaptation at the two scales ([Dang Van \[1999\]](#))

macro upscaling strategy is applied to determine the criteria on the macroscopic scale. The localization law which is used is Lin-Taylor model that assumes equality of deformations at two scales. Using empirical relationships, the harmful role of the mean stress on the fatigue strength of the material is shown for type of uniaxial tensile stress. Dang Van shows the effect of the mean stress with hydrostatic stress term in the criteria expressed as a linear combination of mesoscopic shear stress on the maximum shear plane τ_a and the hydrostatic stress Σ_H .

The resulting Dang Van criterion presented in [Ballard et al. \[1995\]](#) is expressed as:

$$\max_{\underline{n}} \left\{ \max_t \{ \tau_a(\underline{n}, t) + a_D \Sigma_H(t) \} \right\} \leq b_D. \quad (2.2.10)$$

where τ_a denotes the mesoscopic shear stress amplitude and is obtained from a mesoscopic stress tensor $\hat{\sigma}$ defined by:

$$\hat{\sigma}(t) = (\underline{\sigma}(t) - \underline{s}^*).$$

Here \underline{s}^* is the center of the smallest hypersphere circumscribed to the loading path in deviatoric stress space. It is obtained by solving a “min-max” problem as follows:

$$\underline{s}^* = \arg \min_{\underline{s}_1} \left\{ \max_t \left\| \underline{s}(t) - \underline{s}_1 \right\| \right\}.$$

In the case of fully reversed loading, the values $\underline{s}^* = 0$ can be directly deduced without solving the “min-max problem” as in general case.

The principal stress values of stress tensor $\underline{\sigma}$ being denoted by $\hat{\sigma}_{III}(t) \leq \hat{\sigma}_{II}(t) \leq \hat{\sigma}_I(t)$, one gets the amplitude of shear stress by:

$$\max_{\underline{n}} \tau_a(t) = \frac{1}{2}(\hat{\sigma}_I(t) - \hat{\sigma}_{III}(t)).$$

Here $\Sigma_H(t)$ is the hydrostatic stress as a function of the time, given by:

$$\Sigma_H(t) = \frac{\sigma_{kk}(t)}{3}.$$

The Dang Van criterion then writes

$$\frac{1}{2}(\hat{\sigma}_I(t) - \hat{\sigma}_{III}(t)) + a_D \frac{tr(\underline{\sigma})}{3} \leq b_D. \quad (2.2.11)$$

The material characteristic parameters a_D and b_D of the Dang Van criterion, can be related to the fully reversed bending or tension- compression fatigue limit because of the same stress state between them, denoted by f_{-1} (or s_{-1}), and to the torsion fatigue limit, denoted by t_{-1} ,

$$a_D = \frac{3t_{-1}}{s_{-1}} - \frac{3}{2};$$

$$b_D = t_{-1}.$$

In the particular case of the uniaxial tension with average load $\Sigma_{xx,m}$ and amplitude $\Sigma_{xx,a}$, the criterion is written as:

$$\Sigma_{xx,a} \left(\frac{1}{2} + \frac{a_D}{3} \right) + \Sigma_{xx,m} \left(\frac{a_D}{3} \right) = b_D.$$

Papadopoulos Criterion

The approach proposed by [Papadopoulos \[1993\]](#) also uses the concept of elastic adaptation and even the localization law. According to him, “the observations at the mesoscopic scale show that the initiation of a fatigue crack is defined as the occurrence of micro-cracks corresponding to the rupture of the most deformed crystal grains in an aggregate. Thus, a fatigue limit criterion can be modeled by a limit value of the accumulated plastic strain in the most distorted grain.”

$$\gamma_{cum} \leq \gamma_{\infty}.$$

He proposes to opt for a mean value of the accumulated plastic strain on all possible slip systems of representative elementary volume (REV). So he chose to use a average value of accumulated plastic deformation rather than looking at failure of a single crystal. A spherical coordinate system is shown in Figure 2.3 to guide the normal vector in the material plane, and the unit direction vector r linked to a sliding direction of this plan is used to conduct the integration over all possible orientations.

More precisely, at any point O of a body, a material plane Δ can be defined by its unit normal vector \mathbf{n} . This vector \mathbf{n} makes an angle θ with the z-axis of a $Oxyz$ frame attached to the body, and its projection on the xy plane makes an angle φ with axis x . For each plane Δ a new quantity is

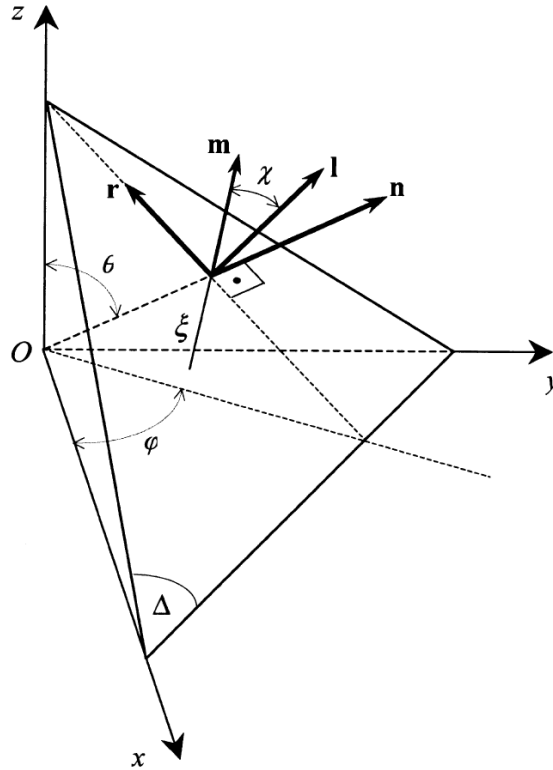


Figure 2.3 – Material plane Δ passing through point O of a body and its associated (n, l, r) frame (Papadopoulos [1993]).

introduced called *generalised shear stress amplitude* and denoted as T_a . This shear stress quantity was first introduced in Papadopoulos [2001] and was subsequently used by other researchers. The critical plane according to our proposal is that onto which $T_a(\varphi, \theta)$ achieves its maximum value. The fatigue limit criterion is written as:

$$\max T_a + \alpha_\infty \Sigma_{h,max} \leq \gamma_\infty \quad (2.2.12)$$

where α_∞ and γ_∞ are material parameters to be determined (Papadopoulos [2001]), and where we take

$$\Sigma_{h,max} = \max_t \left\{ \frac{1}{3} \text{tr}(\underline{\underline{\sigma}}(t)) \right\}$$

To define T_a , he introduced the resolved shear stress τ :

$$\begin{aligned} \tau = & [\sin\theta \cos\varphi \sigma_{xx} + \sin\theta \sin\varphi \sigma_{xy} + \cos\theta \sigma_{xz}] (-\sin\varphi \cos\chi - \cos\theta \cos\varphi \sin\chi) + \\ & [\sin\theta \cos\varphi \sigma_{xy} + \sin\theta \sin\varphi \sigma_{yy} + \cos\theta \sigma_{yz}] (\cos\varphi \cos\chi - \cos\theta \sin\varphi \sin\chi) + \\ & [\sin\theta \cos\varphi \sigma_{xz} + \sin\theta \sin\varphi \sigma_{yz} + \cos\theta \sigma_{zz}] \sin\theta \sin\chi. \end{aligned} \quad (2.2.13)$$

It is clear that the resolved shear stress is a function of φ, θ, χ and of time t in the case of variable loading, i.e. $\tau = \tau(\varphi, \theta, \chi, t)$. Upon fixing a couple (φ, θ) (i.e. a plane Δ) and an angle χ (i.e. a line ξ on Δ), one can define the amplitude of the resolved shear stress τ_a , acting on Δ along ξ by the formula:

$$\tau_a(\varphi, \theta, \chi) = \frac{1}{2} \left[\max_{t \in P} \tau_a(\varphi, \theta, \chi, t) - \min_{t \in P} \tau_a(\varphi, \theta, \chi, t) \right]. \quad (2.2.14)$$

Finally, for a given plane Δ , i.e. for a fixed couple (φ, θ) , the generalized shear stress amplitude T_a is defined as:

$$T_a(\varphi, \theta) = \sqrt{\frac{1}{\pi} \int_{\chi=0}^{2\pi} \tau_a^2(\varphi, \theta, \chi) d\chi} \quad (2.2.15)$$

We note the fatigue limit in fully reversed torsion t_{-1} and the fatigue limit in fully reversed bending f_{-1} . From these two tests we get the parameters:

$$\begin{aligned}\gamma_{\infty} &= t_{-1}, \\ \alpha_{\infty} &= 3 \left(\frac{t_{-1}}{f_{-1}} - \frac{1}{2} \right).\end{aligned}$$

The Papadopoulos fatigue limit criterion achieves the form ([Papadopoulos \[2001\]](#)):

$$maxT_a + 3 \left(\frac{t_{-1}}{f_{-1}} - \frac{1}{2} \right) \Sigma_{h,max} \leq t_{-1}. \quad (2.2.16)$$

In the particular case of the fully reversed uniaxial tension, the criterion is written as ([Papadopoulos \[2001\]](#)):

$$\frac{\Sigma_{xx,a}}{2} + \alpha_{\infty} \frac{\Sigma_{xx,m}}{3} \leq \gamma_{\infty}$$

In conclusion of this part in stress based criteria, we need to observe that these criteria are all based on the notion of cyclic loading, which can be a limitation in general case.

2.2.2 Criteria based on energy

Depending on the type of density of deformation energy considered per cycle, the Energy criteria are divided into three groups ([Macha and Sonsino \[1999\]](#)):

- criteria based on elastic energy
- criteria based on plastic energy
- criteria based on the sum of elastic and plastic energies.

The criteria based on the elastic deformation energy can be used in fatigue with a large number of cycles, whereas those based on the plastic deformation energy are more suitable for oligocyclic fatigue.

[Ellyin \[1974\]](#) is one of the first to propose a fatigue criterion based on cyclic shear deformation energy. This approach was taken up and complemented by [Lefebvre \[1981\]](#) and [Ellyin et al. \[1991\]](#) for the case of multiaxial loadings. In France, this approach is reflected in the work of [Froustey et al. \[1992\]](#) and then in [Palin-Luc \[1996\]](#) and [Banvillet \[2001\]](#).

Energy dissipation based on strain energy density

In their fatigue criterion, [Froustey et al. \[1992\]](#) have considered a complete cycle of stresses. They use the mean value on one cycle of the volumic density of the elastic strain energy, W_a , whatever the point M in the mechanical part.

$$W_a(M) = \frac{1}{T} \int_0^T \frac{1}{2} \sigma_{ij}(M, t) \varepsilon_{ij}^e(M, t) dt$$

where $\sigma_{ij}(M, t)$ and $\varepsilon_{ij}^e(M, t)$ are respectively the tensor of stresses and the tensor of elastic strains at the considered point M function of time t. Thus, in low cycle fatigue W_a can be considered as the mean value on one cycle of the total strain energy density at the considered point. However, in high cycle fatigue usually the endurance limit is low enough to consider that the material remains elastic at the macroscopic scale ([Chaboche and Lesne \[1988a\]](#)).

In 1998 Thierry PALIN-LUC and Serge LASSERRE ([Palin-Luc and Lasserre \[1998\]](#)) proposed a failure criterion based on W_a . Their studies show that another limit, called σ^* , can be defined below

the usual endurance limit of the material, σ_D . At a considered point a stress amplitude below this new limit does not initiate observable damage at the microscopic scale (no micro-cracks). Two static characteristics of the material are necessary: E and ν . Three experimental endurance limits under fully reversed loadings are needed: the endurance limit in traction, $\sigma_{Trac,-1}^D$, the endurance limit in rotative bending, $\sigma_{RotBend,-1}^D$, and the endurance limit in torsion, $\tau_{To,-1}^D$.

This stress limit σ^* can be estimated from fatigue test results in fully reversed tension and in rotating bending

$$\sigma^* = \sqrt{2(\sigma_{Trac,-1}^D)^2 - (\sigma_{RotBend,-1}^D)^2}.$$

From σ^* and by analogy with a sinusoidal traction load the corresponding mean value of the strain energy volumetric density, W_{a^*} , can be calculated, where E is the Young modulus of the material.

$$W_{a^*} = \frac{\sigma^{*2}}{4E}.$$

Around each point it is always possible to define the volume $V^*(C_i)$ by the set of points M where $W_a(M)$ is higher than $W_{a^*}(C_i)$. They postulate that the part of $W_a(M)$ exceeding $W_{a^*}(C_i)$ is the damaging part of the strain energy volumetric density. They thus calculate $\bar{\omega}_a(C_i)$ the volumetric mean value of the strain energy around the critical point C_i

$$V^*(C_i) = \{ \text{points } M(x, y, z) \text{ around } C_i \text{ such that } W_a(M) \geq W_{a^*}(C_i) \}$$

$$\bar{\omega}_a(C_i) = \frac{1}{V^*(C_i)} \int \int \int_{V^*(C_i)} [W_a(x, y, z) - W_{a^*}(C_i)] d\nu$$

At the endurance limit and at the critical point C_i , this new quantity $\bar{\omega}_a(C_i)$ is supposed to be constant, whatever the uniaxial stress state. If we note $\bar{\omega}_a^D(\text{Uniax})$ its value at the endurance limit for any uniaxial stress state our criterion can be written by Eq.(2.2.17). Failure occurs if this equation is not verified.

$$\bar{\omega}_a(C_i) \leq \bar{\omega}_a^D(\text{Uniax}). \quad (2.2.17)$$

The limitation of this criterion is that it only deals with constant amplitude load case.

A critical plane approach based on energy concepts

[Łagoda et al. \[1999\]](#) proposed that under multiaxial loadings the normal strain energy density in the critical plane (i.e. the plane of the maximum damage) to be the energy parameter and translated into deformation or stress amplitude in a given experimental fatigue curve. The history of strain energy density is schematized with use of the rain-flow algorithm. Fatigue damage is accumulated according to Palmgren-Miner hypothesis and endurance limit uses the standard fatigue characteristic of the material, rescaled with use of the considered energy parameter.

$$W(t) = \frac{1}{2} \sigma(t) \varepsilon(t) \text{sgn}[\sigma(t), \varepsilon(t)] \quad (2.2.18)$$

$$\text{sgn}(x, y) = \frac{\text{sgn}(x) + \text{sgn}(y)}{2}$$

$\text{sgn}(x), \text{sgn}(y) = 0, 1, -1$ for distinguishing positive and negative works in a fatigue cycle. Thus, it allows to distinguish energy (specific work) for tension and energy (specific work) for compression.

If the stress and strain reach their maximum values, σ_a and ε_a , then the maximum energy density value is

$$W_a = \frac{1}{2} \sigma_a \varepsilon_a \quad (2.2.19)$$

Taking $W(t)$ as the fatigue damage parameter according to Eq.(2.2.18), we can rescale the standard characteristics of cyclic fatigue $(\sigma_a - N_F)$ and $(\varepsilon_a - N_F)$ and obtain a new one, $(W_a - N_F)$. In the case of high-cycle fatigue, when the characteristic curve $(\sigma_a - N_F)$ is used in order to predict the number of cycles N_F to failure, the axis σ_a should be replaced by W_a , where W_a and σ_a are related by:

$$W_a = \frac{\sigma_a^2}{2E}.$$

In the case of low and high-cycle fatigue, when the characteristic $(\varepsilon_a - N_F)$ is used, we can do similar rescaling.

The full approach is described in Figure 2.4. Having tensors of strain and stress histories we can determine histories of normal strain energy density (stage 3) in all the planes according to Eq.(2.2.18) with the distinguished direction $\bar{\eta}$.

$$W_\eta(t) = 0.25\varepsilon_\eta(t)\sigma_\eta(t)[\operatorname{sgn}\varepsilon_\eta(t) + \operatorname{sgn}\sigma_\eta(t)] \quad (2.2.20)$$

where

$$\sigma_\eta(t) = [\hat{l}_\eta^2\sigma_{xx}(t) + \hat{m}_\eta^2\sigma_{yy}(t)], \quad (2.2.21)$$

$$\varepsilon_\eta(t) = [\hat{l}_\eta^2\varepsilon_{xx}(t) + \hat{m}_\eta^2\varepsilon_{yy}(t) + \hat{n}_\eta^2\varepsilon_{zz}(t)], \quad (2.2.22)$$

with $\hat{l}^2, \hat{m}^2, \hat{n}^2$ = direction cosines of the unit vector $\bar{\eta}$.

In the plane stress state, the normal vector orientation to the fracture plane may be described with use of one angle α in relation with the x-axis. Thus, the direction cosines of the axis $\bar{\eta}$ are: $\hat{l}_\eta = \cos\alpha$, $\hat{m}_\eta = \sin\alpha$, $\hat{n}_\eta = 0$. In stage 4 the critical plane is determined by choosing the plane of maximal

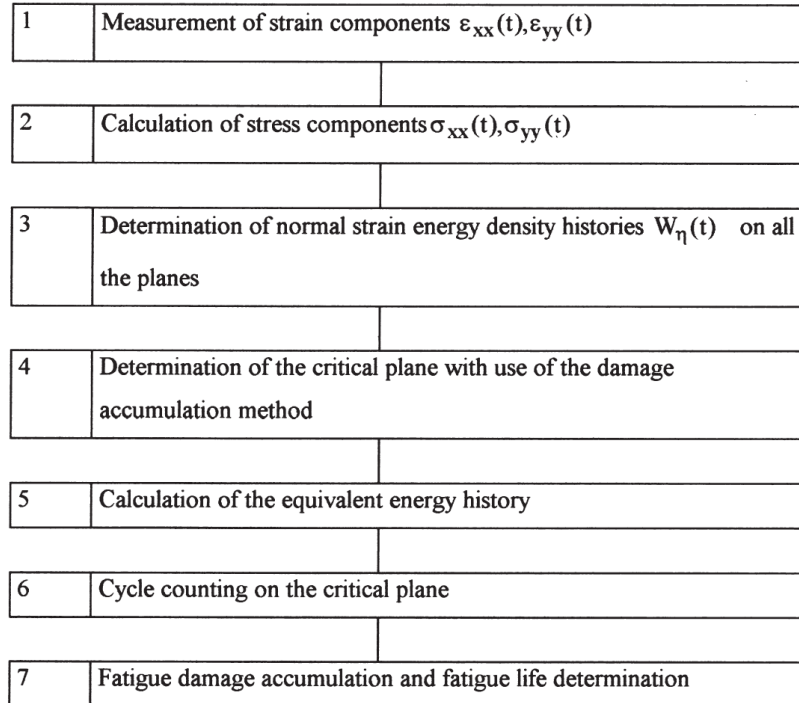


Figure 2.4 – Algorithm of fatigue life determination with use of the energy parameter in the critical plane under biaxial random tension-compression ([Lagoda et al. \[1999\]](#)).

energy variation $\max_\eta \Delta W_\eta(t)$ according to the damage accumulation method Eq.(2.2.20). Fatigue lives were determined at particular expected planes according to the following stages. When the

energy density history at the given plane in stage 6 has been determined, the energy cycles are counted with the rain flow method; next damage is accumulated according to Palmgren- Miner hypothesis taking into account energy cycles of amplitude larger than a W_{af} (with $a = \frac{1}{4}$ and W_{af} the fatigue limit expressed in strain energy density).

$$S(T_0) = \sum_{i=1}^j \frac{n_i}{N_0(W_{af}/W_{ai})^{m'}} \quad \text{for } W_{ai} \geq aW_{af},$$

$$S(T_0) = 0 \quad \text{for } W_{ai} \leq aW_{af},$$

where $S(T_0)$ is material damage up to time T_0 ; j is number of class intervals of the histogram of the amplitudes of the strain energy density; W_{af} is fatigue limit expressed by strain energy density; m' is slope of fatigue curve; N_0 is a number of cycles corresponding to the fatigue limit W_{af} ; n_i is a number of cycles with amplitude W_{ai} .

When the degree of damage at observation time T_0 is determined, the fatigue life is calculated by extrapolation:

$$T_{cal} = \frac{T_0}{S(T_0)}.$$

This method is able to handle general loadings, but still requires cycle counting. And the determination of critical plane in multiaxial load is laborious. Also, they use the Miner's damage law which can not account for the sequencing effect.

Lamefip Criterion

The so-called Lamefip criterion, presented here with its latest version ([Benabes \[2006\]](#)), makes it possible to handle all types of loads and to take into account the effect of the stress gradients. This criterion is based on the notion of the volume of influence around the "critical point" and uses as a parameter the volume density of straining work supplied per cycle to each volume element.

[Ellyin \[2012\]](#) showed that the use of both the plastic and elastic strain work can be used as damage parameter in multiaxial fatigue. The LAMEFIP criterion ([Banville et al. \[2003a\]](#)), devoted to the field of endurance or limited endurance, uses for damage parameter, the volumetric density of the strain work given to the material per loading cycles after elastic shakedown is supposed to be reached after a few thousands cycles.

The proposal is based on two main hypothesis : (i) the strain work given to the material per loading cycle is considered as the driving force for fatigue crack initiation and (ii) it is calculated after macroscopic elastic shakedown.

Many authors use cycle counting techniques (chapter 4) to extract, from a random stress tensor sequence, cycles from which the damage could be estimated. These techniques have two main drawbacks : (i) the choice of the cycle counting algorithm influences the calculated fatigue life since the number of counted cycles is algorithm dependent ([Dowling \[1983\]](#)), and (ii) for multiaxial non-proportional stress states, in many approaches from the literature, the variable chosen for cycle counting differs from the damage parameter. To avoid such drawbacks an incremental model has been developed. The strain work density given at a point M is written in an incremental way as follows :

$$dW_g(M, t) = \sum_{i=1}^3 \sum_{j=1}^3 \langle \sigma_{ij}(M, t) \dot{\epsilon}_{ij}(M, t) \rangle dt.$$

- where $\epsilon_{ij}(M, t)$ are the strain tensor components and $\dot{x} = dx/dt$,
- $\sigma_{ij}(M, t)$ are the stress tensor components,
- and $\langle m \rangle$ gives the positive value of m according to : $\langle m \rangle = 1$ if $m \geq 0$; $\langle m \rangle = 0$ if $m < 0$.

As underlined by [Ellyin \[2012\]](#), the strain work can be calculated as the sum of elastic and plastic strain works, so that :

$$dW_g(M, t) = dW_g^e(M, t) + dW_g^p(M, t).$$

The framework of this study being HCF and MCF, they choose to consider only the elastic part of the strain work (Eq.(2.2.23)) in the elastic shakedown state. The cumulated strain work on a time sequence of duration T is equivalent to the integral of $dW_g^e(M, t)$ over T as in Eq.(2.2.24). [Banville et al. \[2003a\]](#) has shown that for an uniaxial stress state W_g is not shape dependent (sinus, triangle, square, etc...).

$$dW_g^e(M, t) = \sum_{i=1}^3 \sum_{j=1}^3 \langle \sigma_{ij}(M, t) \dot{\epsilon}_{ij}^e(M, t) \rangle dt. \quad (2.2.23)$$

$$W_g(M, T) = \int_t dW_g(M, t). \quad (2.2.24)$$

To take into account the material sensitivity to the stress triaxiality, the triaxiality degree, dT , at a point M is defined by the ratio of the strain work associated with the spherical part of the stress tensor over the total strain work of [Banville et al. \[2003a\]](#), but in an incremental way :

$$dT(M, t) = \frac{dW_g^{Sph}(M, t)}{dW_g(M, t)} \quad if \quad dW_g(M, t) \neq 0, \text{ otherwise } dT(M, t) = 0,$$

with

$$dW_g^{Sph}(M, t) = \left\langle \frac{1}{3} \sum_{k=1}^3 \sigma_{kk}(M, t) \sum_{l=1}^3 \dot{\epsilon}_{ll}^e(M, t) \right\rangle dt.$$

The material sensitivity to stress triaxiality is considered by using an empirical function $F(dT, \beta_m)$ (Eq.(2.2.25)) depending on the material parameter β_m identified from two fully reversed fatigue limits (rotating bending and torsion). At any instant, for a multiaxial stress state, the strain work given to the material is corrected to evaluate an uniaxial equivalent strain work $dW_{g_{eq}}(M, t)$ (Eq.(2.2.26)):

$$F(dT(M, t), \beta_m) = \frac{1}{1 - dT(M, t)} \left[1 - \frac{1}{\beta_m} \ln \left[1 + dT(M, t)(e^{\beta_m} - 1) \right] \right]. \quad (2.2.25)$$

$$dW_{g_{eq}}(M, t) = dW_g(M, t) \frac{F(dT_{uniax}, \beta_m)}{F(dT(M, t), \beta_m)}. \quad (2.2.26)$$

A threshold W_g^* is introduced. It represents the volume density of the minimum elastic deformation work to be provided to create, after a large number of cycles, irreversible damage in a REV. The volume influencing fatigue crack initiation V^* is thus defined whatever the stress state is at the critical point.

$$W_g^* = W_{g,uniax}^* \frac{F(dT_{C_i}, \beta_m)}{F(dT(uniax), \beta_m)}. \quad (2.2.27)$$

$$V^*(C_i) = \left\{ \text{points } M(x, y, z) \text{ around } C_i \text{ so that } W_{g_{eq}}(M, t) \geq W_g^* \right\}. \quad (2.2.28)$$

Assuming that the set of points of the volume of influence plays a significant role in the initiation of a fatigue crack at the critical point C_i , the volume mean value of the damaging work provided in the V^* of influence is written:

$$W_{g_{C_i}} = \frac{1}{V^*(C_i)} \int_{V^*(C_i)} [W_{g_{eq}}(M, T) - W_g^*]$$

In the case of uniaxial loading, the values of W_g^* which serves as reference in Eq.(2.2.27) are given by:

$$W_{g,uniax}^* = \frac{2s_{-1}^2 - f_{rot-1}^2}{E}$$

f_{rot-1} and s_{-1} denote respectively the endurance limits in alternating rotational bending and traction. The final criterion proposed by [Banville et al. \[2003a\]](#) is summarized in the following relation:

$$W_{gC_i} < W_{geq},$$

where W_{geq} is the permissible limit value of W_{gC_i} at the limit of fatigue.

This approach is possible to predict the SN curves from a uniaxial one since the proposal is load type and mean load sensitive. However, the threshold work is another form of the fatigue limit which can be inaccurate microscopically.

2.2.3 Criteria based on plasticity-damage coupling

In recent years, a new class of criteria coupling mesoplasticity and damage has emerged. [Lemaître et al. \[1999\]](#) have, for example, used the approach introduced by [Lemaître and Chaboche \[1985\]](#) based on the thermodynamics of irreversible processes and the mechanics of continuous media. [Flacelière \[2004\]](#) also proposed a model based on a plasticity-damage coupling and attempted to account for the phenomena of damage observed experimentally on a C35 steel. In this work, we will focus on a more recent approach proposed by [Monchiet \[2006\]](#).

Criterion of Monchiet et al

In order to account for the coupling plasticity-damage in high cycle fatigue, [Monchiet \[2006\]](#) uses a micro-mechanical approach based on the work of [Gurson et al. \[1977\]](#). The damage is represented by a magnitude f related to the development of porosity in the sliding bands at the origin of the initiation of the fatigue cracks.

The model is built on the following main assumptions.

- Initiation of cracks in sliding bands by the presence of a high level of porosity in these bands.
- A localization law gives access to the mechanical fields at the mesoscopic scale.
- The elastic adaptation concept is used to access local mechanical fields in a stabilized state.
- A plasticity potential of Gurson type is introduced on the mesoscopic scale in order to show the effects of the plasticity-damage coupling.

The function of charge used (with Δ tensor of order two defining the orientation of the system of slip considered and equals to $\frac{1}{2}(\underline{n} \otimes \underline{m} + \underline{m} \otimes \underline{n})$ where \underline{n} is normal to slip plan and \underline{m} the sliding direction)

$$F = \left(\frac{\overline{\overline{B}} : \overline{\overline{\Delta}}}{\tau_d} \right)^2 + 2fcosh \left(\frac{\sqrt{3} B_h}{2 \tau_h} \right) - 1 - f^2 \leq 0, \quad (2.2.29)$$

where $\overline{\overline{B}} = \overline{\overline{\Sigma}} - \overline{\overline{X}}$, with $\overline{\overline{\Sigma}}$ the macroscopic stress tensor and $\overline{\overline{X}}$ the kinematic hardening variable. $\overline{\overline{X}}$ decomposes into a hydrostatic part X_h and a slip component on the predominant system, denoted X_d . Σ_H . Isotropic hardening is introduced by replacing the plasticity threshold τ_0 by two parameters τ_d and τ_h .

Without going into the details of this model adapted to the problem of fatigue at large number of cycles, it seems very important, in order to understand the rest of the work, to resume the way

in which hardening is introduced into the load function. The main difference with the conventional charge function proposed by Gurson is the existence of a isotropic combined kinematic hardening with decomposition into deviatoric parts (parameters τ_d and X_d) and hydrostatic (parameters τ_h and X_h).

To obtain the expressions of these variables, the authors follow the same approach as [Leblond et al. \[1995\]](#), by postulating paths of pure deviatoric stress and pure effect of fatigue damage at high mean hydrostatic values. The aim is to identify the parameters of hardening from specific exact solutions. The authors reach the relationships:

$$\tau_d = \tau_0 + R_d \quad (2.2.30)$$

$$\tau_h = \tau_0 + R_h \quad (2.2.31)$$

$$R_d = R_0 \gamma_{cum} \quad (2.2.32)$$

$$R_h = h R_0 \gamma_{cum} + R_0 \xi_{cum}^h \quad (2.2.33)$$

with R_0 isotropic hardening parameter and h latent hardening parameter. It is important to note that plastic slip γ and the parameter ξ^h are cumulative, due to applications to fatigue. In the rest of the presentation γ_{cum} and ξ_{cum}^h represent the quantities in the adapted state. For kinematic hardening, the parameters obtained are as follows:

$$X_d = ((1 - f)c)\gamma \quad (2.2.34)$$

$$X_h = \frac{2p_1 c}{\sqrt{3}} \xi^h \quad (2.2.35)$$

with c the parameter of kinematic hardening, p_1 the parameter of cubic anisotropy. The variable ξ^h equals :

$$\xi^h = \frac{2}{\sqrt{3}} \left\{ \operatorname{dilog} \left(\frac{f_a}{f} \right) - \operatorname{dilog} (1 - f_g) \right\} \quad (2.2.36)$$

with $\operatorname{dilog}(x) = \int_1^x \frac{\ln(x')}{1 - x'} dx'$.

The criterion therefore postulates that a fatigue crack appears in a sliding band when the fraction of porosity inside this band reaches a critical value f_c

Plasticity occurs locally when the equivalent stress reaches the yield limit. The authors take into account two mechanisms of damage in the evolution of the porosity:

- The first is related to the creation of gaps by annihilation of dislocations. This mechanism is at the origin of the accumulation of point defects of the lacunar or interstitial type along the persistent slip bands (PSB). The phenomenological model proposed by [Essmann and Mughrabi \[1979\]](#) gives access to the porosity f_a :

$$f_a = A_0 \{k_a \gamma_{cum} - 1 + \exp(-k_a \gamma_{cum})\}. \quad (2.2.37)$$

- The second mechanism is related to the growth of micro-cavities. Using an incompressibility hypothesis, f_g is defined by:

$$f_g = \{1 - \exp(3\epsilon_h^p)\}. \quad (2.2.38)$$

It is important to note that the first mechanism involves the accumulated plasticity γ_{cum} , related to amplitude effects. The second mechanism depends on the hydrostatic plastic deformation ϵ_h^p , and allows the taking into account of the mean stress effects.

The fatigue criterion is established on the basis of the following hypothesis: “a sufficient condition for nucleation of a fatigue crack is obtained if the porosity reaches a critical value f_c ”.

$$f(\gamma_{cum}, \epsilon_h^p) = f_a + f_g \leq f_c. \quad (2.2.39)$$

Noting γ_c , the critical value of the cumulative plasticity for which the fatigue criterion is reached when $\epsilon_h^p = 0$, it becomes:

$$f_c = \{A_0 \{k_a \gamma_c - 1 + \exp(-k_a \gamma_c)\}\}. \quad (2.2.40)$$

$$\gamma_{cum} = \frac{T_a}{\underline{\underline{\epsilon}}} : \Delta \underline{\underline{\epsilon}}. \quad (2.2.41)$$

The use of Eq.(2.2.39) and Eq.(2.2.40) leads, for the limiting cases $k_a \gg 1$ to Eq.(2.2.42), and for $k_a \ll 1$ to Eq.(2.2.43), when noting ϵ_c the critical plastic deformation, equal to $f_c/3$ in the case of $\gamma_{cum} = 0$. In other words, we have

either

$$\frac{\gamma_{cum}}{\gamma_c} + \frac{\epsilon_{h,m}^p}{\epsilon_c} = 1 (k_a \ll 1), \quad (2.2.42)$$

or

$$\left(\frac{\gamma_{cum}}{\gamma_c}\right)^2 + \frac{\epsilon_{h,m}^p}{\epsilon_c} = 1 (k_a \gg 1). \quad (2.2.43)$$

k_a is a parameter involved in the crack nucleation law along the sliding bands. The author recalls that this mechanism is characterized by a saturated state for high values of cumulated plastic deformations. This coefficient k_a makes it possible to adjust the speed of convergence towards this saturated state. $\epsilon_{h,m}^p$ is the average hydrostatic part of the plastic deformation due to the growth of the cavities.

In order to relate these two quantities to the macroscopic constraints, the authors seek the adapted state. They indicate that a necessarily safe condition is obtained when every state of stress satisfies the condition $F(\Sigma(t)) \leq 0$ (Figure 2.5a). A sufficient condition for the macroscopic affine loading paths is obtained when the ends of the cycle belong to the load surface, Let Σ_A and Σ_B satisfy $F(\Sigma_A(t)) = F(\Sigma_B(t)) = 0$ (Figure 2.5b). In a suitable regime, the loading cycle is symmetrized around the mean stresses (Figure 2.5c).

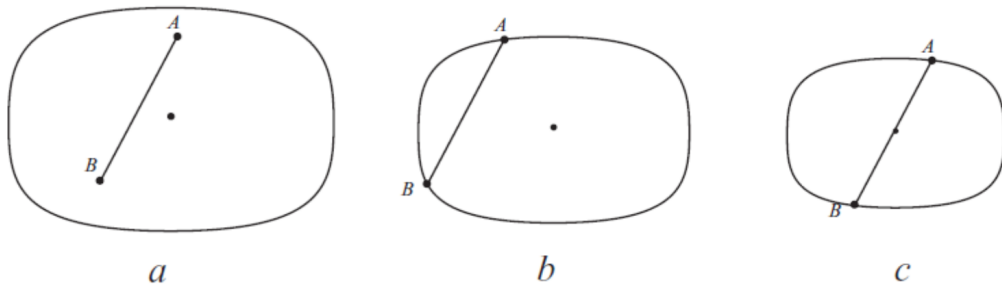


Figure 2.5 – Finding the appropriate state for an affine load path A-B(Koutiri [2011]).

The effect of the mean stress is taken into account by the term of hydrostatic deformation. The hydrostatic pressure is related to the hydrostatic plastic deformation.

$$\Sigma_{h,m} = \left(\frac{4p_1^2 c}{f_c \ln(f_c)} (1 - f_c) + 3k^* \right) \epsilon_{h,m}^p. \quad (2.2.44)$$

In Eq.(2.2.44), c and k^* are parameters related respectively to the kinematic hardening and to the homogenization scheme.

The parameters of the loading can be linked to the parameters of work-hardening thanks to the relations representative of the adapted state, which are presented in Eq.(2.2.29), Eq.(2.2.44) and Eq.(2.2.30) to Eq.(2.2.33).

The parameter ξ_{cum}^h can not be obtained analytically. On the basis of numerical simulations, the authors propose an approximate expression:

$$\xi_{cum}^h = \frac{\sqrt{3}\tau_0}{R_0} \left\{ \frac{\Sigma_{h,a}}{2\tau_0} - 1 + \exp\left(-\frac{\Sigma_{h,a}}{2\tau_0}\right) \right\}. \quad (2.2.45)$$

The implementation of this criterion requires the identification of 12 parameters:

- two parameters, γ_c and ϵ_c linked to the local criterion.
- two parameters, A_0 and k_a , related to the mechanisms of nucleation of cracks.
- three parameters related to hardening, R_0 And τ_0 linked to the isotropic hardening, c linked to the kinematic hardening
 - two coefficients linked to the homogenization scheme, μ and k .
 - a cubic anisotropy coefficient of the grain p_1
 - a latent coefficient of strain hardening h
 - a critical porosity coefficient f_c

All of these parameters are microscopic, which poses a problem in their identification. Some elements of this modeling have been taken up by Charkaluk et al. [2009], Charkaluk and Constantinescu [2007] in dissipative approaches. The limitation of this method is that it still requires cycle counting which in complex load case is not feasible.

2.3 Calculation method without cycle counting

This part presents the existing method of prediction of lifetime, which does not need the algorithm of cycle counting. These kind of methods are still minority and usually more delicate to implement, but present the advantage of free the choice of variable of counting proved to be “dangerous”. The method presented here is the morel method which is based on stress.

2.3.1 Morel's method

Morel's method (Morel [2000]) is based on a mesoscopic approach of critical plane type with the choice of plastic deformation as mesoscopic cumulative damage variable. The description below is taken from his paper. Multiaxial and variable amplitude loading can be analyzed with this method. To depict the fatigue crack initiation phenomenon in polycrystalline metallic materials, two scales of description of a material will be distinguished: the usual macroscopic scale and a mesoscopic one. The macroscopic scale is defined with the help of an elementary volume V determined at any point O of a body as the smallest sample of the material surrounding O that can be considered to be homogeneous. V contains a large number of grains (crystals) and the mesoscopic scale is defined as a small portion of this volume. In the high cycle fatigue regime, some grains undergo local plastic strain while the rest of the matrix behaves elastically (the overall plastic strain is negligible).

Macroscopic quantities. They are:

Mesoscopic quantities. They are:

$\underline{\Sigma}$	macroscopic stress tensor
\underline{E}	macroscopic strain tensor
\underline{C}	macroscopic shear stress vector
\underline{T}	macroscopic resolved shear stress vector acting on an easy glide direction
T_a	amplitude of the macroscopic resolved shear stress
P	macroscopic hydrostatic stress.
$\underline{\sigma}$	mesoscopic stress tensor
$\underline{\varepsilon}$	mesoscopic strain tensor
$\underline{\tau}$	mesoscopic resolved shear stress vector acting on an easy glide direction
γ^p	mesoscopic shear plastic strain
Γ	accumulated plastic mesostrain
H	phase-difference coefficient.

Constant amplitude loading

Local stress estimation in high cycle fatigue

By assuming that only one glide system (defined by a normal vector \underline{n} to a plane and a vector (direction) \underline{m} within this plane) is active for every plastically deforming grain of the metal, [Papadopoulos \[1993\]](#) established a macromeso passage for a glide system activated in a flowing crystal:

$$\underline{\tau} = \underline{T} - \mu \gamma^p \underline{m} \quad (2.3.1)$$

where $\underline{\tau}$ and \underline{T} are the mesoscopic and macroscopic resolved shear stresses acting along the slip direction \underline{m} and are defined by:

$$\underline{\tau} = (\underline{m} \cdot \underline{\sigma} \cdot \underline{n}) \underline{m} \quad (2.3.2)$$

$$\underline{T} = (\underline{m} \cdot \underline{\Sigma} \cdot \underline{n}) \underline{m} \quad (2.3.3)$$

and γ^p is the magnitude of the plastic mesoscopic shear strain deduced from the plastic flow rule associated to Eq.(2.3.4).

Schmid's law with isotropic and kinematic hardening:

$$f(\underline{\tau}, \underline{b}, \tau_y) = (\underline{\tau} - \underline{b}) \cdot (\underline{\tau} - \underline{b}) - \tau_y^2 = 0 \quad (2.3.4)$$

where \underline{b} is the kinematic back stress, and τ_y is the yield limit subjected to hardening.

Three successive linear isotropic hardening rules have been adopted on τ_y to describe the crystal behavior from initial yield to failure (Figure 2.7a). The damage variable is the accumulated plastic mesostrain Γ (Figure 2.7b). In the first phase, we have a linear increase $\dot{\tau}_y = g\dot{\Gamma}$, in the second phase when τ_y reaches a saturation τ_{lim} , $\dot{\tau}_y = 0$, and then above a certain threshold, we have softening $\dot{\tau}_y = -h\dot{\Gamma}$.

In the description and implementation of his method, Morel draws heavily on the work developed by Papadopoulos including the use of a measure of cumulative mesoscopic plastic deformation and modeling the behavior of grain in three distinct phases (hardening, saturation and softening); he considers the cumulative mesoscopic plastic deformation Γ as damage parameter and assumes that the initiation of a fatigue crack occurs when the latter reaches a critical value $D = D_R = \Gamma_R$ (Figure 2.7).

Number of cycles to failure

Once the accumulated plastic mesostrain Γ along the particular gliding system reaches a critical value Γ_R , these grains are said to be broken. An analytical expression of the number of cycles to

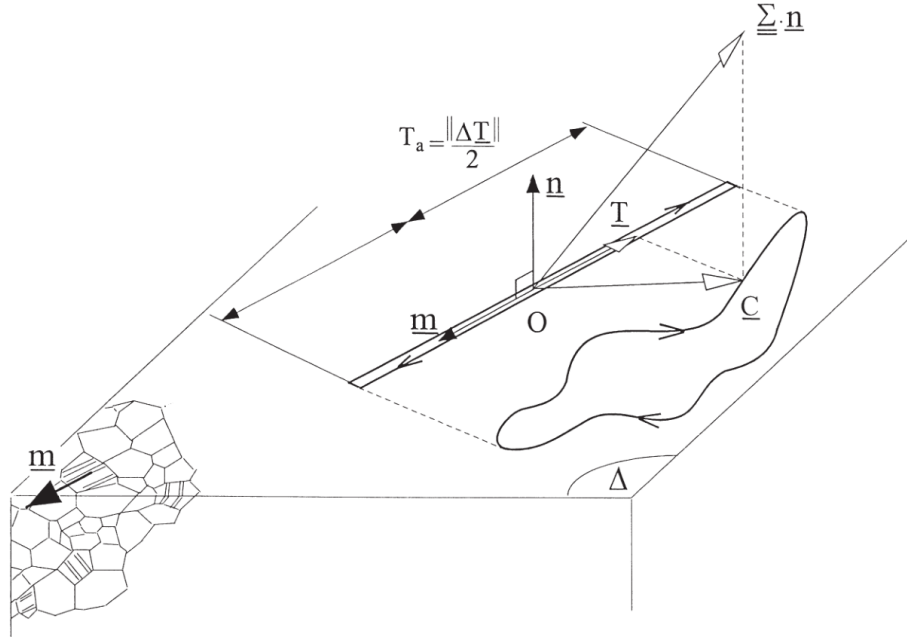


Figure 2.6 – Path of the macroscopic shear stress \underline{C} acting on a material plane Δ and the corresponding path of the macroscopic resolved shear stress \underline{T} acting on an easy glide direction (Morel [2000]).

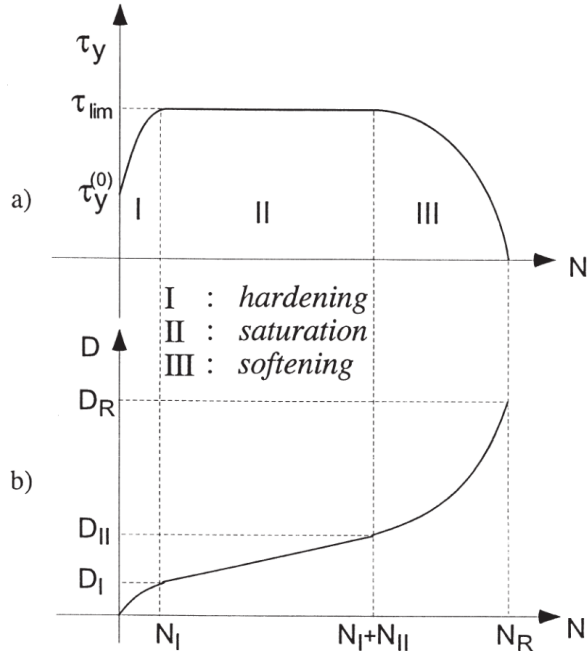


Figure 2.7 – (a) Yield limit evolutions and (b) damage evolution in the three behavior phases (hardening, saturation and softening) when a cyclic loading is applied (Morel [2000]).

initiation (SN curve) can be achieved:

$$\Gamma = \Gamma_R \Rightarrow N_i = p \ln \left(\frac{C_A}{C_A - \tau_{lim}} \right) + q \left(\frac{\tau_{lim}}{C_A - \tau_{lim}} \right) - \frac{r}{C_A} \quad (2.3.5)$$

where p , q and r are functions of the hardening parameters of the three phases defined above.

From Eq.(2.3.6) we can find the yield point τ_s of the crystal in the saturation phase as a function of the amplitude P_a and the mean value P_m of the hydrostatic pressure, the phase difference of

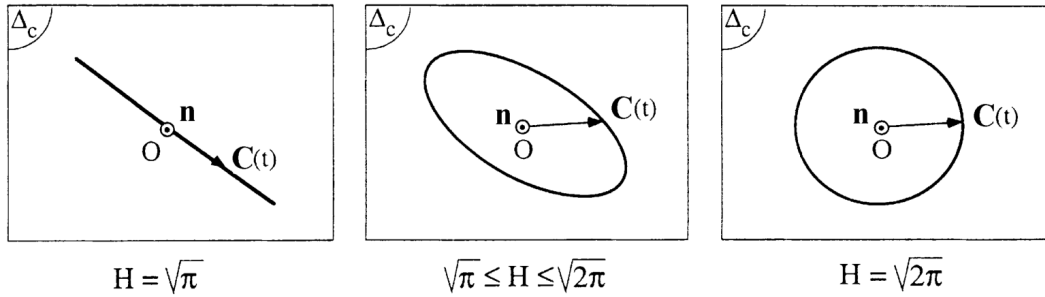


Figure 2.8 – Different paths of loading in the plane and corresponding values of the phase-difference coefficient H (Morel [2000]). For a proportional loading, H is equal to $\sqrt{\pi}$. In the case of a particular circular path, H reaches the maximum value $\sqrt{2\pi}$ (Figure 2.8). The linear path and the circular one lead to two bounds of the coefficient H .

coefficient H and two material related parameters α and β :

$$\tau_{lim} = \tau_s = \frac{-\alpha P_m + \beta}{\alpha \frac{P_a}{C_A} + H} \quad (2.3.6)$$

In the last relation Eq.(2.3.5), the detrimental effect of out- of-phase loading is introduced through τ_{lim} . As the coefficient H increases, τ_{lim} as well as N_i decrease and therefore more damage is accumulated. The identification of the model parameters requires two endurance limits (parameters a and b of the endurance criterion) and a single SN curve (parameters p , q and r).

The fatigue control mechanism is embedded in the construction of the saturation limit τ_{lim} of τ_y which is constructed separately on each slip system using fatigue test data. More precisely, we assume that the given material has an endurance limit in uniaxial loading given as in Papadopoulos by

$$\Delta T/2 + \alpha P_{max} = \beta$$

with material coefficients α and β , $\Delta T/2$ the amplitude of the resolved shear stress, and P_{max} the maximum hydrostatic stress. For a given cyclic shear loading on the considered slip line of amplitude T_a , average hydrostatic stress P_m and amplitude of hydrostatic stress P_a , we introduce the amplitude scaling k where we have

$$kT_a + \alpha(kP_a + P_m) = \beta$$

which is given by

$$k = \frac{\beta - \alpha P_m}{T_a + \alpha P_a}$$

and which will send this loading to the endurance curve, and a shape factor $\sqrt{\pi} \leq H \leq \sqrt{2\pi}$ characterizing the shape of the loading path in the considered plane of normal \underline{n} (Figure 2.8). The local saturation limit $\tau_{lim}(\underline{m}, \underline{n})$ is then defined by the amplitude of the shear loading T_a once multiplied by the scaling factor k and corrected by the shape factor H , giving

$$\tau_{lim}(\underline{m}, \underline{n}) = \frac{k}{H} T_a(\underline{m}, \underline{n}) = \frac{1}{H} \frac{\beta - \alpha P_m}{T_a + \alpha P_a} T_a(\underline{m}, \underline{n}).$$

General loading

In this framework, Morel's method uses three successive steps for computing the damage created by repeated loading sequences:

1. Find the critical plane \underline{n} maximizing the in-plane plastic deformation $\int_{\underline{m}} \gamma^p$ which will be induced by the loading sequence, assuming linear isotropic hardening without saturation.

2. On this plane \underline{n}_c , on each direction \underline{m} , compute the plastic history, that is

- (a) compute the shear history $T(t) = \underline{m} \cdot \underline{\Sigma} \cdot \underline{n}_c$
- (b) decompose in local loading cycles (i) counted $n_{(i)}$ times with load amplitude $T_a^{(i)}$, mean hydrostatic load of mean $P_m^{(i)}$ and amplitude $P_a^{(i)}$, using a standard scalar rainflow counting method (chapter 4)
- (c) compute the local saturation limit

$$\tau_{lim}^{(i)} = \frac{1}{H} \frac{\beta - \alpha P_m^{(i)}}{T_a^{(i)} + \alpha P_a^{(i)}} T_a^{(i)}$$

and its sequence average $\langle \tau_{lim} \rangle$

- (d) compute the accumulated plastic strain

$$\Gamma_{\underline{m}, \underline{n}_s} = \sum_{(i)} n_{(i)} \frac{4}{c + \mu} \left(T_a^{(i)} - \tau_{lim}^{(i)} \right)_+ \quad (2.3.7)$$

3. Find the critical direction \underline{m}_s maximizing among the directions \underline{m} with the accumulated plastic strain $\Gamma_{\underline{m}_s, \underline{n}_s}$, and use this accumulated plastic strain to compute the incremental damage occurring during the repeated loading sequence

$$\Delta D = l \frac{\Gamma_{\underline{m}_s, \underline{n}_s}}{\langle \tau_{lim} \rangle_{\underline{m}_s, \underline{n}_s}} \quad (2.3.8)$$

thus assuming linear damage accumulation.

With the present way, a new counting method is defined. Indeed, damage is deduced step by step from the hardening rules. Each time the plasticity criterion is violated (the yielding sphere is exceeded) some plastic strain is accumulated and then damage increases. This fact is quite new because most of the fatigue life prediction methods in the literature successively apply a counting method (e.g. “Rainflow method”) and a damage law (e.g. Miner rule), without any link between them. The choice of accumulated plastic mesostrain as damage variable and the use of appropriate hardening rules seem then to be a promising and efficient way to understand and describe the physical mechanisms of crack nucleation.

Experimental verification

In case of constant amplitude test

The author [Morel \[1998\]](#) consider the example of an out-of-phase bending-torsion test on a high strength steel (30NCD16). The endurance limits of this material in reversed bending and torsion are, respectively, $f = 680$ MPa and $t = 426$ MPa. The multiaxial sinusoidal loading is characterized by the amplitudes $\Sigma_{11a} = 600$ MPa, $\Sigma_{12a} = 335$ MPa (no mean stresses) and the phase difference $\beta_{12} = 90^\circ$.

The maximum value of T_σ (denoted as T_Σ) can be deduced numerically. For this loading, we find $T_\Sigma = 697$ MPa. On the critical material plane (where T_Σ is reached), C_A is estimated to be 282 MPa. The phase difference coefficient H is then simply deduced: $H = T_\Sigma/C_A = 2.47$.

Besides noting that $P_m = 0$ MPa, $P_a = 200$ MPa and $a = 0.67$, $b = 775$ MPa, $T_{\Sigma lim}$ is readily computed with the help Eq.(2.3.6): $T_{\Sigma lim} = 633$ MPa. Finally, $\tau_{lim} = T_{\Sigma lim}/H = 256$ MPa. Once p , q and r have been identified from a SN curve with the least squares line method, C_A and τ_{lim} can be introduced into Eq. (2.3.7) and the number of cycles to initiation can be finally calculated, i.e. $N_F = 2 \times 10^5$ cycles.

In case of variable amplitude test

According to the previous endurance data and the definition of the generalized fatigue limit (for bending $\tau_{lim} = f/2$ and for torsion $\tau_{lim} = t$), one can estimate the parameter $q = 20800$.

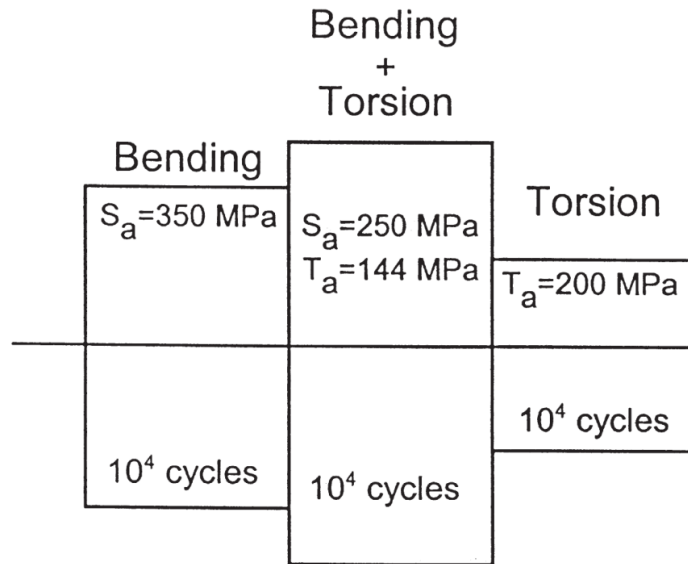


Figure 2.9 – block sequence tests (bending/bending+torsion/torsion) performed on a mild steel XC18.

Let us consider now a block sequence composed of 10^4 cycles of bending ($\Sigma_a = 350$ MPa) followed by 10^4 cycles of combined in-phase bending-torsion ($\Sigma_a, T_a = 250$ MPa, 144 MPa) followed by 10^4 cycles of torsion ($T_a = 200$ MPa). This sequence is repeated until the initiation of a crack. The mean lifetime is found to be $N = 1.73 \times 10^5$.

The three generalized fatigue limits relative to the three blocks are estimated according to Eq.(2.3.6):

$$\tau_{lim}^{bending} = 155 \text{ MPa}$$

$$\tau_{lim}^{torsion} = 179 \text{ MPa}$$

$$\tau_{lim}^{bend+tors} = 157 \text{ MPa}$$

These three values and the parameter q are enough to accumulate the damage in the three blocks using Eq.(2.3.8):

$$\frac{\Gamma^{(bending)}}{\Gamma_R^{(bending)}} + \frac{\Gamma^{(bend+tors)}}{\Gamma_R^{(bend+tors)}} + \frac{\Gamma^{(torsion)}}{\Gamma_R^{(torsion)}} = 1$$

The corresponding number of cycles to initiation is: $N_{prediction} < 1.5 \times 10^5$, that is to say five successive applications of the sequence. This prediction, close to the experimental result $N = 1.73 \times 10^5$, is a conservative one.

It is important to note that if only one critical plane (either from bending, torsion or bending+torsion loading) is used for damage accumulation, one-third of the damage would be calculated, resulting in a nonconservative prediction.

Morel's method is promising in its description aspect of limited endurance fatigue phenomenon, through the choice of the mesoscopic plastic deformation. By using cumulative plasticity, a fatigue mechanisms occurring at the mesoscopic scale takes into account the main factors affecting the lifetime cycle fatigue (hydrostatic pressure and influence of phase shift).

However, at the present stage, it does not completely meet the demand of a predictive tool. Indeed, it is a relatively complicated method (search critical plane Δ_c and accumulated damage in each direction in the plan); its application for multiaxial variable amplitude fatigue loads requires data that are still not available (an S-N curve, two endurance limits and a particular damage accumulation test). Moreover, it is not completely free of counting method because its author uses the counting of the extrema of the evolution of the resolved shear T_a to get the macroscopic resolved shear stress T_A and the corresponding amplitude P_a and mean values P_m of the hydrostatic stress in each direction (m) in Δ_c . Again, this makes it difficult and daunting task.

3

Space gradient effects

Contents

4.1	The notion of damage in fatigue	50
4.1.1	Linear and nonlinear accumulation of damage	50
4.1.2	Classical Chaboche damage law	53
4.2	Verification method of Chaboche law	59
4.3	Chaboche law containing different criteria	60
4.3.1	Chaboche law with Crossland criterion	60
4.3.2	Chaboche law with Dang Van criterion	60
4.4	Numerical testing on different loading patterns	60
4.4.1	Test on pure rotation	61
4.4.2	Test on 4-point bending	62
4.4.3	Test on rotative bending	63
4.5	Cycle Counting Method	66

This chapter is based on the paper entitled “Multi-axial Fatigue Criteria with Length Scale and Gradient Effects” ([Zepeng et al. \[2015\]](#))

The objective of the work is first to extend some classic high cycle fatigue (HCF) criteria (as Crossland, Dang Van, Papadopoulos, ...) introduced in Chapter 2 in order to take into account a sensitivity of the criteria to stress spatial variations occurring at length scale l_g , and second to compare the performances of the extensions through several experimental fatigue tests. After an introduction of the basic criteria and their gradient based extensions proposed by Luu et al., we focus on the Crossland criterion and we propose a more practical and simple expression taking into account the gradient of the stress amplitude and the maximum hydrostatic stress. The generalization of the approach to other multiaxial fatigue criteria is also proposed. The proposition is then tested and applied to different simple situations such as 4-point bending and cantilever rotative bending. The relative errors between the exact solutions and the experimental data are estimated. Biaxial bending-torsion tests are also simulated to demonstrate the capabilities of the approach. In this work only stress gradient with a beneficial effect on fatigue have been considered.

3.1 Introduction

In several industries, the required design lifetime of many components often exceeds 10^8 cycles. This requirement is applicable to aircraft (gas turbine disks 10^{10} cycles), automobiles (car engine 10^8 cycles), and railways (high speed train 10^9 cycles) (Wachtman et al. [2009]). Although a large amount of fatigue data has been published in the form of S-N (where S is stress and N the number of cycles to fatigue) curves, the data in the literature have been usually limited to fatigue lives up to 10^7 cycles. Beyond that, a near hyperbolic relationship between stress and fatigue life is assumed, with an asymptotic limit defined as the fatigue limit (or endurance stress). A large number of multiaxial fatigue criteria, generalizing this notion of fatigue limit, are available in the literature (Papadopoulos et al. [1997], Ballard et al. [1995], Suresh [1998],...). They are used to design industrial components against failure. Nevertheless, most of these criteria present some drawbacks, for instance when dealing with out-of-phase loading or with metals of different kinds from those used to develop the criteria. In fact, most of them are not designed to cope with high stress gradients such as those introduced by surface treatments or notches, or to handle scale effects as specially present in nano or micro components.

More precisely, as mentioned by Luu et al. (Luu et al. [2014]), in problems related to small electronic components and electro-mechanical devices, at sufficiently small sizes, factors as size, gradient and loading effects affecting fatigue limits are not captured by classical fatigue criteria. In particular, for the same stress distribution as well as nominal maximum stress of the material, the smaller the sample size is, the smaller the surface or the volume of the most stressed zone is, the higher the fatigue limit is. Moreover, the nominal fatigue limit increases in the presence of stress gradient corresponding to a decreasing stress from the surface. Papadopoulos illustrates with experimental example and makes clearer the “beneficial gradient effect” (Papadopoulos and Panoskaltsis [1996]).

The quantitative estimate of the contribution of the pure size effect made in Papadopoulos and Panoskaltsis [1996], using the results of the constant moment tests on specimens of the same radius but different lengths (Figure 3.1(a)) or of the same length with different radius (Figure 3.1(b)), is recalled and used. The slope of the linear trend observed for the (fatigue limit-R) data in Figure 3.1(b) is much higher than the one for the (fatigue limit-L) data in Figure 3.1(a).

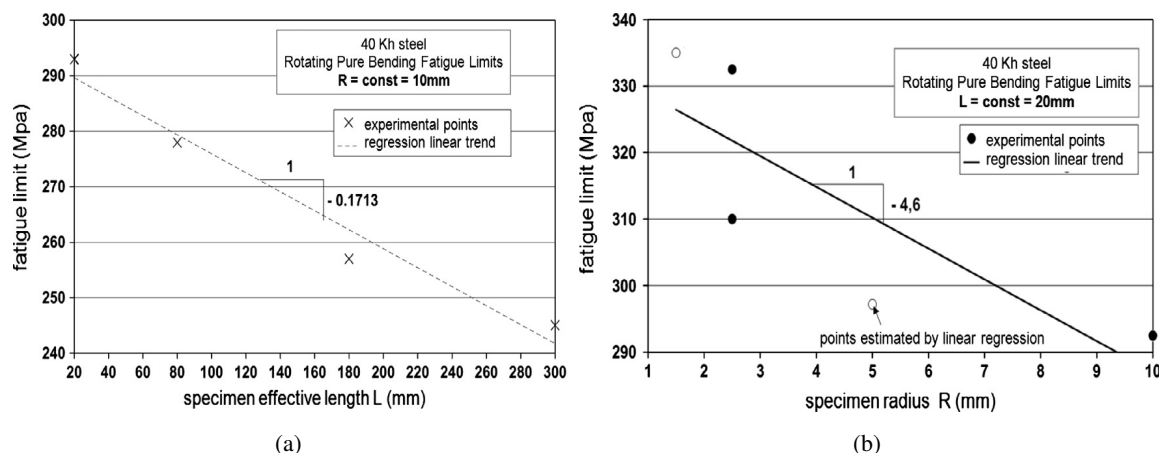


Figure 3.1 – Constant moment bending fatigue limit data: (a) constant radius R; (b) constant length L (Results of Pogoretskii [1966], represented by Weber [1999]).

The results of the constant moment tests on specimens of the same radius but different lengths shows that the gradient effect is an order of magnitude higher than the pure size effect. In this case, size effect is proved insignificant compared to the gradient effect at the considered scale. Once the

gradient correction is made and a proper multiaxial criterion is used, it appears that the size effect due to increasing the loaded surface area at the notch tip for the different geometries is negligible compared to the gradient effect.

From above it is concluded that the stress gradient factor is the most important contributor to the beneficial effect phenomenon. Fatigue criteria have been generalized by several authors by including a gradient dependence ([Papadopoulos and Panoskaltsis \[1996\]](#)) in order to introduce a sensitivity of the endurance limit to difference in stress as a function of length along a gradient field occurring at length scale l_g . Uniaxial normal cyclic stress states with non-zero and zero normal stress gradients, respectively, give some indication about the normal stress gradient effect. The larger the normal stress due to bending, the larger the difference between bending test points and tension-compression ellipse arc (as is shown in Figure 3.2).

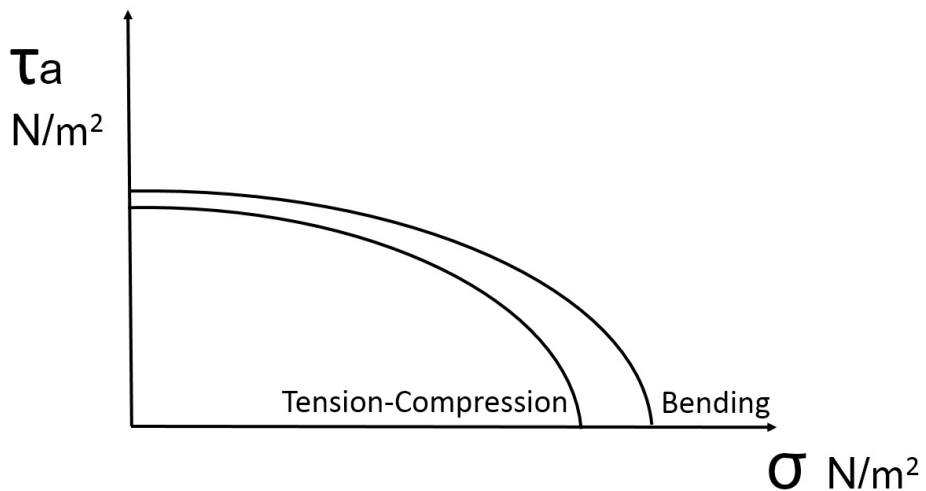


Figure 3.2 – Schematic representation of the nominal fatigue limit (ellipse arc) for two different tests: the arc is larger in the case of bending-torsion (presence of stress gradient) than in tension-compression.

Apart from gradient approaches ([Amargier et al. \[2010\]](#), [Papadopoulos and Panoskaltsis \[1996\]](#)), to take into account the beneficial effect, others approaches such critical volume ([Maitournam et al. \[2009\]](#)), critical distance ([Taylor \[2010\]](#), [Araújo et al. \[2007\]](#)), critical layer ([Flavenot and Skalli \[1983\]](#)), averaging over a specific volume ([Palin-Luc \[2000\]](#), [Banvillet et al. \[2003b\]](#)) are used. In fact, all the approaches are equivalent to introducing a length scale.

In the paper, we consider specifically the gradient approach. We start from the proposition of Luu et al., and propose and analyze a simpler way to account for the gradient effect at a specific length scale. The Crossland criterion ([Crossland \[1956\]](#)), one of the most widely known HCF criteria, is used to illustrate the approach. Crossland proposed that the second invariant of the deviatoric stress tensor and the hydrostatic stress are the variables governing the endurance limit.

The new proposition adds two gradient terms; it is then calibrated and its predictions are compared to experimental results to check its relevancy.

3.2 A first gradient approach

3.2.1 General formulation

[Luu et al. \[2014\]](#) proposed extensions of classical HCF fatigue criteria using the gradients of the shear and normal stress to account for the gradient effect. In the case of critical plane type criteria,

they defined a generalized shear stress amplitude including shear stress gradient and a generalized maximum normal (or hydrostatic) stress. A general form of classical fatigue limit criteria can be written as follows:

$$f(C_a(n^*), N_{max}(n^*)) = C_a(n^*) + aN_{max}(n^*) - b \leq 0, \quad (3.2.1)$$

with a, b being two material parameters. f is a function, chosen in many cases as linear, and n^* is the normal vector of the critical plane; $C_a(n^*), N_{max}(n^*)$ are respectively the amplitude of shear stress and the maximum value of the normal stress on the critical plane.

A new class of fatigue criteria extended from classical ones with stress gradient terms introducing not only in the normal stress but also in the shear stress components, was proposed in [Luu et al. \[2014\]](#). It concerns only defect free materials and can model both phenomena “smaller is Stronger and Higher Gradient is Stronger”.

Besides the stress gradient term appearing in the normal stress part in form of $G = \Delta(\sigma_{11} + \sigma_{22} + \sigma_{33})$, another gradient term, the gradient of the stress tensor amplitude (or alternatively of deviatoric stress tensor amplitude) $\| Y_a \| = \Delta\sigma_a$ is added to the shear stress amplitude part. Basing on all these analyses a new form of fatigue criteria taking into account gradient effects, is proposed:

$$f(\widetilde{C}_a(n^*), \widetilde{N}_{max}(n^*)) = \widetilde{C}_a(n^*) + a\widetilde{N}_{max}(n^*) - b \leq 0, \quad (3.2.2)$$

where $\widetilde{C}_a(n^*)$ and $\widetilde{N}_{max}(n^*)$ are extended definitions of the amplitude of shear stress and of the normal stress taking into account the presence of local gradient.

In the following we first focus on the Crossland criterion and its extension.

3.2.2 The classical Crossland criterion

The classical Crossland criterion ([Crossland \[1956\]](#)) defines the fatigue limit of metallic specimens subjected to multi-axial cyclic stress by :

$$f(\sqrt{J_{2,a}}, \sigma_{H,max}) = \sqrt{J_{2,a}} + a\sigma_{H,max} - b \leq 0, \quad (3.2.3)$$

where $\sqrt{J_{2,a}}$ measures the amplitude of variation of the second invariant of the deviatoric stress and $\sigma_{H,max}$ is the maximum hydrostatic stress observed during a loading cycle. The parameters a and b are material constants to be calibrated experimentally. The amplitude of the square root of the second invariant of the stress deviator can be defined, in general case, as the half-length of the longest chord of the deviatoric stress path or as the radius of the smallest hypersphere circumscribing the stress deviator loading path ([Papadopoulos et al. \[1997\]](#))

$$\sqrt{J_{2,a}} = \sqrt{\frac{1}{2} \min_{\underline{\underline{S}}_1} \left\{ \max_t \left((\underline{\underline{S}}(t) - \underline{\underline{S}}_1) : (\underline{\underline{S}}(t) - \underline{\underline{S}}_1) \right) \right\}}. \quad (3.2.4)$$

The deviatoric stress $\underline{\underline{S}}$ associated with a stress tensor $\underline{\underline{\sigma}}$ is defined by

$$\underline{\underline{S}} = \underline{\underline{\sigma}} - \frac{1}{3} \text{tr} \underline{\underline{\sigma}} \underline{\underline{I}}, \quad (3.2.5)$$

where $\text{tr} \underline{\underline{\sigma}}$ is the trace of the stress tensor $\underline{\underline{\sigma}}$ and $\underline{\underline{I}}$ the second order unit tensor.

The maximum value that the hydrostatic stress reaches during the loading cycle is on the other hand:

$$\sigma_{H,max} = \max_t \left\{ \frac{1}{3} \text{tr} (\underline{\underline{\sigma}}(t)) \right\}. \quad (3.2.6)$$

For a proportional cyclic loading, if one introduces the two extreme stress tensors $\underline{\underline{\sigma}}^A$ and $\underline{\underline{\sigma}}^B$ observed during the loading path, together with the stress range

$$\underline{\underline{\Delta\sigma}} = \underline{\underline{\sigma}}^B - \underline{\underline{\sigma}}^A \quad (3.2.7)$$

and its deviatoric part $\underline{\underline{\Delta s}}$, the variation of the second invariant of the stress deviator reduces to

$$\sqrt{J_{2,a}} = \frac{1}{2} \max_t \sqrt{\frac{1}{2} \underline{\underline{\Delta s}} : \underline{\underline{\Delta s}}} = \frac{1}{2} \max_t \sqrt{\frac{1}{2} (\Delta s_{11}^2 + \Delta s_{22}^2 + \Delta s_{33}^2 + 2\Delta s_{12}^2 + 2\Delta s_{13}^2 + 2\Delta s_{23}^2)}. \quad (3.2.8)$$

The material constants a and b can be related to the limit t_{-1} of endurance in alternate torsion and to the limit s_{-1} of endurance in alternate tension-compression by

$$a = \frac{3t_{-1}}{s_{-1}} - \sqrt{3}, \quad b = t_{-1}. \quad (3.2.9)$$

3.2.3 Formulation of Crossland criterion with gradient effect

In particular, using as a basis the classical Crossland criterion Eq.(3.2.3) and the general framework for the development of a gradient dependent fatigue limit criterion Eq.(3.2.2), a new version can be written in the form:

$$\sqrt{\widetilde{J_{2,a}}} + a\widetilde{\sigma_{H,max}} \leq b. \quad (3.2.10)$$

This formula takes into account the indicator of the influence of the gradient of the stress deviator which reflects the spatial non-uniform distribution of stress state.

In practice, [Luu et al. \[2014\]](#) had proposed:

$$\sqrt{J_{2,a}} \sqrt{1 - \left(l_\tau \frac{\| \underline{\underline{Y}} \|,a}{\| \underline{\underline{S}} \|,a} \right)^{n_\tau}} + a\sigma_{H,max} \left(1 - \left\langle l_\sigma \frac{\| G \|}{\sigma_{H,max}} \right\rangle^{n_\sigma} \right) - b < 0. \quad (3.2.11)$$

Here $\| \underline{\underline{Y}} \|,a$ is the full stress gradient and $\| G \|$ is used as an indicator of the influence of the normal stresses gradient.

$$\| G \| = \| \nabla \sigma_{H,max} \| = \sqrt{\left(\frac{\partial \sigma_{H,max}}{\partial x} \right)^2 + \left(\frac{\partial \sigma_{H,max}}{\partial y} \right)^2 + \left(\frac{\partial \sigma_{H,max}}{\partial z} \right)^2}. \quad (3.2.12)$$

3.3 Optimized Crossland Criterion formulation

The precedent Luu and al. formula has six materials parameters $a, b, l_\tau, l_\sigma, n_\tau, n_\sigma$ to be identified experimentally. The calibration can be complicated ; it does not lead to a unique set of parameters. Physical considerations, such as the length scales, have to be taken into account for choosing the optimized material constants. For practical application in an industrial context, it is essential to reduce the number of parameters. We therefore wish to investigate a simpler construction, departing from the classical Crossland criterion.

Surfaces with stresses decreasing in depth are, here and after, considered. Failure occurs at the point x_0 when, $(\sqrt{J_{2,a}} + a\sigma_{H,max} - b)(x_0) \geq 0$. To be more general and avoid singularity, this condition should be satisfied in some x_0 neighboring volume of size l_g , leading to a criterion given by:

$$\inf_{x \in B(\underline{x}_0, \underline{l}_g)} \left(\sqrt{J_{2,a}} + a\sigma_{H,max} - b \right) (x) \geq 0. \quad (3.3.1)$$

To obtain a suitable expression, an expansion of Eq.(3.3.1) is performed in the neighborhood of \underline{x}_0 . The sought formula should account for the beneficial effect of the stress gradient. Considering that the stress is decreasing in depth, we consider the most favorable point in the neighborhood (inf), thus a negative sign is associated with the norm of the gradient of stress tensor in the proposed formula. In addition, the gradient term should not only affect hydrostatic stress but also shear stress.

An objective formulation based on the maximum value of deviatoric stress invariants $\sqrt{J_{2,a}}$ and of $\sigma_{H,max}$ in the neighborhood, is finally:

$$\sqrt{J_{2,a}} + a\sigma_{H,max} - l_g \parallel \nabla \sqrt{J_{2,a}} + a\nabla\sigma_{H,max} \parallel \leq b, \quad (3.3.2)$$

In this updated model, we keep the same material parameters a and b as before, and l_g is a characteristic length to be optimized to match the experimental results. The approach has thus only one supplementary material constant, l_g , whose calibration is easy.

3.4 Optimized Papadopoulos Criterion formulation

As seen in Chapter 2, Papadopoulos [1993] has proposed to opt for a mean value of the accumulated plastic strain on all possible slip systems of representative elementary volume (REV). So he chose to use an average value of accumulated plastic deformation rather than looking at failure of a single crystal. A spherical coordinate system (Figure 3.3) to guide the vector of normal in material plane, and the unit orientation vector r linked to a sliding direction of this plane is used to conduct the integration over all possible orientations.

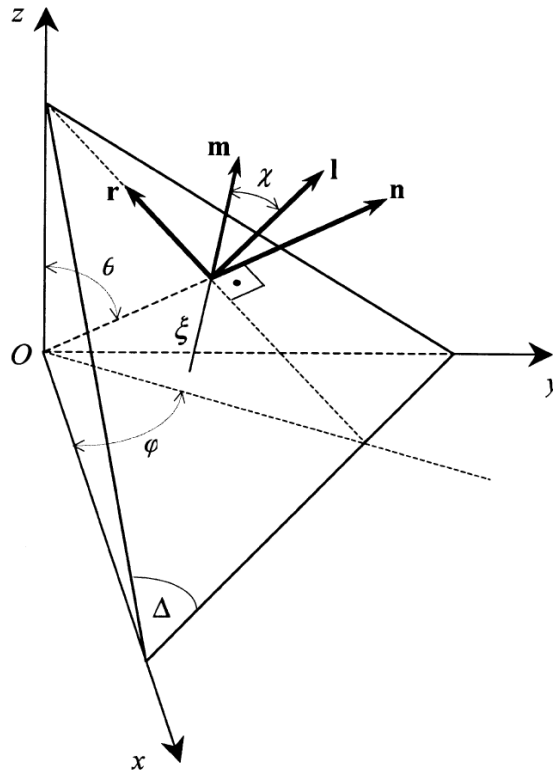


Figure 3.3 – Material plane Δ passing through point O of a body and its associated (n, l, r) frame.

At any point O of a body, a material plane Δ can be defined by its unit normal vector \mathbf{n} . This vector \mathbf{n} makes an angle θ with the z -axis of a $Oxyz$ frame attached to the body, and its projection on the xy plane makes an angle φ with axis x . For each plane Δ a new quantity is introduced as the quadratic mean value, over all the sliding directions of the considered plane, of the resolved shear stress amplitude and denoted as T_a . This shear stress quantity was first introduced in [Papadopoulos and Panoskaltsis \[1996\]](#) and was subsequently used by other researchers. The critical plane according to his proposal is that onto which $T_a(\varphi, \theta)$ achieves its maximum value. The fatigue limit criterion is written as:

$$\max T_a + \alpha_\infty \sigma_{h,max} \leq \gamma_\infty \quad (3.4.1)$$

where α_∞ and γ_∞ are material parameters to be determined ([Papadopoulos \[2001\]](#)).

$$\sigma_{h,max} = \max_t \left\{ \frac{1}{3} \operatorname{tr}(\underline{\underline{\sigma}}(t)) \right\}.$$

As seen earlier, the construction of T_a is based on the calculation of a local shear stress τ :

$$\begin{aligned} \tau = & [\sin \theta \cos \varphi \sigma_{xx} + \sin \theta \sin \varphi \sigma_{xy} + \cos \theta \sigma_{xz}] (- \sin \varphi \cos \chi - \cos \theta \cos \varphi \sin \chi) + \\ & [\sin \theta \cos \varphi \sigma_{xy} + \sin \theta \sin \varphi \sigma_{yy} + \cos \theta \sigma_{yz}] (\cos \varphi \cos \chi - \cos \theta \sin \varphi \sin \chi) + \\ & [\sin \theta \cos \varphi \sigma_{xz} + \sin \theta \sin \varphi \sigma_{yz} + \cos \theta \sigma_{zz}] \sin \theta \sin \chi \end{aligned} \quad (3.4.2)$$

It is clear that this shear stress is a function of φ, θ, χ and of time t in the case of variable amplitude and out-of-phase loading, i.e. $\tau = \tau(\varphi, \theta, \chi, t)$. Upon fixing a pair of angles (φ, θ) (i.e. a plane Δ) and an angle χ (i.e. a line ξ on Δ), one can define the amplitude of the resolved shear stress τ_a , acting on Δ along ξ by the formula:

$$\tau_a(\varphi, \theta, \chi) = \frac{1}{2} \left[\max_{t \in P} \tau_a(\varphi, \theta, \chi, t) - \min_{t \in P} \tau_a(\varphi, \theta, \chi, t) \right] \quad (3.4.3)$$

Now, for a given plane Δ , i.e. for a fixed pair of angles (φ, θ) , the generalized shear stress amplitude T_a is defined as the L^2 average in the plane Δ of the amplitude of resolved shear stress:

$$T_a(\varphi, \theta) = \sqrt{\frac{1}{\pi} \int_{\chi=0}^{2\pi} \tau_a^2(\varphi, \theta, \chi) d\chi} \quad (3.4.4)$$

We note the fatigue limit in fully reversed torsion t_{-1} and the fatigue limit in fully reversed bending f_{-1} . From these two tests we get the parameters from Eq.(3.4.1):

$$\gamma_\infty = t_{-1},$$

$$\alpha_\infty = 3 \left(\frac{t_{-1}}{f_{-1}} - \frac{1}{2} \right).$$

The Papadopoulos fatigue limit criterion is therefore:

$$\max T_a + 3(t_{-1}/f_{-1} - 1/2) \sigma_{h,max} \leq t_{-1}. \quad (3.4.5)$$

Now, the Papadopoulos Criterion can be simply extended to cases with gradient effects by

$$\max T_a + \alpha_\infty \sigma_{H,max} - l_g \parallel \nabla \max T_a + \alpha_\infty \nabla \sigma_{H,max} \parallel \leq \gamma_\infty. \quad (3.4.6)$$

3.5 Optimized Dang Van Criterion formulation

The Dang Van criterion as presented in [Ballard et al. \[1995\]](#) and reviewed in Chapter 2 is expressed as:

$$\max_t \{\tau(t) + a_D \sigma_H(t)\} \leq b_D. \quad (3.5.1)$$

Here, τ_a denotes the mesoscopic shear stress amplitude and is obtained from a mesoscopic stress tensor $\hat{\sigma}$ defined by:

$$\hat{\underline{\sigma}}(t) = (\underline{\sigma}(t) - \underline{s}^*).$$

Here \underline{s}^* is the center of the smallest hypersphere circumscribed to the loading path in deviatoric stress space. It is obtained by solving a “min-max” problem as follows:

$$\underline{s}^* = \arg \min_{\underline{s}_1} \left\{ \max_t \left\| \underline{\sigma}(t) - \underline{s}_1 \right\| \right\}.$$

In the case of fully reversed loading, the values $\underline{s}^* = 0$ can be directly deduced without solving the “min-max problem” as in general case.

The principal stress values of stress tensor $\hat{\underline{\sigma}}$ being denoted by $\hat{\sigma}_{III}(t) \leq \hat{\sigma}_{II}(t) \leq \hat{\sigma}_I(t)$, one gets the amplitude of shear stress by:

$$\max_n \tau_a(t) = \frac{1}{2}(\hat{\sigma}_I(t) - \hat{\sigma}_{III}(t)).$$

Moreover, $\sigma_H(t)$ denotes the hydrostatic stress as a function of the time. The material characteristic parameters a_D and b_D are finally given from traction compression and torsion fatigue limits by :

$$a_D = \frac{3t_{-1}}{s_{-1}} - \frac{3}{2};$$

$$b_D = t_{-1}.$$

Now, the Dang Van criterion can be extended to a gradient dependent criterion by

$$\max_t \{\tau(t) + a_D \sigma_H(t)\} - l_g \left\| \max_t \{\nabla \tau(t) + a_D \nabla \sigma_H(t)\} \right\| \leq b_D. \quad (3.5.2)$$

3.6 Calibration of the criteria

In this section, two different uniaxial fatigue tests with stress gradient effects are used to calibrate the optimized gradient Crossland, Papadopoulos and Dang Van criteria. An application to a biaxial test fatigue test shows the ability of the proposed approach to account for stress gradient in multiaxial cases.

3.6.1 Fully reversed 4-point bending and rotating cantilever bending fatigue tests

With Crossland criterion

The model of 4-point bending is first considered. The bar made of steel has both ends fixed. The radius R is a variable ranging from 1mm to 30mm in order to challenge the fact “the smaller, the stronger”. The length L of the bar is 100 mm.

The bending moment is the same in the interval $L \leq x \leq L+l$ and equal to $M = FL$ (Figure 3.4). For $L \leq x \leq L+l$ and $-R \leq y \leq R$, the bending stress σ is

$$\underline{\sigma}(t) = \sigma_{xx} \sin(\omega t) e_x \otimes e_x = \frac{FLy}{I} \sin(\omega t) e_x \otimes e_x \quad (3.6.1)$$

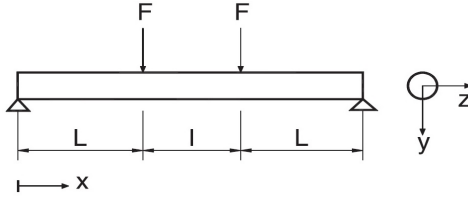


Figure 3.4 – 4-point bending test (Papadopoulos and Panoskaltsis [1996])

with $I = \pi R^4/4$, ω is the angular velocity. The maximum stress during the cyclic loading in the bar is thus $\sigma_{max} = \frac{FLy}{I}$, while the macroscopic stress range is $\Delta\underline{\sigma}(t) = 2\sigma_{max}e_x \otimes e_x$, and the hydrostatics stress takes the value

$$\sigma_{H,max} = \max_t \left\{ \frac{1}{3} \text{tr}(\sigma(t)) \right\} = \frac{1}{3} \sigma_{max} = \frac{FLy}{3I}. \quad (3.6.2)$$

From the value of the deviatoric stress

$$\Delta\underline{\underline{\sigma}} = \Delta\underline{\sigma} - \frac{1}{3}(\text{tr}\Delta\underline{\sigma})\underline{\underline{1}} = \begin{pmatrix} \frac{4}{3}\sigma_{max} & 0 & 0 \\ 0 & -\frac{2}{3}\sigma_{max} & 0 \\ 0 & 0 & -\frac{2}{3}\sigma_{max} \end{pmatrix}, \quad (3.6.3)$$

we can compute the second invariant of the stress deviator :

$$\sqrt{J_{2,a}} = \frac{1}{2\sqrt{2}} \sqrt{\Delta\underline{\underline{\sigma}} : \Delta\underline{\underline{\sigma}}} = \frac{\sigma_{max}}{\sqrt{3}} = \frac{FLy}{\sqrt{3}I}. \quad (3.6.4)$$

Then the gradient part is given by:

$$\nabla \sqrt{J_{2,a}} = \frac{\partial \sqrt{J_{2,a}}}{\partial x} e_x + \frac{\partial \sqrt{J_{2,a}}}{\partial y} e_y + \frac{\partial \sqrt{J_{2,a}}}{\partial z} e_z = \left(0, \frac{FL}{\sqrt{3}I}, 0 \right), \quad (3.6.5)$$

and

$$\nabla \sigma_{H,max} = \left(0, \frac{FL}{3I}, 0 \right). \quad (3.6.6)$$

The parameters a and b of the standard Crossland criterion, are obtained from fully reversed tension-compression fatigue limit s_{-1} and torsion fatigue limit t_{-1} using Eq.(3.2.9).

From Eq.(3.2.3), standard Crossland criterion without gradient effect (for radius R) is:

$$\sqrt{J_{2,a}} + a\sigma_{H,max} = \frac{FLR}{\sqrt{3}I} + \frac{aFLR}{3I} \leq b. \quad (3.6.7)$$

The gradient term here is given by:

$$\| \nabla \sqrt{J_{2,a}} + a\nabla \sigma_{H,max} \| = \frac{FL}{\sqrt{3}I} + \frac{aFL}{3I}. \quad (3.6.8)$$

By comparison we can see in 4-point bending test the difference between classical and modified Crossland criterion corresponds to the product of the characteristic length l_g by the term (3.6.8) associated to the decrease of the stress in depth. This value shows how much the modification affects the Crossland criterion.

Crossland criterion with beneficial gradient term as shown in Eq.(3.3.2) is given by:

$$\begin{aligned} \sqrt{J_{2,a}} + a\sigma_{H,max} - l_g(\| \nabla \sqrt{J_{2,a}} + a\nabla \sigma_{H,max} \|) &= \\ \frac{FLR}{\sqrt{3}I} + \frac{aFLR}{3I} - l_g \left(\frac{FL}{\sqrt{3}I} + \frac{aFL}{3I} \right) &= \\ \frac{1}{\sqrt{3}}\sigma_{max} + \frac{a}{3}\sigma_{max} - l_g \left(\frac{1}{\sqrt{3}R}\sigma_{max} + \frac{a}{3R}\sigma_{max} \right) &\leq b, \end{aligned} \quad (3.6.9)$$

which is to say:

$$\sigma_{max} \leq \frac{b}{\frac{1}{\sqrt{3}} + \frac{a}{3} - l_g \left(\frac{1}{\sqrt{3}R} + \frac{a}{3R} \right)}. \quad (3.6.10)$$

The material parameters a and b are obtained using their classical expressions as Eq.(3.2.9) from tests free of stress gradient. The corresponding fatigue limit are denoted s_{ref} for the alternate tension-compression test, and $t_{ref} = b$ for the alternate torsion test. For a specimen of radius R the alternate bending fatigue limit is denoted $f_c(R)$. We can observe that:

$$f_c(R) = \frac{b}{\frac{1}{\sqrt{3}} + \frac{a}{3} - l_g \left(\frac{1}{\sqrt{3}R} + \frac{a}{3R} \right)} \geq s_{ref} = \frac{b}{\frac{1}{\sqrt{3}} + \frac{a}{3}}, \quad (3.6.11)$$

and that $f_c(R)$ tends to s_{ref} for large values of R .

With Papadopoulos criterion

From Eq.(3.6.1), the resolved shear stress τ acting along a line ξ of a plane Δ is given by Eq.(3.4.2), which in this case leads to:

$$\tau(\varphi, \theta, \chi, t) = \sigma_{xx} \sin(2\pi t/P) \sin\theta \cos\theta \sin\chi. \quad (3.6.12)$$

Clearly, for the worse case in χ , the resolved shear stress amplitude is equal to:

$$\tau_a(\varphi, \theta, \chi) = \sigma_{xx} |\sin\theta \cos\theta \sin\chi|. \quad (3.6.13)$$

The generalized shear stress amplitude T_a becomes:

$$T_a(\varphi, \theta) = \sqrt{\frac{1}{\pi} \int_{\chi=0}^{2\pi} (\sigma_{xx} |\sin\theta \cos\theta \sin\chi|)^2 d\chi} \quad (3.6.14)$$

The maximum value of T_a is obtained at $(\theta = \pi/4)$ and at $(\theta = 3\pi/4)$. It is equal to:

$$\max T_a = \sigma_{xx}/2 \quad (3.6.15)$$

The hydrostatic stress is given by:

$$\sigma_H(t) = \frac{1}{3} \sigma_{xx} \sin(2\pi t/P) \quad (3.6.16)$$

The maximum value of σ_H reached in a loading cycle is:

$$\sigma_{H,max} = \sigma_{xx}/3 \quad (3.6.17)$$

Papadopoulos criterion with beneficial gradient term as shown in Eq.(3.4.6) is then given by:

$$\begin{aligned} \max T_a + \alpha_\infty \sigma_{H,max} - l_g \|\nabla \max T_a + \alpha_\infty \sigma_{H,max}\| = \\ \frac{FLR}{2I} + \frac{\alpha_\infty FLR}{3I} - l_g \left(\frac{FL}{2I} + \frac{\alpha_\infty FL}{3I} \right) = \\ \frac{1}{2} \sigma_{max} + \frac{\alpha_\infty}{3} \sigma_{max} - l_g \left(\frac{1}{2R} \sigma_{max} + \frac{\alpha_\infty}{3R} \sigma_{max} \right) \leq \gamma_\infty = t_{ref}, \end{aligned} \quad (3.6.18)$$

which is to say:

$$\sigma_{max} \leq \frac{\gamma_\infty}{\frac{1}{2} + \frac{\alpha_\infty}{3} - l_g \left(\frac{1}{2R} + \frac{\alpha_\infty}{3R} \right)}. \quad (3.6.19)$$

For a specimen of radius R the alternate bending fatigue limit is denoted $f_p(R)$. We can observe that:

$$f_p(R) = \frac{\gamma_\infty}{\frac{1}{2} + \frac{\alpha_\infty}{3} - l_g \left(\frac{1}{2R} + \frac{\alpha_\infty}{3R} \right)} \geq s_{ref} = \frac{\gamma_\infty}{\frac{1}{2} + \frac{\alpha_\infty}{3}}. \quad (3.6.20)$$

With Dang Van criterion

Under fully reversed loading we have:

$$\tau(t) = \frac{1}{2}(\sigma_{xx}(t) - 0)$$

From Eq.(3.5.2) we can deduce Dang Van criterion.

$$\begin{aligned} \max_t \{ \tau(t) + a_D \sigma_H(t) \} - l_g \| \nabla \tau(t) + a_D \nabla \sigma_H(t) \| = \\ \frac{FLR}{2I} + \frac{aFLR}{3I} - l_g \left(\frac{FL}{2I} + \frac{aFL}{3I} \right) = \\ \frac{1}{2} \sigma_{max} + \frac{a}{3} \sigma_{max} - l_g \left(\frac{1}{2R} \sigma_{max} + \frac{a}{3R} \sigma_{max} \right) \leq b_D = t_{ref}, \end{aligned} \quad (3.6.21)$$

which is to say:

$$\sigma_{max} \leq \frac{b}{\frac{1}{2} + \frac{a}{3} - l_g \left(\frac{1}{2R} + \frac{a}{3R} \right)}. \quad (3.6.22)$$

We can observe that the corresponding bending limit is thus

$$f_D(R) = \frac{b}{\frac{1}{2} + \frac{a}{3} - l_g \left(\frac{1}{2R} + \frac{a}{3R} \right)} \geq s_{ref} = \frac{b}{\frac{1}{2} + \frac{a}{3}}. \quad (3.6.23)$$

Comparison with experimental data

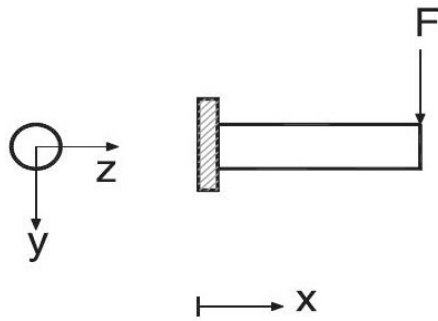


Figure 3.5 – Cantilever bending test (Papadopoulos and Panoskaltsis [1996])

The case of cantilever fully reversed bending corresponds to the four point bending test except that there, the bending moment is function of x . Thus, the maximum stress σ_{max} for a given section is a function of x . But, the y dimension of the beam is much smaller than its x dimension, which allows us to neglect gradients in x . All expressions of the four point bending case thus apply to this case.

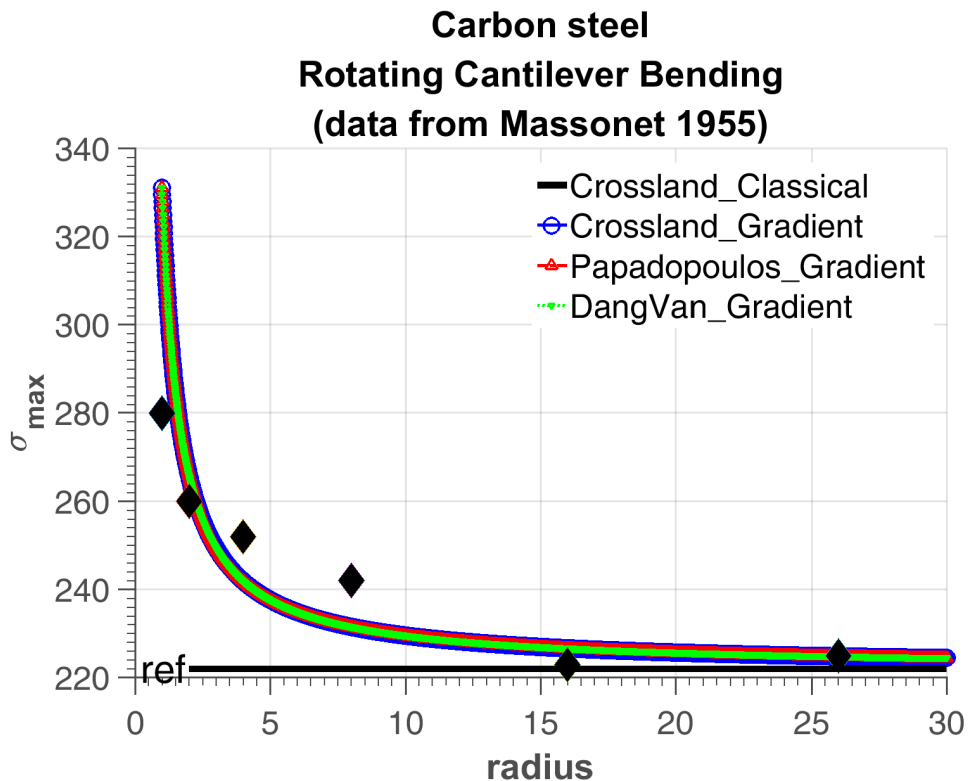


Figure 3.6 – Fatigue limits with gradient effect for different radii (Massonet [1955]).

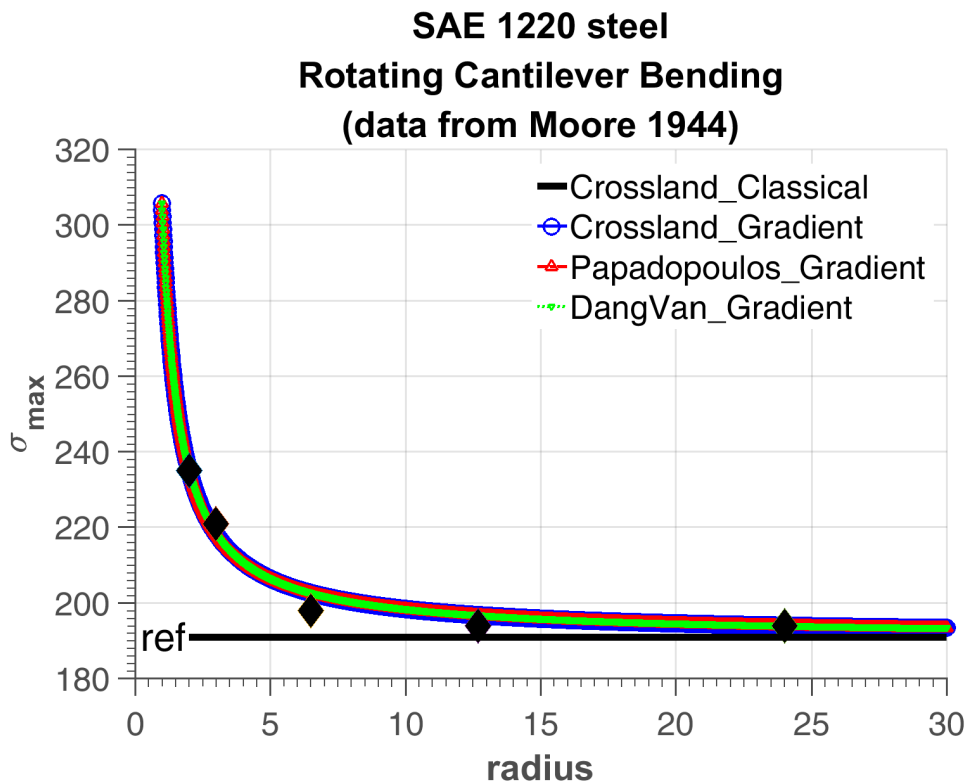


Figure 3.7 – Fatigue limits with gradient effect for different radii (Moore and Morkovin [1944]).

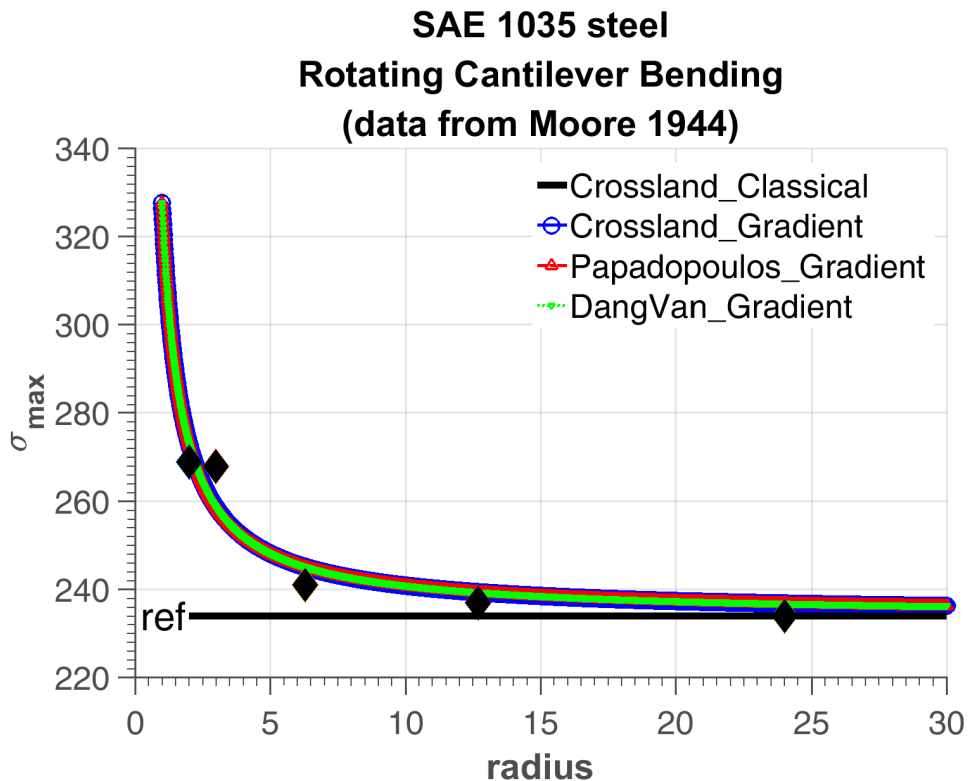


Figure 3.8 – Fatigue limits with gradient effect for different radii (Pogoretskii [1966]).

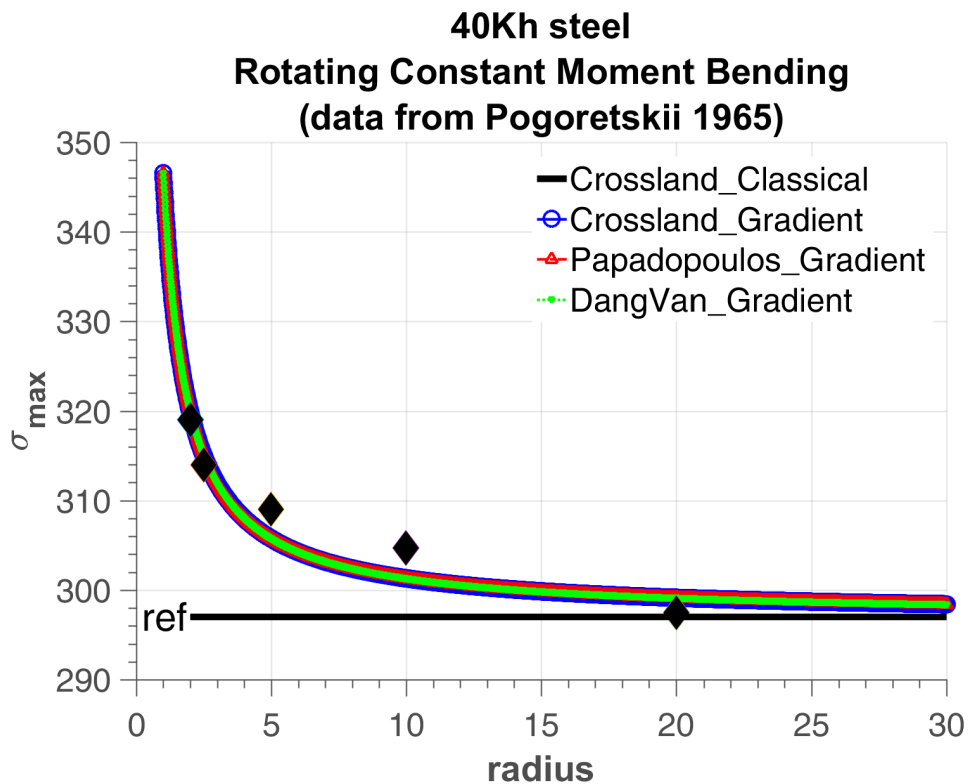


Figure 3.9 – Fatigue limits with gradient effect for different radii (Papadopoulos and Panoskaltsis [1996]).

Figure 3.6 to Figure 3.9 shows some test results of rotating bending fatigue limits from the literature in which the fatigue limits are plotted against the specimen radii. In the absence of gradient effect, we get the horizontal lines indicated in black. We observe that the three criteria here give very similar results when they are calibrated on uniaxial tests. Figure 3.6, Figure 3.7 and Figure 3.8 are related to cantilever bending tests and Figure 3.9 depicts constant moment tests.

Eq.(3.6.11) with a et b calibrated from given S_{ref} and t_{ref} is used to estimate the characteristic length l_g in order to give the best correlation between simulated and experimental fatigue limit obtained in rotating cantilever bending tests for different materials and radii. The results are sketched and the corresponding parameters are shown in Table 3.1.

Table 3.1 – Length scales of different materials

	1220 steel	Carbon steel	1035 steel	40Kh steel
S_{ref} [MPa]	191	222	234	297
t_{ref} [MPa]	143	151	172	180
l_g [mm]	0.3755	0.3297	0.2861	0.1424

We can observe a very interesting phenomenon that the smaller fatigue limit is, the larger influence of gradient effect is. This phenomenon is due to the fact that the smaller the grain size, the higher the strength. This happens because of the greater interactions between dislocations as the grain size and the available room for their gliding through the lattice, is reduced. With this experimental result we can say there is positive correlations between the length scale l_g and the grain size.

3.6.2 Bending-torsion fatigue tests

With Crossland criterion

The bending moment is a linear function of x , $M_b = -F(L - x)$. The twisting moment is denoted M_t . The stress σ_{xx} now varies along the depth (i.e. y-axis) and the length (i.e. x-axis) of the specimen, but as above we will neglect the gradient in x as compared to the gradient in y . The bending stress is given here by :

$$\sigma_a = \frac{-F(L - x)}{I} R = \frac{M_b}{I} y \quad \text{with} \quad I = \frac{\pi R^4}{4}, \quad (3.6.24)$$

while the twisting shear stress is given by $\tau_a = \frac{M_t}{J} y \quad \text{with} \quad J = \frac{\pi R^4}{2}$. The stress tensor $\underline{\underline{\sigma}}$ is then:

$$\underline{\underline{\sigma}}(t) = \begin{pmatrix} \sigma_a \sin(\omega t) & \tau_a \sin(\omega t) & 0 \\ \tau_a \sin(\omega t) & 0 & 0 \\ 0 & 0 & 0 \end{pmatrix}. \quad (3.6.25)$$

Its range tensor is:

$$\Delta \underline{\underline{\sigma}} = \begin{pmatrix} 2\sigma_a & 2\tau_a & 0 \\ 2\tau_a & 0 & 0 \\ 0 & 0 & 0 \end{pmatrix}, \quad (3.6.26)$$

with deviator

$$\Delta_{\underline{S}} = \Delta_{\underline{\sigma}} - \frac{1}{3}(\text{tr}\Delta_{\underline{\sigma}})\underline{1} = \begin{pmatrix} \frac{4}{3}\sigma_a & 2\tau_a & 0 \\ 2\tau_a & -\frac{2}{3}\sigma_a & 0 \\ 0 & 0 & -\frac{2}{3}\sigma_a \end{pmatrix}. \quad (3.6.27)$$

The second invariant of the stress deviator is then:

$$\sqrt{J_{2,a}} = \frac{1}{2\sqrt{2}}\sqrt{\Delta_{\underline{S}} : \Delta_{\underline{S}}} = \sqrt{\frac{1}{3}\sigma_a^2 + \tau_a^2} = \sqrt{\frac{M_b^2}{3I^2} + \frac{M_t^2}{J^2}}y. \quad (3.6.28)$$

As for the hydrostatics stress, we have

$$\sigma_{H,max} = \max_t \left\{ \frac{1}{3}\text{tr}(\sigma(t)) \right\} = \frac{\sigma_a}{3} = \frac{M_b}{3I}y. \quad (3.6.29)$$

Then the gradient part has the value:

$$\begin{aligned} \nabla \sqrt{J_{2,a}} &= \frac{\partial \sqrt{J_{2,a}}}{\partial x} \underline{e}_x + \frac{\partial \sqrt{J_{2,a}}}{\partial y} \underline{e}_y + \frac{\partial \sqrt{J_{2,a}}}{\partial z} \underline{e}_z = \left(0, \sqrt{\frac{M_b^2}{3I^2} + \frac{M_t^2}{J^2}}, 0 \right) \\ &= \left(0, \frac{\sqrt{\frac{1}{3}\sigma_a^2 + \tau_a^2}}{y}, 0 \right), \end{aligned} \quad (3.6.30)$$

and

$$\nabla \sigma_{H,max} = \left(0, \frac{M_b}{3I}, 0 \right) = \left(0, \frac{\sigma_a}{3y}, 0 \right). \quad (3.6.31)$$

The parameters a and b of the standard Crossland criterion, are obtained from fully reversed tension-compression fatigue limit s_{ref} and torsion fatigue limit t_{ref} using Eq.(3.2.9).

From Eq.(3.2.3), standard Crossland criterion without gradient effect writes:

$$\sqrt{J_{2,a}} + a\sigma_{H,max} = \sqrt{\frac{\sigma_a^2}{3} + \tau_a^2} + \frac{\sigma_a}{3} \leq b. \quad (3.6.32)$$

The gradient term here is given by:

$$\| \nabla \sqrt{J_{2,a}} + a\nabla \sigma_{H,max} \| = \frac{\sqrt{\frac{\sigma_a^2}{3} + \tau_a^2}}{y} + \frac{a\sigma_a}{3y}. \quad (3.6.33)$$

Crossland criterion with beneficial gradient term as shown in Eq.(3.3.2) now writes

$$\begin{aligned} \sqrt{J_{2,a}} + a\sigma_{H,max} - l_g \| \nabla \sqrt{J_{2,a}} + a\nabla \sigma_{H,max} \| &= \\ \sqrt{\frac{\sigma_a^2}{3} + \tau_a^2} + \frac{a\sigma_a}{3} - l_g \left(\frac{\sqrt{\frac{\sigma_a^2}{3} + \tau_a^2}}{y} + \frac{a\sigma_a}{3y} \right) &\leq b. \end{aligned} \quad (3.6.34)$$

With Papadopoulos criterion

We can find the resolved shear stress $\tau(\varphi, \theta, \chi, t)$ with Eq.(3.4.2). Although the intermediate calculations are complicated, the result achieves the very simple form [Papadopoulos et al. \[1997\]](#). The generalized shear stress amplitude T_a is then:

$$T_a(\varphi, \theta) = \sqrt{\frac{1}{\pi} \int_{\chi=0}^{2\pi} \tau^2(\varphi, \theta, \chi) d\chi} = \sqrt{\frac{\sigma_a^2}{3} + \tau_a^2}.$$

$$\sigma_{H,max} = \frac{1}{3}\sigma_a$$

The modified Papadopoulos criterion from Eq.(3.4.6) is:

$$\max T_a + \alpha_\infty \sigma_{H,max} - l_g \parallel \nabla \max T_a + \alpha_\infty \sigma_{H,max} \parallel \leq \gamma_\infty,$$

From the above calculation and the linear dependance of the stress field as function of y , Papadopoulos criterion with beneficial gradient term reduces to

$$\begin{aligned} \max T_a + \alpha_\infty \sigma_{H,max} - l_g \parallel \nabla \max T_a + \alpha_\infty \sigma_{H,max} \parallel = \\ \sqrt{\frac{\sigma_a^2}{3} + \tau_a^2} + \frac{\alpha_\infty \sigma_a}{3} - l_g \left(\frac{\sqrt{\frac{\sigma_a^2}{3} + \tau_a^2}}{y} + \frac{\alpha_\infty \sigma_a}{3y} \right) \leq \gamma_\infty. \end{aligned} \quad (3.6.35)$$

With Dang Van criterion

The principal stresses in 2D tensor are expressed as:

$$\sigma_1 = \frac{\sigma_a}{2} + \sqrt{\left(\frac{\sigma_a}{2}\right)^2 + \tau_a^2}$$

$$\sigma_2 = \frac{\sigma_a}{2} - \sqrt{\left(\frac{\sigma_a}{2}\right)^2 + \tau_a^2}$$

With this one gets the amplitude of shear stress by:

$$\max_t \tau(t) = \frac{1}{2}(\sigma_1 - \sigma_2) = \sqrt{\left(\frac{\sigma_a}{2}\right)^2 + \tau_a^2}$$

Dang Van criterion with beneficial gradient term as shown in Eq.(3.6.36) now becomes :

$$\begin{aligned} \max_t \{\tau(t) + a_D \sigma_H(t)\} - l_g \parallel \nabla \tau(t) + a_D \nabla \sigma_H(t) \parallel = \\ \sqrt{\left(\frac{\sigma_a}{2}\right)^2 + \tau_a^2} + \frac{a_D \sigma_a}{3} - l_g \left(\frac{\sqrt{\left(\frac{\sigma_a}{2}\right)^2 + \tau_a^2}}{y} + \frac{a \sigma_a}{3y} \right) \leq b_D. \end{aligned} \quad (3.6.36)$$

Comparison with experimental data

This classical Crossland ellipse arc delimits in the $s_{ref} - t_{ref}$ plane the safe domain against fatigue failure. In the case of fully reversed in-phase tension-compression and torsion fatigue tests, it gives the “ellipse arc equation” (Papadopoulos and Panoskaltsis [1996]) which is Eq.(3.6.34) with $b = t_{ref}$ and $a = \frac{3t_{ref}}{s_{ref}} - \sqrt{3}$:

$$\left(\frac{\tau_a}{t_{ref}}\right)^2 + \left(\frac{2s_{ref}}{\sqrt{3}t_{ref}} - 1\right) \left(\frac{\sigma_a}{s_{ref}}\right)^2 + \left(2 - \frac{2s_{ref}}{\sqrt{3}t_{ref}}\right) \frac{\sigma_a}{s_{ref}} \leq 1 \quad (3.6.37)$$

However, if one tries to predict the behavior of the material in combined bending and torsion, which involves the gradients of normal and shear stresses, high discrepancies between predictions and experimental data will be found.

By introducing the values of $\sqrt{J_{2,a}}$ and $\sigma_{H,max}$ in the the classical Crossland criterion, along with the change of parameter a from $\left(\frac{3t_{-1}}{s_{-1}} - \sqrt{3}\right)$ to $\left(\frac{3t_{-1}}{f_{-1}} - \sqrt{3}\right)$ in Eq.(3.2.3), we obtain the "Papadopoulos ellipse arc" based on (t_{-1}, f_{-1}) in the plane of amplitudes σ_a and τ_a :

$$\left(\frac{\tau_a}{t_{-1}}\right)^2 + \left(\frac{2f_{-1}}{\sqrt{3}t_{-1}} - 1\right) \left(\frac{\sigma_a}{f_{-1}}\right)^2 + \left(2 - \frac{2f_{-1}}{\sqrt{3}t_{-1}}\right) \frac{\sigma_a}{f_{-1}} \leq 1 \quad (3.6.38)$$

This apparent size effect, which is actually a gradient effect, is taken into account intrinsically by gradient fatigue criteria, as for instance proposed in [Papadopoulos and Panoskaltsis \[1996\]](#). Nevertheless, these criteria do not take into account the possible dependence of the fatigue limit on the shear stress gradient and consequently do not distinguish between t_{-1} and t_{ref} .

It can be seen from Figure 3.10 that the Crossland ellipse arc (Eq. 3.6.37) based on the s_{ref} - t_{ref} fatigue limits and the Crossland ellipse arc (Eq. 3.6.38) based on f_{-1} - t_{-1} are different demonstrating clearly the effect of stress gradient. The first curve, obtained within zero normal stress gradient assumption, does not fit the experimental data from combined bending-twisting tests having a non-zero stress gradient. The difference between test points and classical Crossland ellipse arc near the x-axis where the normal load is predominant, is a proof of the beneficial "size and gradient effects. Indeed, the difference between two kinds of fatigue test can be clearly seen: the bending test (test points) includes the beneficial effects of the normal stress gradient; the tension-compression test (Crossland ellipse arc) excludes these effects due to the gradient-free stress state. To account for the shear gradient amplitude effect, a clear distinction must be made between t_{ref} determined at the radius R_∞ of specimen large enough and t_{-1} determined at the radius R of the considered specimen. Then all these above analyses affirm, first, the "size effect" on fatigue limits (Smaller is Stronger) as well as the beneficial effect of the normal stress gradient (Higher Gradient is Stronger), and second, the necessity of a distinction between $t_{ref} = t(R_\infty)$ and $t_{-1}(R)$ when applied to the classical Crossland criterion and the new gradient criterion, respectively. With all such conceptions, the experimental data now agree very well with the ellipse arc based on the new criteria proposed, as plotted in Figure 3.10. It is also noticed that the substitution of the material parameters by the bending and torsion limits is an unorthodox way to bypass the above described problems for classical criterion. The same ellipse arc is obtained in a more intrinsic way using the proposed criterion.

Our proposal takes into account both gradients of hydrostatic stress and shear stress. For SAE 4340 steel, the tension-compression fatigue limit $S_{ref} = 397$ MPa and the torsion fatigue limit $t_{ref} = 258$ MPa. We use the same set of parameters as the original criteria except the gradient term with length scale l_g . Choosing the proper l_g (here $l_g = 2.5mm$) allows us to predict the experiments within the acceptable range as shown in Figure 3.10 at the critical locations $y = R$. These results, represented in the σ_a, τ_a plane (the so called fatigue ellipse arc) illustrate that our proposal is quite satisfactory in biaxial case.

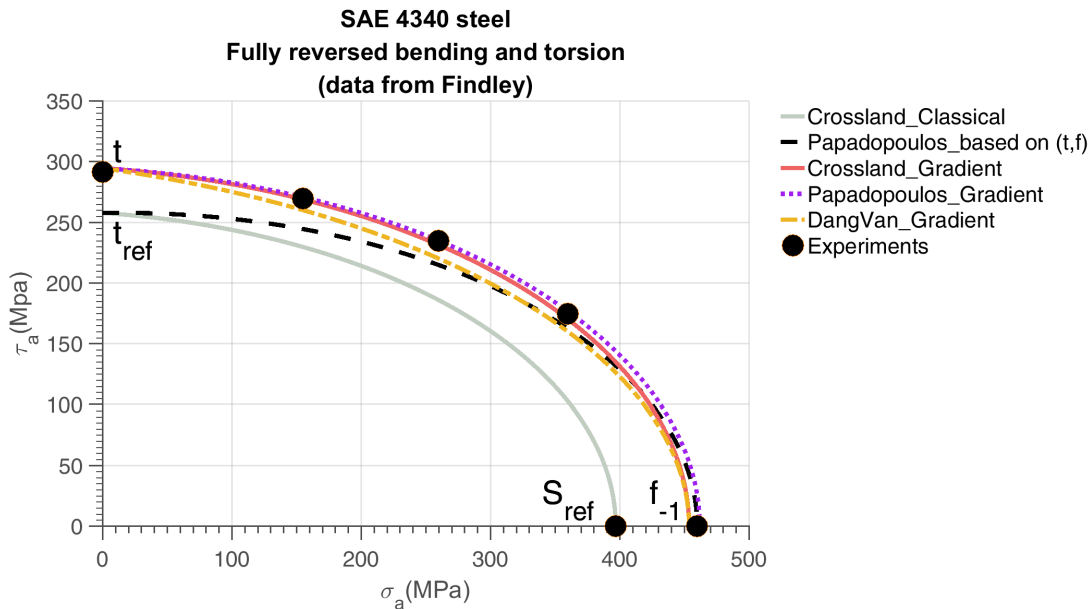


Figure 3.10 – Fully reversed combined bending-twisting fatigue limit data (Findley et al. [1956], Papadopoulos and Panoskaltsis [1996]) compared with updated values computed with gradient effects using Eq.(3.6.34), Eq.(3.6.35), Eq.(3.6.36), Eq.(3.6.37) and Eq.(3.6.38) with $l_g = 2.5 \text{ mm}$. In absence of gradient effect, we would get the inner gray ellipse corresponding to classical Crossland criterion.

3.7 Discussion

Remark 1 (Gradient terms). In this work, the pure size effect has not been considered and only stress gradient effect is modeled. Whereas the latter is dominant rather than totally to the pure size effect as usually believed. A unique gradient term is enough to model the gradient and loading effects. This is introduced either in the normal stress component of the classical fatigue criterion as Papadopoulos and Panoskaltsis [1996] proposed, or in the shear stress part as presented in Massonnet [1956]. However, in multiaxial fatigue tests, combining both normal and shear stress gradient terms is in principle indispensable to capture the previous effects.

Remark 2 (Material characteristic length scale l_g). The values of l_g of the model proposed extend from several hundredths of a micron to about a millimeter for cases considered, while the one of the model proposed very recently by Ferré et al. [2013] takes about a micron. The very difference between them is physically explained by the following reason: we study here the fatigue endurance of macroscopic specimens and components for which the crack initiation is generally detected by loss of stiffness corresponding to crack length which can reach a millimeter; whereas Ferré et al. consider crack nucleation in the scale is few dozen microns.

Remark 3 (Extensions to other load case). The dependence of fatigue limits on both “size” and gradient effects according to the specimen size (e.g. length, radius) has a “saturated” or “insensitive” threshold. That means, there always exists a certain “saturated” value for the specimen size (L_∞, R_∞) from which the fatigue behavior is insensitive to both effects and the proposed criteria exactly reduce to the respective classical ones. Nevertheless, it is not easy to compute the gradient in multiaxial loading case.

3.8 Conclusion and perspectives

The present work develops a simple formulation of gradient multiaxial fatigue criteria extending the classical HCF criteria. The objective is to model the "size", surface gradient and loading effects, not included yet in classical mechanics but become important at small scale, by taking into account just the gradient effect. Basing on some experimental observations, and departing from classical fatigue criteria, new class of criteria with stress gradient terms entering not only in the normal stress but also in the shear stress amplitude, are proposed. Such a formulation allows the new criteria to capture the "size" and gradient effects, and to cover a large range of loading mode (traction, bending, shearing). These new criteria are then generalized to multiaxial cases to capture both well-known phenomena "Smaller is Stronger" and "Higher Gradient is Stronger" and thus can reproduce fatigue experimental data even at small scale. Here in this work, the nature of these two phenomena is also clarified. "Higher Gradient is Stronger" is only related to the gradient effect, while "Smaller is Stronger" is related to both pure size and gradient effects where the latter is dominant - rather than totally to the pure size effect as usually believed. Extensions of some classical fatigue limit criteria such Crossland and Dang Van are done as illustrations. The proposed criteria shown a good agreement with a number of experiments from the literature. A more comprehensive introduction of a practical strategy to compute local gradient and validation for complex loading (real multiaxial loads) could be perspective for this research direction.

In methodological aspect, gradient approach just allows modeling the volumetric stresses instant distribution (related to loading case such as: tension-compression, torsion, plane bending), not volumetric stresses distribution all over the loading cycle (related to rotative bending). Thus the adopted criteria indifferently deal with the plane bending and the rotative bending tests, although their fatigue limits are actually different. Fatigue problems concerning other factors (machining, notches, defects, inclusions, corrosion, etc.) have been left out in this approach and need another approach to address. In particular for notched fatigue problems, this approach may be still applicable. A validation by means of experimental data is needed to examine this possibility. Cases with critical points located inside specimens where the gradient effect can be presumably negative on fatigue resistance, for instance those with presence of residual stresses, can be encountered and have not examined yet. A reexamination of the approach will be the object of the further work.

4

Time varying load : the standard approach

Contents

5.1	Multiscale energy dissipation approach	73
5.2	Kinematic Hardening Models	75
5.2.1	Linear Kinematic Hardening	75
5.2.2	Non-linear Kinematic Hardening	76
5.3	Mean stress effect in local model	76
5.4	Weakening scales and yield function	79
5.4.1	The concept of weakening scales	79
5.4.2	Distribution of weakening scales	79
5.4.3	Yield function with mean stress effect	80
5.4.4	Local plastic model	80
5.5	Construction of an energy based fatigue approach	81
5.6	Nonlinearity of damage accumulation	83
5.6.1	Energy approach with Chaboche law	83
5.6.2	Sequence effect	85
5.6.3	The final model	87
5.7	Numerical strategy	89
5.7.1	Scale discretization	89
5.7.2	Calculation of local plastic dissipation	89
5.7.3	Damage integration algorithm	91
5.8	Validation on recovery tests	98
5.8.1	Recovery of Chaboche law on cyclic loading	98
5.8.2	Numerical recovery of sequence effect	106
5.9	Identification strategy	111

4.1 The notion of damage in fatigue

In the case of fatigue, we usually employ the concept of the loading cycle instead of time to evaluate the evolution of damage and to measure the fatigue lifetime. The equations then depend on the load through globally defined quantities over a cycle, such as amplitude, maximum value, mean value. The growth equation of fatigue damage is therefore taken in the form:

$$\delta D = f(D)\delta N$$

$$\delta N = f_n \delta t$$

where δt is a time sampling of the history in a given number of time intervals $\delta t_1, \delta t_2, \dots, \delta t_i, \dots$ and f_n is the mean frequency of those cycles during the considered time step. The issue is thus to identify the function $f(D, S_a, S_m)$ relating the damage growth to the present damage, the load amplitude, the load mean value and so on. We will focus in this chapter on the classical ways of taking into account a possible dependence on D .

4.1.1 Linear and nonlinear accumulation of damage

Cumulative effects, whether linear or nonlinear, are of great importance in fatigue. The rule of linear accumulation is in fact a property of any linear or nonlinear differential equation with separable variables. One approach to variable load histories uses the concept of fraction of life (also referred to as cycle ratio) used up by an event. These fractions are added together; when their sum reaches 1.0 or 100 percent we expect failure. This is the most common measure of damage, and is the quantifying measure we present here.

The Palmgren-Miner linear rule as explained in [Lemaître and Chaboche \[1990\]](#) is based on the assumption that damage is accumulated additively when it is defined by the associated life ratio N_i/N_{F_i} where N_i is the number of cycles applied under a given load for which the number of cycles to fracture (under periodic conditions) would be N_{F_i} . The fracture criterion is:

$$\sum_i N_i/N_{F_i} = 1.$$

Therefore, in periodic tests, damage evolution is considered to be linear in that:

$$D = N/N_F.$$

For a test at two stress levels, the evolution is as shown schematically in Figure 4.2. In fact, the linear accumulation rule can be applied even to a damage which evolves nonlinearly. For this it is sufficient that a one-to-one relationship between D and N/N_F exists, or even that the damage evolution curve be a unique function (independent of the applied cycle) of the life ratio N/N_F .

There are, therefore, two ways of defining a damage incremental law incorporating the linear accumulation rule. It can be linear of the form described below and shown in Figure 4.1:

$$\delta D = \delta N/N_F(\dots),$$

where N_F is the number of cycles to failure defined by the chosen parametric data. The damage evolution can be nonlinear such as:

$$\delta D = \frac{(1 - D)^{-k}}{k + 1} \frac{\delta N}{N_F(\dots)}.$$

Above, the damage evolution curve as function of life ratio $\delta N/N_F$ is supposed to be independent of the local state of stress (Figure 4.2). In contrast, if the damage evolution curve, as a function of

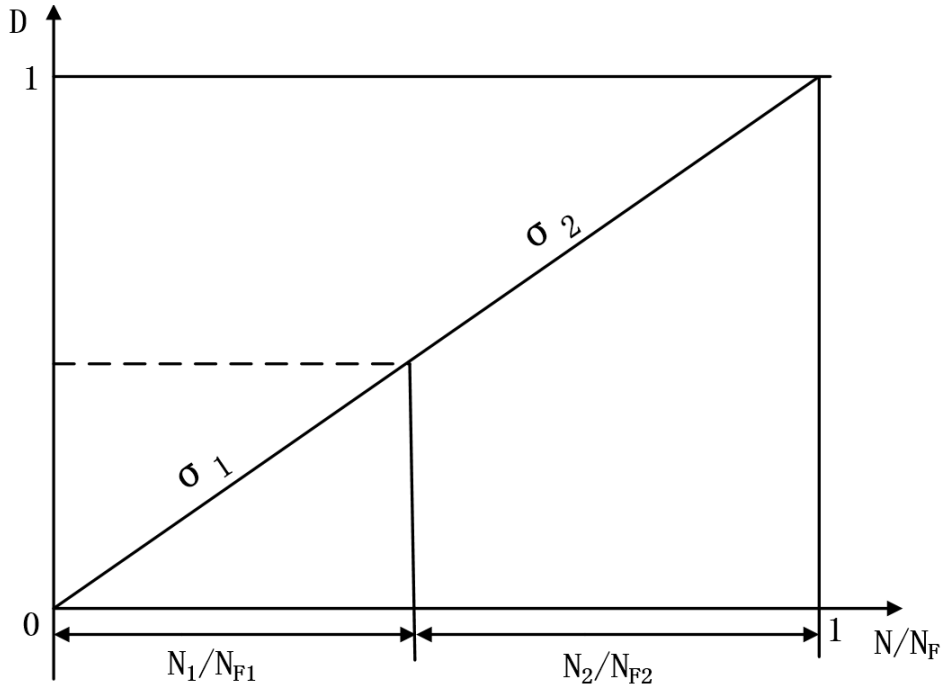


Figure 4.1 – Linear accumulation of damage with linear evolution

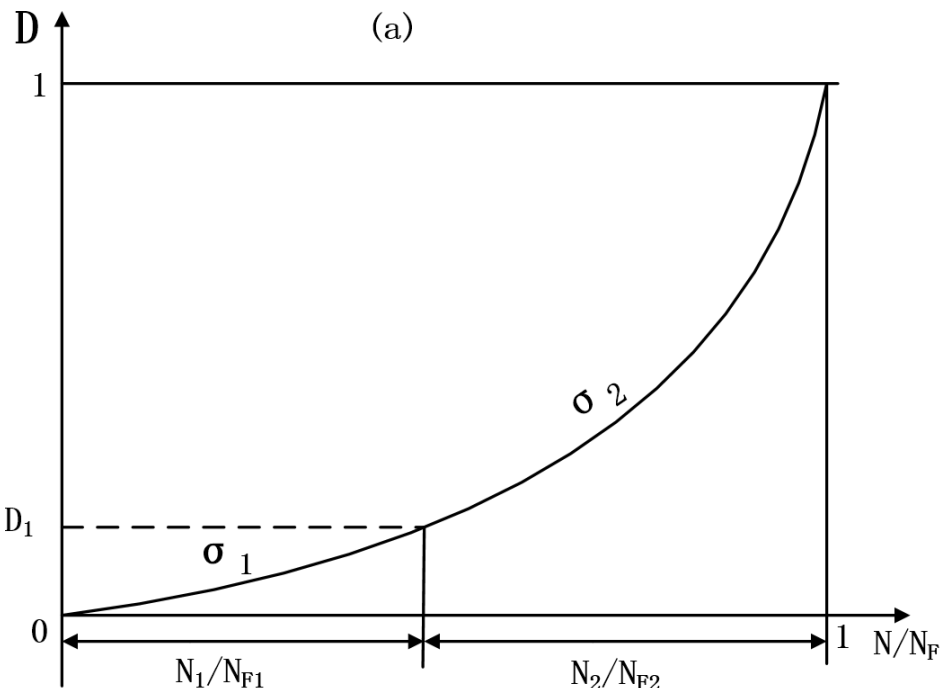


Figure 4.2 – Damage with nonlinear evolution and linear accumulation, where high then low stress loading sequence leads to the same fatigue life.

the life ratio N/N_F , depends on the applied loading we have the effect of nonlinear accumulation as shown in Figure 4.3. There, D_1 represents the state of internal damage at the end of the first level σ_1 . Evolution at the second level σ_2 continues from the same state, and it is clear that the sum of the life ratio is less than 1. From the point of view of the damage law, this nonlinearity always corresponds to the case where the variables which represent the load σ and the damage variable D have coupled evolution.

The Palmgren-Miner linear accumulation law gives good results for loads for which there is little

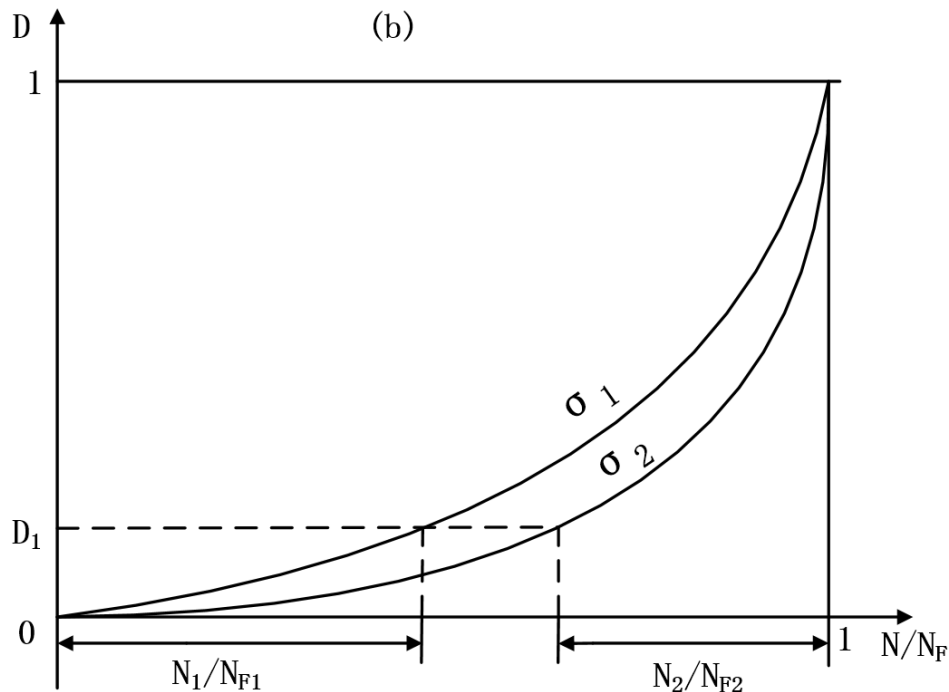


Figure 4.3 – Damage with nonlinear evolution and nonlinear accumulation, where high stress and low stress follow different damage evolution curve. This leads to differences into the summation of fatigue life proportion between different loading sequences.

variation in the amplitude and mean value of stress. The assumption of linear damage is open to many objections. For example, sequence and interaction of events may have major influences on life, the rate of damage accumulation may depend on the load amplitude, experimental evidence often indicates that $\sum_i N_i/N_{F_i} \neq 1$ for a low-to-high or a high-to-low loading sequence, all effects which are not taken into account in the linear damage assumption.

4.1.2 Classical Chaboche damage law

In cyclic loading, one way of writing a damage law which expresses the experimental results is to assume that the damage per cycle is a function of the maximum and the mean values of the stress:

$$\delta D / \delta N = f(\sigma_{Max}, \sigma_m).$$

In order to recover, after integration, one of the many forms proposed to represent the Wohler curves, Chaboche ([Chaboche and Lesne \[1988b\]](#)) proposes to use a law such as:

$$\delta D / \delta N = \frac{\sigma_{Max} - \sigma_l(\sigma_m)}{\sigma_u - \sigma_{Max}} \left(\frac{\sigma_{Max} - \sigma_m}{B(\sigma_m)} \right)^\gamma. \quad (4.1.1)$$

with:

$$\sigma_l(\sigma_m) = \sigma_m + s_{-1}(1 - b\sigma_m) : \text{fatigue limit.}$$

$$B(\sigma_m) = B_0(1 - b\sigma_m) : \text{the mean stress component in the fatigue limit.}$$

$$\sigma_u : \text{ultimate stress of the material.}$$

The number of cycles to failure is obtained by an obvious integration, with the condition:

$$N = 0 \rightarrow D = 0 \text{ (initial undamaged state),}$$

$$N = N_F \rightarrow D = 1 \text{ (macro-crack initiation).}$$

By integration Eq.(4.1.1) from $D = 0$ to $D = 1$ we therefore get:

$$N_F = \frac{\sigma_u - \sigma_{Max}}{\sigma_{Max} - \sigma_l(\sigma_m)} \left(\frac{\sigma_{Max} - \sigma_m}{B(\sigma_m)} \right)^{-\gamma}. \quad (4.1.2)$$

Eq.(4.1.1) then writes:

$$\delta D = \frac{\delta N}{N_F(\sigma_{Max}, \sigma_m, \sigma_u)}.$$

The constants are determined from conventional data: σ_u is usually known, s_{-1} , b fit the results on the fatigue limits with relation $\sigma_l(\sigma_m) = \sigma_m + s_{-1}(1 - b\sigma_m)$. Exponent γ is obtained from the S-N curve for reversed conditions, by plotting σ_{Max} as function of $N_F(\sigma_{Max} - \sigma_l(\sigma_m)) / (\sigma_u - \sigma_{Max})$, as deduced from Eq.(4.1.2). Coefficient $B(\sigma_m)$ is obtained from one point of the S-N curve.

Uniaxial case

The equation studied below allows us to describe the effects of nonlinear accumulation in the case of non-periodic cyclic loads ([Chaboche and Lesne \[1988b\]](#)). A simple way to introduce such effects in the damage growth equation consists in rendering the load and damage variables non-separable. For example, we may take:

$$\delta D = D^{\alpha(\sigma_{Max}, \sigma_m)} \left(\frac{\sigma_{Max} - \sigma_m}{B(\sigma_m)} \right)^\gamma \delta N$$

The exponent α depends on the loading (σ_{Max}, σ_m) , which results in non-separability. A reference choice is

$$\alpha(\sigma_{Max}, \sigma_m) = 1 - a \left\langle \frac{\sigma_{Max} - \sigma_l(\sigma_m)}{\sigma_u - \sigma_{Max}} \right\rangle$$

The exponent α represents the effect of the internal variables (for example the hardening state of the material), which depends on the loading (σ_{Max}, σ_m) , resulting in non-separability. It induces a non-linear damage cumulative rule as it is experimentally observed. Above, a and γ are material parameters. The coefficient γ is determined from experimental Wohler curves.

The concept of effective stress applied to fatigue provides an indirect measure. The measured evolutions are extremely nonlinear. With this concept, damage can really be measured only in the last part of the life-time, when microscopic initiations have already occurred (this is the phase of micro-propagation of defects). And these damage evolutions are extremely nonlinear. To reproduce this phenomenological aspect it is sufficient to make a change of variable by replacing D in the previous equation by a different measure of damage described by:

$$1 - (1 - D)^{\gamma+1}.$$

The differential law can be written as:

$$\delta D = [1 - (1 - D)^{\gamma+1}]^{\alpha(\sigma_{Max}, \sigma_m)} \left[\frac{\sigma_{Max} - \sigma_m}{M(\sigma_m)(1 - D)} \right]^\gamma \delta N \quad (4.1.3)$$

This form is more complex, but its properties are identical to the properties of the previous equation, except for the current value of damage. Now we integrate it to see how damage D evolves with cycle numbers N and the influence of different parameters. By differential calculus, we get from Eq.(4.1.3):

$$\delta[1 - (1 - D)^{\gamma+1}]^{1-\alpha} = (1 - \alpha)(\gamma + 1) \left[\frac{\sigma_{Max} - \sigma_m}{M(\sigma_m)} \right]^\gamma \delta N. \quad (4.1.4)$$

The number of cycles to failure, obtained by integrating D from 0 to 1 is thus:

$$N_F = \frac{1}{(\gamma + 1)(1 - \alpha)} \left(\frac{\sigma_{Max} - \sigma_m}{M(\sigma_m)} \right)^{-\gamma} \quad (4.1.5)$$

and we find by comparing with Eq.(4.1.2) that $M(\sigma_m) = B(\sigma_m)(\gamma + 1)^{1/\gamma}$. This form Eq.(4.1.5) can be used in experimental Woehler's curve in order to identify the coefficient a and γ . In differential form, from Eq.(4.1.4) and Eq.(4.1.5), we get equivalently

$$\delta[1 - (1 - D)^{\gamma+1}]^{1-\alpha} = \frac{\delta N}{N_F} \quad (4.1.6)$$

When we integrate Eq.(4.1.4) from 0 to D at constant loading conditions, the damage, expressed as a function of N/N_F is:

$$D = 1 - \left[1 - \left(\frac{N}{N_F} \right)^{\frac{1}{1-\alpha}} \right]^{\frac{1}{\gamma+1}}. \quad (4.1.7)$$

This expression is in good agreement with experimental results (Lemaître and Chaboche [1990]).

Multiaxial case

The applied stress and strain tensors are often multiaxial and present a complex path during a loading cycle. In the case of multiaxial loading fatigue, the Chaboche model is represented by the following equation:

$$\delta D = (1 - (1 - D)^{\gamma+1})^\alpha \left(\frac{\tilde{A}_{II}}{M(\sigma_H)} \right)^\gamma \delta N \quad (4.1.8)$$

where the amplitude $\sigma_{Max} - \sigma_l(\sigma_m)$ is replaced by the deviatoric norm \tilde{A}_{II} and the average stress is replaced by the hydrostatic pressure. We should note that for an isotropic damage theory, we will have from Eq.(4.1.4)

$$\tilde{A}_{II} = A_{II}/(1 - D)$$

$$\alpha = 1 - a \left\langle \frac{A_{II} - A_{II}^*(\sigma_H)}{\sigma_u - \sigma_{eqMax}} \right\rangle. \quad (4.1.9)$$

Again, α represents the influence of internal variables, characterizes the non-linearity of the damage evolution, allows to take into account the mean stress effect and describes the damage occurrence of the material: as long as $\alpha < 1$, there is damage creation. The coefficient a gives the amount of fragility which is induced by a given occurrence of fatigue limit violation.

In this formula, A_{II} is the amplitude of octahedral shear stress given by:

$$A_{II} = \frac{1}{2} \max_t \sqrt{\frac{1}{2} \underline{\Delta s} : \underline{\underline{\Delta s}}} = \sqrt{J_2 a} = \frac{1}{2} \Delta \sigma_{eqmax}, \quad (4.1.10)$$

The quantity $A_{II}^*(\sigma_H)$ represents the infinite life fatigue limit. For example, the Sines fatigue limit criterion is formulated by the following equation:

$$A_{II}^*(\sigma_H) = s_{-1}(1 - 3b\sigma_H). \quad (4.1.11)$$

Above, s_{-1} and σ_u are respectively the fatigue limit at zero mean stress and the ultimate tensile stress. For steel, we usually have $s_{-1} \approx 0.48\sigma_u$.

The function $M(\sigma_H)$ in Eq.(5.6.1) quantifies the mean stress effect through Low Cycle Fatigue (LCF) loading range:

$$M(\sigma_H) = s_{-1} \left(1 - 3 \frac{\sigma_H}{\sigma_u} \right).$$

We can get the $D - N$ curve in Figure 4.4 by integrating Eq.(5.6.1). This is in the case of constant loading conditions because we regard α and γ as invariable parameters.

$$N = \frac{(1 - (1 - D)^{\gamma+1})^{1-\alpha}}{(1 + \gamma)(1 - \alpha)} \left[\frac{A_{II}}{M(\sigma_H)} \right]^{-\gamma} \quad (4.1.12)$$

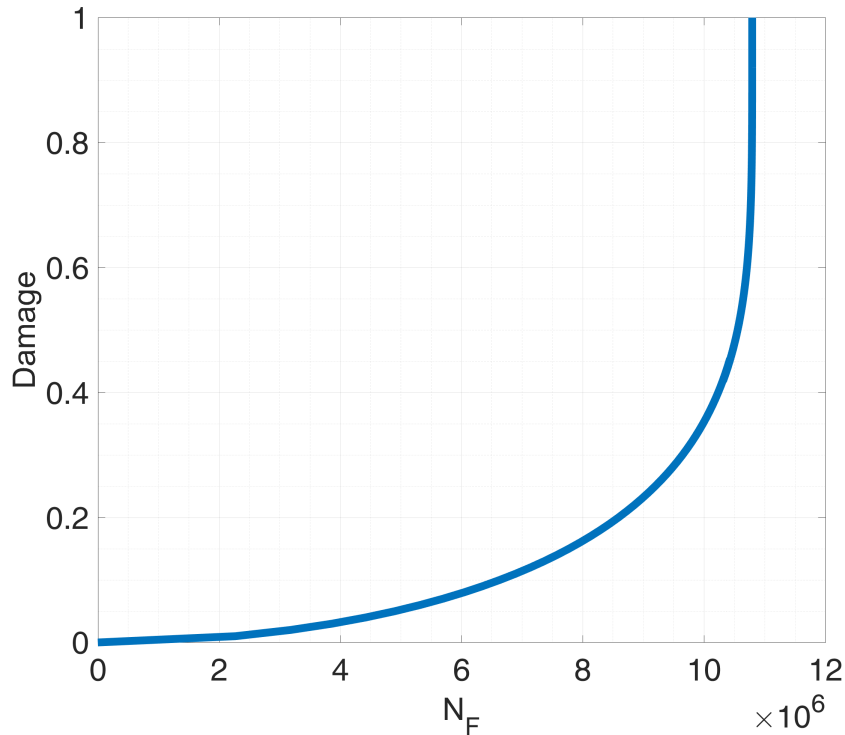


Figure 4.4 – Damage accumulation in terms of N in constant loading condition, with D and N are related by the evolution equation (4.1.12)

The number of cycles to failure, obtained at $D = 1$, is:

$$N_F = \frac{1}{(\gamma + 1)(1 - \alpha)} \left[\frac{A_{II}}{M(\sigma_H)} \right]^{-\gamma} \quad (4.1.13)$$

In Eq.(4.1.13), γ , b and a are material parameters determined from fatigue tests.

In the case of multiaxial fatigue loading, an infinite life is obtained if the stress amplitude A_{II} respects:

$$A_{II} \leq A_{II}^*(\sigma_H) = s_{-1}(1 - 3b\sigma_H). \quad (4.1.14)$$

In terms of Sines criterion which Chaboche uses, it writes:

$$\sqrt{J_{2a}} + 3bs_{-1}\sigma_H - s_{-1} \leq 0. \quad (4.1.15)$$

Finally, σ_H is the mean hydrostatic stress defined by:

$$\sigma_H = \frac{1}{6}[\max \operatorname{tr}(\underline{\sigma}(n)) + \min \operatorname{tr}(\underline{\sigma}(n))], \quad (4.1.16)$$

In terms of number of cycles at given load, the damage is expressed as in uniaxial case:

$$D = 1 - \left[1 - \left(\frac{N}{N_F} \right)^{\frac{1}{1-\alpha}} \right]^{\frac{1}{\gamma+1}}. \quad (4.1.17)$$

These theories account for the nonlinear nature of fatigue damage accumulation by using nonlinear relations such as Eq.(4.1.17) where the power α depends on the load level (see Figure 4.5). The same equation with frozen α leads to linear damage accumulation.

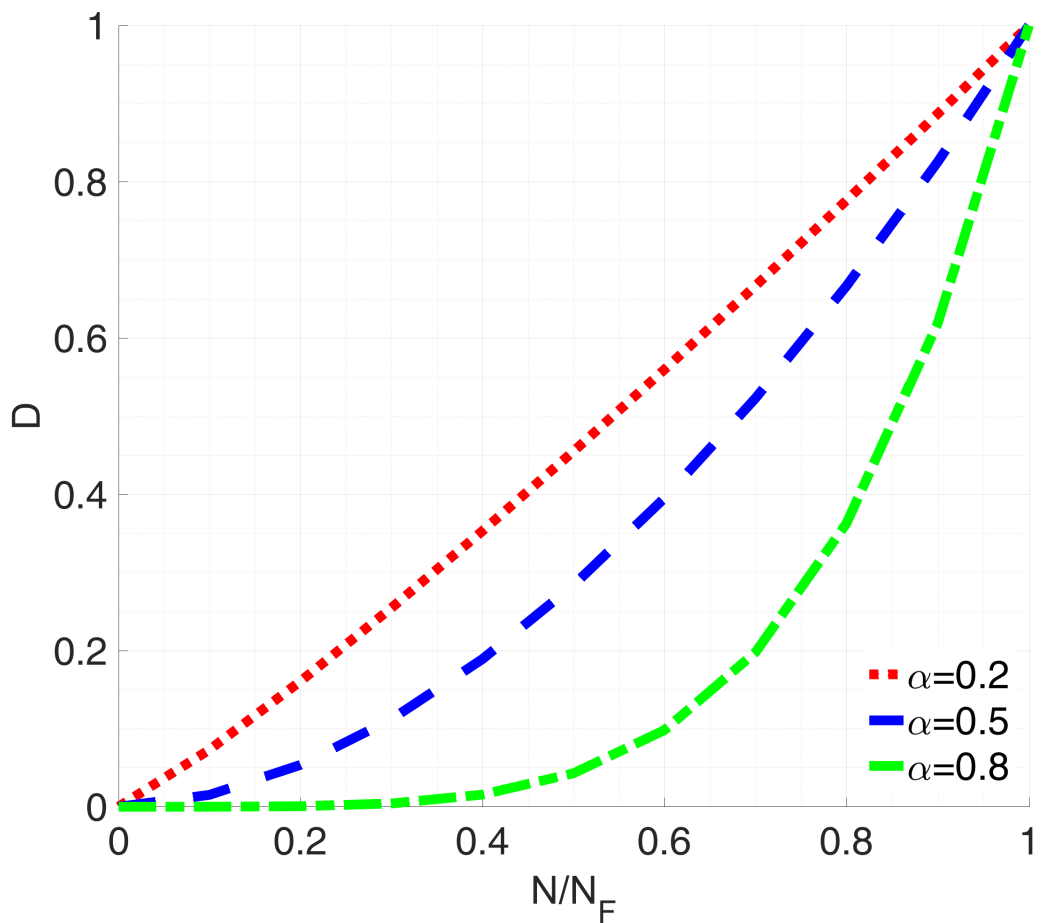


Figure 4.5 – Influence of function α in fatigue damage versus fatigue life ratio ($\gamma = 0.1$)

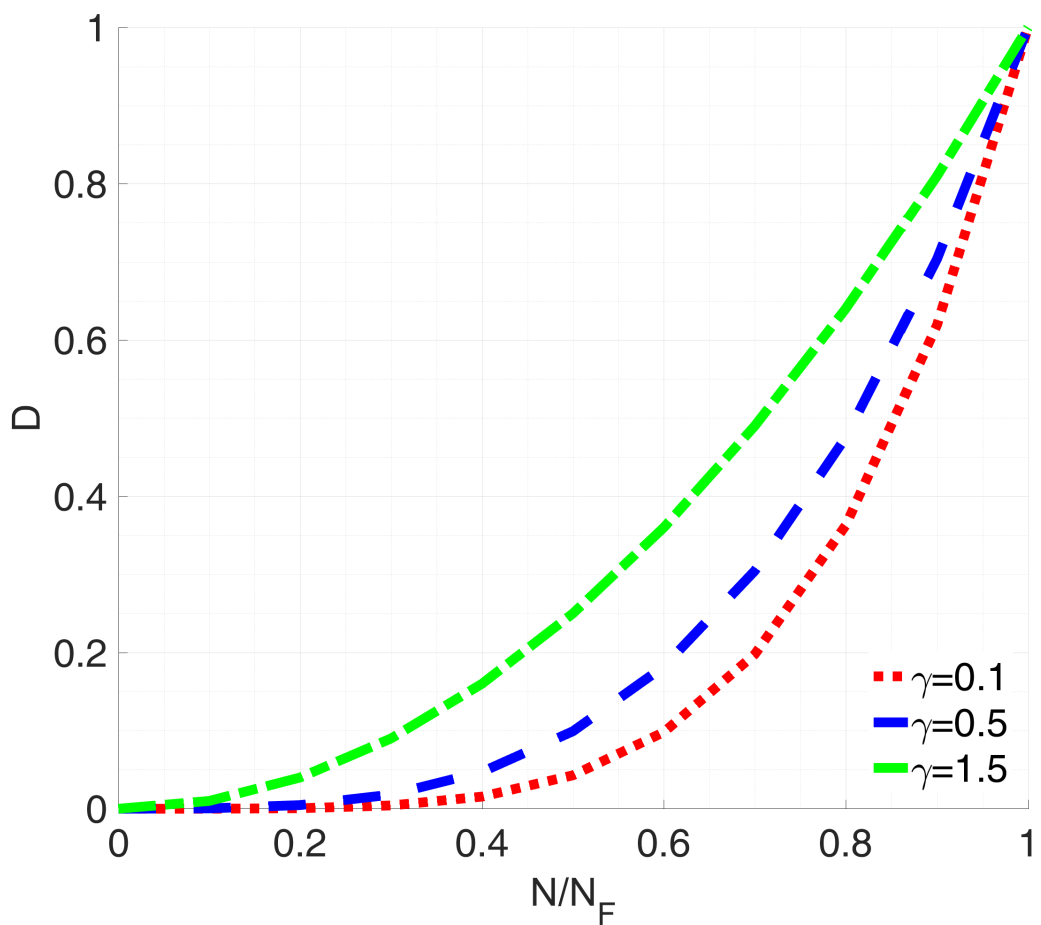


Figure 4.6 – Influence of function γ in a plot of damage versus fatigue life ratio with $\alpha = 0.8$

4.2 Verification method of Chaboche law

To facilitate our verification of the law we use two-stress level loading, the specimen is firstly loaded at stress σ_1 for N_1 cycles and then at stress σ_2 for N_2 cycles until failure. We can then observe if the experimental results are satisfactory.

After N_1 cycles, we have from Eq.(4.1.17), a damage D_1 given by:

$$[1 - (1 - D_1)^{\gamma+1}]^{1-\alpha_1} = \frac{N_1}{N_{F1}}. \quad (4.2.1)$$

By integrating Eq.(4.1.6) from $D = D_1$ to $D = 1$, we get:

$$1 - [1 - (1 - D_1)^{\gamma+1}]^{1-\alpha_2} = \frac{N_2}{N_{F2}}, \quad (4.2.2)$$

which yields:

$$1 - \frac{N_2}{N_{F2}} = 1 - [1 - (1 - D_1)^{\gamma+1}]^{1-\alpha_2}. \quad (4.2.3)$$

From Eq.(4.2.1) and Eq.(4.2.3), after elimination of $[1 - (1 - D_1)^{\gamma+1}]$ we get:

$$\frac{N_2}{N_{F2}} = 1 - \left(\frac{N_1}{N_{F1}}\right)^{\frac{1-\alpha_2}{1-\alpha_1}} = 1 - \left(\frac{N_1}{N_{F1}}\right)^\eta \quad (4.2.4)$$

with

$$\begin{aligned} \eta &= \frac{1 - \alpha_2}{1 - \alpha_1} \\ &= \frac{A_{II2} - A_{II}^*(P_{m2})}{A_{II1} - A_{II}^*(P_{m1})} \frac{\sigma_u - \sigma_{eqMax1}}{\sigma_u - \sigma_{eqMax2}} \\ &= \frac{\sqrt{J_{2,a2}} - s_{-1}(1 - 3bP_{m2})}{\sqrt{J_{2,a1}} - s_{-1}(1 - 3bP_{m1})} \frac{\sigma_u - \max(2\sqrt{J_{2,a1}})}{\sigma_u - \max(2\sqrt{J_{2,a2}})}. \end{aligned} \quad (4.2.5)$$

In the case of high-low loading sequence($\sigma_1 > \sigma_2$ thus $\alpha_1 < \alpha_2$):

$$\eta = \frac{1 - \alpha_2}{1 - \alpha_1} < 1 \Rightarrow \frac{N_2}{N_{F2}} = 1 - \left(\frac{N_1}{N_{F1}}\right)^\eta < 1 - \frac{N_1}{N_{F1}},$$

in other words, we have

$$\frac{N_1}{N_{F1}} + \frac{N_2}{N_{F2}} < 1.$$

The cumulative damage under high-low loading sequence, as we deduced, has the addition of partial lives less than 1.

Similarly, the cumulative damage under low-high loading sequence has has a beneficial effect:

$$\frac{N_1}{N_{F1}} + \frac{N_2}{N_{F2}} > 1.$$

For constant two-level stress loading, $\alpha_1 = \alpha_2$, the Chaboche law returns to the Miner's rule where we have:

$$\frac{N_1}{N_{F1}} + \frac{N_2}{N_{F2}} = 1.$$

4.3 Chaboche law containing different criteria

4.3.1 Chaboche law with Crossland criterion

In the previous model we used Sines fatigue criterion constructing the damage criterion exponent α . Now we want to test Chaboche law with different criteria and compare the numerical results after n cycles. Since α represents the internal variables and contains the fatigue criterion, we first change α to satisfy Crossland Criterion:

$$\alpha = 1 - a \left\langle \frac{\max_n \sqrt{J_{2a}}(n) + a_c P_{max}(n) - b_c}{\sigma_u - 2 \max \sqrt{J_{2a}}} \right\rangle, \quad (4.3.1)$$

with

$$a_c = \frac{(t_{-1} - \frac{f_{-1}}{\sqrt{3}})}{\frac{f_{-1}}{3}}, \quad b_c = t_{-1}. \quad (4.3.2)$$

Therefore, the coefficient η characterizing the high low sequential loading will now be given by

$$\eta_c = \frac{1 - \alpha_2}{1 - \alpha_1} = \frac{\sqrt{J_{2,a_2}} + a_c P_{M_2} - b_c}{\sqrt{J_{2,a_1}} + a_c P_{M_1} - b_c} \frac{\sigma_u - \max(2\sqrt{J_{2,a_1}})}{\sigma_u - \max(2\sqrt{J_{2,a_2}})}. \quad (4.3.3)$$

In Eq.(5.6.1) and (4.1.12), the amplitude of octahedral shear stress A_{II} remain unchanged.

4.3.2 Chaboche law with Dang Van criterion

We can also change α to express it through Dang Van Criterion, leading to:

$$\alpha = 1 - a \left\langle \frac{\max_n \{\tau(n) + a_D P(n)\} - b_D}{\sigma_u - 2 \max \sqrt{J_{2a}}} \right\rangle. \quad (4.3.4)$$

with

$$\begin{aligned} \tau(n) &= \frac{1}{2}(\hat{\sigma}_I(n) - \hat{\sigma}_{III}(n)) \\ a_D &= \frac{3t_{-1}}{f_{-1}} - \frac{3}{2}, b_D = t_{-1}. \end{aligned} \quad (4.3.5)$$

In this case, the coefficient η of high low sequential loading becomes

$$\eta_D = \frac{1 - \alpha_2}{1 - \alpha_1} = \frac{\max_t \{\tau_2(n) + a_D P_2(n)\} - b_D}{\max_t \{\tau_1(n) + a_D P_1(n)\} - b_D} \frac{\sigma_u - \max(2\sqrt{J_{2a_1}})}{\sigma_u - \max(2\sqrt{J_{2a_2}})} \quad (4.3.6)$$

In Eq.(5.6.1) and (4.1.12), we change A_{II} to $\max \tau(n)$:

$$N_F = \frac{1}{(\gamma + 1)(1 - \alpha)} \left[\frac{\max \tau(n)}{M(\sigma_H)} \right]^{-\gamma} \quad (4.3.7)$$

4.4 Numerical testing on different loading patterns

The fatigue limit with different criteria are distinctive. We compare different criteria in a $A_{II} - N_F$ figure as predicted in Eq.(4.1.13). Here γ , b and a are material parameters determined from fatigue tests.

In this case we have

$$N_F = \frac{1}{(\gamma + 1)(1 - \alpha)} \left[\frac{A_{II}}{M(\sigma_H)} \right]^{-\gamma},$$

$$M(\sigma_H) = s_{-1} (1 - 3\sigma_H/\sigma_u).$$

For Sines and Crossland criteria:

$$A_{II} = \sqrt{J_2} = \frac{1}{2} \max_t \sqrt{\frac{1}{2}(\Delta s_{11}^2 + \Delta s_{22}^2 + \Delta s_{33}^2 + 2\Delta s_{12}^2 + 2\Delta s_{13}^2 + 2\Delta s_{23}^2)}.$$

For Dang Van criterion:

$$A_{II} = \max \tau(n).$$

4.4.1 Test on pure rotation

From the fatigue zone we select $r = 0.1$ as the radius to study. We select here:

$$s_{-1} = f_{-1} = 0.8 \text{ MPa},$$

$$\sigma_u = 1.67 \text{ MPa}$$

$$\gamma = 6$$

$A_{II} - N_F$ figure is shown in Figure 4.7.

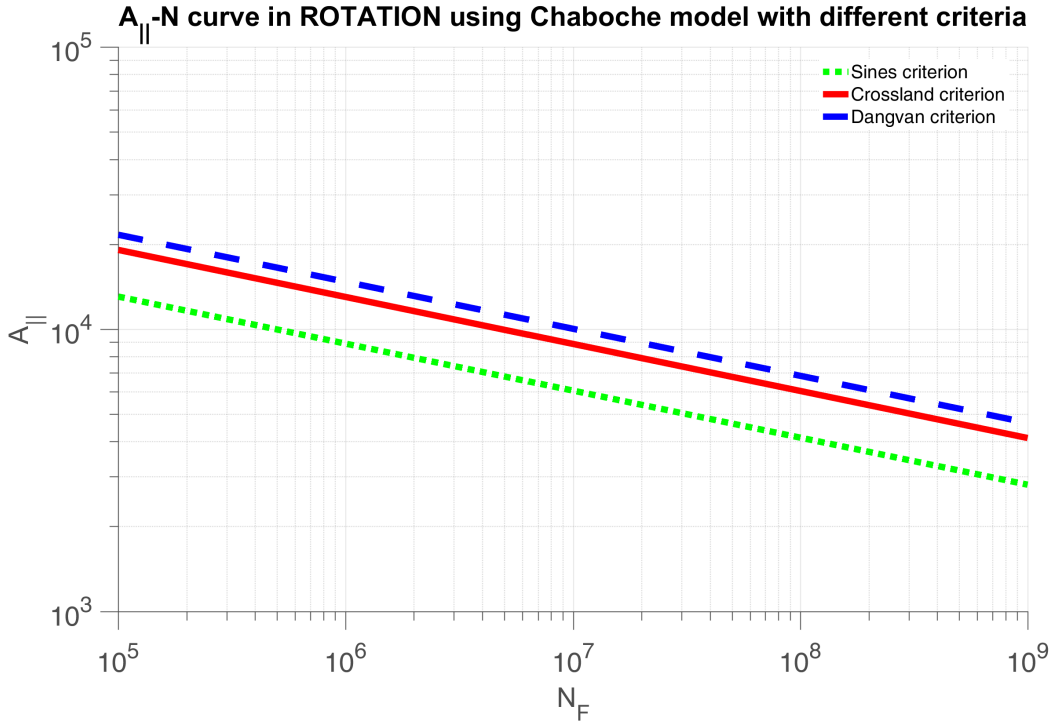


Figure 4.7 – $A_{II} - N_F$ curve in rotation at $r=0.1$

In pure rotation, we assume the first and second rotating speed are respectively $w_1 = 20 \text{ rpm}$ and $w_2 = 15 \text{ rpm}$.

$$A_{II1} = \sqrt{J_{2,a_1}} = 7.7606E5 \text{ Pa}$$

$$A_{II2} = \sqrt{J_{2,a_2}} = 4.3653E5 \text{ Pa}$$

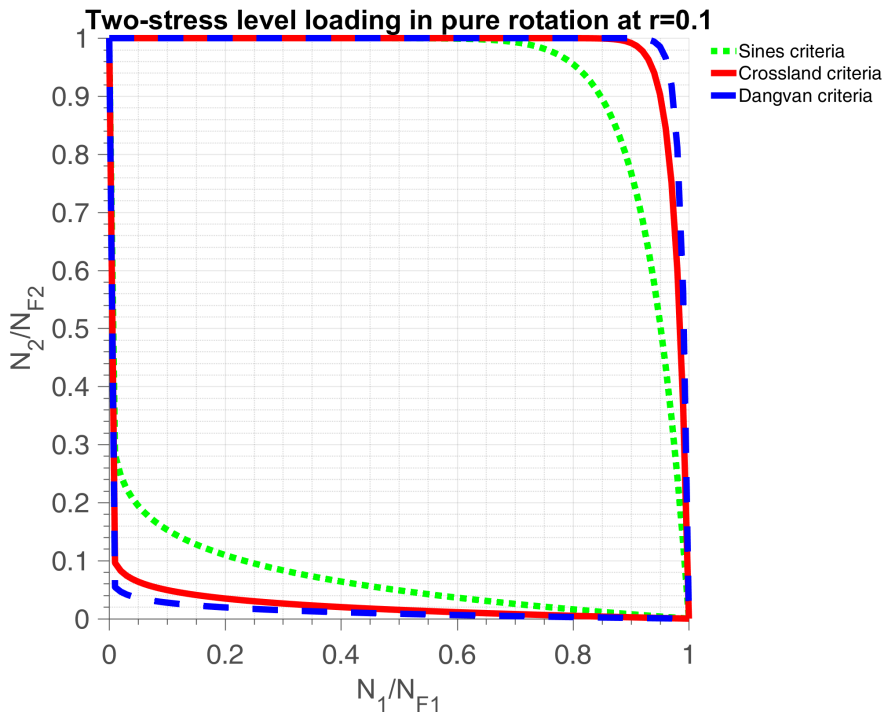
$$P_{m_1} = 8.8342E5 \text{ Pa}$$

$$P_{m_2} = 4.9693E5 \text{ Pa}$$

Substituting the above to Eq.(4.2.5), we can get η in High-Low sequence and in Low-High sequence as shown in Table.4.1:

The predicted results are shown in Figure 4.8.

η value	Sines	Crossland	Dang Van
High-low	0.0721	0.0219	0.0121
Low-high	13.8654	45.6118	82.5689

Table 4.1 – α induced sequence effect parameter η value with different criteria in pure rotationFigure 4.8 – Two-stress level loading in pure rotation at $r=0.1$. The lower curve displays the relative proportion of cycles in high-low sequence, the upper curve displays the same information in a low-high sequence

4.4.2 Test on 4-point bending

From the fatigue zone we select $y = 3$ to study. We select here:

$$s_{-1} = f_{-1} = 0.8 \text{ MPa},$$

$$\sigma_u = 1.67 \text{ MPa}$$

$$\gamma = 6$$

The $A_{II} - N_F$ figure is shown in Figure 4.9.

In 4-point bending, we assume the first and second loading are respectively $F_1 = 1E6N$ and $F_2 = 0.8E6N$.

$$\sqrt{J_{2a_1}} = 7.2194E5 \text{ Pa}$$

$$\sqrt{J_{2a_2}} = 5.7755E5 \text{ Pa}$$

$$P_{m_1} = 3.9298E5 \text{ Pa}$$

$$P_{m_2} = 3.1438E5 \text{ Pa}$$

Substituting the above to Eq.(4.2.5) we can get η in High-Low sequence: and in Low-High sequence as shown in Table 4.2:

The predicted results are shown in Figure 4.10.

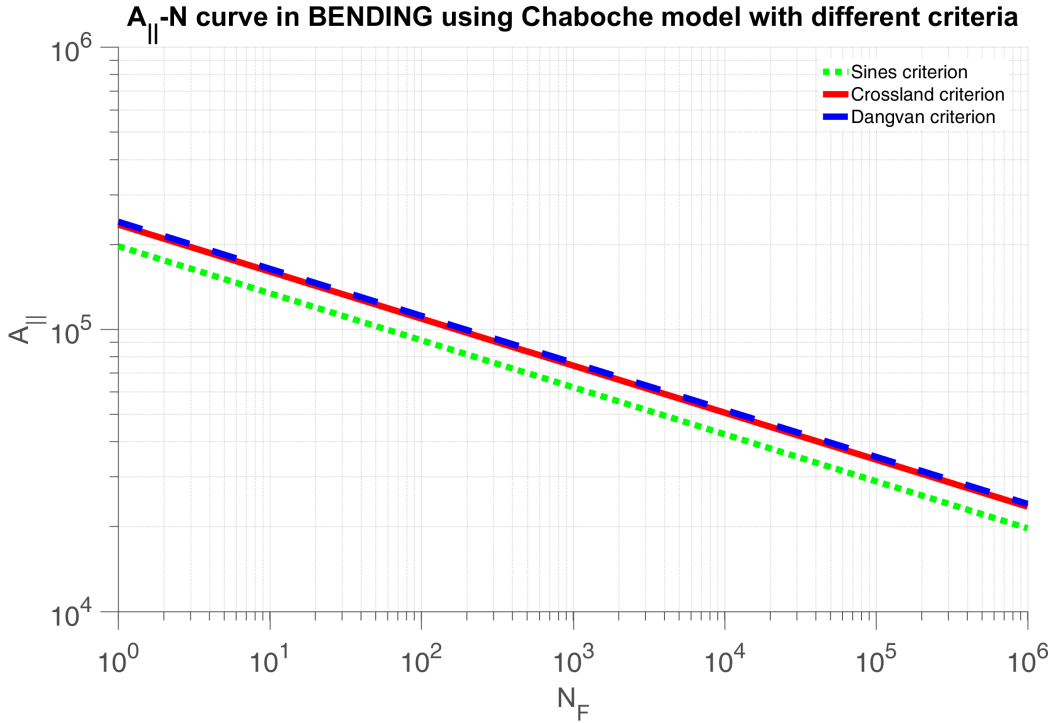


Figure 4.9 – $A_{II} - N_F$ curve in 4-point bending at $y=3$

η value	Sines	Crossland	Dang Van
High-low	0.3174	0.1894	0.1659
Low-high	3.1510	5.2794	6.0280

Table 4.2 – α induced sequence effect parameter η value with different criteria in bending

4.4.3 Test on rotative bending

From the fatigue zone we select $r = 0.5$ as the radius to study. The $A_{II} - N_F$ figure is shown in Figure 4.11.

In rotative bending, we assume the rotating speed are $w = 5$ rpm. The applied force are respectively $F = 9E5$ N and $F = 3E5$ N. We select:

$$s_{-1} = f_{-1} = 400 \text{ MPa}, \sigma_u = 1000 \text{ MPa}$$

$$\sqrt{J_{2a_1}} = 702 \text{ MPa}$$

$$\sqrt{J_{2a_2}} = 665 \text{ MPa}$$

$$P_{m_1} = 689 \text{ MPa}$$

$$P_{m_2} = 717 \text{ MPa}$$

Substituting the above to Eq.(5.6.11) we can get η in High-Low sequence: and in Low-High sequence as shown in Table 4.3:

η value	Sines	Crossland	Dang Van
High-low	0.7170	0.7392	0.6608
Low-high	1.3947	1.3528	1.5133

Table 4.3 – α induced sequence effect parameter η value with different criteria in rotative bending

The predicted results are shown in Figure 4.12 which are very close to a situation of linear damage

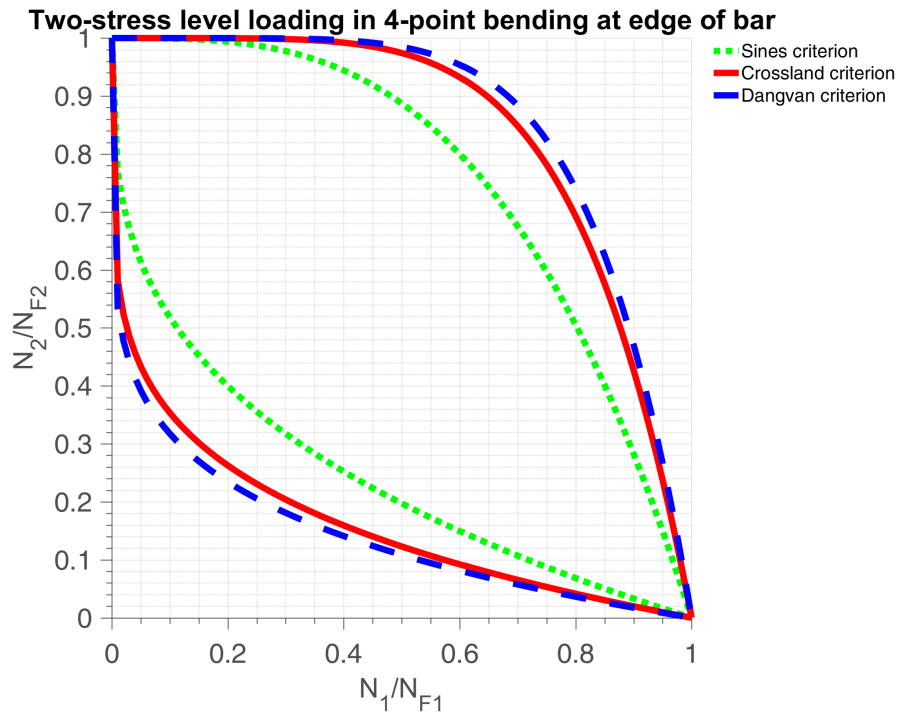


Figure 4.10 – Two-stress level loading in 4-point bending at $y=3$. The lower curve displays the relative proportion of cycles in high-low sequence, the upper curve displays the same information in a low-high sequence

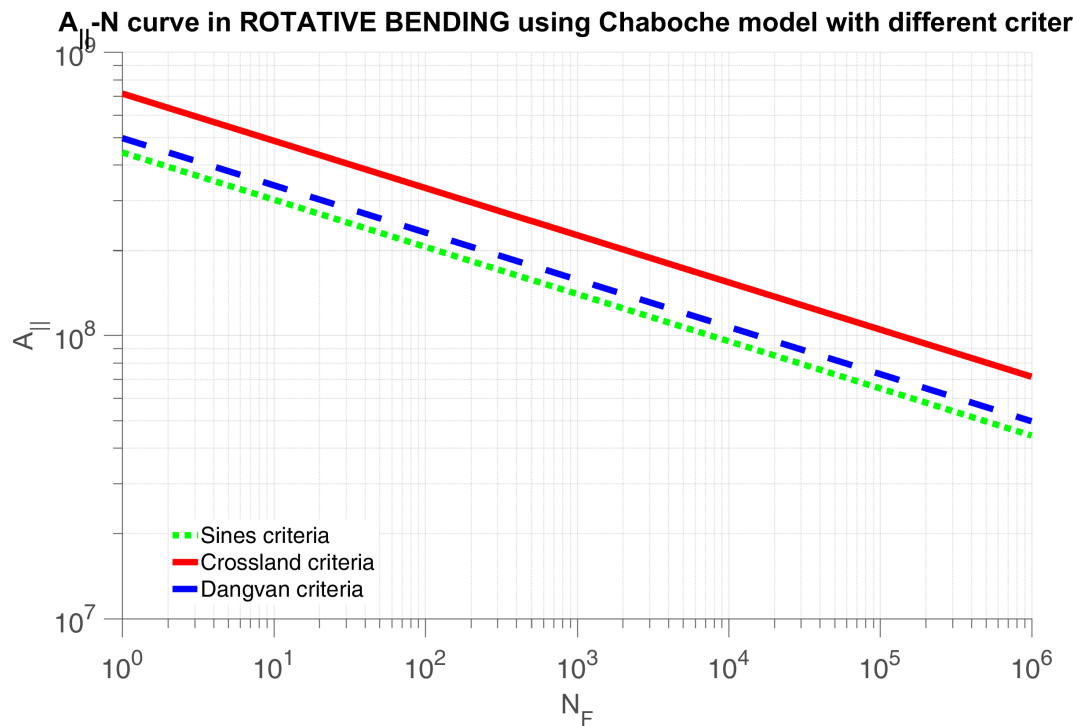


Figure 4.11 – $A_{II} - N_F$ curve in rotative bending at $r=3$

accumulation.

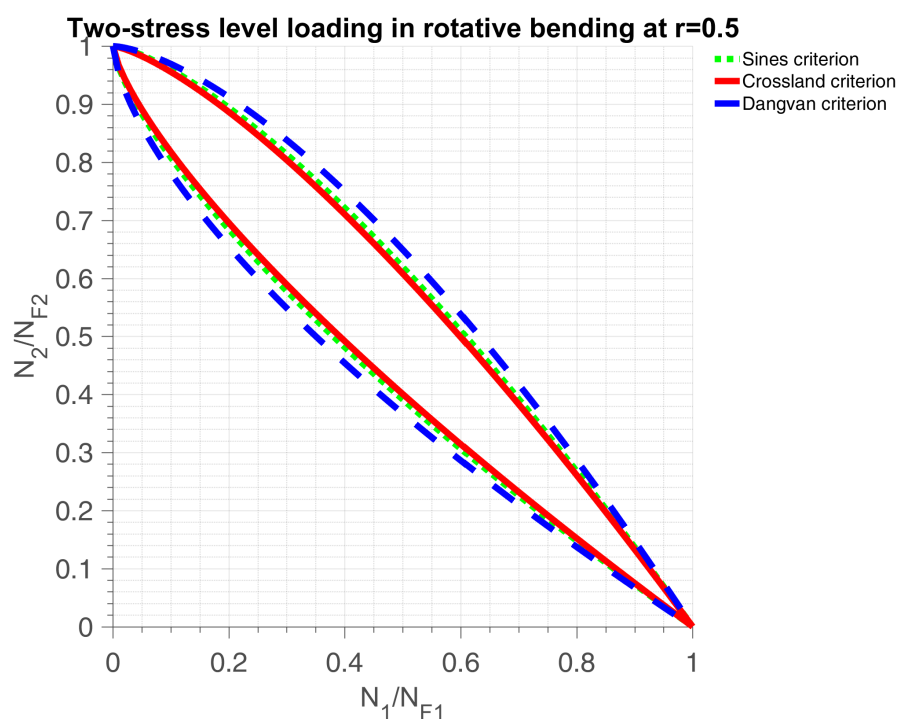


Figure 4.12 – Two-stress level loading in rotative bending at $r=0.5$. The lower curve displays the relative proportion of cycles in high-low sequence, the upper curve displays the same information in a low-high sequence

Discussion

The Chaboche law is based on this assumption: fatigue damage occurs and accumulates only when the loading stress is higher than its fatigue limit. Therefore, Eq.(5.6.1) neglects the damage contribution of the loading stress which is lower than the fatigue limit. According to some experimental results such as: Lu and Zheng [Xi and Songlin \[2008\]](#) [Xi and Songlin \[2009a\]](#) [Xi and Songlin \[2009b\]](#), Sinclair [Sinclair \[1952\]](#), and Makajima et al. [Nakajima et al. \[2007\]](#), however, it appears that the damage of low amplitude loads is one of the main reasons for prediction errors.

Impurities in the material affect the fatigue life. So does the material's hardness, and especially its surface condition. How the components were heat-treated in the factory is another factor. The operating temperature makes a difference, too. Worse still is the structural component's shape: notches and sharp corners create concentrations of stress that can initiate cracks. Thus further studies should be carried out concerning these factors whilst studying damage accumulation.

4.5 Cycle Counting Method

Whatever damage accumulation law is used, whatever fatigue criterion is used (Sines, Crossland, Dang Van,...), up to now all fatigue predictions which have been presented are based on the notion of cyclic loads of different amplitudes applied successively. How do we identify those cycles in a random loading history?

In this framework, a counting method is a method for identifying a statistical event in a random loading sequence. This event can be, for example, extrema, ranges or cycles of the signal. A method of counting stress cycles determines therefore the number or the density of presence of the stress cycles in the loading signal. In other words, the counting method consists in discretizing the loading sequence variable in simple elementary cycles easy to implement in any forecasting process of fatigue life. Indeed, each elementary cycle, extracted from the sequence of load, is denoted by its amplitude and its mean value to which corresponds one well-defined lifetime. Then, the elementary damage of the extracted cycle is calculated using a rule of damage. The process repeats along the sequence studied to evaluate the total damage by means of an accumulation law, and consequently to determine the number of sequences at break.

Some methods of counting have been developed by the experts. They all lead to different results and therefore, for some, to errors in the calculation of the duration of life. We can cite by way of example six major families of counting techniques, described in various works [ASTM \[1985\]](#):

- the counting of the loading time,
- the counting of extrema between two passages by the mean value,
- the counting of areas,
- the counting of paired ranges,
- the counting of overflows,
- rainflow cycle counting, say "the drop of water."

The object of all cycle counting methods is to compare the effect of variable amplitude load histories to fatigue data and curves obtained with simple constant amplitude load cycles. Rainflow counting is a process to obtain cyclic data of complex loading. Its name comes from the original description from the Japanese researchers Matsuiski and Endo where they describe the process in terms of rain falling off a pagoda style roof. A more insightful description based on cyclic plasticity is usually used to explain the method.

In Figure 4.13 (retrieved from <https://www.efatigue.com/variable/background/rainflow.html>) a simple loading history (points A - I) is plotted vertically so that it resembles a Japanese pagoda. The resulting deformation, stresses and strains, is plotted directly below the loading history. In the

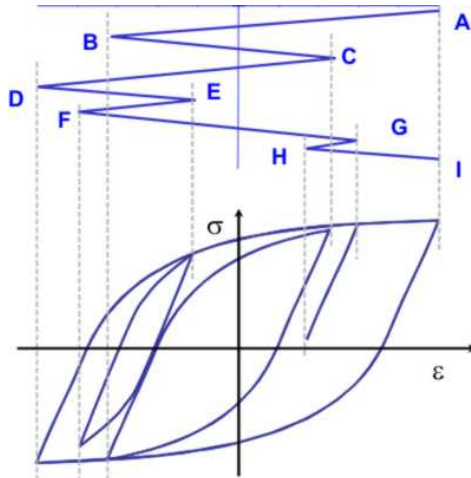


Figure 4.13 – Complex Cyclic Loading

lower part of the figure, four cycles are easily identified. One large overall cycle, one intermediate cycle in the center of the plot, and two smaller cycles. Each cycle has its own strain range and mean stress. From a deformation viewpoint the process proceeds as follows. Start at A, the maximum strain, and unload the material to B. Then reload to point C and unload to D. When the material reaches the strain at point B during the unloading from C to D the material remembers its prior deformation and deforms along a path from A to D as if the event C-D never happened. This is better illustrated in the next part of the loading. Load from D to E and unload to F. Now load from F to G. When the material reaches the strain at point E during the loading from F to G the material remembers its prior deformation and deforms along a path from D to G as if the event E-F never happened. The same process occurs for G-H.

Rainflow counting will identify four cycles, A-D-I, B-C-B, E-F-E and G-H-G. Rainflow counting identifies the major load excursions, for example D to I, and treats subcycles like E-F and G-H as interruptions to the overall loading event D-I.

The five-step procedure to extract the cyclic data is summarized as follows:

1. Determine the peaks and valleys of the stress/strain during cycling, and recognize in order to center at the absolute maximum stress (Figure 4.14).
2. Visualize the resulting landscape draining water from the deepest valley (Figure 4.15).
3. Measure total depth drained (stress range) and mean depth (mean stress) of this valley, (Figure 4.15), and the number of these cycles in the load history.
4. Continue by draining the next lowest (Figure 4.16) and repeat until all valleys are drained. A Rainflow cycle is counted if the second segment is vertically shorter than the first and the third segments(i.e. 6-7 is smaller than 5-6 and 7-8).
5. Use the damage rule to obtain the life from all cycles.

Once all the cycles have been categorized, the Palmgren-Miner Rule is applied. Even though the linear damage rule ignores sequence effects, it is most widely used because of its simplicity and the fact that though many nonlinear damage models have been developed, unfortunately none can encompass many of the complicating factors encountered during complex variable amplitude loading. As an example, for this case assuming mean stress is ignored, we get in this example:

$$\sum_i \frac{N_i}{N_{F_i}} = \frac{1}{N_{F_{450}}} + \frac{1}{N_{F_{200}}} + \frac{1}{N_{F_{50}}} + \dots = 1.$$

where n is replaced with the number of actual cycles of its corresponding type in the load history,

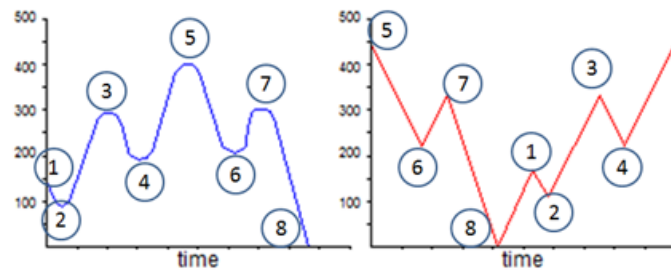


Figure 4.14 – Reorder to Start from Absolute Maximum (retrieved from “How to Calculate Fatigue Life When The Load History Is Complex”, February 13, 2015, author: Michael Bak, <https://caeai.com/blog/how-calculate-fatigue-life-when-load-history-complex>)

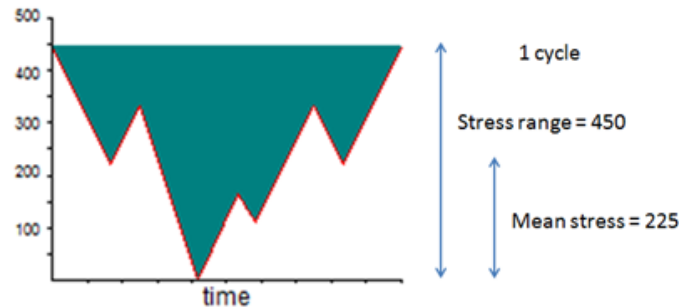


Figure 4.15 – Imagine Filling with Water and Extract Stress Range and Mean Stress (retrieved from “How to Calculate Fatigue Life When The Load History Is Complex”, February 13, 2015, author: Michael Bak, <https://caeai.com/blog/how-calculate-fatigue-life-when-load-history-complex>)

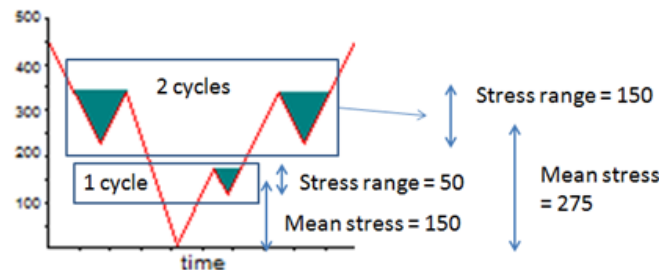


Figure 4.16 – Drain Water Starting at Lowest Valley and Repeat Cycle Extraction (retrieved from “How to Calculate Fatigue Life When The Load History Is Complex”, February 13, 2015, author: Michael Bak, <https://caeai.com/blog/how-calculate-fatigue-life-when-load-history-complex>)

for instance $N_{F_{450}}$ represents the life obtained from the $S - N$ data for a stress range of 450 MPa. From this equation, the number of total cycles through the entire load history can be found.

The rainflow procedure can be automated so that cyclic content of complex loading can be extracted efficiently. For example, fatigue computer codes such as *nCodeDesignLife* will accept files of test data, or the input of multiple load steps from a static or transient finite element analysis, and use the rainflow approach to automatically extract the cyclic data. In addition, *DesignLife* automates the Palmgren-Miner Damage Rule calculation to determine number of cycles to failure, with the term cycle here defined as one pass through the entire time history. A computer program in matlab that accomplishes rainflow cycle counting applied to a complex history such as that in Figure 4.18 results in a histogram of amplitudes and mean values shown in Figure 4.19, Figure 4.20 and Figure 4.21.

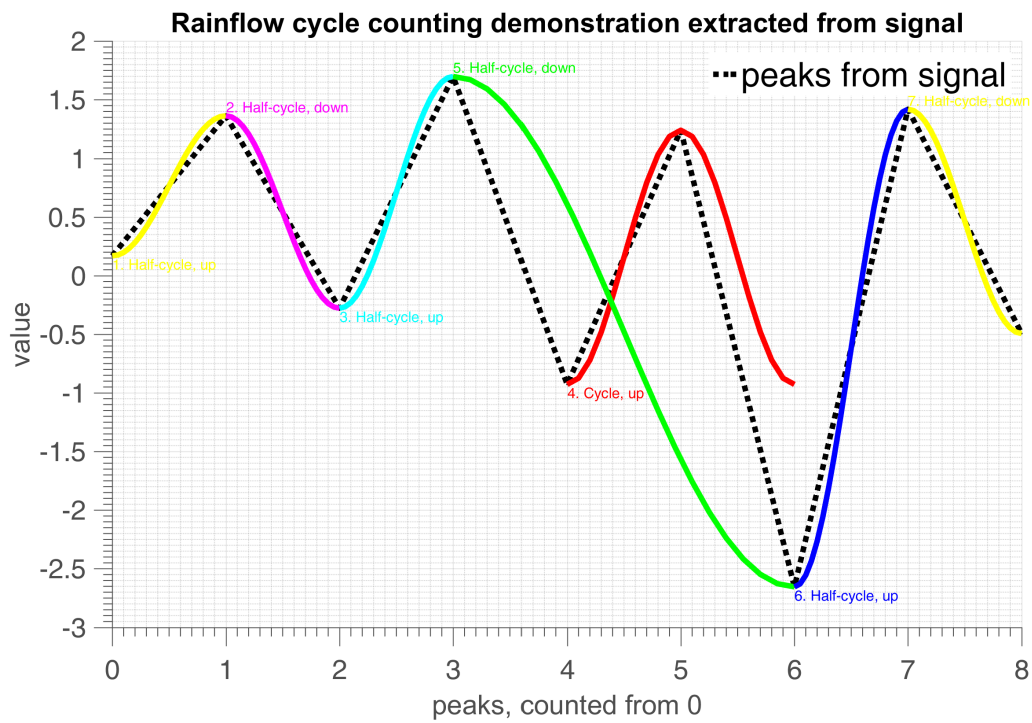


Figure 4.17 – Rainflow counting method demonstration

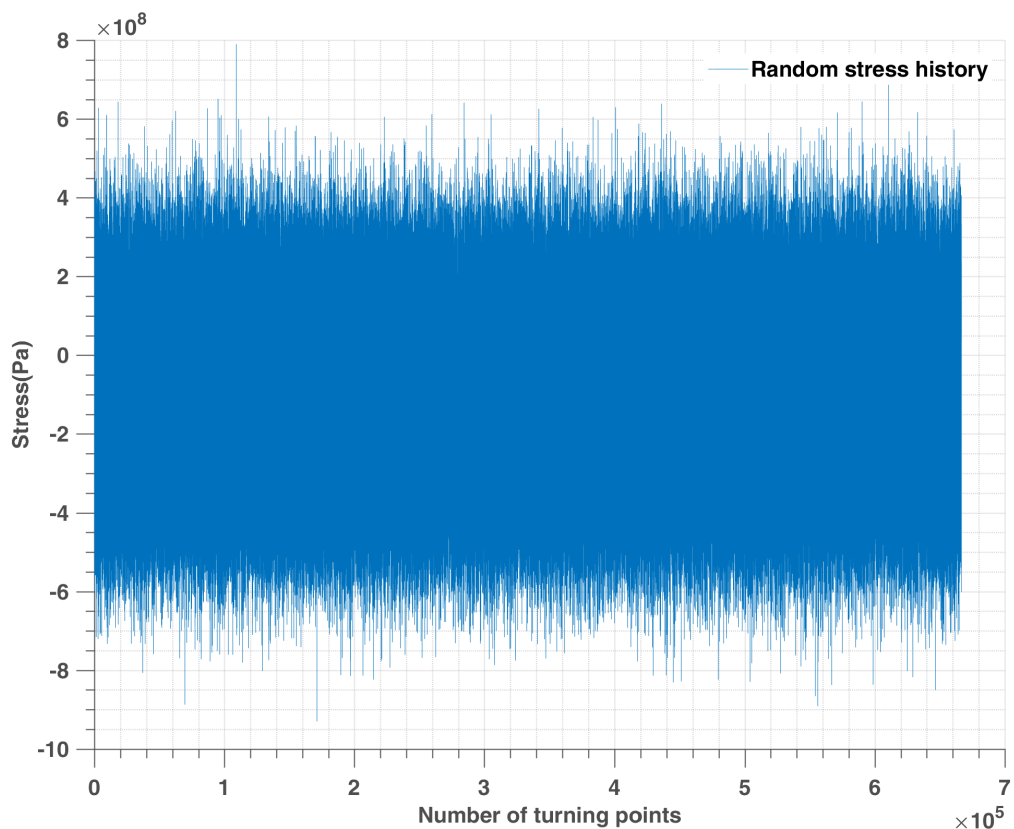


Figure 4.18 – One million normally distributed random stresses around -100MPa

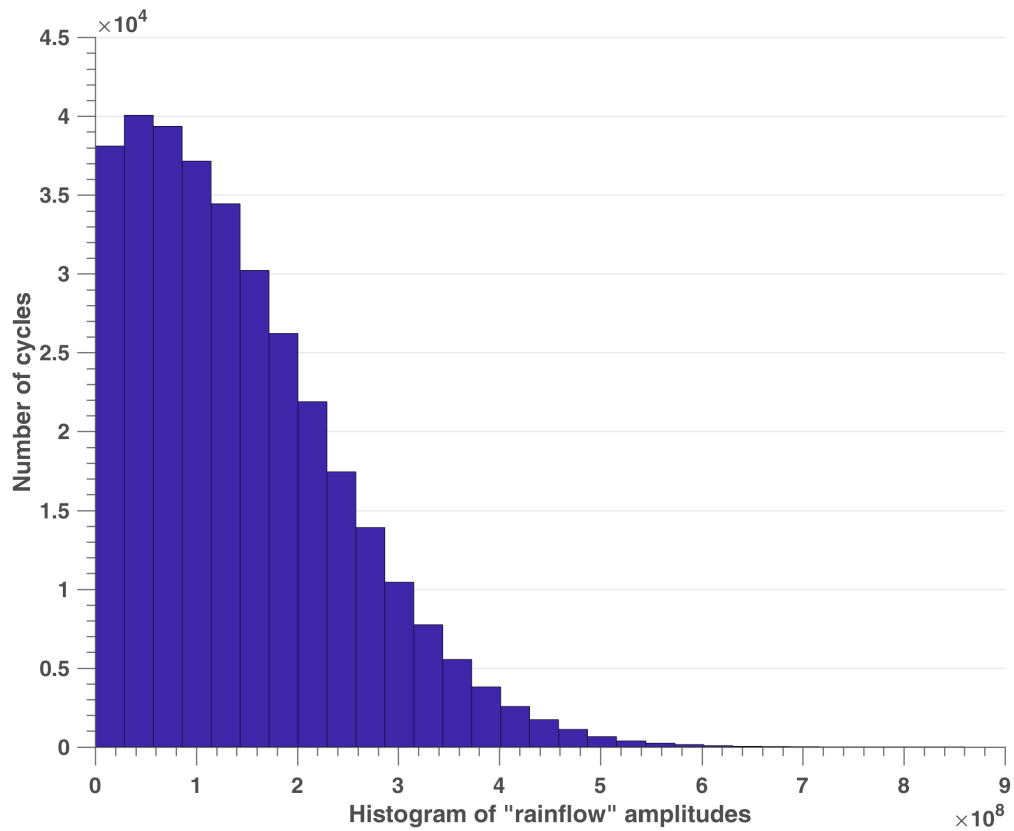


Figure 4.19 – Amplitudes distribution extracted from Figure 4.18

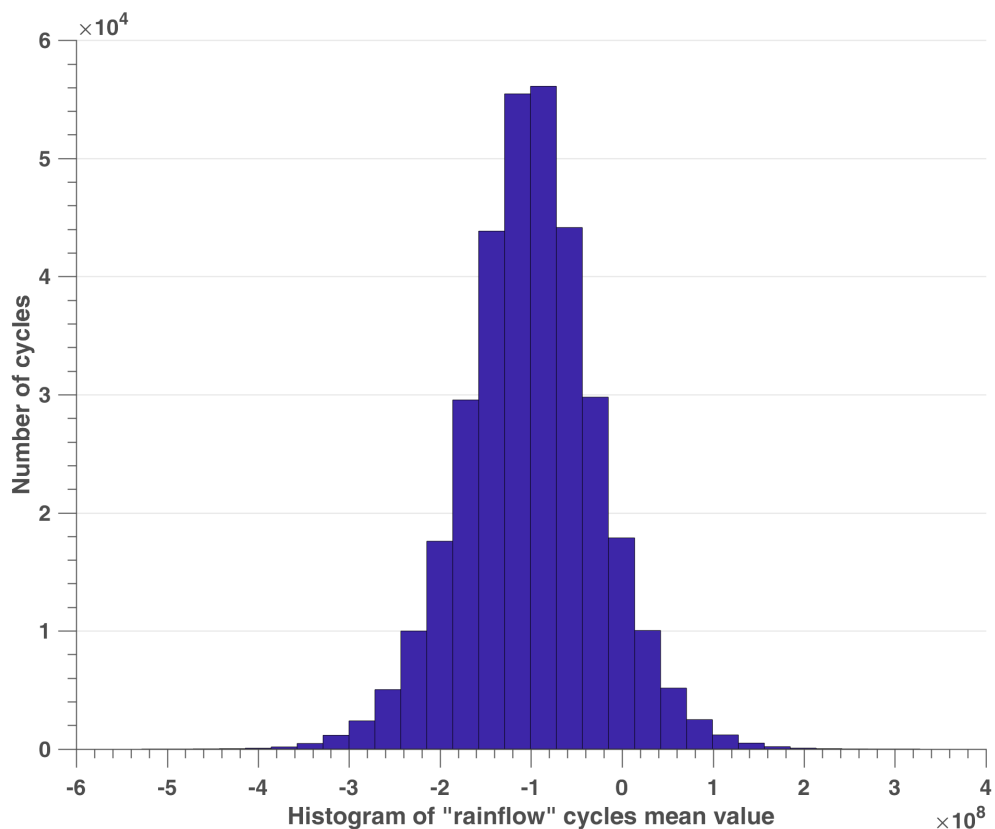


Figure 4.20 – Mean stresses distribution extracted from Figure 4.18

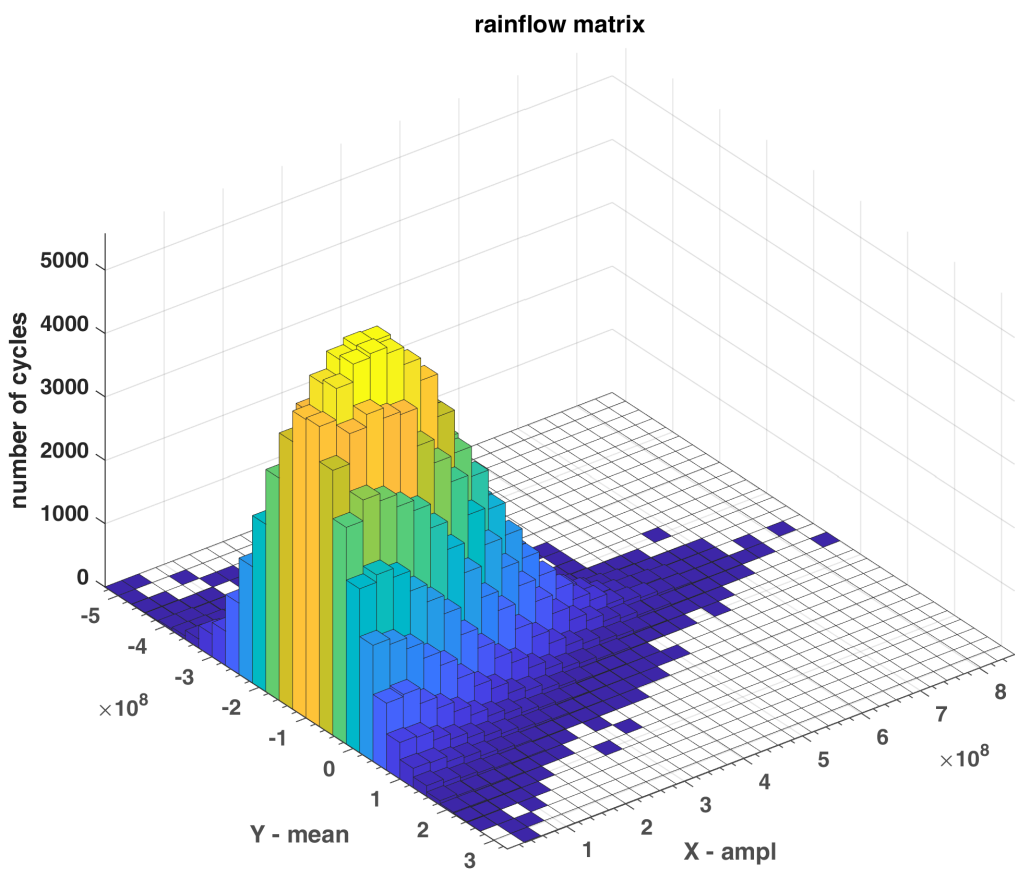


Figure 4.21 – Rainflow matrix extracted from Figure 4.18

5

Handling general loadings

Contents

6.1	Experimental verification	115
6.1.1	Introduction	115
6.1.2	Random amplitude 1D tests from Cetim on AW-6106 T6 aluminum	115
6.2	Experimental validation of the model on aluminum 6082 T6	121
6.2.1	Presentation of aluminum 6082 T6	121
6.2.2	Fatigue tests on aluminum 6082 T6	121
6.2.3	Identification of model parameters on aluminum 6082 T6	122
6.3	Experimental validation of the model on 30NCD16 steel	126
6.3.1	Presentation of steel 30NCD16	126
6.3.2	Fatigue tests performed by Dubar on steel 30 NCD 16	126
6.3.3	Identification of model parameters for steel 30 NCD 16	126
6.4	Experimental validation of the model on SM45C steel	129
6.4.1	Presentation of steel SM45C	129
6.4.2	Fatigue tests performed by Dubar on steel SM45C	130
6.4.3	Identification of model parameters for steel SM45C	132
6.5	Experimental validation of the model on 10 HNAP steel	135
6.5.1	Presentation of the material	135
6.5.2	Description of fatigue tests on 10 HNAP steel	135
6.5.3	Identification of model parameters of 10HNAP steel	137
6.5.4	Simulation of fatigue tests performed on 10HNAP steel	139
6.6	Conclusions	148

5.1 Multiscale energy dissipation approach

Fatigue failure is a damage accumulation process in which material property deteriorates continuously under fatigue loading and the damage depends on the size of stress and strain. With the

accumulation of fatigue damage, some accidents occur for these components. Thus, it is important to formulate an accurate method to evaluate the fatigue damage accumulation and effectively predict the fatigue life of these components even when subjected to complex loadings.

The problem is then to define criteria able to predict this endurance limit. The micro-macro approach applied to the field of endurance was born with the work of [Dang Van \[1973\]](#), and since it has been used many times, including by [Papadopoulos \[2001\]](#) to take better account of loading path effects. For simplicity and to avoid too costly identification procedures of fatigue data, criteria are often expressed using two parameters. The first relates generally to a shear stress τ (on a plane or on average over an elementary volume) while the second σ reflects the normal stress effects (mean and amplitude) often through the hydrostatic stress are the most numerous ([Crossland \[1956\]](#), [Sines \[1959\]](#), [Morel \[1998\]](#), [Thu \[2008\]](#)). The normal stress acting on the material plane is sometimes defined from a critical plane ([Findley \[1959b\]](#)), or through integration at every plane of an elementary volume ([Liu and Zenner \[1993\]](#)). In particular, a probabilistic approach based on this type of integration is proposed in [Thu \[2008\]](#).

Other authors use energy based approaches. [Ellyin \[1974\]](#) is one of the first to propose a fatigue criterion based on cyclic shear deformation energy. This approach was taken up and complemented by [Lefebvre \[1981\]](#) and [Ellyin et al. \[1991\]](#) for the case of multiaxial loadings. In France, this approach is reflected in the work of [Froustey et al. \[1992\]](#) and then in [Palin-Luc \[1996\]](#) and [Banvillet \[2001\]](#). In recent years, a new class of criteria coupling mesoplasticity and damage has also emerged. In [Lemaître et al. \[1999\]](#), for example, the author use the approach introduced by [Lemaître and Chaboche \[1985\]](#) based on the thermodynamics of irreversible processes and the mechanics of continuous media. Models based on plasticity-damage coupling were also proposed in [Flacelière \[2004\]](#), [Monchiet \[2006\]](#). In the case of fatigue, we usually employ in this damage framework the concept of the loading cycle instead of time to evaluate the evolution of damage and to measure the fatigue lifetime. The equations then depend on the load through globally defined quantities over a cycle, such as amplitude, maximum value, mean value. The growth equation of fatigue damage is therefore taken in the form as described in Chapter 4:

$$\delta D = f(D)\delta N$$

$$\delta N = f_n \delta t$$

where δt is a time sampling of the history in a given number of time intervals $\delta t_1, \delta t_2 \dots \delta t_i, \dots$ and f_n is the mean frequency of those cycles during the considered time step.

The problem in these approaches is then to take into account the presence of complex variations of the stress tensor. Heuristic formulations with different multiaxial fatigue criteria have been proposed, but most of them still requires the notion of load cycles. The objective of the present chapter is to contribute to the development of life models that take into account such complex variations while avoiding the notion of load cycle. Our fundamental thought is to assume within a micro-macro approach that the local dissipated energy at small scale contributes to the damage which governs fatigue at failure. We follow the Dang Van paradigm. The structure is elastic at the macroscopic scale. At each material point, there is a stochastic distribution of weak points which will undergo strong plastic yielding, which contributes to energy dissipation and cause damage, without affecting the overall macroscopic stress.

Our model considers a plastic behavior at the mesoscopic scales with a dependence of the yield function not only on the deviatoric part of the stress but also on the hydrostatic part. A kinematic hardening under the assumption of associative plasticity is also introduced.

Instead of using the number of cycles, we will use in addition as in [Lemaître et al. \[1999\]](#) the concept of nonlinear damage accumulation during the loading history. To approach real life loading history more accurately, non-linear damage accumulation laws are also considered in our model to

take into account the sequencing effect. Fatigue will then be determined from the energy plastically dissipated at all scales during plastic shakedown cycles and from a phenomenological fatigue law linking damage evolution and accumulated mesoscopic plastic dissipation.

The chapter is organized as follows. From section 5.1 to 5.3, we present the existing methods and background of our strategy. In section 5.4 we propose the notion of weakening scales and multiscale yield function and describe the plastic dissipation resulting from this notion. And in section 5.5, based on microscopic plasticity we construct the energy dissipation formula. Section 5.6 gives the proposed nonlinear damage accumulation law and summarizes the full model that we propose. Then we combine the energy dissipation law and nonlinear damage accumulation law with its numerical implementation presented in section 5.7, while section 5.8 is devoted to various validations on typical load histories classically treated in the literature. Parameter identification strategy is presented in section 5.9.

5.2 Kinematic Hardening Models

5.2.1 Linear Kinematic Hardening

A hardening rule is needed in microplasticity to describe the behavior of the material once it is plastically deformed or yielded. One possible hardening rule is the isotropic rule, which assumes that strain hardening corresponds to an enlargement of the yield surface (i.e. an increase in yield stress) without change of shape or position in the stress space. Another is the kinematic rule, which assumes that strain hardening shifts the yield surface without changing its size or shape. Kinematic hardening

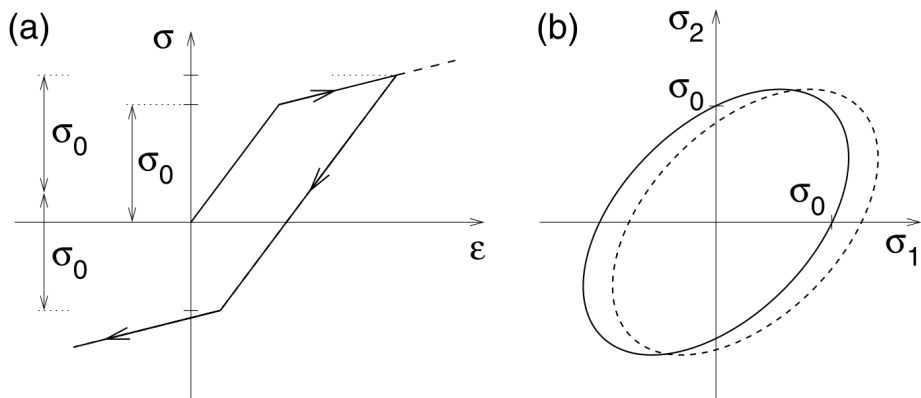


Figure 5.1 – Kinematic hardening: a) uniaxial stress-strain diagram, b) evolution of the yield surface in the biaxial stress plane

rules are necessary, especially for the case of unloading and cyclic loading. In Kinematic Hardening the current loading surface is assumed not to expand but to move as a rigid body within the stress space (Figure 5.1(b)). The use of kinematic hardening is, for example, necessary to model the so-called Bauschinger effect (Bauschinger, 1881). This effect is often observed in metals subjected to cyclic loading. Even if the magnitudes of the yield stress in tension and in compression are initially the same, this is no longer the case when the material is preloaded into the plastic range and then unloaded. For example, after previous yielding in tension, yielding in compression may start at a stress level lower than the initial yield stress (Figure 5.1(a)).

Kinematic hardening leads to a translation of the loading surface, i.e. to a shift of the origin of the initial yield surface. If the initial yield surface is described by a yield function of the form

$$f(\underline{\sigma}) = F(\underline{\sigma}) - \sigma_0$$

the shifted surface is obviously described by

$$f(\underline{\underline{\sigma}}, \underline{\underline{\sigma}}_b) = F(\underline{\underline{\sigma}} - \underline{\underline{\sigma}}_b) - \sigma_0$$

where σ_b is the so-called backstress that represents the center of the shifted elastic domain and plays the role of a tensorial hardening variable. Now we need a kinematic hardening law that governs the evolution of the back stress. [Melan \[1938\]](#) proposed a law of the form

$$\dot{\underline{\underline{\sigma}}}_b = \overline{H}_K \dot{\underline{\underline{\varepsilon}}}_p \quad (5.2.1)$$

where $\dot{\underline{\underline{\varepsilon}}}_p$ is the rate of the plastic strain. According to which the rate of the back stress is proportional to the plastic strain rate. It is a macroscopic variable representing the dislocation sub-structure resistance to deformation. The proportionality factor \overline{H}_K is directly related to the plastic modulus and is derived from a simple monotonic uniaxial curve. The linear hardening law Eq.(5.2.1) is often credited to Prager (1955, 1956); we will call it the Melan-Prager hardening rule.

5.2.2 Non-linear Kinematic Hardening

To describe cyclic plasticity, one of the famous model is the non-linear kinematic hardening model formulated by Armstrong and Frederick. It is based on a physical mechanism of strain hardening and dynamic recovery and is capable of simulating the multiaxial Bauschinger effect (movement of the yield surface in the stress space). Therefore, the model has been examined and implemented in commercial software and finite element analysis.

The Armstrong-Frederick model (AF) is a modification of the Melan-Prager linear kinematic hardening model. The only modification of this simple model is the "recall" term which changes the evolution law for the symmetric backstress tensor $\underline{\underline{\sigma}}_b$ from a classical linear kinematic hardening law (MelanPrager) to a nonlinear kinematic hardening law. The term is proportional to the current back stress multiplied by the norm of the plastic strain rate. According to the Armstrong-Frederick rule, the evolution of the back stress is governed by the differential equation:

$$\dot{\underline{\underline{\sigma}}}_b = \underbrace{\overline{H}_K \dot{\underline{\underline{\varepsilon}}}_p}_{lin.kin.hardening} - \underbrace{\gamma \dot{p} \underline{\underline{\sigma}}_b}_{recall-term,nonlinearhardening} \quad (5.2.2)$$

where \dot{p} is the accumulated plastic strain rate given as $\sqrt{\frac{2}{3} \|\dot{\underline{\underline{\varepsilon}}}_p\|^2}$. The constants \overline{H}_K and γ are determined from uniaxial tests. At the onset of yielding, the back stress is still zero and Eq.(5.2.2) gives the same response as the linear hardening law Eq.(5.2.1). As the back stress develops, the additional term becomes activated and slows down the rate at which the back stress grows (i.e. reduces the tangent plastic modulus).

5.3 Mean stress effect in local model

Positive mean stress clearly reduces the fatigue life of the material. In design evaluation of multi-axial fatigue with mean stress, a simplified, conservative relation between mean stress and equivalent alternating stress is necessary. We can improve the model by modifying the yield function σ_y and the localization tensor in order to take mean stress effect into account.

Christensen approach

The yield function that was given by [Christensen \[2000\]](#) integrates measures of damage, as well as intrinsic yield strength and concept of transitions. The derived yield function formalism resulted in the form as:

$$\frac{\alpha K}{\sqrt{3}}\sigma_{kk} + \frac{(1+\alpha)^2}{2}s_{ij}s_{ij} \leq \frac{K^2}{(1+\alpha)}. \quad (5.3.1)$$

Here α changes the shape of the yield function, thus it is called the shape parameter.

$$\alpha = \frac{|\sigma_{11}^C|}{\sigma_{11}^T} - 1.$$

The new parameter K is called the ideal or intrinsic strength which uniformly expands or contracts the yield function, thus is called the scale parameter:

$$K = \frac{(\sigma_{11}^C)^2}{\sqrt{3}\sigma_{11}^T}.$$

The intrinsic strength would occur if there were no damage or microstructure disturbance. σ_{11}^C and σ_{11}^T are respectively compressive and tensile yield stress in uniaxial states where $|\sigma_{11}^C| \geq \sigma_{11}^T$ (for ductile materials, $\frac{1}{2} \leq \frac{|\sigma_{11}^C|}{\sigma_{11}^T} \leq 1$). The yield stress in uniaxial and shear states are given by:

$$\begin{aligned} \sigma_{11}^C &= \frac{-\sqrt{3}K}{(1+\alpha)} \\ \sigma_{12}^Y &= \frac{K}{(1+\alpha)^{3/2}} \\ \sigma_{11}^T &= \frac{\sqrt{3}K}{(1+\alpha)^2}. \end{aligned} \quad (5.3.2)$$

At $\alpha = 0$, relations Eq.(5.3.1) and Eq.(5.3.2) show the behavior to be that of purely Mises type. This is taken to be the ideal condition where the intrinsic strength K solely determines the yield strength. As the shape parameter increases beyond the value $\alpha = 1$, the yield function behaves in accordance with a state of increasing crack density or any other physical weakening. The term fracture, as used here for behavior at or near $\alpha = 1$, actually corresponds to fracture mechanics for non-interacting cracks. Beyond this range near $\alpha = 1$ or $\alpha \rightarrow \infty$ has simply been called yield or failure. Parameter α could be easily viewed as a damage measure or microstructure parameter since it represents microstructure changes on any scale that causes deviation from the ideal state.

It is concluded a decrease in mean stress σ_{kk} reduces the effective value of α . That is, moving the behavior toward ductile case. Alternatively, increasing the mean stress moves α toward larger values, which is taken to be that of brittle behavior.

The fully expanded form of the yield function Eq.(5.3.1) is:

$$\begin{aligned} &\frac{\alpha K}{\sqrt{3}}(\sigma_{11} + \sigma_{22} + \sigma_{33}) \\ &+ (1+\alpha)^2 \left[\frac{(\sigma_{11} - \sigma_{22})^2 + (\sigma_{22} - \sigma_{33})^2 + (\sigma_{33} - \sigma_{11})^2}{6} + (\sigma_{12}^2 + \sigma_{23}^2 + \sigma_{31}^2) \right] \\ &\leq \frac{K^2}{(1+\alpha)}. \end{aligned} \quad (5.3.3)$$

The most compact form of Eq.(5.3.1) is:

$$\frac{1}{2}s_{ij}s_{ij} \leq \eta K^2, \quad (5.3.4)$$

where η is a nondimensional scaling factor on K^2 , determined by mean normal stress.

$$\eta = \frac{1 - \frac{\alpha(1+\alpha)}{\sqrt{3}K}\sigma_{kk}}{(1+\alpha)^3} < 1$$

The mean stress σ_{kk} has a positive relationship with the shape parameter α . We suppose the material endures transition from ductile to brittle when α reaches 1. That means α has a very similar physical meaning with the damage parameter D .

The Gerber parabola

Several models are available addressing the influence of tensile mean stress on fatigue life. Among these are the Gerber (Germany, 1874), Goodman (England, 1899), and Soderberg (USA, 1930) models. The modified Goodman criterion is often used as a design criterion because it is more conservative than the Gerber criterion. The use of the Gerber criterion in the determination of member size is generally more computationally intensive and so rather unattractive for many designers.

The effect of mean stress on the fatigue strength is commonly presented in Haigh diagrams as shown in Figure 5.2, where S_a/S_f is plotted against S_m/S_u at fatigue limit. S_a is the fatigue strength at a given life under fully reversed ($S_m = 0, R = -1$) conditions. S_u is the ultimate tensile strength. S_f is the reversed fatigue strength in absence of mean stress. The data points thus represent combinations of S_a and S_m giving that life. The results were obtained for small unnotched specimens, tested at various tensile mean stresses. The straight lines are the modified Goodman and the Soderberg lines, and the curved line is the Gerber parabola. These are empirical relationships that are represented by the following equations:

$$\text{Modified Goodman: } S_a/S_f + S_m/S_u = 1$$

$$\text{Gerber: } S_a/S_f + (S_m/S_u)^2 = 1$$

$$\text{Soderberg: } S_a/S_f + S_m/S_u = 1$$

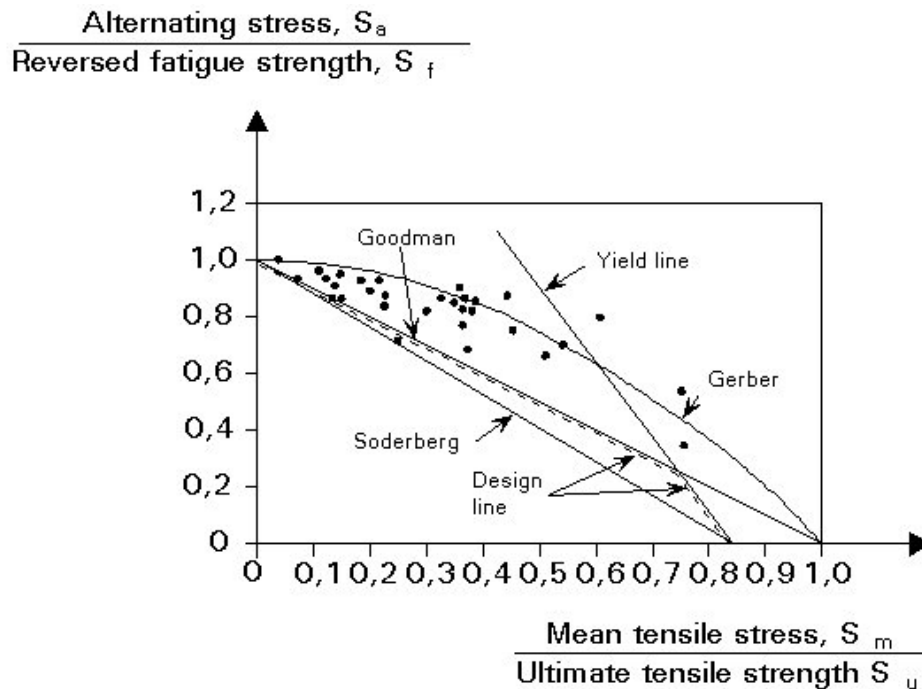


Figure 5.2 – Haigh diagram showing test data points for the effect of mean stress, and the Gerber, modified Goodman and Soderberg relations.

In the following section, we introduce the sale dependent mean stress effect in our model.

5.4 Weakening scales and yield function

5.4.1 The concept of weakening scales

We follow the Dang Van paradigm. The structure is elastic at the macroscopic scale. At each material points, there is a stochastic distribution of weak points which will undergo strong plastic yielding, without contributing to the overall macroscopic stress. From a microscopic point of view, there is a distribution of weakening scales, namely $s \in [1, \infty)$. In order to introduce our concept, let us imagine that we can measure the macroscopic stress intensity at present time by a given value S_a . Let σ_y be the yield limit before weakening. Then we imagine that for a given scale s :

- either $1 \leq s \leq \sigma_y/S_a$, then $S_a \leq \sigma_y/s$, the material stays in the elastic regime and there is no energy dissipation at this scale.
- or $\sigma_y/S_a \leq s \leq \infty$, then $S_a \geq \sigma_y/s$, the material is in plastic regime at this scale, which evolves through kinematic hardening, say from zero initial plastic strain $\underline{\varepsilon}_p(s)$ and zero initial backstress $\underline{b}(s)$ at initial time t_0 . There is then dissipated energy at scale s contributing to the fatigue limit.

5.4.2 Distribution of weakening scales

We assume the weakening scales have a probability distribution function following a power law:

$$P(s) = Hs^{-\beta} = (\beta - 1)s^{-\beta}, \quad (5.4.1)$$

where β is a material constant. The choice of a power law comes with two reasons: on the one hand, this type of distribution corresponds to a scale invariant process, on the other hand it leads, for cyclic loading, to a prediction of a number of cycles to life limit as a power law function of the stress intensity. More general laws can also be proposed, without changing the spirit of the model.

The probability of weakening scales is shown in Figure 5.3 and Figure 5.4. We can see that smaller β leads to larger probability of weakening for large s .

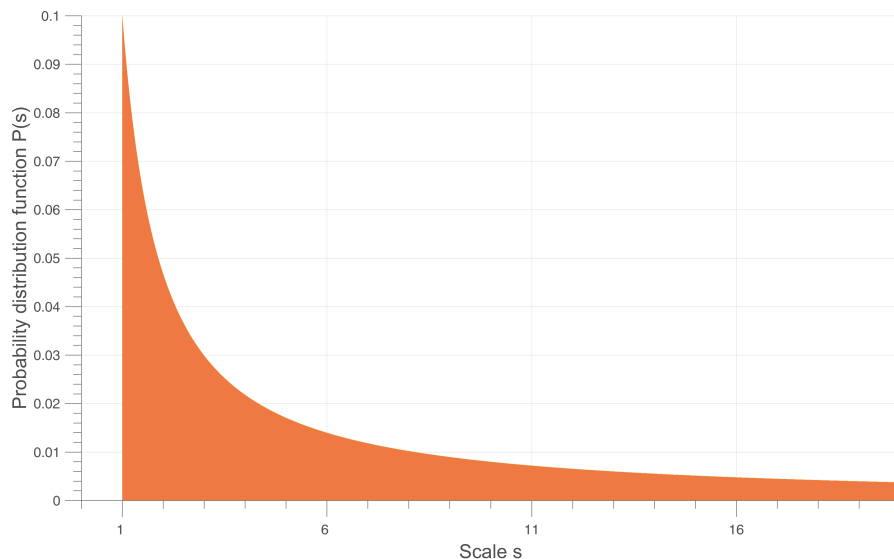


Figure 5.3 – Weakening scales s probability distribution curve when $\beta = 1.5$

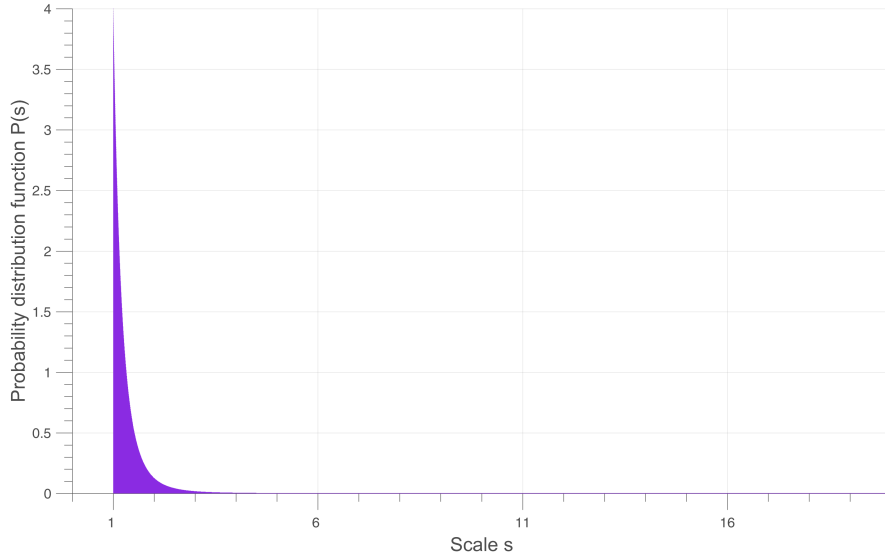


Figure 5.4 – Weakening scales s probability distribution curve when $\beta = 5$

5.4.3 Yield function with mean stress effect

Positive mean stress clearly reduces the fatigue life of the material. In design evaluation of multi-axial fatigue with mean stress, a simplified, conservative relation between mean stress and equivalent alternating stress is necessary. We can improve the model to come by modifying the yield function σ_y and the localization tensor.

Present choice

In the model to come, our idea is to consider as in [Maitournam et al. \[2011\]](#) that the yield limit σ_y can be reduced in presence of positive mean stress. The mesoscopic yield function can therefore be written as:

$$f(s) = \|\underline{\underline{S}}(s) - \underline{\underline{b}}(s)\| + (\lambda \Sigma_H - \sigma_y) / s \leq 0 \quad (5.4.2)$$

with $\underline{\underline{S}}$ denoting the deviatoric part of the stress tensor at microscale, and $\underline{\underline{b}}(s)$ the corresponding backstress at the same scale. The material remains in elastic regime when $f < 0$ and in plastic regime when $f = 0$. The parameter λ can itself be a function of Σ_H with a different value in traction (λ_+) than in compression (λ_-).

5.4.4 Local plastic model

We can now describe the mesoscopic stress state. The model considers a plastic behavior at the mesoscopic scale. The mesoscopic stress evolution equations are thus:

$$\dot{\underline{\underline{S}}}(s, M, t) = \text{dev} \dot{\underline{\underline{\Sigma}}}(M, t) - \frac{E}{1 + \nu} \dot{\underline{\underline{\varepsilon}}}^p(s, M, t), \quad (5.4.3)$$

which defines a Taylor-Lin scale transition model with unit localization tensor ([Bosia and Constantinescu \[2012\]](#)). The mesoscopic deviatoric strain rate tensor is thus equal to the macroscopic strain rate tensor $\text{dev} \dot{\underline{\underline{\Sigma}}} = \frac{1 + \nu}{E} \text{dev} \dot{\underline{\underline{\varepsilon}}}$ with $\text{dev} \dot{\underline{\underline{\Sigma}}}$ the deviatoric part of the macroscopic stress tensor. It is complemented by

$$\dot{\underline{\underline{b}}}(s, M, t) = \frac{kE}{E - k} \dot{\underline{\underline{\varepsilon}}}^p(s, M, t), \quad (5.4.4)$$

which is our kinematic hardening model, and by

$$\dot{\underline{\varepsilon}}^p(s, M, t) = C \frac{\partial f(s, M, t)}{\partial \underline{\underline{S}}}, \quad (5.4.5)$$

which is the associated plastic flow rule assuming $C = 0$ when $f < 0$ and $C \geq 0$ when $f = 0$.

Here E denotes the Young's modulus and k the hardening parameter. The local dissipated energy rate per unit volume at weakening scales s is given by the local entropy dissipation:

$$\dot{w}(s, M, t) = (\underline{\underline{S}} - \underline{\underline{b}})(s, M, t) : \dot{\underline{\varepsilon}}^p(s, M, t). \quad (5.4.6)$$

5.5 Construction of an energy based fatigue approach

In a preliminary step, we will consider a simple macroscopic loading history

$$\underline{\underline{\Sigma}}(M, t) = \Sigma_a \sin(\omega t) \underline{\underline{e}}_1 \times \underline{\underline{e}}_1,$$

which is uniaxial along direction $\underline{\underline{s}}_1$, with $\underline{\underline{s}}_1$ a given stress tensor of unit norm. In traction there is

$$\underline{\underline{s}}_1 = \sqrt{\frac{3}{2}} \begin{pmatrix} 2/3 & 0 & 0 \\ 0 & -1/3 & 0 \\ 0 & 0 & -1/3 \end{pmatrix}.$$

Time periodic deviatoric stress amplitude S_a , constant mean stress Σ_H and a Von Mises flow rule are taken into account to see if we get a prediction of local failure for a number of cycles N_F varying as $S_a^{-\gamma}$.

In uniaxial cyclic loading, there will be 3 kinds of loading regimes, as is shown in Figure 5.5:

1. Elastic regime, in phase 2 and 4, where we have no plastic flow $\dot{\underline{\varepsilon}}^p(s, M, t) = \dot{\underline{\underline{S}}} = 0$, and where the stress is below the yield limit $|\underline{\underline{S}} - \underline{\underline{b}}| < (\sigma_y - \lambda \Sigma_H) / s$, and where we have therefore $\dot{\underline{\underline{S}}} = \text{dev} \dot{\underline{\underline{\Sigma}}}$.
2. Plastic regime according to plastic flow rule, with increasing plastic deformation, in phase 5 and 1, where $\dot{\underline{\varepsilon}}^p(s, M, t) = \xi \frac{\underline{\underline{S}}(s) - \underline{\underline{b}}(s)}{\|\underline{\underline{S}}(s) - \underline{\underline{b}}(s)\|} > 0$ with $\xi = \left| \text{dev} \dot{\underline{\underline{\Sigma}}} \right| \left(\frac{kE}{E - k} + \frac{E}{1 + \nu} \right)^{-1}$ (detailed in annex), $\underline{\underline{S}} - \underline{\underline{b}} = \underline{\underline{s}}_1 (\sigma_y - \lambda \Sigma_H) / s$ and $\dot{\underline{\underline{S}}} - \dot{\underline{\underline{b}}} = 0$.
3. Plastic regime in the other direction, in phase 3, where we now have $\dot{\underline{\varepsilon}}^p(s, M, t) < 0$, then $\underline{\underline{S}} - \underline{\underline{b}} = -\underline{\underline{s}}_1 (\sigma_y - \lambda \Sigma_H) / s$ and $\dot{\underline{\underline{S}}} - \dot{\underline{\underline{b}}} = 0$.

In phase 1, a direct analysis yields the energy dissipation at scale s :

$$dW = (S - b) d\varepsilon^p = \frac{(E - k)(1 + \nu)}{E(E + k\nu)} \frac{(\sigma_y - \lambda \Sigma_H)}{s} \left(S_a - \frac{(\sigma_y - \lambda \Sigma_H)}{s} \right). \quad (5.5.1)$$

A similar analysis yields

$$dW(\text{phase1}) = dW(\text{phase5}) = \frac{1}{2} dW(\text{phase3}),$$

which yields the energy dissipation at one scale s during unit cycle:

$$W_s = 4dW.$$

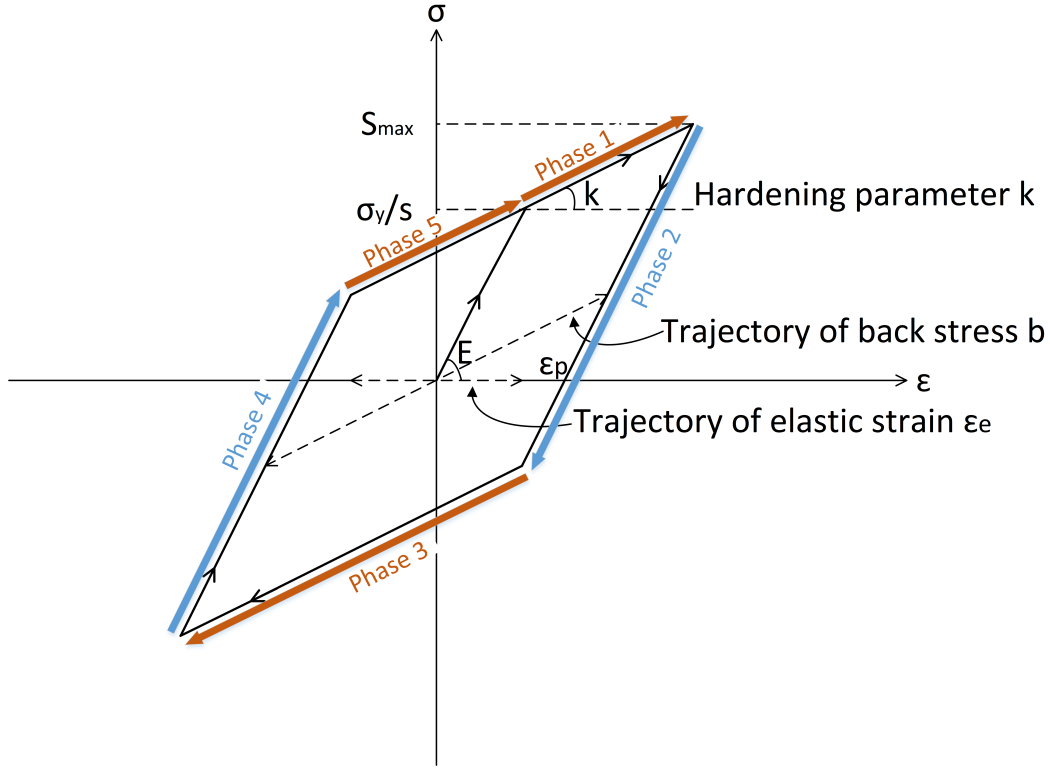


Figure 5.5 – Illustration of uniaxial cyclic load with microscopic plastic dissipation at scale s

We can then calculate the local dissipated energy W at point M during one cycle by cumulating the input of all sub-scales plastic regime with their probabilities (Zepeng [2017]).

$$\begin{aligned}
 W_{cyc} &= 4 \int_{(\sigma_y - \lambda \Sigma_H)/S_a}^{\infty} dW(s, M, t) P(s) ds \\
 &= 4 \int_{(\sigma_y - \lambda \Sigma_H)/S_a}^{\infty} \frac{(E - k)(1 + \nu)}{E(E + k\nu)} \frac{(\sigma_y - \lambda \Sigma_H)}{s} \left(S_a - \frac{(\sigma_y - \lambda \Sigma_H)}{s} \right) (\beta - 1) s^{-\beta} ds \\
 &= \frac{4(E - k)(1 + \nu)(\beta - 1)}{E(E + k\nu)\beta(\beta + 1)} \frac{S_a^{\beta+1}}{(\sigma_y - \lambda \Sigma_H)^{\beta-1}}.
 \end{aligned} \tag{5.5.2}$$

So we have a power law relationship between stress intensity and the dissipated energy per cycle.

$$W_{cyc} = C_1 S_a^{\beta+1}, \tag{5.5.3}$$

with

$$C_1 = f(\lambda, \beta) = \frac{4(E - k)(1 + \nu)(\beta - 1)}{E(E + k\nu)\beta(\beta + 1)(\sigma_y - \lambda \Sigma_H)^{\beta-1}}.$$

If the dissipated energy accumulates until a failure value W_0 , we can get directly the number of cycles to failure from Eq.(5.5.3) as:

$$N_F = \frac{W_0}{W_{cyc}} = \frac{W_0}{C_1} S_a^{-\beta-1}. \tag{5.5.4}$$

As for the time to failure in cyclic loading, it will be:

$$T_F = N_F t_{cyc}.$$

From Eq.(5.5.2), we then obtain that in uniaxial cyclic loading the model predicts as expected (Chapter 4) a power law dependence of the number of cycles to failure in function of S_a . However, experiments shows that the damage or the energy accumulation of a material evolves non-linearly in time

and present a load dependent cycle (Chapter 4). We should introduce below a method to handle such a nonlinearity.

5.6 Nonlinearity of damage accumulation

5.6.1 Energy approach with Chaboche law

The Chaboche law (Lemaître and Chaboche [1990]) is essentially a damage incremental law for cyclic loads with a deviatoric stress intensity A_{II} and hydrostatic mean part Σ_H , defining the damage increase by:

$$\delta D = (1 - (1 - D)^{\gamma+1})^\alpha \left(\frac{A_{II}}{M(\sigma_H)(1 - D)} \right)^\gamma \delta N, \quad (5.6.1)$$

using an effective intensity $A_{II}^* = A_{II} / (1 - D)$ evolving with damage D . And the mean stress effect is present both in exponential factor α and in denominator $M(\sigma_H)$.

$$\alpha = 1 - a \left\langle \frac{\frac{1}{2}A_{II} - \sigma_{-1}M(\sigma_H)}{\sigma_u - A_{II}} \right\rangle,$$

$$M(\sigma_H) = M_0 (1 - 3c\sigma_{H,max}).$$

$M(\sigma_H)$ is chosen so as to describe the well-known linear dependency (section 5.3), between mean stress and the fatigue limit.

Eq.(5.6.1) writes equivalently:

$$\delta[1 - (1 - D)^{\gamma+1}]^{1-\alpha} = (1 - \alpha)(\gamma + 1) \left(\frac{A_{II}}{M(\sigma_H)} \right)^\gamma \delta N = \frac{1}{N_F(\sigma)} \delta N. \quad (5.6.2)$$

Here $N_F(\sigma)$ denotes the number of cycles at intensity σ to failure as obtained by integration of Eq.(5.6.2) from $D = 0$ to $D = 1$.

Similar to Eq.(5.6.2), we define here the “equivalent damage” \tilde{D} (Figure 5.6.3) :

$$\tilde{D} = 1 - (1 - D)^{\gamma+1}, \quad (5.6.3)$$

with D the damage variable introduced by Chaboche in its model to scale the stress intensity:

$$A_{II} \longrightarrow \frac{A_{II}}{1 - D}.$$

We have

- $\tilde{D} = 0$ when $D = 0$ (undamaged material),
- $\tilde{D} = 1$ when $D = 1$ (failure of material),

and a nonlinear relation in between as in Figure 5.6:

$$\delta\tilde{D} = (\gamma + 1)(1 - D)^\gamma \delta D.$$

Change of damage measure $\tilde{D} = 1 - (1 - D)^{\gamma+1}$ makes the evolution (5.6.1) explicit. It writes

$$\frac{d\tilde{D}}{dN} = c_D \tilde{D}^\alpha \left(\frac{A_{II}}{M(\Sigma_H)} \right)^\gamma, \quad (5.6.4)$$

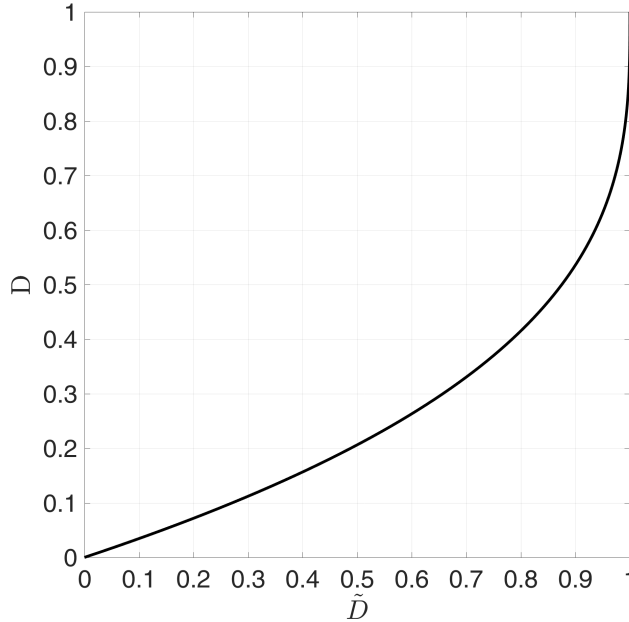


Figure 5.6 – The relation between \tilde{D} and D when $\gamma = 2$

yielding after integration from $\tilde{D} = 0$ to $\tilde{D} = 1$ a number of cycles to fatigue at constant load given by

$$N_F = \frac{1}{(1-\alpha)} \left(\frac{A_{II}}{M(\Sigma_H)} \right)^{-\gamma}.$$

This method as written requires cycle counting which is difficult and technical for complex load histories. In addition, it allows only a limited influence of multiaxiality.

Now in our model we use the same growth rule as in Chaboche in cyclic load regime, but replace stress intensity by multiscale dissipated energy in Eq.(5.6.4), which removes cycle counting.

The evolution (5.6.4) then writes

$$\frac{d\tilde{D}}{dt} = \tilde{D}^\alpha \dot{W}/W_0,$$

or in a differential form

$$d\tilde{D} = \tilde{D}^\alpha \frac{dW}{W_0} = \tilde{D}^\alpha \frac{W_{cyc} dN}{W_0}. \quad (5.6.5)$$

The replacement of dW by $W_{cyc} dN$ is only introduced to handle cyclic loadings if they occur. The number of cycles to failure in constant loading case, obtained by integrating \tilde{D} from \tilde{D}_0 to 1 is then:

$$N_F = \frac{W_0}{(1-\alpha) W_{cyc}} \left(1 - \tilde{D}_0^{1-\alpha} \right).$$

With initial damage $\tilde{D}_0 = 0$, we finally get with our proposed expression Eq.(5.5.3) of cyclic energy dissipation:

$$N_F = \frac{W_0}{(1-\alpha) W_{cyc}} = \frac{W_0}{(1-\alpha) C_1} S_a^{-\beta-1}. \quad (5.6.6)$$

From Eq.(5.6.6), we see $(-\beta - 1) = -\gamma$ is related to the slopes in S-N curve and that $\frac{W_0}{(1-\alpha) C_1}$ defines the number of cycles to failure.

5.6.2 Sequence effect

Experiments show fatigue tests started with high stress then change to low stress has less fatigue life than the combination of high stress life proportion plus the low one. This phenomenon of sequence effect is load history dependent, so we need a stress induced parameter to describe it.

This is done in Chaboche with three ingredients:

1. a damage sensitive effective stress:

$$\sigma_D^{eff} = J_2(\underline{\Sigma})/(1 - D) = A_{II}/(1 - D);$$

2. a $(\sigma_D^{eff})^\gamma$ controlled law for damage growth

$$\frac{dD}{dN} = c_\gamma \tilde{D}^\alpha (\sigma_D^{eff})^\gamma;$$

3. a load dependence of exponent α (from 1 at zero load to 0 at large loads). In Chaboche model, the proposition of α is

$$\alpha = 1 - a \left\langle \frac{\sigma_{eq} - \sigma_{fatigue}}{\sigma_u - \sigma_{eq}} \right\rangle \quad (5.6.7)$$

in order to recover the proper high-low sequencing effect.

Many fatigue damage accumulation models are based on the two level loading experiments which is one of the basic random loading analysis. To facilitate the validation and interpretation of an α dependence on stress we will also use two-stress level loading, the specimen is firstly loaded at stress Σ_1 for T_1 cycles and then at stress Σ_2 for T_2 cycles until failure. We can then observe if the experimental results are satisfactory.

During a loading time T_1 , we cycle from $\tilde{D} = 0$ to $\tilde{D} = \tilde{D}_1$. By integrating Eq.(5.6.5) of our proposed approach, we get:

$$(1 - \tilde{D}_1)^{1-\alpha_1} = \frac{T_1}{T_{F1}}, \quad (5.6.8)$$

with T_{F1} the time to failure with this loading.

Then we cycle from $\tilde{D} = \tilde{D}_1$ to failure $\tilde{D} = 1$, which yields

$$1 - (1 - \tilde{D}_1)^{1-\alpha_2} = \frac{T_2}{T_{F2}}. \quad (5.6.9)$$

From Eq.(5.6.8) and Eq.(5.6.9), after elimination of $(1 - D_1)$ we get:

$$\frac{T_2}{T_{F2}} = 1 - \left(\frac{T_1}{T_{F1}} \right)^\eta, \quad (5.6.10)$$

with

$$\eta = \frac{1 - \alpha_2}{1 - \alpha_1}. \quad (5.6.11)$$

In the case of high-low loading sequence we have $\Sigma_1 > \Sigma_2$, which gives $\alpha_1 < \alpha_2$, so it comes to:

$$\eta = \frac{1 - \alpha_2}{1 - \alpha_1} < 1 \implies \frac{T_2}{T_{F2}} = 1 - \left(\frac{T_1}{T_{F1}} \right)^\eta < 1 - \frac{T_1}{T_{F1}} \implies \frac{T_1}{T_{F1}} + \frac{T_2}{T_{F2}} < 1.$$

The α dependence on stress intensity does therefore predict a sequencing effect where a low loading sequence following a high one will reduce the life of the structure if α decreases when the load increases.

To get the same effect in our construction, we propose here to introduce s_{min} , which is the minimum scale that experiences plastic dissipation thus causes energy loss:

$$s_{min} = \frac{(\sigma_y - \lambda \Sigma_H)}{S_a}. \quad (5.6.12)$$

We propose a load dependent α through s_{min} . Possible choice of α is expressed as Eq.(5.6.13):

$$\alpha = 1 - a \left(\frac{\frac{1}{s_{min}}}{1 - \frac{1}{s_{min}}} \right). \quad (5.6.13)$$

There is no notion of fatigue limit in our model, $\sigma_{fatigue} = 0$. The intensity of loading

$$\frac{\sigma_{eq} - \sigma_{fatigue}}{\sigma_u - \sigma_{eq}} = \frac{1}{\frac{\sigma_u}{\sigma_{eq}} - 1}$$

is measured by

$$\left(\frac{\frac{1}{s_{min}}}{1 - \frac{1}{s_{min}}} \right) = (s_{min} - 1)^{-1}.$$

This means that we measure the distance of load to ultimate failure by local variable s_{min} through

$$\frac{\sigma_u}{\sigma_{eq}} - 1 \longrightarrow (s_{min} - 1)$$

We can see from Figure 5.7 that with our proposition, cycling 1 for fifty percent of its failure time leaves a reserve before failure to cycling 2 of much less than fifty percent. To conclude, the cumulative damage under high-low loading sequence, as we deduced, has the addition of partial lives less than unit. Similarly, the cumulative damage under low-high loading sequence has addition of partial lives more than 1:

$$\frac{T_1}{T_{F1}} + \frac{T_2}{T_{F2}} > 1.$$

The curve in both cases is depicted in Figure 5.7. For constant two-level stress loading, $\alpha_1 = \alpha_2$, the Chaboche law returns to the Miner rule when $F_{low} = F_{high}$ where:

$$\frac{T_1}{T_{F1}} + \frac{T_2}{T_{F2}} = 1.$$

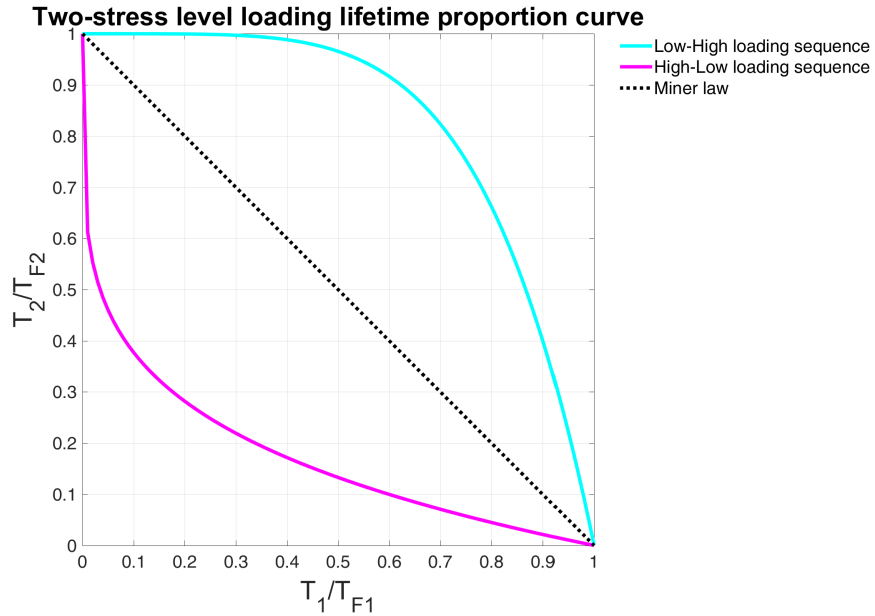


Figure 5.7 – High to low and low to high loading sequence comparison in 4-point bending($F_{low} = 5000N$, $F_{high} = 30000N$, $Radius = 0.2m$, $\Sigma_u = 1.67E8$), with the proposed damage accumulation law (Eq.(5.6.5)) induced equation Eq.(5.6.10) and Chaboche type α (Eq.(5.6.7)) containing Crossland criterion

5.6.3 The final model

In summary, our damage based fatigue life criterion using a damage evolution governed by a multiscale plastic energy dissipation, has four ingredients.

- a scale dependent yield limit

$$\frac{1}{s}(\sigma_y - \lambda \Sigma_H^{macro})$$

associated to a microscopic plastic evolution governed by the standard plastic evolution laws Eq.(5.4.3) - Eq.(5.4.5);

- a multiscale plastic energy dissipation obtained by summing plastic dissipation across our power law scale distribution

$$\dot{W}(M, t) = \int_{s=1}^{\infty} (\underline{S} - \underline{b})(s, M, t) : \underline{\dot{\varepsilon}}^p(s, M, t) s^{-\beta} ds; \quad (5.6.14)$$

- a load intensity sequencing effect that we have represented by the formula :

$$1 - \alpha = a(s_{min} - 1)^{-f}; \quad (5.6.15)$$

- a exponential damage evolution law with load dependent exponent α given by the above formula and coefficient \dot{W}/W_0 governed by the multiscale plastic dissipation rate:

$$\frac{d\tilde{D}}{dt} = \tilde{D}^\alpha \dot{W}/W_0. \quad (5.6.16)$$

In this model we have five independent coefficients in addition to the construction of the local plastic model Eq.(5.4.3) - Eq.(5.4.5) :

1. reference density of damage energy : W_0 (in MPa)
2. mean stress effect coefficient : λ
3. slope of SN curve : $\beta + 1$
4. sensitivity to load intensity a .
5. exponent in the load sequence effect f .

5.7 Numerical strategy

5.7.1 Scale discretization

We now need to propose a practical implementation strategy for our final model of section 5.6.3. Our first approach takes one cycle as unit time. We compute analytically by Eq.(5.5.2) the energy dissipation at each scale during this cycle. The method is valid for simple loading history and which includes the integration on all weakening scales. The damage \tilde{D} is then accumulated after each cycle by numerical integration of Eq.(5.6.16) until we get to the fatigue limit of $\tilde{D} = 1$.

However, there are certain limitations of this method. Firstly we need a load history decomposition in cycles. Secondly in real life the perfect close loop cycle is hardly applicable. Finally, we need to approximate α by its average value per cycle which is computed numerically and can not be done analytically.

Thus we propose in a more general method which can be integrated by a step by step strategy. We compute numerically the dissipation at different scales using an implicit Euler time integration of the constitutive laws of section 5.7.2. After which we make a numerical integration on different scales. Then we can update the damage and go to next time step.

Instead of doing the scale integration directly which can be difficult for complex loading, the Gaussian Quadrature rule with Legendre points is used to give the value of local dissipated energy rate. To use the Gaussian quadrature rule the limit range of integral must be from -1 to 1 , while the total dissipated energy is expressed by integrating all the weakening scale s ranging from 1 to infinity with their occurrence probabilities:

$$\dot{W} = \int_1^\infty \dot{w}(s)(\beta - 1)(s)^{-\beta} ds.$$

To change the limit range of integral from $[1, \infty]$ to $[1, 0]$ we take as new integration variable $u(s) = s^{1-\beta}$. Therefore the dissipated energy summed on all scales is:

$$\begin{aligned} \dot{W} &= \int_1^\infty \dot{w}(s)(\beta - 1)(s)^{-\beta} ds \\ &= \int_0^1 \dot{w}\left(u^{\frac{1}{1-\beta}}\right) du \\ &= \frac{1}{2} \int_{-1}^1 \dot{w}\left[\left(\frac{x+1}{2}\right)^{\frac{1}{1-\beta}}\right] dx \end{aligned} \quad (5.7.1)$$

given $u = \frac{x+1}{2}$. So the dissipated energy rate integrated over all scales takes the form of Eq.(5.7.2):

$$\dot{W} = \frac{1}{2} \int_{-1}^1 \dot{w}\left[\left(\frac{x+1}{2}\right)^{\frac{1}{1-\beta}}, t\right] dx \approx \frac{1}{2} \sum_i \omega_i \dot{w}\left[\left(\frac{x_i+1}{2}\right)^{\frac{1}{1-\beta}}, t\right], \quad (5.7.2)$$

where ω_i and x_i are respectively the weights and nodes of the Gauss Legendre integration rule used for the numerical integration. In this work, we used a 1024 points Gaussian Legendre integration rule (Leg) with $s_i = \left(\frac{x_i+1}{2}\right)^{\frac{1}{1-\beta}}$ being the associated scale.

5.7.2 Calculation of local plastic dissipation

The material could be both in elastic and plastic regime depending on the considered scale. To be more elaborate, we reuse the fundamental equations in different regimes. At scale s , we have a dissipation rate given by:

$$\dot{w}(s) = (\underline{S} - \underline{b}) : \dot{\underline{\varepsilon}}^p,$$

which differs between plastic and elastic regime.

Elastic regime:

There we have plastic strain rate $\dot{\underline{\varepsilon}}^p = 0$, back stress rate $\dot{\underline{b}} = 0$ and deviatoric stress rate $\dot{\underline{S}} = \text{dev} \dot{\underline{\Sigma}}$, leading to

$$\dot{\underline{S}} - \dot{\underline{b}} = \text{dev} \dot{\underline{\Sigma}},$$

meaning

$$(\underline{S} - \underline{b})(t + dt) = (\underline{S} - \underline{b})(t) + \text{dev} \dot{\underline{\Sigma}} dt.$$

At each time step we define a trial stress:

$$(\underline{S} - \underline{b})_{\text{trial}} := (\underline{S} - \underline{b})(t + dt). \quad (5.7.3)$$

We are in elastic regime at scale s as long as we satisfy

$$\|\underline{S} - \underline{b}\|_{\text{trial}} \leq (\sigma_y - \lambda \Sigma_H) / s. \quad (5.7.4)$$

Plastic regime:

When we leave elastic regime at scale s , i.e. when the above inequality Eq.(5.7.4) is violated, we have:

$$\begin{cases} \dot{\underline{\varepsilon}}^p = \xi \frac{\underline{S} - \underline{b}}{\|\underline{S} - \underline{b}\|}, \xi > 0, & \text{plastic flow,} \\ \|\underline{S} - \underline{b}\| = (\sigma_y - \lambda \Sigma_H) / s, & \text{yield limit,} \end{cases} \quad (5.7.5)$$

$$\begin{cases} (\underline{S} - \underline{b}) : (\dot{\underline{S}} - \dot{\underline{b}}) = 0, & \text{yield limit time invariance,} \\ \dot{\underline{b}} = \frac{kE}{E - k\underline{\varepsilon}} \dot{\underline{\varepsilon}}^p, & \text{kinematic hardening rule,} \end{cases} \quad (5.7.6)$$

$$\begin{cases} \dot{\underline{S}} = \text{dev} \dot{\underline{\Sigma}} - \frac{E}{1 + \nu} \dot{\underline{\varepsilon}}^p, & \text{localisation rule.} \end{cases} \quad (5.7.7)$$

In all cases, we get by integrating Eq.(5.7.9), Eq.(5.7.8) with the use of Eq.(5.7.5).

$$(\underline{S} - \underline{b})(s, t + dt) = \frac{(\underline{S} - \underline{b})_{\text{trial}}(s, t + dt)}{1 + \eta}, \quad (5.7.10)$$

and because of the yield condition Eq.(5.7.6), we have

$$\eta = \max \left\{ \underbrace{0}_{\text{elastic regime}}, \underbrace{\frac{\|\underline{S} - \underline{b}\|_{\text{trial}}}{(\sigma_y - \lambda \Sigma_H) / s} - 1}_{\text{plastic regime when this number is positive}} \right\},$$

That is to say, when the structure is in elastic regime at time t and scale s , we have $(\underline{S} - \underline{b})(s, t) = (\underline{S} - \underline{b})_{\text{trial}}(s, t)$. Otherwise, if the norm of $(\underline{S} - \underline{b})_{\text{trial}}(s, t)$ is greater than the local yield limit $(\sigma_y - \lambda \Sigma_H) / s$, $(\underline{S} - \underline{b})(s, t)$ will be projected on the yield limit.

Knowing the distinction between elastic and plastic regime under multiple scales, we compute the general expression of the dissipated energy rate at scale s .

$$\dot{w}(s) = (\underline{S} - \underline{b}) : \dot{\underline{\varepsilon}}^p = \xi \frac{(\sigma_y - \lambda \Sigma_H)}{s}. \quad (5.7.11)$$

From Eq.(1.5) and Eq.(1.8) in annex, we get:

$$\begin{aligned}
E\xi dt &= \left\langle \left| \underline{\underline{S}} - \underline{\underline{b}} \right|_{trial} - \frac{(\sigma_y - \lambda \Sigma_H)}{s} \right\rangle / \left(\frac{1}{1+\nu} + \frac{k}{E-k} \right) \\
&= \left\langle \left| \underline{\underline{S}} - \underline{\underline{b}} \right|_{trial} - \frac{(\sigma_y - \lambda \Sigma_H)}{s} \right\rangle \frac{(E-k)(1+\nu)}{(E+k\nu)},
\end{aligned} \tag{5.7.12}$$

where $\langle \rangle$ is Macaulay bracket symbol defined as $\langle m \rangle = 0$ if $m \leq 0$, otherwise $\langle m \rangle = m$. Thus the dissipated energy rate only depends on the evolution of the variable $(\underline{\underline{S}} - \underline{\underline{b}})$, which must therefore be mentioned during the whole cycle under study.

We replace ξ deduced from Eq.(5.7.12) in Eq.(5.7.11) to give the expression of local energy dissipation rate at scale s :

$$\dot{w}(s)dt = \frac{(E-k)(1+\nu)}{E(E+k\nu)} \left\langle \left| \underline{\underline{S}} - \underline{\underline{b}} \right|_{trial} - \frac{(\sigma_y - \lambda \Sigma_H)}{s} \right\rangle \frac{(\sigma_y - \lambda \Sigma_H)}{s}. \tag{5.7.13}$$

With Eq.(5.7.2), the final expression of energy dissipation W during time step dt writes:

$$\begin{aligned}
W &= \dot{W}dt \\
&= \frac{1}{2} \sum_i \omega_i \dot{w} \left[\left(\frac{x+1}{2} \right)^{\frac{1}{1-\beta}} \right] dt \\
&= \frac{(E-k)(1+\nu)}{2E(E+k\nu)} \sum_i \omega_i \left\langle \left| \underline{\underline{S}} - \underline{\underline{b}} \right|_{trial} - \frac{(\sigma_y - \lambda \Sigma_H)}{\left(\frac{x_i+1}{2} \right)^{\frac{1}{1-\beta}}} \right\rangle \frac{(\sigma_y - \lambda \Sigma_H)}{\left(\frac{x_i+1}{2} \right)^{\frac{1}{1-\beta}}}.
\end{aligned} \tag{5.7.14}$$

The mean stress effect term in Chaboche model is $s_{-1} \left(1 - 3 \frac{\sigma_H}{\sigma_u} \right)$, where the fatigue limit at zero mean stress s_{-1} is reduced in the presence of σ_H . In our model, the yield limit decreases with positive mean stress. Because of the presence of the term $\lambda \Sigma_H$ which will be positive when Σ_H is positive. In Eq.(5.7.14), the coefficient λ can change values if Σ_H changes sign (see section 5.4.3).

5.7.3 Damage integration algorithm

Numerically the change of α is extremely nonlinear with time. From Figure 5.8 we can see the mean value of α depends on loading pattern.

Because of the possible large variations in time of α , the evolution problem in damage is very nonlinear and thus, one needs to develop and validate an improved numerical time integration strategy at least for two specific cases: the constant amplitude case and the random load case.

We propose in constant amplitude load with very small evolution of damage per cycle to numerically calculate W_{cyc} and the mean values of α through one cycle or several cycles(out-of-phase condition) and apply the result to life prediction by using Eq.(5.6.6):

$$N_F = \frac{W_0}{(1 - \alpha_m) W_{cyc}}, \tag{5.7.15}$$

which is obtained by direct integration of our damage law assuming time uniform dissipation in one cycle and frozen α . In this way the numerical cost is not as high as for the numerical implementation of all the loading points in random loading case. Because of the symmetrical shape of the evolution of α , numerically the mean value of α does not strongly depend on the number of steps per cycle. In the verification process we have compared 100 \sim 1000 time steps per cycle (Figure 5.10).

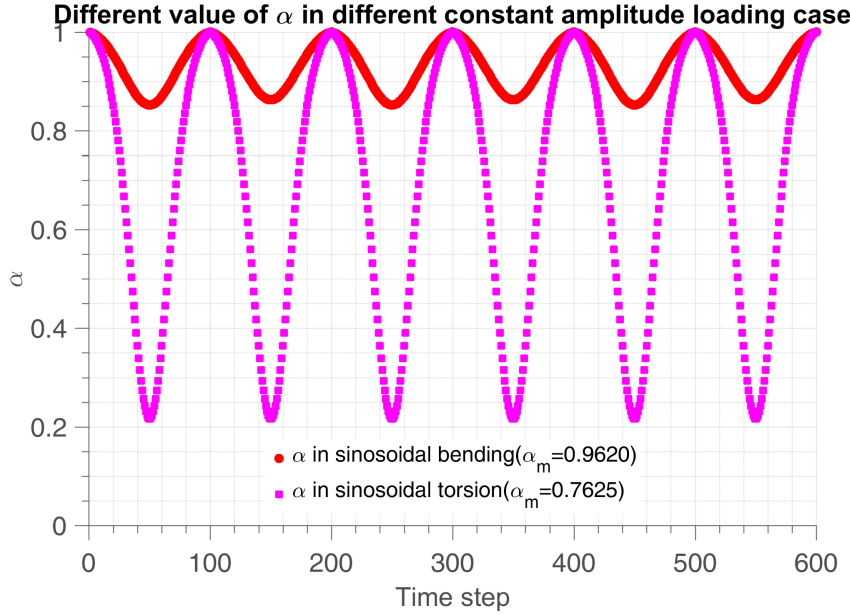


Figure 5.8 – The evolution of α in bending and torsion with $\Sigma_y = 1080$ MPa, $\Sigma_{bending} = \Sigma_{torsion} = 500$ MPa, $a = 0.3$ and 200 time steps in one cycle

For complex cyclic load cases, the idea is to accurately compute the history of plastic dissipation during one cycle (multiscale calculation with time refinement), and to use this precomputed result in the time integration of the scalar damage evolution law with a time stepping which is adapted to the time variation of α .

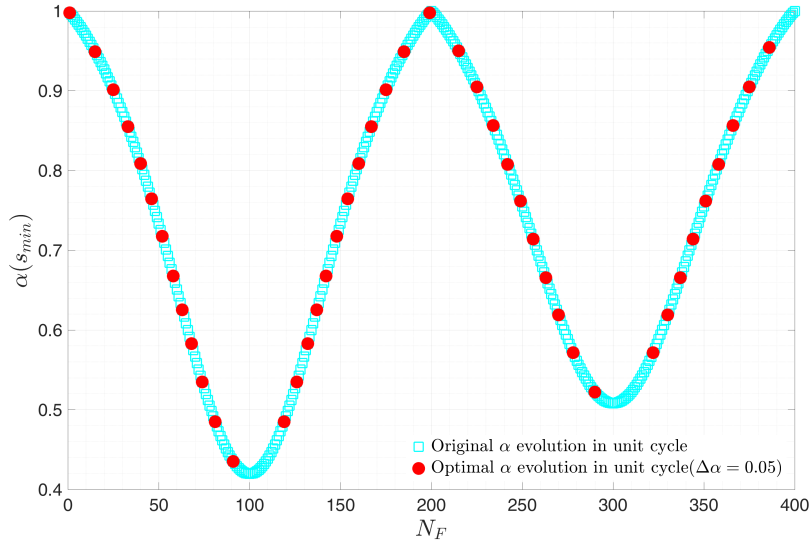


Figure 5.9 – Comparing numerical strategy with optimal time steps in one cycle with the old one, in this way the number of steps in unit cycle is reduced from 400 to 35, meaning a cost reduction factor of 0.0875 (with $\Delta\alpha = 0.05$, $a = 0.4$, $\lambda = 0.1$, $\Sigma_y = 230$ MPa, $\Sigma_{bending} = 225$ MPa)

If α varies significantly, we use optimal time step numerical method to update D during one time step. In more details, let us suppose that our first few cycles calculation with fine time steps Δt has produced a sequence $\alpha(i)$ and $W_{cyc}(i)$ of exponent and dissipation at time $i\Delta t$. We then construct an adaptive time stepping strategy with variable time steps $\Delta t_{ref}(j)$, reference exponent $\alpha_{ref}(j)$ and

dissipated energy $W_{ref}(j)$ by regrouping together adjacent time steps $\Delta t(i)$ with similar exponents $\alpha(i)$. This sequence is incremented as follows.

For $t_{ref}(j)$ and $\alpha_{ref}(j) = \alpha(t_{ref}(j))$ given, we set

$$\Delta t_{ref}(j) = \sum_{\substack{t(i) \geq t_{ref}(j) \\ \|\alpha(i) - \alpha_{ref}(j)\| \leq \Delta\alpha}} \Delta t,$$

$$t_{ref}(j+1) = t_{ref}(j) + \Delta t_{ref}(j).$$

The same goes for the dissipated energy:

$$\Delta W_{ref}(j) = \sum_{\substack{t(i) \geq t_{ref}(j) \\ \|\alpha(i) - \alpha_{ref}(j)\| \leq \Delta\alpha}} W_{cyc}(i),$$

$$W_{ref}(j+1) = W_{ref}(j) + \Delta W_{ref}(j).$$

We finally use these new time steps with corresponding α_{ref} and W_{ref} to update the damage by looping on all the following cycles with the new optimal time steps j and cycles N , and updating damage in each cycle by:

$$D = D + D^{\alpha_{ref}(j)} \frac{\Delta W_{ref}(j)}{W_0}, \quad (5.7.16)$$

with values $\alpha_{ref}(j)$ and $\Delta W_{ref}(j)$ precomputed in the first few cycles. This strategy is validated in Figure 5.9.

Complexity analysis

The optimal time step method clearly reduces the numerical cost. Typically, we assume the material has fatigue life of 1×10^6 cycles to failure and we implement 1000 time steps in unit cycle. The reduction factor of points in unit cycle for example as in Figure 5.9 equals $35/400 = 0.0875$. We can then compare the cost between full numerical strategy and the new one.

Full numerical strategy:	$1000 \text{ time steps} \times 1024 \text{ scales} \times 1 \times 10^6 \text{ cycles}$
Optimal cyclic strategy:	$1000 \text{ time steps} \times 1024 \text{ scales} \times 5 \text{ cycles until stabilization}$ + $1 \times 10^6 \text{ cycles} \times (1000 \text{ time steps} \times \text{reduction factor})$
Ratio between optimal and full:	$\approx \frac{\text{reduction factor}}{1024 \text{ scales}} = \frac{1}{11703}$

The same strategy is applied to random loading situations which are made of repeated sequence of random loads:

- calculation of dissipated energy and exponent on one sequence;
- time coarsening;
- repeated integration of damage through the different sequences using Eq.(5.7.16).

In such a strategy, the extra cost of introducing multiple scales in the calculation becomes negligible as compared to the time integration of damage in the evolution process.

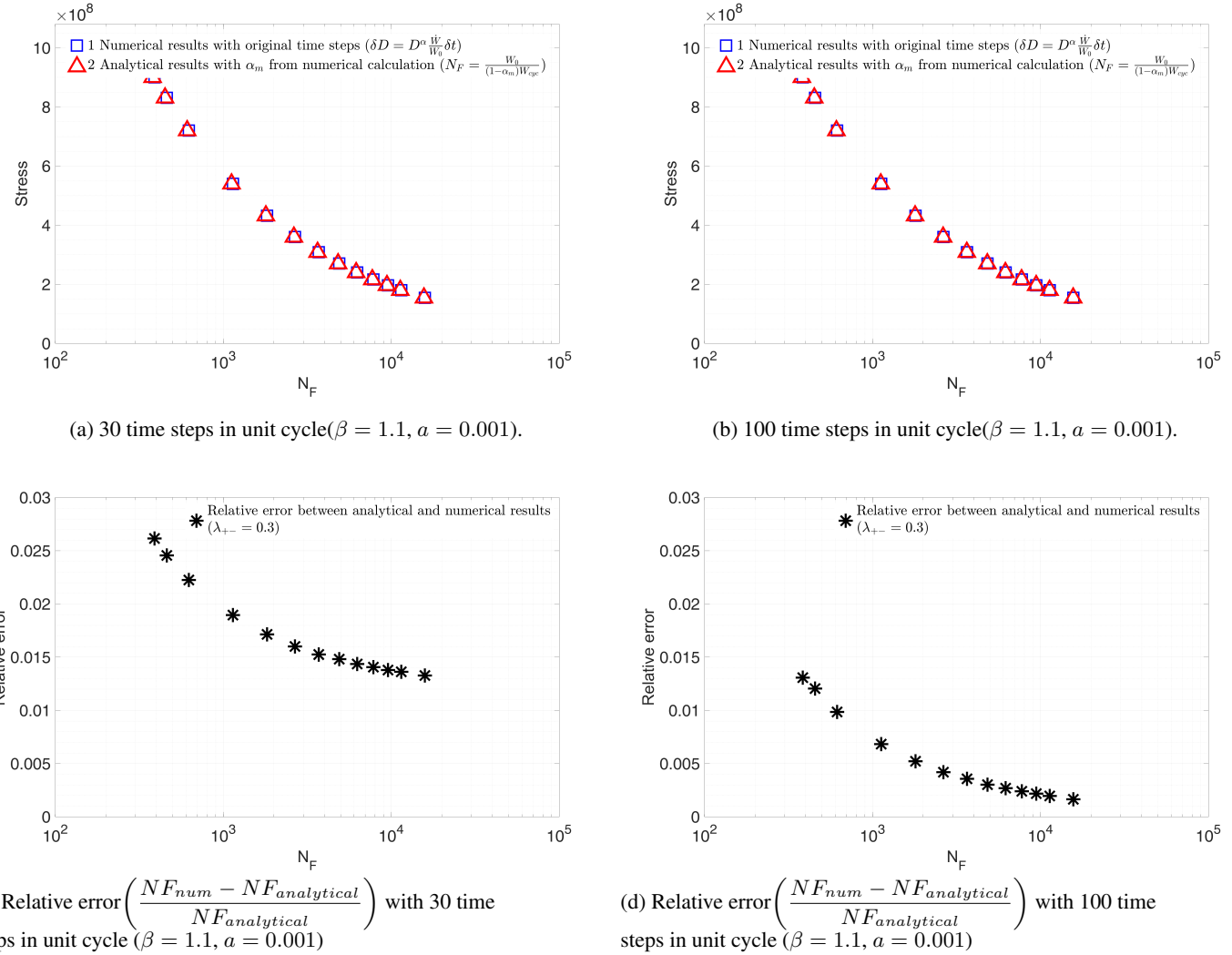


Figure 5.10 – S-N curve of bending test on 30NCD16 steel using numerical and analytical method (Eq.(5.7.15)) with different time steps. Data are those of table 5.1

Altogether, we have three numerical approaches for integrating damage.

1. Numerical results with varying α (equally divide time in unit cycle), and do the scale integration all along the fatigue life time, which can be of high numerical cost

$$\delta D = D^\alpha \frac{\dot{W}}{W_0} \delta t.$$

This method only serves for qualification purposes.

2. Numerical results with optimal time steps (equally divide α in unit cycle), here we have $\Delta\alpha = 0.01$, to reduce time steps needed, after several cycles adaptation we iterate using the recorded scalar values of α_{ref} , W_{ref} and t_{ref} to decide fatigue life time.

$$\delta D = D^{\alpha_{ref}} \frac{W_{ref}}{W_0} \delta t_{ref}.$$

3. Analytical results after integration of D (with mean alpha from numerical strategy)

$$N_F = \frac{W_0}{(1 - \alpha_m)W_{cyc}},$$

which is derived from the differential equation

$$\delta D = D^{\alpha_m} \frac{W_{cyc}}{W_0} \delta N.$$

Although method 2 is much more numerically efficient than the original numerical method 1, it is still not cheap in the experimental fitting process. We need the analytical formula method 3 to do the fitting process. To validate the feasibility, we now compare only the analytical (method 3) one and optimal time steps (method 2) one. The results are shown in Figure 5.11 and Figure 5.12, the relationship between relative error and $\Delta\alpha$ with 2000 time steps in unit cycle is shown in Figure 5.13 and Figure 5.14.

Now we can conclude that with more time steps in unit cycle, we get closer results with the original numerical method (method 2) in HCF regime. With smaller $\Delta\alpha$ value, we get less relative error between numerical (method 3) and analytical (method 1) results. This indicates that in constant amplitude cyclic loading, with moderate values of β it is feasible to use the analytical formula, given α_m is calculated using sufficient large time steps and small $\Delta\alpha$ in the first several cycles.

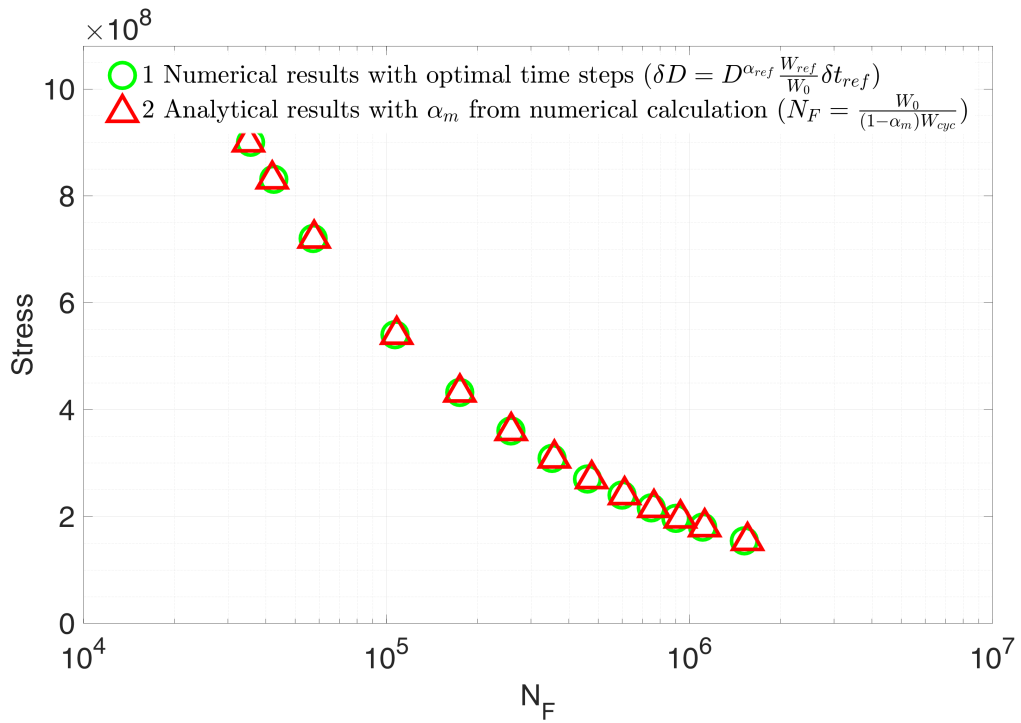


Figure 5.11 – S-N curve using analytical and numerical results with optimal time steps methods ($\beta = 1.1$, $a = 0.01$, $\Delta\alpha = 2E - 5$ in unit cycle), yielding 200 full time steps reduced to 197 optimal time steps

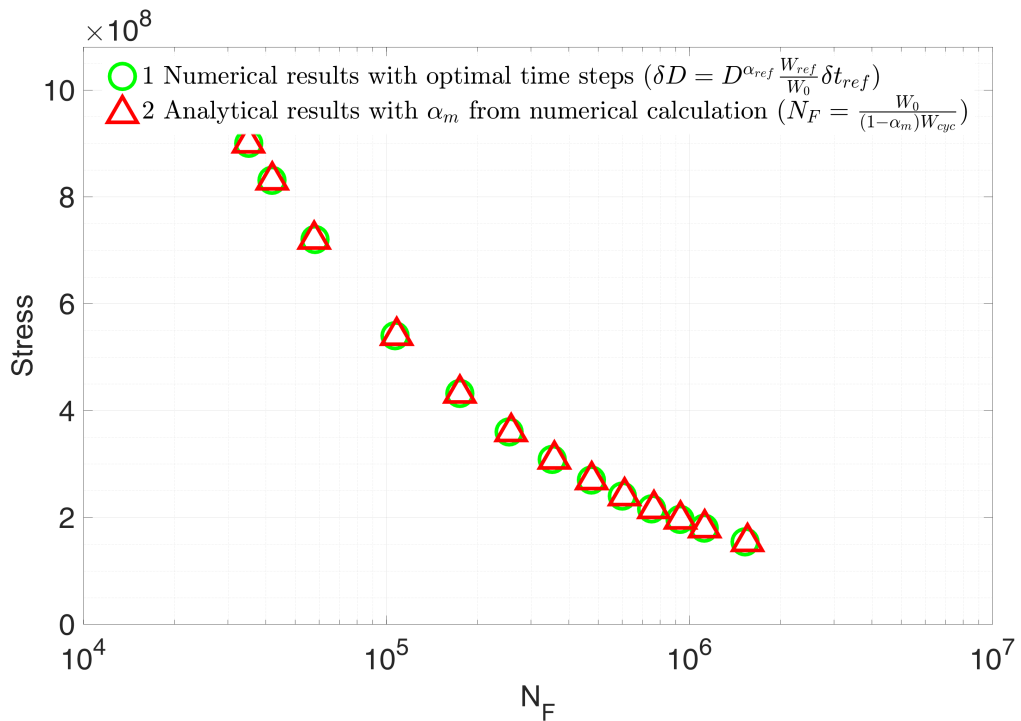


Figure 5.12 – S-N curve using analytical and numerical results with optimal time steps methods ($\beta = 1.1$, $a = 0.01$, $\Delta\alpha = 1E - 5$ in unit cycle), yielding 200 full time steps reduced to 199 optimal time steps

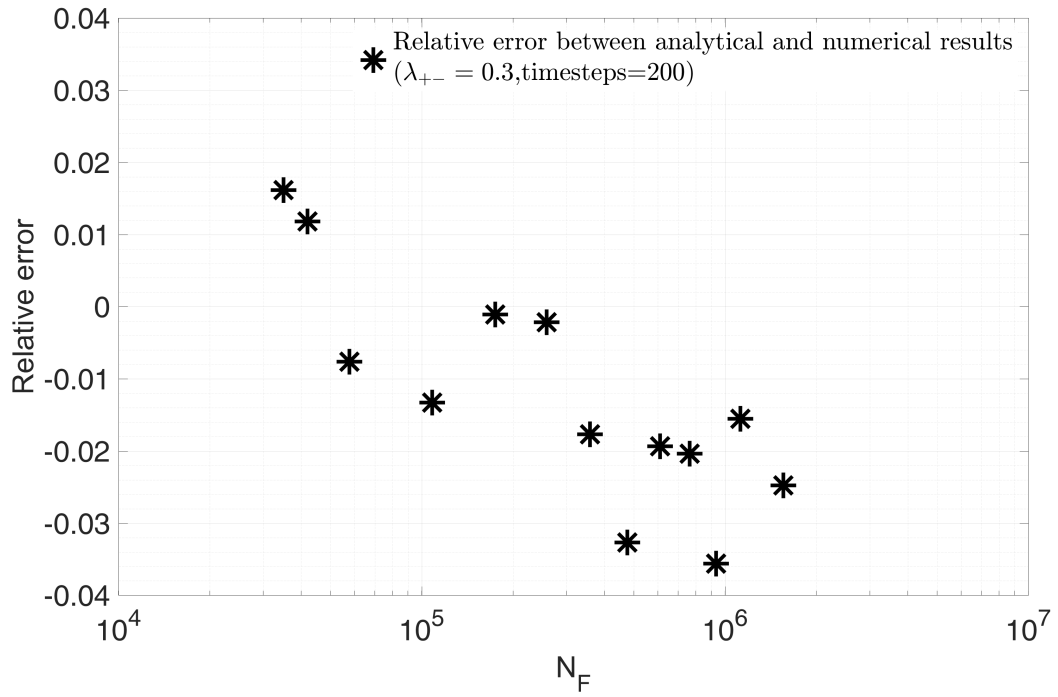


Figure 5.13 – Relative error $\left(\frac{NF_{opt} - NF_{analytical}}{NF_{analytical}} \right)$ between analytical and numerical results with optimal time steps methods ($\beta = 1.1$, $a = 0.01$, $\Delta\alpha = 2 \times 10^{-5}$ in unit cycle)

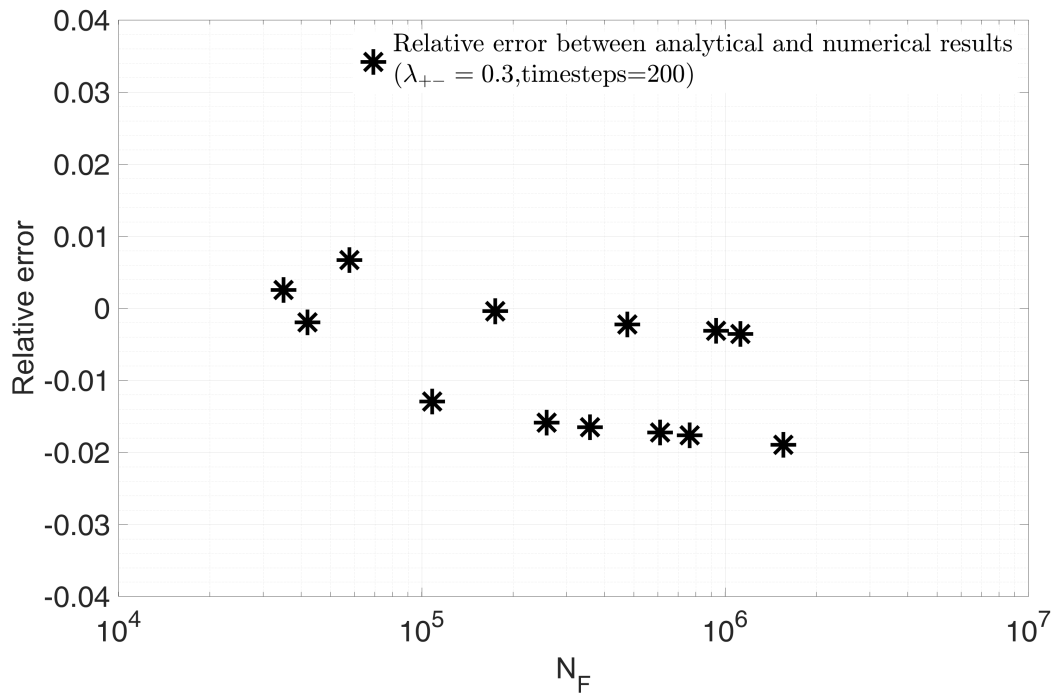


Figure 5.14 – Relative error $\left(\frac{NF_{opt} - NF_{analytical}}{NF_{analytical}} \right)$ between analytical and numerical results with optimal time steps methods ($\beta = 1.1$, $a = 0.01$, $\Delta\alpha = 1 \times 10^{-5}$ in unit cycle)

5.8 Validation on recovery tests

5.8.1 Recovery of Chaboche law on cyclic loading

The test is first performed on a sinusoidal uniaxial load $\Sigma_{11}(t) = A\sin(t)$, giving a deviatoric amplitude $S_a(t) = \sqrt{J_{2,a}(t)}$ so that $S_a(t) = \left\| \sqrt{\frac{1}{3}}\Sigma_{11}(t) \right\|$. We use parameters in Table 5.1 to recover the classic Chaboche law in cyclic loading.

Parameters	Value
Young's modulus	$E = 191 \text{ GPa}$
Hardening parameter	$k = 1 \text{ GPa}$
Weakening scales distribution exponent	$\beta = 1.5$
Hydrostatic pressure sensitivity	$\lambda_{+-} = 0.6$
Macroscopic yield stress	$\sigma_y = 1080 \text{ MPa}$
Sequencing effect sensitivity	$a = 0.1$
Dissipated energy to failure per unit volume	$W_0 = 5 \text{ MJ(MPa)}$

Table 5.1 – Material parameters in a simple cyclic load

We use matlab to numerically realize our method. The plot of $\|\underline{S} - \underline{b}\|_{trial}$ and $\|\underline{S} - \underline{b}\|$ during the first cycles at two different scales ($s_3 = 1.21$ and $s_{10} = 1.13$) are shown in Figure 5.15 and Figure 5.16. We use here a fixed value of λ ($\lambda_+ = \lambda_-$), thus the local yield limit is reduced in traction and increased in compression.

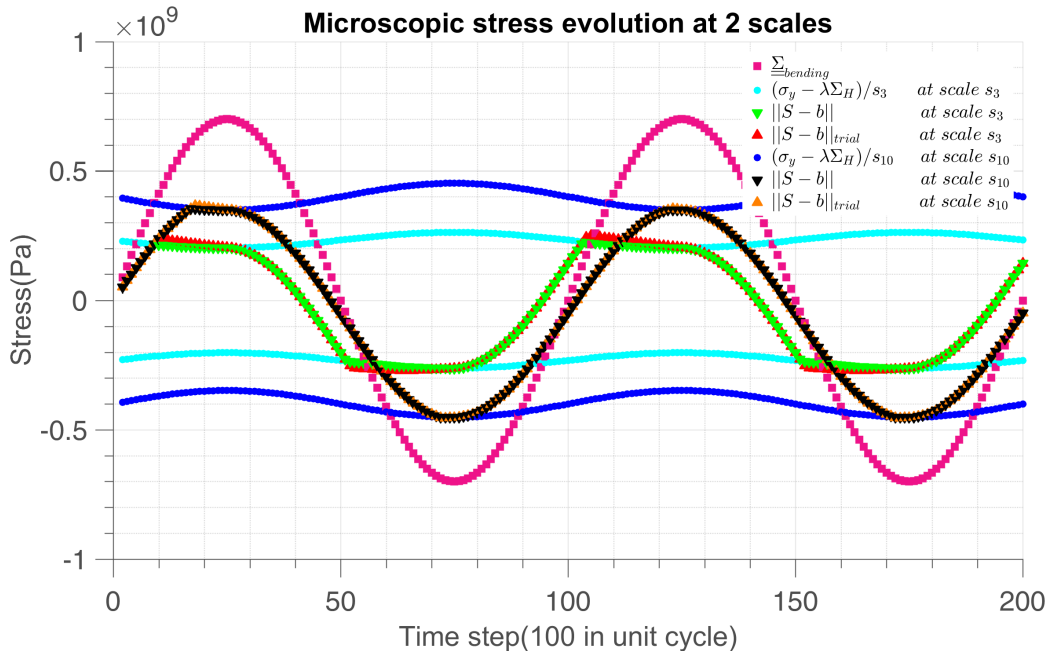


Figure 5.15 – Microscopic $(\underline{S} - \underline{b})_{trial}$ and $(\underline{S} - \underline{b})$ evolution with time under different weakening scales ($s_3 = 1.21$ and $s_{10} = 1.13$) in sinusoidal load with zero mean stress

The time history of dissipated energy is depicted in Figure 5.17. We scale S_a in the plot to see more clearly the relation between energy dissipation and stress intensity. The choice of α does not affect W ; it only concerns damage accumulation rate. Smaller α causes faster accumulation.

The “jump” in energy evolution is due to activation of new scales while in-between two scales the dissipated energy follows the stress increment at each time step. In other words, because in our

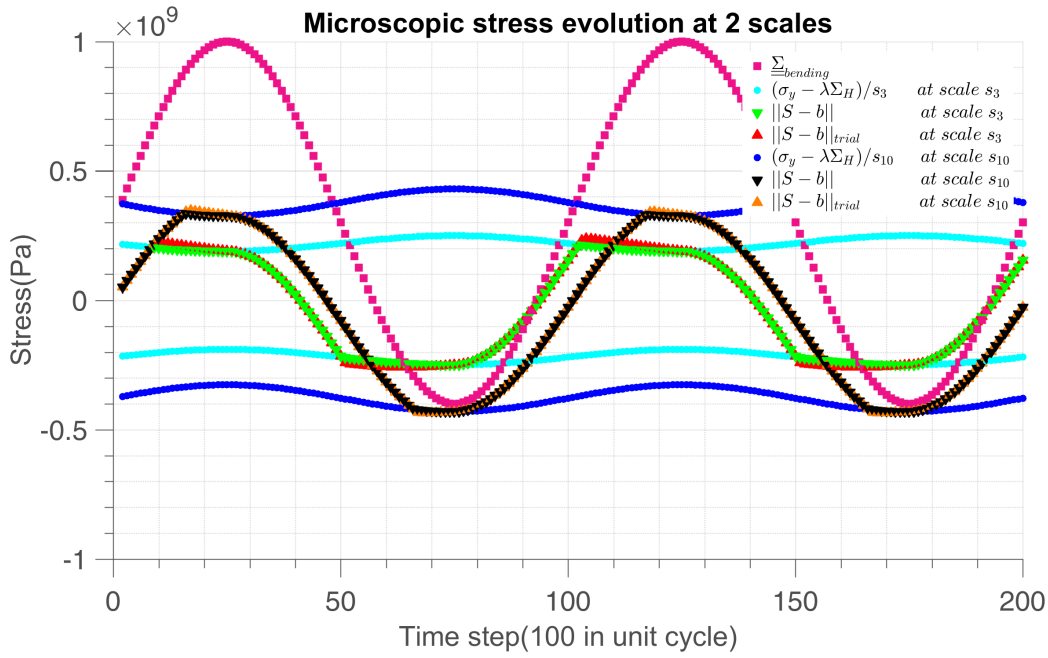


Figure 5.16 – Microscopic $(\underline{S} - \underline{b})_{trial}$ and $(\underline{S} - \underline{b})$ evolution with time under different weakening scales ($s_3 = 1.21$ and $s_{10} = 1.13$) in sinusoidal load with mean stress=300 MPa

method the dissipated energy W (Figure 5.17), sums energy dissipation at all scales, any additional violation of $\|\underline{S} - \underline{b}\|_{trial}$ at local yield limit (Figure 5.15) introduces an additional dissipation.

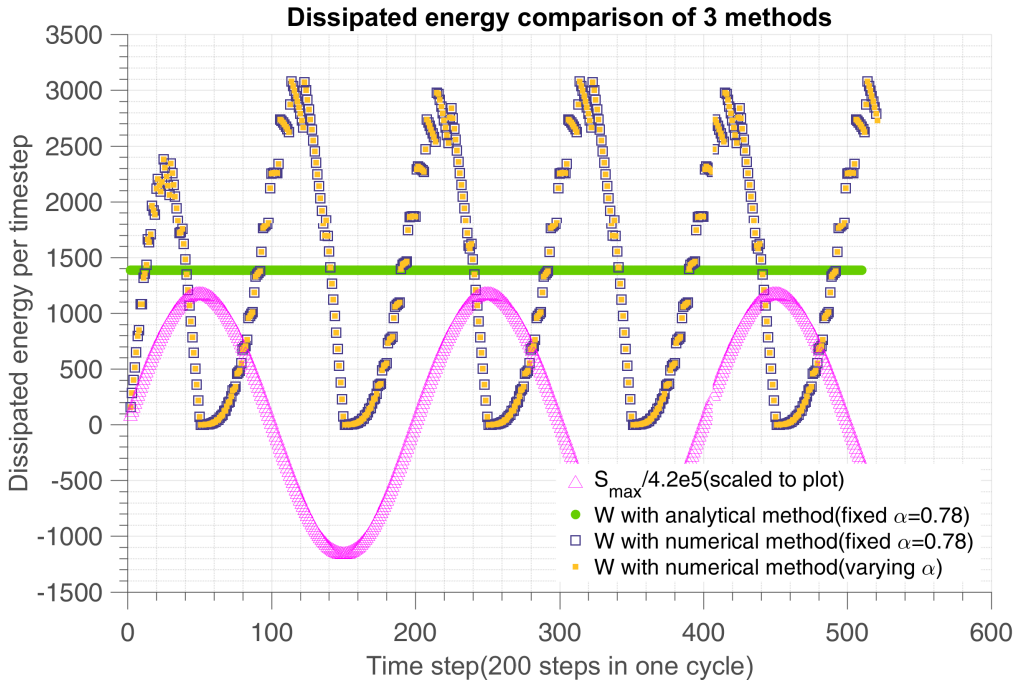


Figure 5.17 – Validation of dissipated energy in all scales with analytical (method 3) and numerical method (method 1) with $\beta = 1.1, \Sigma = 0.85\sigma_y$. The time evolution of α does not play a role in the dissipation calculation which is normal since α does not enter in the dissipation calculation

We take the mean value of α during all the iteration process of numerical method as α_m . The energy and damage accumulation is shown in Figure 5.19 and Figure 5.22. Here we give 100 time steps in one cycle to see the relative difference between changing α and α_m , also \dot{W} and $W_{cyc}/stepnumber$

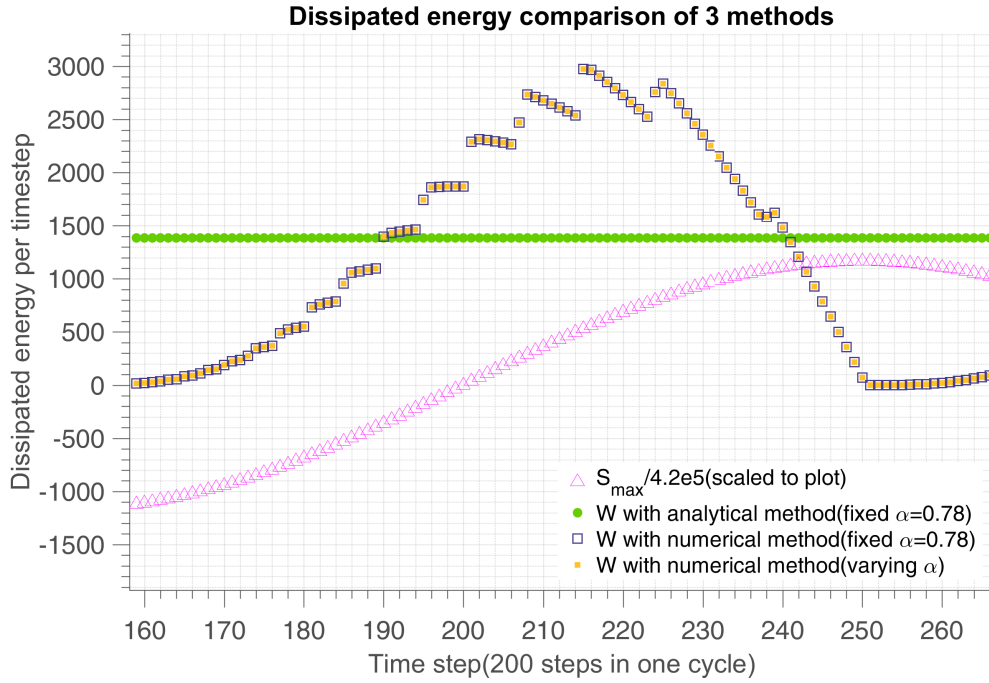


Figure 5.18 – Validation of dissipated energy in all scales with analytical and numerical method(enlargement of Figure 5.17)

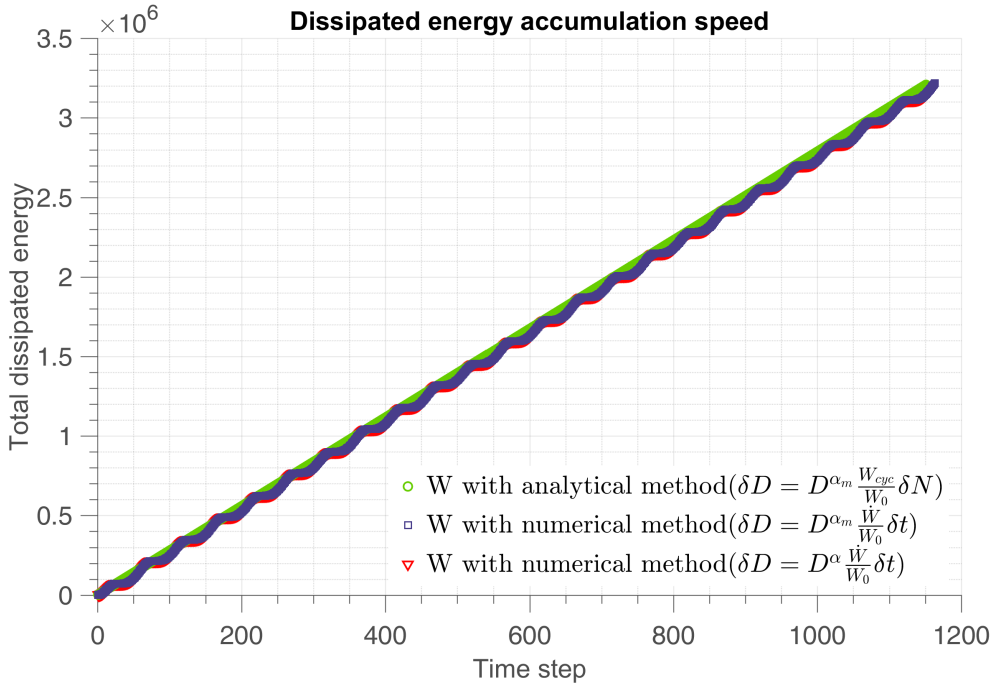


Figure 5.19 – Dissipated energy accumulation through time with different methods, there are 100 time steps in unit cycle

method. The more time steps we give, the more precision we get. The relative difference between analytical energy loss and numerical one is shown in Figure 5.21 from which we conclude that the three methods converge in terms of elastic energy dissipation, but due to nonlinear effects the damage evolution does not have the same history per cycle. The frozen α delays damage, the varying α increases damage during the phase of strong loading. The difference has a significant impact if damage

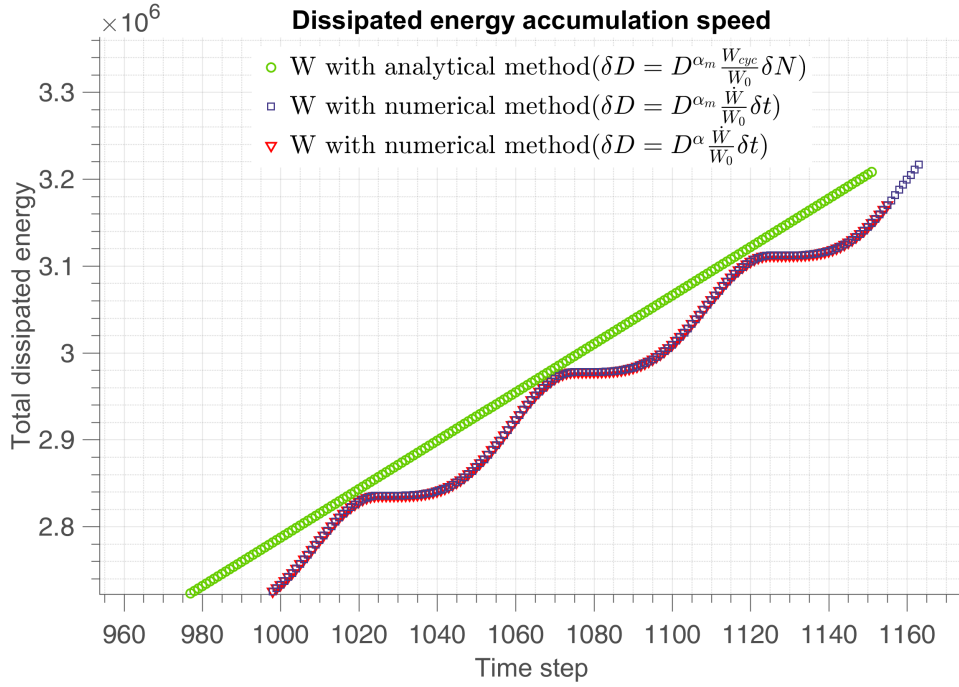


Figure 5.20 – Dissipated energy accumulation through time with of 3 methods(enlargement of Figure 5.19)

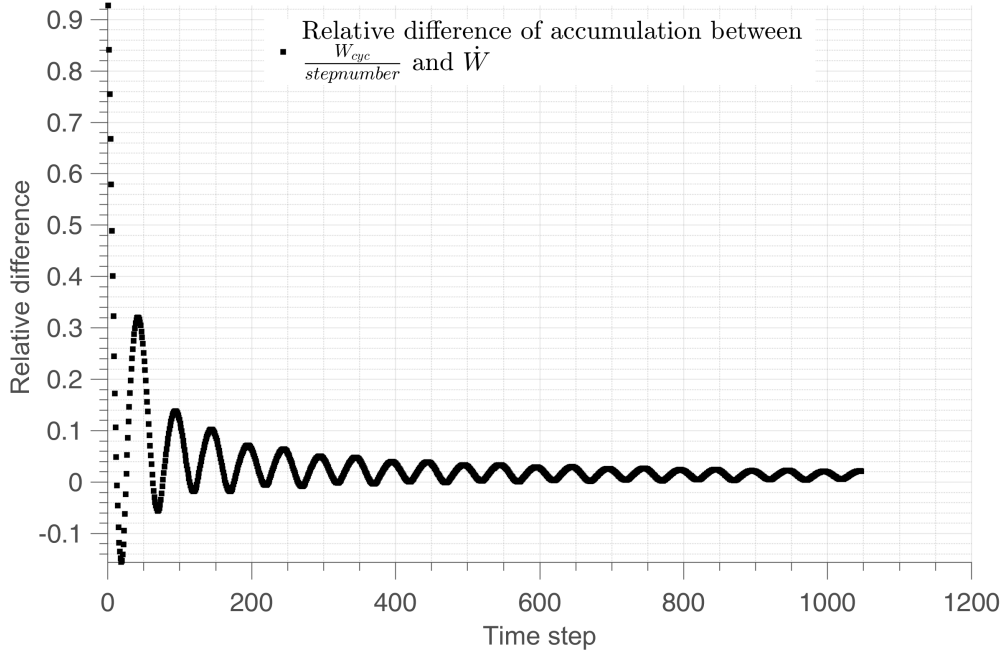


Figure 5.21 – Relative difference $\frac{W_{analytical} - W_{numerical}}{W_{analytical}}$ between analytical energy loss and numerical one with α varying with time of Figure 5.19

occurs with very few cycles. It will not when computing on a large number of cycles.

The cyclic load calculation is only valid for very simple such as proportional loading in fatigue. However, the convergence of the two methods is based on the small value of β (close to 1), in case of large values of β (typically around 5), the numerical strategy gives shorter life than the analytical one due to extreme non-linearity in the energy dissipation history per cycle. The relative error is around

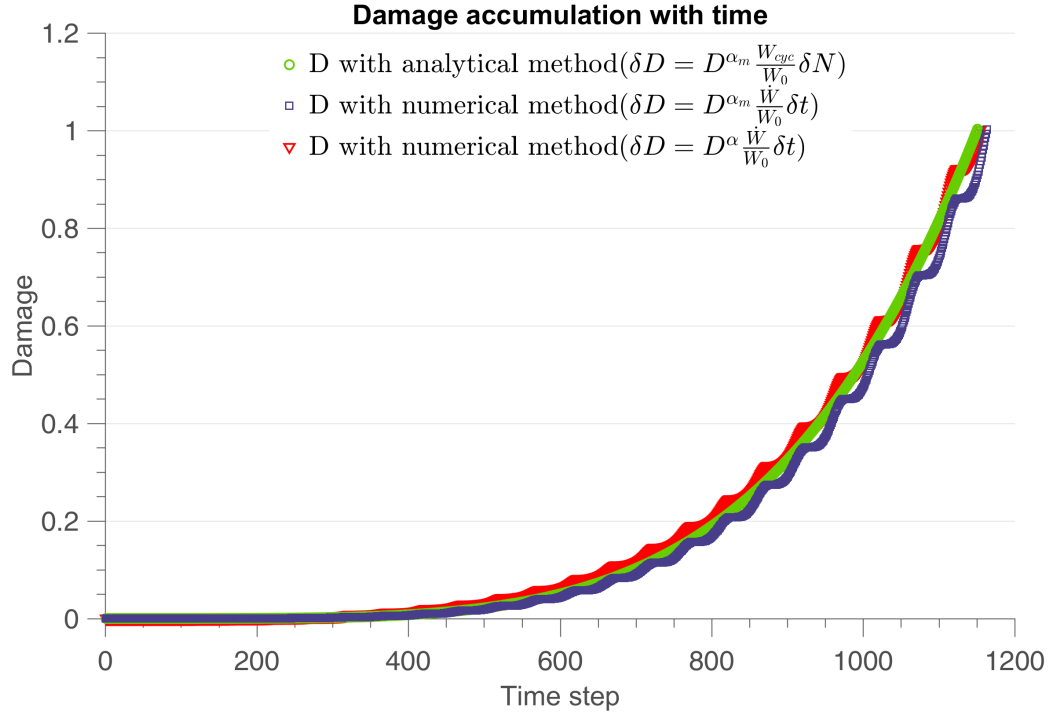


Figure 5.22 – Damage evolution with time under sinusoidal load with different methods, there are 100 time steps in unit cycle($\beta = 1.1, \Sigma = 0.85\sigma_y$)

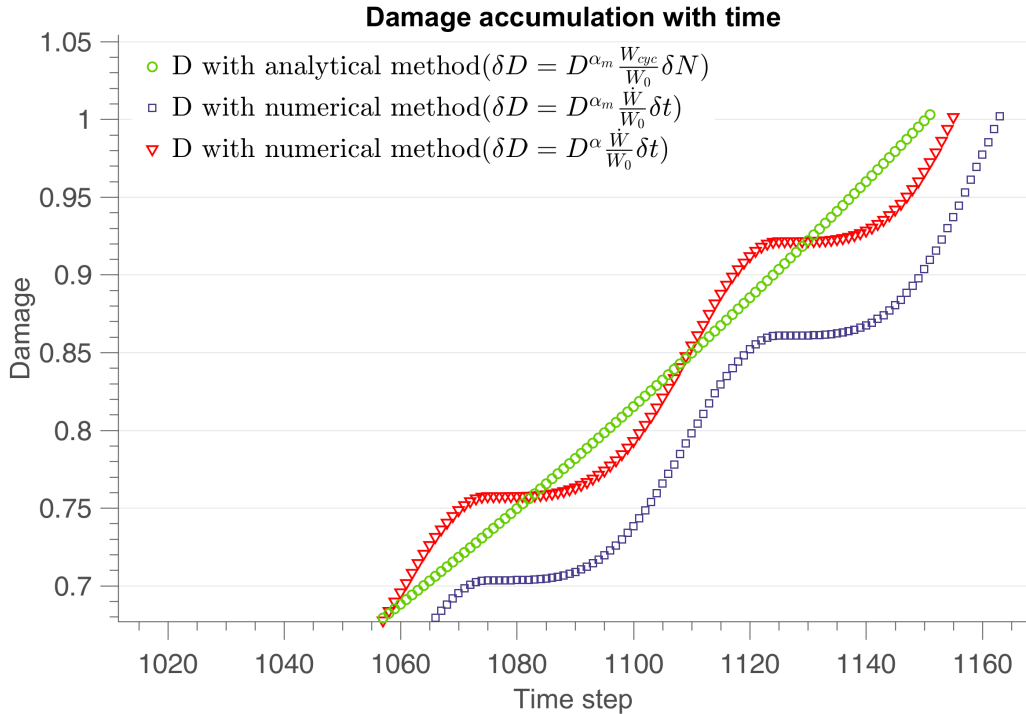


Figure 5.23 – Damage evolution with time under sinusoidal load with two different methods(enlargement of Figure 5.22)

20% as shown in Figure 5.25 and Figure 5.26. Nevertheless the analytical formula can still be used as a comparison group to verify the numerical results. And in the identification process we need the analytical form to fit the $S - N$ curve of a certain material. The outcome is satisfactory. Hence, to be

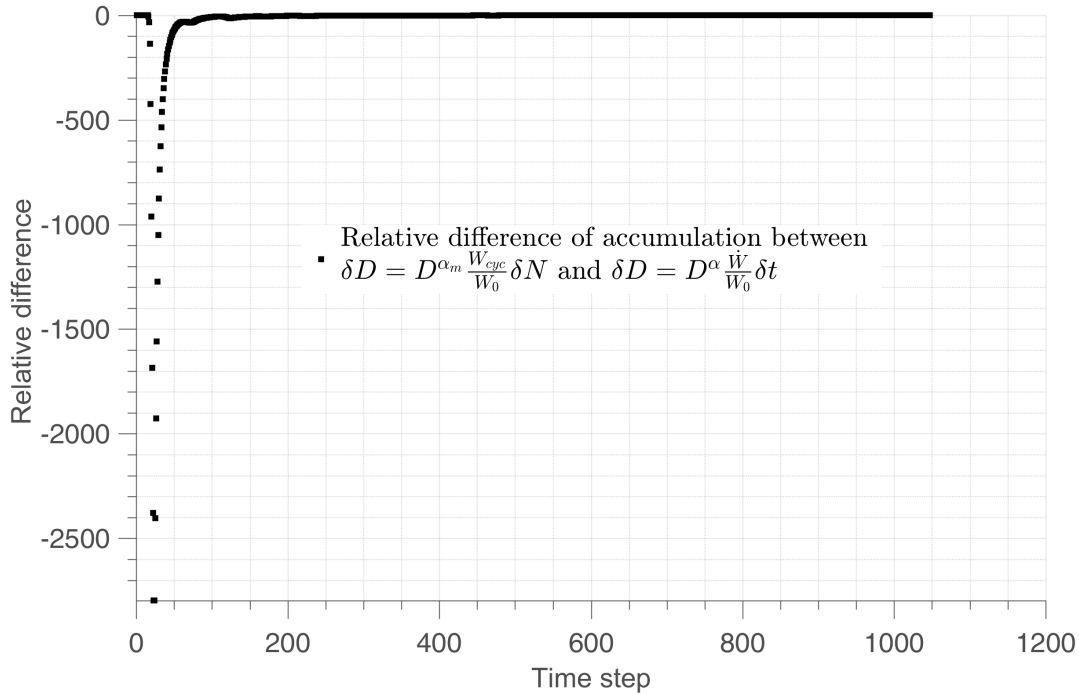


Figure 5.24 – Relative difference $\frac{D_{analytical} - D_{numerical}}{D_{analytical}}$ evolution with time of Figure 5.22

more general for any loading history, we adopt the numerical method after identification of β .

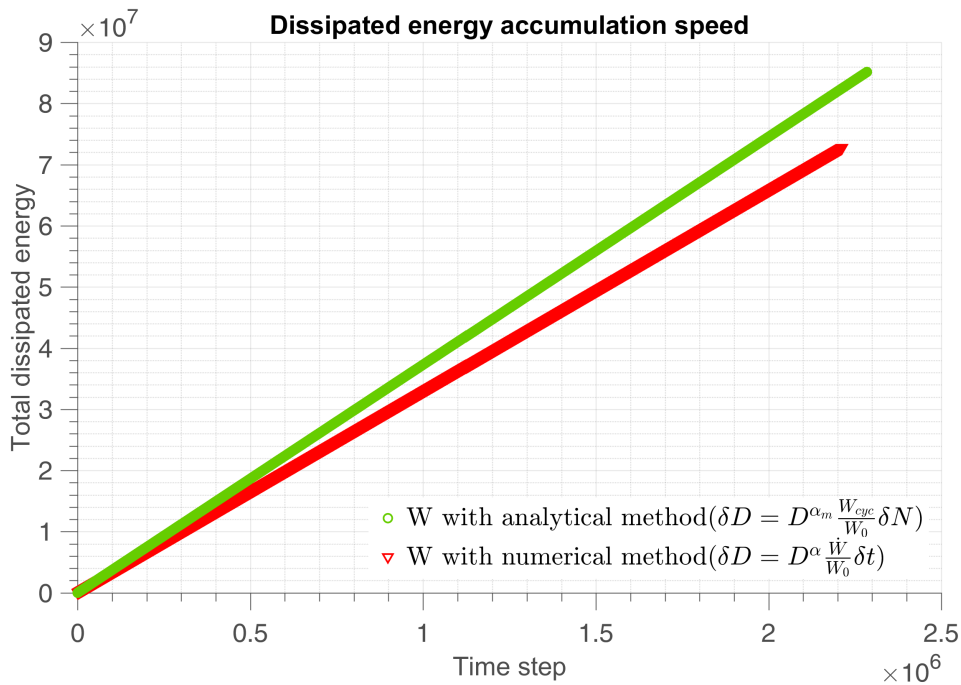


Figure 5.25 – Validation of dissipated energy in all scales with analytical and numerical method with $\beta = 5$, $\Sigma = 0.4\sigma_y$

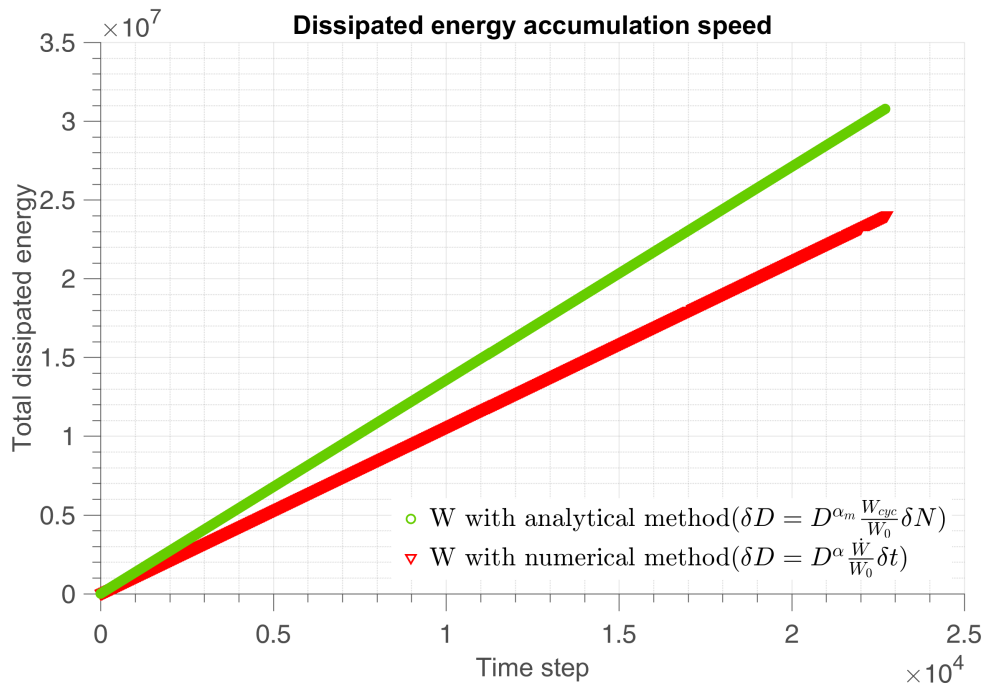


Figure 5.26 – Validation of dissipated energy in all scales with analytical and numerical method with $\beta = 5$, $\Sigma = 0.8\sigma_y$

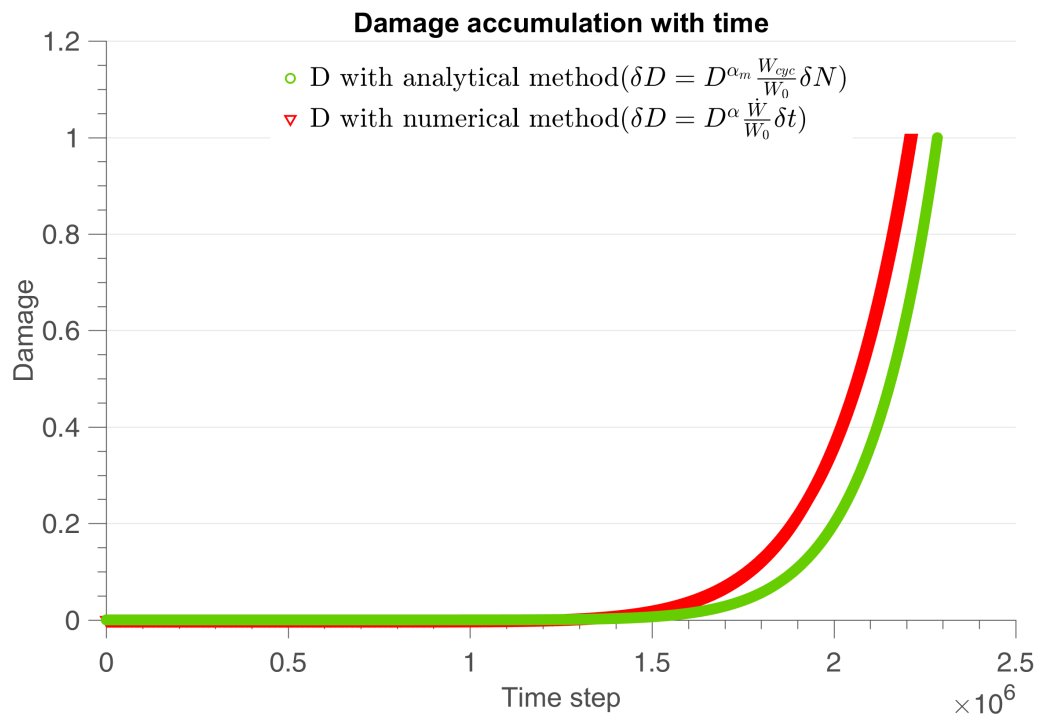


Figure 5.27 – Damage evolution with time under sinusoidal load with $\beta = 5$, $\Sigma = 0.4\sigma_y$. In such a severe loading and with extreme non-linearity, the simple Chaboche like formula with frozen α departs from the outcome of the full numerical model

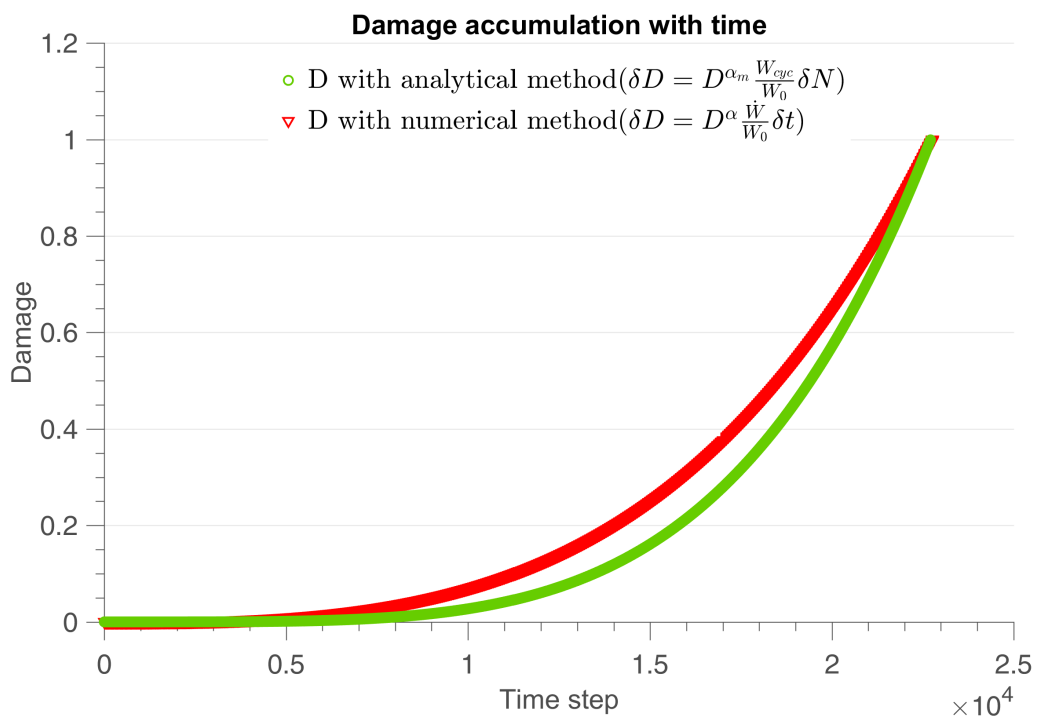


Figure 5.28 – Damage evolution with time under sinusoidal load with $\beta = 5$, $\Sigma = 0.8\sigma_y$

5.8.2 Numerical recovery of sequence effect

We adopt the parameter α to take into account the sequence effect. The high-low loading sequence clearly reduces the fatigue life, as depicted in Figure 5.29. In order to cover this phenomenon, we let α change with time ($\alpha = 1 - a (s_{min}(t) - 1)^{-f}$). Here a is the sequence effect sensitivity. According to Eq.(5.6.12), we have:

$$s_{min}(t) = \frac{\Sigma_y - \lambda \Sigma_H(t)}{S_a(t)},$$

which is the minimum weakening scale that activates energy loss. We use a general law for α of the type $\alpha = \alpha(s_{min})$ with the idea that for us s_{min} is a measure of present intensity of macroscopic stress. It is therefore a mechanical based stress norm. The impact of this construction of α can be seen on Figure 5.30, on a test case specifically built to illustrate such a sequence effect.

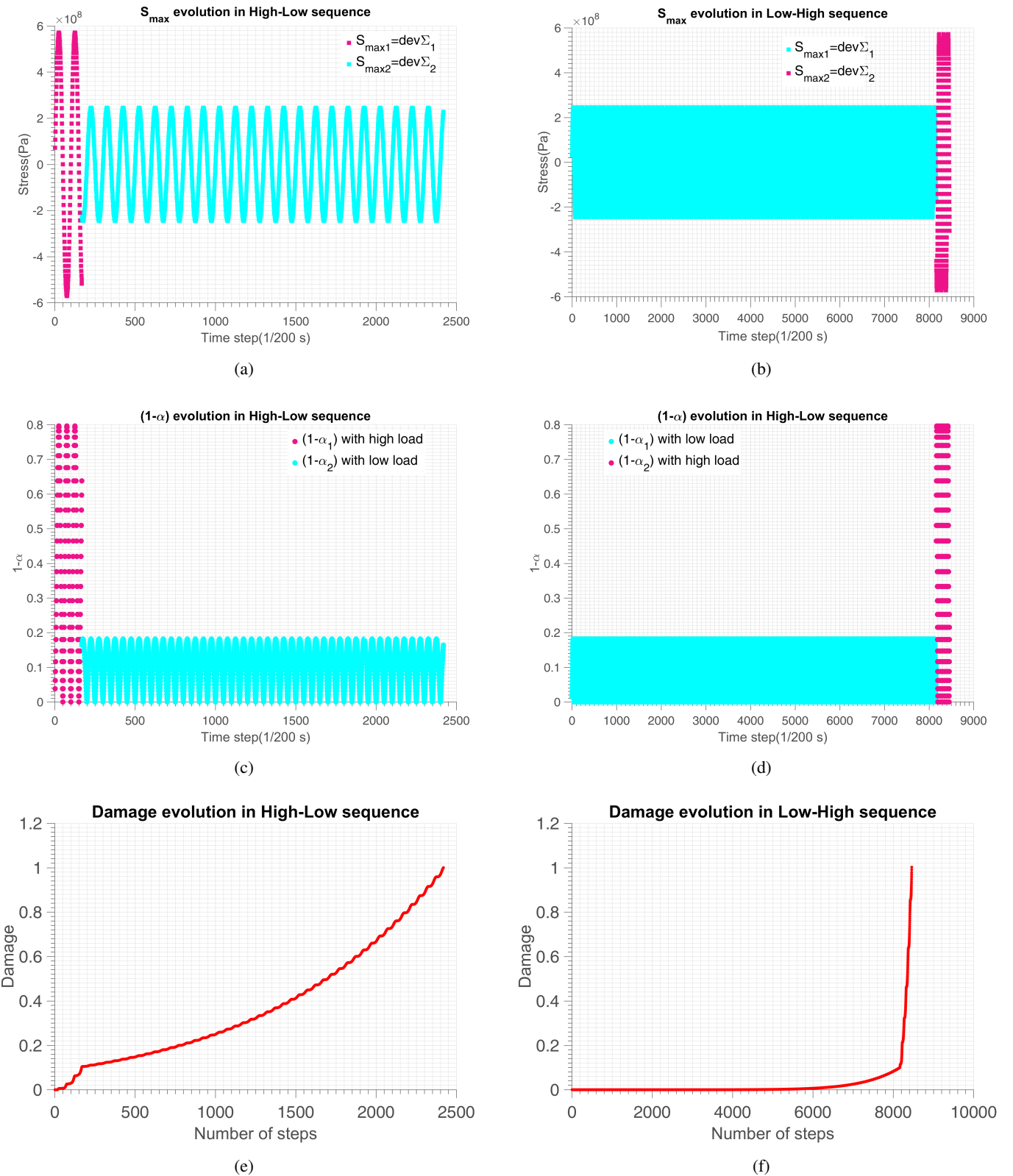


Figure 5.29 – Two level sequence effect. By comparing the vertical figures we can see high stress gives high $(1 - \alpha)$ value which causes fast damage accumulation speed. The evolution of $(1 - \alpha)$ is highly nonlinear and follows the value of stress at each time step.

Major damage effect

To see the influence of sequence effect factor of α , we first fix α for all tests to see the results. When α is fixed, it becomes denominator in the final expression of N_F (Eq.(5.6.6)) and has the same impact as W_0 . We find that the fatigue life of random loading is widely dispersed (Figure 5.30). In this case we need to use $\alpha = f(s_{min})$ which evolves with time to make large stress intensity bring more damage.

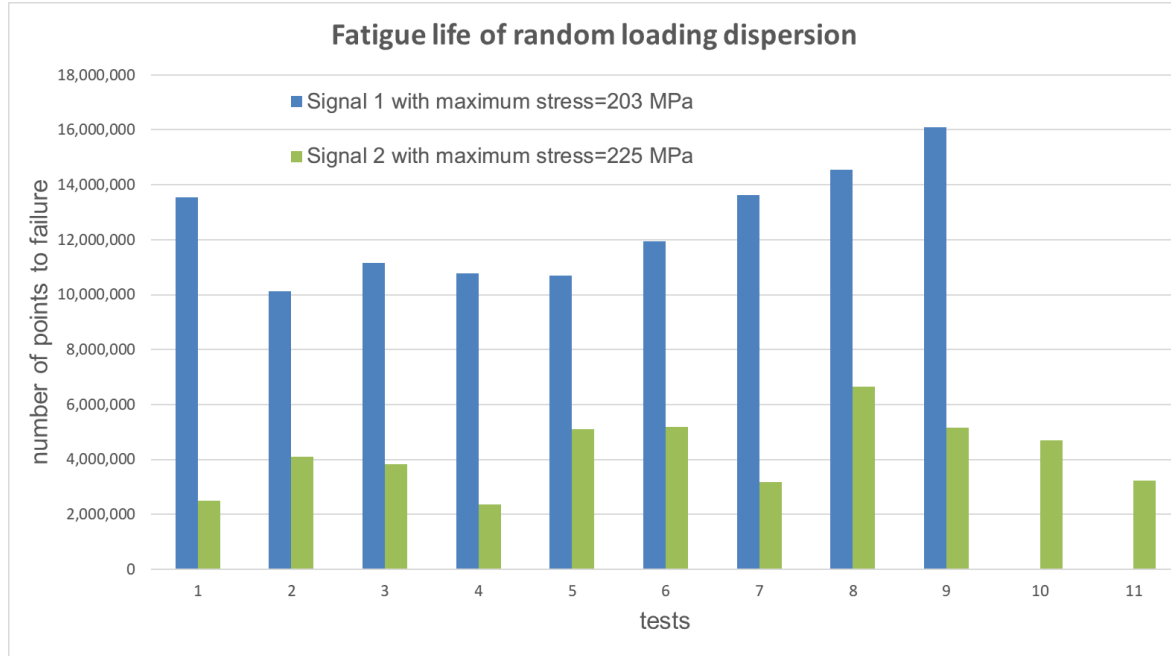


Figure 5.30 – Fatigue life of random loading dispersion

After comparison with the experimental data we find out that large stresses cause much more damage than the smaller ones. It is necessary to include this major stress induced damage to our stress intensity parameter α . With the new α used in Eq.(5.6.15) compared to Eq.(5.6.13) we are able to calibrate our model better with the experimental results by using

$$\alpha = 1 - a \left(\frac{\frac{1}{s_{min}}}{1 - \frac{1}{s_{min}}} \right)^f. \quad (5.8.1)$$

With $f = 1.1$, we use the power to magnify large stress impact and minify lower stress damage. The demonstration of major damage effect using magnification power is depicted in Figure 5.31. With larger value of power, the sequence effect is more significant (bigger dispersion between high-low and low-high sequence).

The larger value of S_a causes more damage in the presence of the power β , leading to faster increase of

$$(1 - \alpha) = a \left(\frac{\frac{1}{s_{min}}}{1 - \frac{1}{s_{min}}} \right)^f = a(s_{min} - 1)^{-f}.$$

which causes faster damage accumulation. We can also see this effect in Figure 5.32.

To assess large stress correctly we define the larger stress intensity as the value of stress which makes expression in the bracket in the second term of α greater than 1 ($\frac{1}{s_{min}(t) - 1} > 1$), then we use power β to magnify this term. In this way the damage is accelerated for large stresses. The

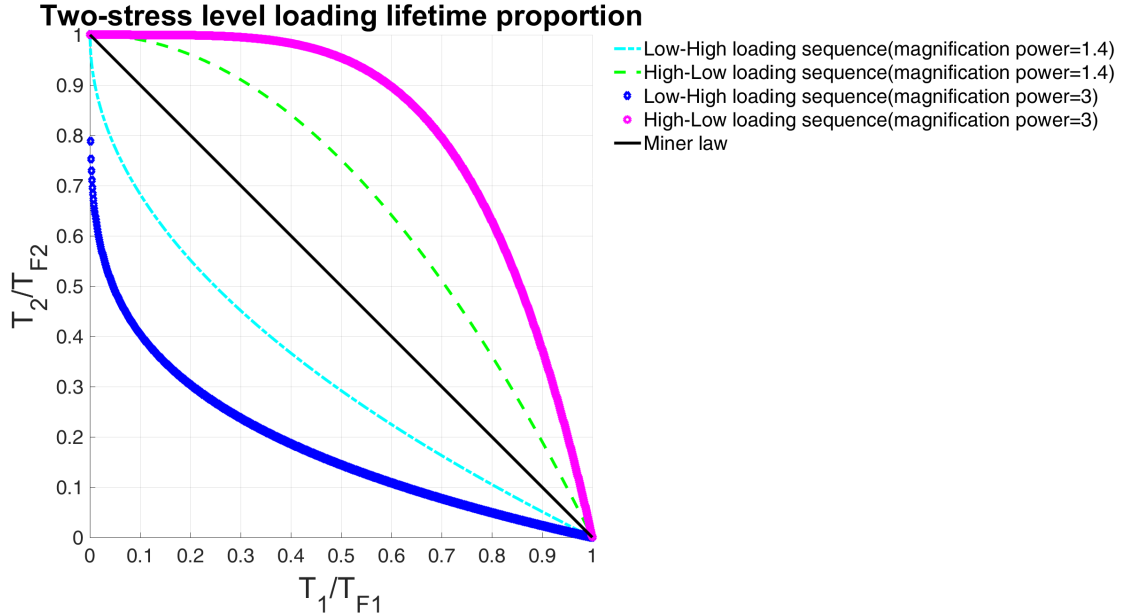


Figure 5.31 – Major damage effect using different magnification power of Eq.(5.8.1) on sequence effect. Here high stress is 1 MPa and low stress is 0.8 MPa. We see that using a large power f in Eq.(5.8.1) induces a stronger sequence effect.

deviatoric stress S_a , above which the damage is magnified, is determined from:

$$\alpha(t) = 1 - a \left(\frac{1}{s_{min}(t) - 1} \right)^{1.1},$$

$$s_{min}(t) = \frac{\Sigma_y - \lambda \Sigma_H(t)}{S_a(t)} < 2,$$

$$S_{large}(t) > \frac{\Sigma_y - \lambda \Sigma_H(t)}{2}.$$

The major damage effect can be seen in Figure 5.32, which occurs when S is more than half the macroscopic yield stress of the material.

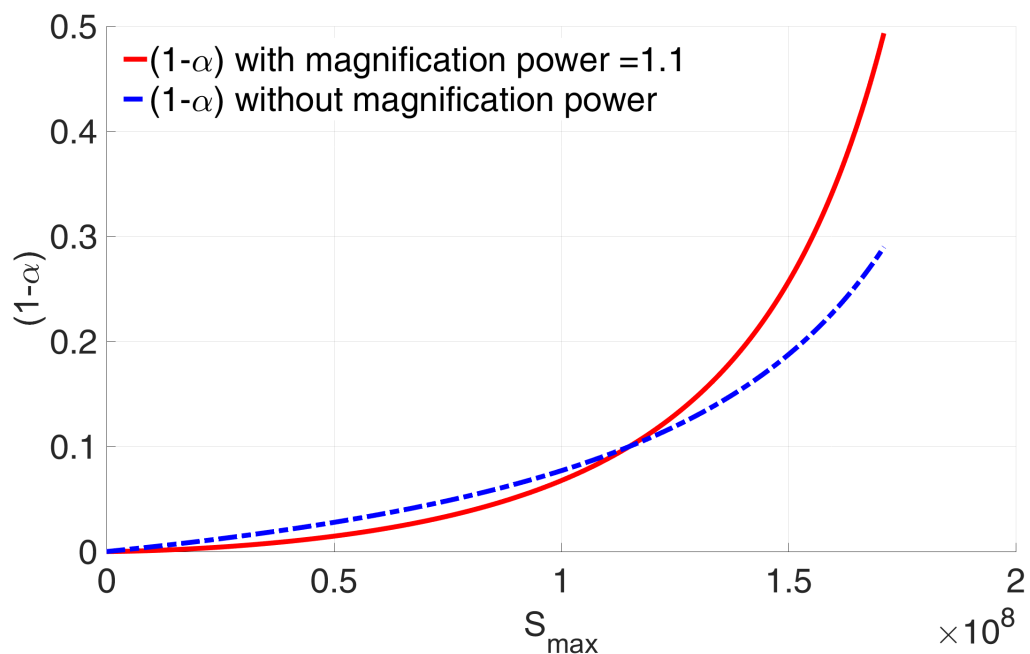


Figure 5.32 – $(1-\alpha)$ term which stands for the load intensity evolution, both with and without the magnification power f

5.9 Identification strategy

In our tests we keep $f = 1.1$ (justified in Chapter 6 by Figure 6.4 and Figure 6.5). The positive hydrostatic stress and negative one have different effect on the yield limit. It is necessary to adopt 2 parameters to describe this behavior. So we divide the hydrostatic sensitivity λ into 2 parts. λ_+ and λ_- . In the analytical formula, the amplitude of the stress intensity is adopted and the average value of tension hydrostatic stress(+) and compressive hydrostatic stress(-) is introduced.

For a good lifetime prediction, it is necessary to first identify the appropriate parameters of the model. For this purpose, we use the analytical formula Eq.(5.7.15) obtained in uniaxial cyclic loading case. With distinction of the hydrostatic stress in the presence of non-zero mean stress and since in fully reversed uniaxial loading we spend an equal time in compression and in traction, Eq.(5.5.2) now writes:

$$W_{cyc} = \frac{2(E - k)(1 + \nu)(\beta - 1)}{E(E + k\nu)\beta(\beta + 1)} \left[\frac{S_a^{\beta+1}}{(\sigma_y - \lambda_+ \bar{\Sigma}_{H+}(t))^{\beta-1}} + \frac{S_a^{\beta+1}}{(\sigma_y - \lambda_- \bar{\Sigma}_{H-}(t))^{\beta-1}} \right]. \quad (5.9.1)$$

$$N_{Fnum} = \frac{W_0}{(1 - \alpha)} \frac{E(E + k\nu)\beta(\beta + 1)}{2(E - k)(1 + \nu)(\beta - 1)} \frac{1}{\frac{S_a^{\beta+1}}{(\sigma_y - \lambda_+ \bar{\Sigma}_{H+}(t))^{\beta-1}} + \frac{S_a^{\beta+1}}{(\sigma_y - \lambda_- \bar{\Sigma}_{H-}(t))^{\beta-1}}}. \quad (5.9.2)$$

To use our analytical model Eq.(5.9.2) to fit the experiments, we employ Matlab Least-Squares (model fitting) algorithm.

The best fitted parameters in uniaxial cyclic loading case are deduced from the minimization of the sum of square of difference between uniaxial numerical and experimental results:

$$\min_{\beta, \lambda, W_0} \left\{ \sum_i (N_{Fnum} - N_{Fexp})^2 \right\} \quad (5.9.3)$$

Assume there are i sets of experimental data. To clarify the identification process, let us separate the parameters into:

- Experimental data: $S_{a(i)}$, $\Sigma_{H(i)}$, $N_{Fexp(i)}$, σ_y , E , k , ν .
- Material constants: β , λ_{+-} , W_0 (to be fitted)
- Input data from experimental data: $S_{max(i)}$, $\Sigma_{H(i)}$
- Input data from experimental data and parameter constants: $\alpha_{(i)}$
- Output data: $N_{Fnum(i)}$

In this process, σ_y , E , k and ν are given elastoplastic material constants. For each test (i), the load parameters are maximum amplitude $S_{a(i)}$, mean hydrostatic stress $\bar{\Sigma}_{H(i)}$, and the experimental number of cycles to failure is given by $N_{Fexp(i)}$.

The exponent $\alpha_{(i)}$ is cycle average obtained by

$$\alpha_{(i)} = \text{mean} \left[1 - a \left(\frac{1}{\frac{\Sigma_y - \lambda_{+-} \bar{\Sigma}_{H(i)}}{S_a(t)} - 1} \right)^{1.1} \right] (i). \quad (5.9.4)$$

The parameters to be calibrated are W_0 , β and λ . Since the exponent $\alpha_{(i)}$ depends on β and λ , we proceed iteratively by:

1. We first identify the S-N curve slope β and the energy scale W_0 using the analytical formula with torsion tests because there is no λ_{+-} impact in this kind of loading. We start from an initial guess β from which we can deduce $\alpha_{(i)}$ by numerical calculation of Eq.(5.9.4) and identify β and W_0 by least squares. Because our analytical formula is not derivable in all ranges, numerically when the identified value of β and its corresponding W_0 get stuck in a local minimum least square value, we regenerate a random β in its range so as to get the global optimal parameters.
2. Then, the parameter λ_+ are identified from numerical bending tests and we keep $\lambda_- = 0$. The final parameters correspond to the λ leading to the lowest identification error in β and W_0 . This strategy handles the nonlinearity in β and is well adapted to the low sensitivity in λ .

The analytical formula Eq.(5.9.2) with mean stress effect converges with the numerical method very well in the case of small β and λ_{+-} .

Parameter sensitivity analysis

The parameters we introduced during the deduction need to be calibrated. The source of the parameter identification are listed in Table.5.2. We perform a sensitivity analysis to see the influence of each parameter by comparing the results obtained respectively for the reference value, an upper bound and a lower bound of each parameter.

Parameters	Strategy
Hydrostatic pressure sensitivity λ_+	hydrostatic stress sensitivity (identified)
Non-linearity of damage accumulation a	amplification factor of load intensity (guessed)
Weakening scales distribution exponent β	to be calibrated (identified)
Dissipated energy to failure per defect W_0	energy scaling (identified)

Table 5.2 – Parameters concerned

We analyze the sensitivity of parameters separately as in Table.5.3 (uniaxial) and Table.6.4 (random loading). The parameter β has more influence on the random loading case because it acts not only as the S-N curve slope but also the power magnification factor of large stress intensity. The λ has little influence because both tests are conducted on very small or zero mean stress load history.

In Miner's law the parameter α is zero, the maximum value is below 1. For $\alpha = 1$ the damage accumulation line becomes flat and there will be unlimited lifetime. To keep α in the range of $[0, 1]$ where in random amplitude tests there is $S_a = 163.3$ MPa; we set the sensitivity of load intensity a to a maximum value of 0.29 to keep α positive.

The weakening scale distribution exponent(also the slope of S-N curve of the material) β ranges from 1 to 5. The hydrostatic pressure sensitivity λ is from positive mean stress test, which has the range of $0 \sim 0.8$. In constant amplitude cyclic loading, the dissipated energy to failure per defect W_0 (in MPa) is related to fatigue lifetime of the material.

Constant amplitude sensitivity test with $f(\beta) = \beta$							
	Ref	Min	Max	Ref_n	Min_n	Max_n	Sensitivity
β	1.1	1.05	1.50	414233	783723	243300	-3.19
λ_+	0.1	0.05	0.50	414233	449598	443376	0.00
W_0	3.27e8	1.00e8	5.00e8	414233	137498	687209	1.08
a	0.1	0.05	0.15	414233	672869	324754	-0.84

Table 5.3 – Example of parameters sensitivity at cyclic loading of BATCH_A_02 on AW-6106 T6 aluminum (table [6.2](#))

6

Numerical implementation and validation

6.1 Experimental verification

6.1.1 Introduction

The aim of this chapter is to validate the predictive model proposed. This consists in simulating tests available in the literature to determine the lifetime at initiation of crack by the application of the model and to compare these with the experimental lifetimes. The validation of the model involves a wide variety of metallic materials. The loads tested are of two types: cyclic loading of multiaxial stress of constant amplitude and repeated sequences of uniaxial stresses of variable amplitudes. The fatigue data of the materials used and the loads tested are taken from laboratory experiments or the literature.

6.1.2 Random amplitude 1D tests from Cetim on AW-6106 T6 aluminum

What makes automobile fatigue so difficult to predict is that, unlike standard tests done in a laboratory, an automobile's structure has to endure a complex, mostly random, set of static as well as cyclical stresses when in service. For example in Figure 6.1 which could represent load data from testing or measurement, extracting the cyclic information can be challenging.

As we mentioned before, the mean value of α depends on the loading pattern (sinusoidal, linear division points between max and min stresses in unit cycle,...), but our optimal time step numerical strategy is not loading pattern dependent because it equally divides the range of α during the load history, which means the variation amplitude of stress intensity. So in random loading case with only recorded maximum and minimum load history, we first divide linearly between every 2 recorded points into 100 time steps, and then perform numerical tests with optimal time step method.

The first tests are performed on aluminum batches, the characteristics of the sample are shown in Tab.6.1.

There are 12 validated uniaxial fatigue tests on the AW-6106 T6 aluminum sample, in which 2 are of constant amplitude load case and 10 involve random load case. The cyclic stress of test number 1 (BATCH_A_01) and test number 2 (BATCH_A_02) are respectively 131.9 MPa and 97.0 MPa. We first identify the parameters from these two tests.

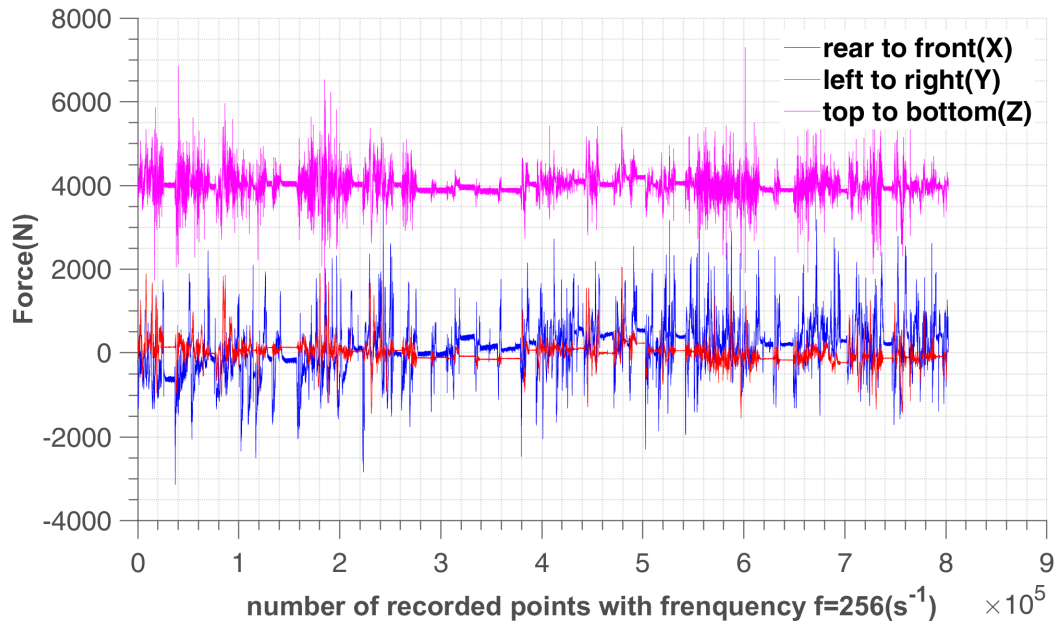


Figure 6.1 – Complex loading of a car suspension arm (data from PSA tests)

Specimen geometry for fatigue and corrosion fatigue tests ($t < 3.5$ mm):

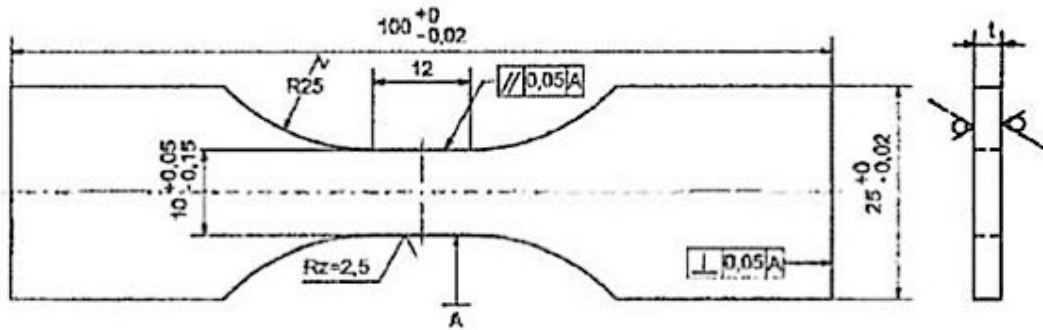


Figure 6.2 – Specimen geometry for fatigue tests of AW-6106 T6 aluminum (sample given by PSA)

Parameters	Value
Young's modulus	$E = 72$ GPa
Hardening parameter	$k = 8.5$ MPa
Macroscopic yield stress	$\sigma_y = 230$ MPa
Thickness	$e = 2.9$ mm
Width	$l = 9.95$ mm

Table 6.1 – Material parameters of AW-6106 T6 aluminum

The detailed tests information are shown in Tab.6.2. There are 27000 ($\pm 2.4\%$) recorded points per repetition.

We assume the material parameters like Young's modulus E , hardening parameter k , hydrostatic pressure sensitivity λ_+ (for $\bar{\Sigma}_H = 0$ in all cases), macroscopic yield stress σ_y and sequence effect sensitivity a are known. We first identify the weakening scales distribution β , and dissipated energy to failure W_0 from cyclic tests BATCH_A_01 and BATCH_A_02. Then fit the major damage effect

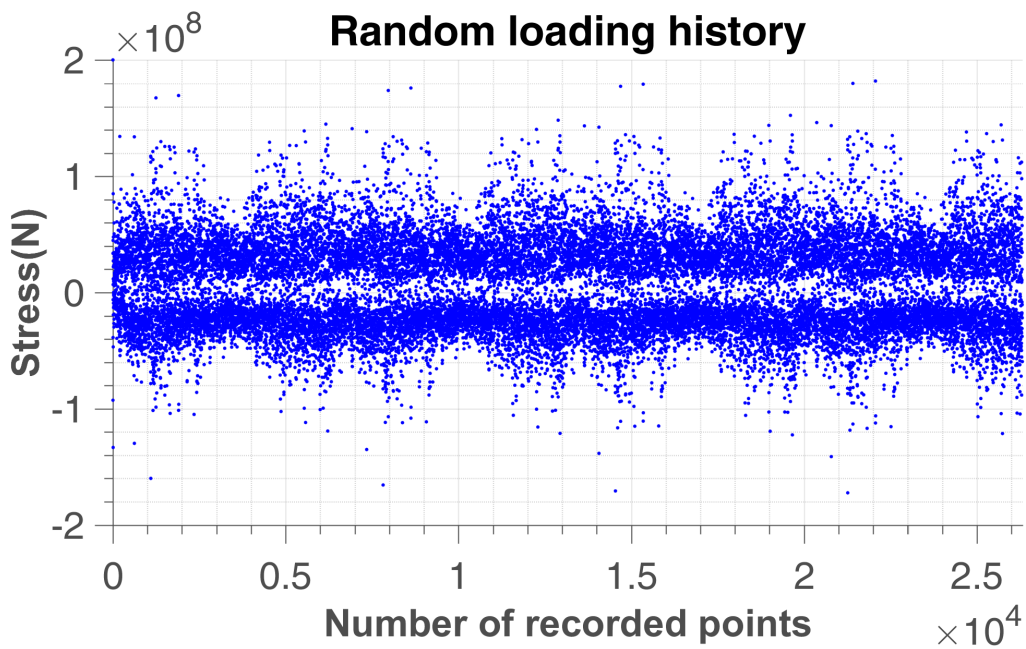


Figure 6.3 – Random loading history on BATCH_A_06 of AW-6106 T6 aluminum (see Tab.6.2)

Specimen	Fmax (kN)	Σ_{max} in the block	Number of repetition	Number of points
BATCH_A_01	3.375			99892
BATCH_A_02	2.475			414298
BATCH_A_04	nom	225.88	95	2500000
BATCH_A_05	nom	225.88	156	4105263
BATCH_A_06	nom	225.88	145	3815789
BATCH_A_07	nom	225.88	90	2368421
BATCH_A_08	nom	225.88	194	5105263
BATCH_A_09	nom	225.88	197	5184211
BATCH_A_10	nom x 0,9	203.292	515	13552632
BATCH_A_11	nom x 0,9	203.292	385	10131579
BATCH_A_12	nom x 0,9	203.292	424	11157895
BATCH_A_13	nom x 0,9	203.292	409	10763158
BATCH_B_01	nom	225.88	121	3184211
BATCH_B_02	nom x 0,8	180.704	380	10000000
BATCH_B_03	nom x 0,8	180.704	380	10000000
BATCH_B_04	nom x 0,9	203.292	406	10684211
BATCH_B_05	nom x 0,9	203.292	454	11947368
BATCH_B_06	nom x 0,9	203.292	518	13631579
BATCH_B_07	nom x 0,9	203.292	553	14552632
BATCH_B_08	nom x 0,9	203.292	612	16105263
BATCH_B_09	nom	225.88	253	6657895
BATCH_B_10	nom	225.88	196	5157895
BATCH_B_11	nom	225.88	178	4684211
BATCH_B_12	nom	225.88	123	3236842

Table 6.2 – Fatigue tests result on AW-6106 T6 aluminum, test data provided by CETIM

parameter f to see if our assumption is correct or need to be changed.

The numerical fitting process show that the damage is caused mainly by large stresses (see later). The definition of major stress which affects the value of α now needs to be specified according to the material. To take into account this effect we first find out the proportion stress above a certain value in the repetition signal of random loading, as shown in Tab.6.3. Here BATCH_A and BATCH_B are the same material. Since the samples were extracted from aluminum profiles of industrial products, the two batches correspond to two different times of sampling in the production. The variation is supposed to be representative of the regular tolerances you might have in the production. BATCH_A_01 and BATCH_A_02 are constant amplitude loading which helps identify the power of weakening scale distribution β . BATCH_A_03 is low cycle fatigue data. BATCH_B_02 and BATCH_B_03 have infinite life time. The data in the table are grabbed from random signal high cycle fatigue loading history.

Σ_a (MPa)>	70	90	110	130	150	170	190
S_a (MPa)>	57.15	73.48	89.81	106.14	122.47	138.80	155.13
BATCH_A_04	1.962%	0.904%	0.077%	0.037%	0.018%	0.007%	
BATCH_A_05	1.604%	0.784%	0.044%	0.030%	0.007%	0.007%	
BATCH_A_06	1.645%	0.784%	0.045%	0.030%	0.007%	0.007%	
BATCH_A_07	1.632%	0.788%	0.048%	0.029%	0.007%	0.007%	
BATCH_A_08	1.644%	0.787%	0.048%	0.037%	0.007%	0.007%	
BATCH_A_09	1.655%	0.800%	0.048%	0.037%	0.007%	0.007%	
BATCH_A_10	0.768%	0.134%	0.007%	0.000%	0.000%	0.000%	
BATCH_A_11	0.772%	0.145%	0.007%	0.000%	0.000%	0.000%	
BATCH_A_12	0.779%	0.133%	0.011%	0.000%	0.000%	0.000%	
BATCH_A_13	0.775%	0.141%	0.007%	0.000%	0.000%	0.000%	
BATCH_B_01	4.739%	1.737%	0.840%	0.224%	0.049%	0.034%	0.004%
BATCH_B_04	1.999%	0.745%	0.156%	0.034%	0.004%	0.000%	0.000%
BATCH_B_05	2.010%	0.749%	0.148%	0.034%	0.008%	0.000%	0.000%
BATCH_B_06	1.999%	0.790%	0.118%	0.034%	0.008%	0.000%	0.000%
BATCH_B_07	2.029%	0.756%	0.152%	0.034%	0.008%	0.000%	0.000%
BATCH_B_08	1.999%	0.737%	0.137%	0.034%	0.008%	0.000%	0.000%
BATCH_B_09	4.663%	1.687%	0.798%	0.205%	0.049%	0.034%	0.004%
BATCH_B_10	4.712%	1.744%	0.809%	0.224%	0.046%	0.034%	0.004%
BATCH_B_11	4.636%	1.664%	0.790%	0.209%	0.049%	0.034%	0.004%
BATCH_B_12	0.775%	0.141%	0.007%	0.000%	0.000%	0.000%	0.000%

Table 6.3 – Proportion of stress above different thresholds with $\Sigma_y=230$ MPa, test data provided by CETIM on AW-6106 T6 aluminum.

Random amplitude sensitivity test with $f(\beta) = \beta$						
Ref	Min	Max	Ref_n	Min_n	Max_n	Sensitivity
β	1.1	1.05	1.50	4220452	7469257	1799585
λ	0.1	0.05	0.50	4220452	4566335	2175991
W_0	3.27e8	1.00e8	5.00e8	4220452	1321761	6420810
a	0.1	0.05	0.15	4220452	7156622	2827894

Table 6.4 – Parameters sensitivity at random loading of ep05 on AW-6106 T6 aluminum

From Tab.6.5 and Tab.6.6 we can see f has positive correlation with β in high cycle fatigue which is the regime we focus on. However, very large value of f may ignore the small stress variations in the loading history, which goes against our assumption that small stresses also contribute to material damage. So we give $f = 1.1$ in high cycle random loading case to minimize the relative error. The

Constant amplitude sensitivity test with $f(\beta) \neq \beta$							
Ref	Min	Max	Ref_n	Min_n	Max_n	Sensitivity	
β	1.1	1.05	1.50	414233	797377	213682	-3.44
λ	0.1	0.05	0.50	414233	449598	443376	0.00
W_0	3.27e8	1.00e8	5.00e8	414233	137498	687209	1.08
a	0.1	0.05	0.15	414233	672869	324754	-0.84
$f(\beta)$	1.1	1.05	1.5	414233	441661	511644	0.41

Table 6.5 – Parameters sensitivity at cyclic loading of ep02 on AW-6106 T6 aluminum

Random amplitude sensitivity test with $f(\beta) \neq \beta$							
Ref	Min	Max	Ref_n	Min_n	Max_n	Sensitivity	
β	1.1	1.05	1.50	4220452	7254554	2472791	-2.77
λ	0.1	0.05	0.50	4220452	4566335	2175991	-0.13
W_0	3.27e8	1.00e8	5.00e8	4220452	1321761	6420810	0.99
a	0.1	0.05	0.15	4220452	7156622	2827894	-1.03
$f(\beta)$	1.1	1.05	1.5	4220452	4341560	3052299	-0.75

Table 6.6 – Parameters sensitivity at random loading of ep05 on AW-6106 T6 aluminum

sensitivity of parameters is calculated by dividing the percentage of variation of number of points to failure with respect to the reference number of points to failure, by the percentage of variation of parameter with respect to the reference parameter, as shown in Eq.(6.1.1).

$$sensitivity = \frac{(Max_n - Min_n) / Ref_n}{(Max - Min) / Ref}. \quad (6.1.1)$$

After the fitting process, the reference parameters value we use are in Tab.6.7.

Constant α	W_0 (MPa)	$\lambda_+ = \lambda_-$	β	α	f
	326.9	0.1	1.1	0.7	1.1
Changing α	W_0 (MPa)	$\lambda_+ = \lambda_-$	β	α	f
	326.9	0.1	1.1	0.1	1.1

Table 6.7 – The parameters in 1D cyclic and random loading on AW-6106 T6 aluminum fatigue tests by Cetim

The best fitted results with constant α are shown in Figure 6.4. The dispersion is relatively large. In conclusion, we are not able to predict the random stress amplitude fatigue life with fixed α , because random stresses not only cause different energy dissipations, but also show a distinctive load sequence effect. So we have to update the value of α at each time step.

We can find that the numerical results are satisfactory when we introduce a major damage influence through the construction of a load dependent α . The dispersion figure with distinction of major damage is depicted in Figure 6.5. Here it is necessary to control the parameter a to make sure $\alpha > 0$ in the most severe situation.

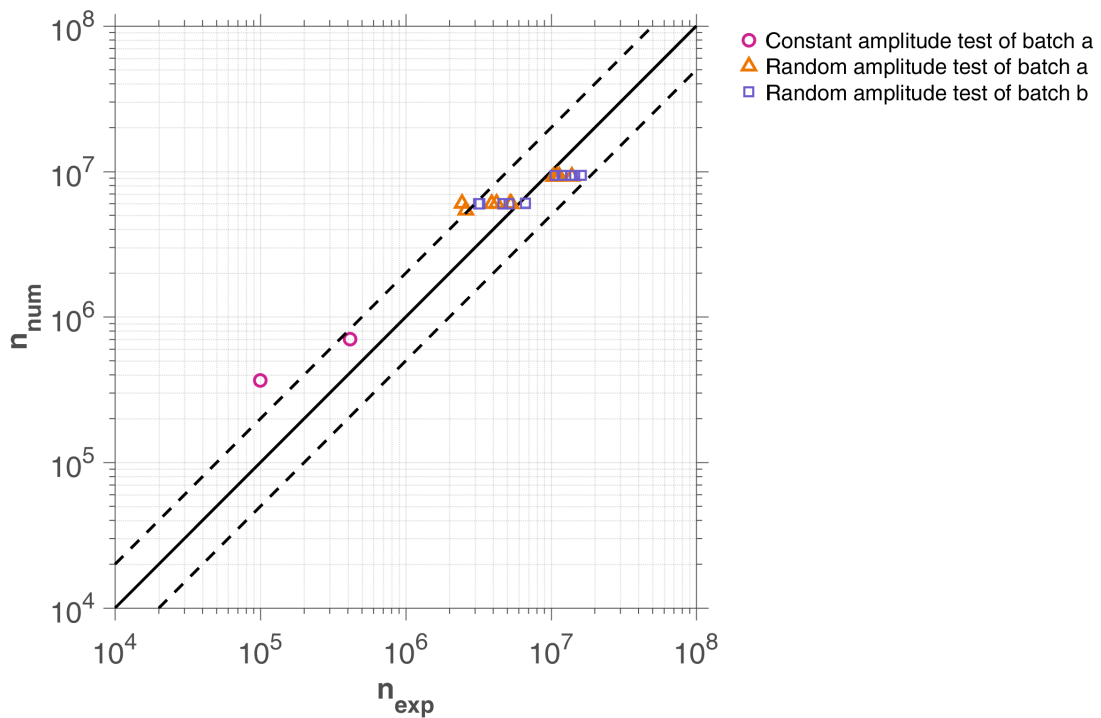


Figure 6.4 – Comparison between experimental and numerical results of 1D cyclic and random loading on aluminum fatigue tests by CETIM with constant α from the first row of Tab.6.7

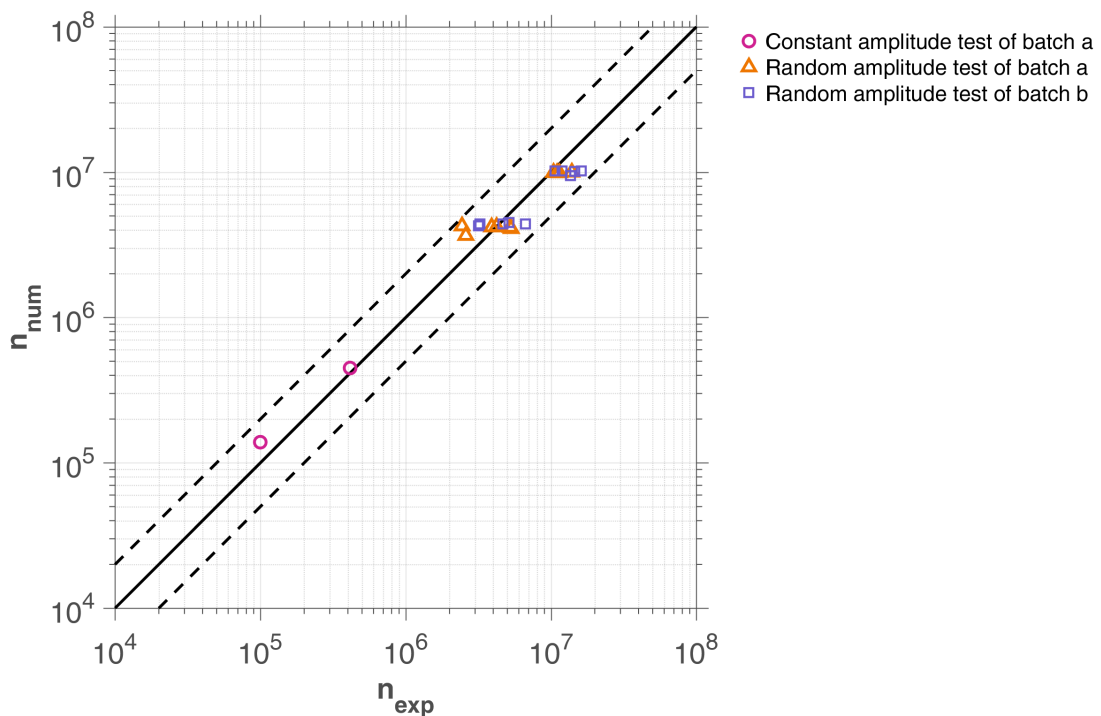


Figure 6.5 – Comparison between experimental and numerical results of 1D cyclic and random loading on aluminum fatigue tests by Cetim with load dependent α . Coefficients data are given in the second row of Tab.6.7

6.2 Experimental validation of the model on aluminum 6082 T6

6.2.1 Presentation of aluminum 6082 T6

The material tested is aluminum 6082 T6, used by [Susmel and Petrone \[2003\]](#) to validate their method of lifetime prediction. The mechanical properties of this material are summarized in Tab.6.8.

$E[\text{GPa}]$	$\sigma_y[\text{MPa}]$	$\sigma_u[\text{MPa}]$	ν
69.4	298	343	0.33

Table 6.8 – Mechanical and dynamic characteristics of aluminum 6082 T6 ([Susmel and Petrone \[2003\]](#))

Specimens of aluminum 6082 T6

The specimens were made from the drawn bars (diameter 30 mm) and the geometrical shape of which is given in Figure 6.6. They are successively polished with $6 - \mu\text{m}$ diamond compounds until a good mirror-like finish is obtained.

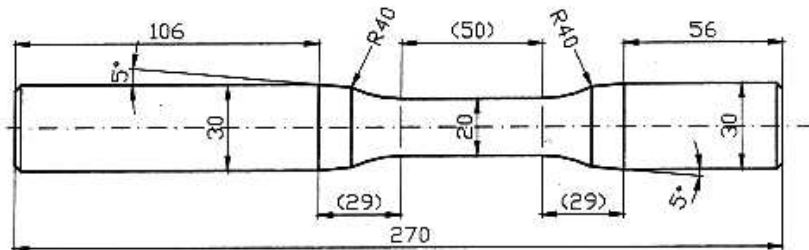


Figure 6.6 – Specimen geometry for fatigue tests of aluminum 6082 T6 (dimension in millimeters), from [Susmel and Petrone \[2003\]](#)

6.2.2 Fatigue tests on aluminum 6082 T6

The simulated tests are purely alternate and summarized in Tables 6.9 and 6.10. They consist of simple tests in bending, torsion and bending-torsion in phase and out-phase for two cases of biaxial stress ratio, $\lambda = \tau_{xy,a}/\sigma_{x,a}$ ($\lambda > 1$ and $\lambda < 1$). The expected lifetimes range from 10^4 to 1.5×10^6 cycles.

In the Tables 6.9 and 6.10, $\sigma_{x,a}$ is the normal stress amplitude, $\tau_{xy,a}$ is the torsion amplitude, λ is the biaxial stress ratio, δ is the phase shift between the components of applied stresses and $N_{f,5\%}$ represents the number of cycles at break, defined by a 5% decrease in flexural or torsional stiffness.

It is interesting to note that a reduced amount of plasticity was measured by strain gauges in the PC10T2, PC14T2 and P36BT11 tests ([Susmel and Petrone \[2003\]](#)). They are therefore located in the field of oligocyclic fatigue. Therefore, they are not simulated as we only deal with the field of polycyclic fatigue3.

Batch N°	$\sigma_{x,a}$ [MPa]	$\tau_{xy,a}$ [MPa]	λ	δ [°]	$N_{f,5\%}$ [Cycles]
P1B1	190	0	0	0	160000
P2B2	180	0	0	0	248518
P3B3	164	0	0	0	444411
P4B4	144	0	0	0	1069220
P5B5	224	0	0	0	56285
P6B4	145	0	0	0	1238325
P7B1	187	0	0	0	200480
P8B3	161	0	0	0	423590
PC9T1	0	117	∞	0	534032
PC10T2	0	155	∞	0	26987
PC11T3	0	127	∞	0	76665
PC12T3	0	127	∞	0	132295
PC13T1	0	117	∞	0	203535
PC14T2	0	155	∞	0	16195
PC15T4	0	106	∞	0	>1.1E6
PC16T4	0	104	∞	0	565150

Table 6.9 – Simple bending and torsion tests ($R = -1$), data from [Susmel and Petrone \[2003\]](#)

6.2.3 Identification of model parameters on aluminum 6082 T6

Once the average coefficient α_m is fixed in constant amplitude cyclic loading, it has the same influence as W_0 . The parameters remain to calibrate are λ_+ on the mean stress sensitivity which makes a distinction between bending and torsion, and the exponent β on the slope of $S - N$ curve. The identification strategy is as described in Section [5.9](#).

In Figure [6.9a](#) and Figure [6.9b](#) the diagonal represents a good correlation between the experimental and predicted lifetimes. The line segments on either side of the diagonal correspond to a fatigue lifetime error of a factor of two. The parameters of the 6082 T6 aluminum model are given in Tab.[6.11](#).

Non-proportional Hardening

Non-proportional hardening is used to describe loading paths where the principal strain axes rotate during cyclic loading. The simplest example would be a bar subjected to alternating cycles of tension and torsion loading. Between the tension and torsion cycles the principal axis would rotate 45° . Out-of-phase loading is a special case of non-proportional loading and is used to denote cyclic loading histories with sinusoidal or triangular waveforms and a phase difference between the loads. ([EFA](#))

Materials show additional cyclic hardening during this type of loading that is not found in uniaxial or any proportional loading path. Here is an example for 90° out-of-phase tension-torsion loading. (Figure [6.7](#))

The 90° out-of-phase loading path has been found to produce the largest degree of non-proportional hardening. The magnitude of the additional hardening observed for this loading path as compared to that observed in uniaxial or proportional loading is highly dependent on the microstructure and the ease with which slip systems develop in a material. A non-proportional effective stress, $S_{a90} = \sqrt{\sigma_{11}^2 + \tau_{12}^2}$, can be introduced which is defined as the equivalent stress under 90° out-of-phase loading at high plastic strains in the flat portion of the stress-strain curve. This term reflects the maximum degree of additional hardening that might occur for a given material.

The model predictive results for the periodic loads of constant amplitude with a radial path are in

Batch N°	$\sigma_{x,a}$ [MPa]	$\tau_{xy,a}$ [MPa]	λ	δ [°]	$N_{f,5\%}$ [Cycles]
P17BT1	57	100	1.75	0	266435
P18BT2	51	84	1.65	0	1119254
P19BT2	51	84	1.65	0	1416225
P20BT3	71	118	1.66	0	83000
P21BT3	70	118	1.69	0	75695
P22BT1	59	99	1.68	0	630325
P23BT4	132	97	0.73	0	157210
P24BT4	132	99	0.75	0	126470
P25BT5	144	107	0.74	0	35450
P26BT5	149	105	0.7	0	68465
P27BT6	122	90	0.74	0	252658
P28BT7	116	83	0.72	0	316149
P30BT8	148	66	0.45	90	278836
P31BT9	152	47	0.31	90	465010
P32BT8	149	68	0.46	90	118965
P33BT9	155	72	0.46	90	447525
P34BT10	190	105	0.55	90	47940
P35BT10	189	106	0.56	90	30995
P36BT11	79	129	1.63	90	23080
P37BT12	69	110	1.59	90	202807
P38BT13	68	99	1.46	90	262980
P39BT13	68	99	1.46	90	398615
P41BT15	79	116	1.47	90	46045

Table 6.10 – In-phase and out-of-phase bending-torsion tests ($R = -1$), data from [Susmel and Petrone \[2003\]](#)

β	λ_+	λ_-	W_0	a	f
5.126	0.9	0	1E8 Pa	0.4	1.1

Table 6.11 – Parameter identification of AL6082T6 steel

good agreement with the durations of experimental life. For the latter condition, 90 deg out-of-phase loading was also investigated (Figure 6.9c). These tests indicated a dramatic change in the number of cycles to failure, N_F , as a result of out-of-phase loading. The influence of the plastic strain path on life is thus clearly demonstrated. It is shown that the total strain energy density, $\Delta W_t = \Delta W_e + \Delta W_p$ ([Ellyin et al. \[1991\]](#)), correlates with both the in-phase and out-of-phase cyclic tests, and therefore is a proper damage parameter to be used for life predictions. Our microplasticity model does not take this strain path effect into account and we get inaccurate results on this test.

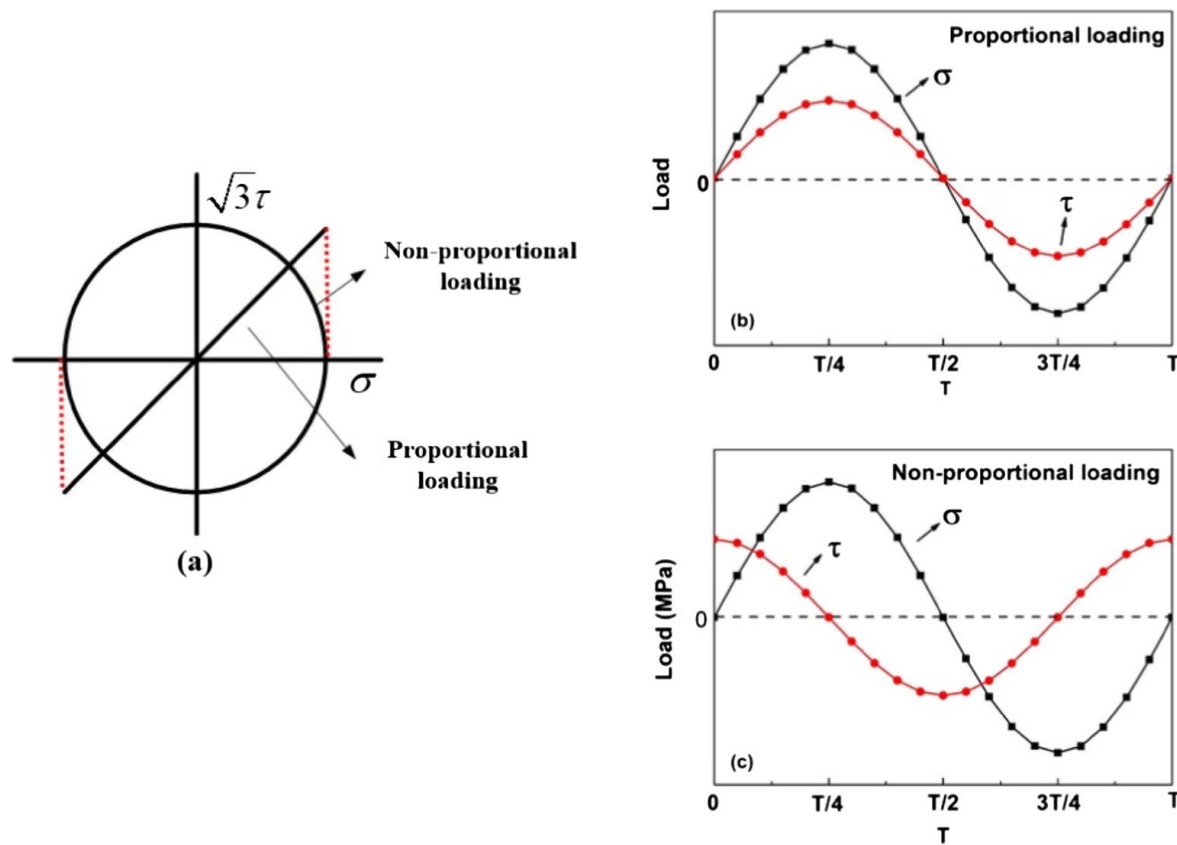


Figure 6.7 – The loading path and loading waveform of multiaxial corrosion fatigue (stress control)
 (a) loading path of proportional and non-proportional, (b) loading waveform of proportional loading,
 (c) loading waveform of non-proportion ([Huang et al. \[2017\]](#))

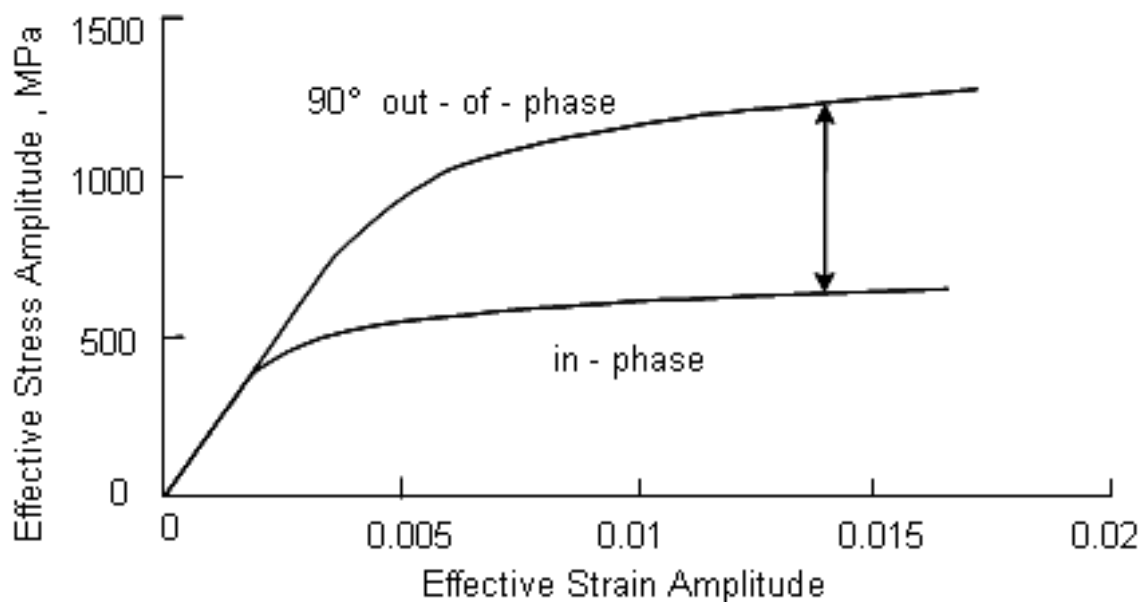


Figure 6.8 – The 90° out-of-phase loading path has been found to produce the largest degree of non-proportional hardening ([EFA](#)).

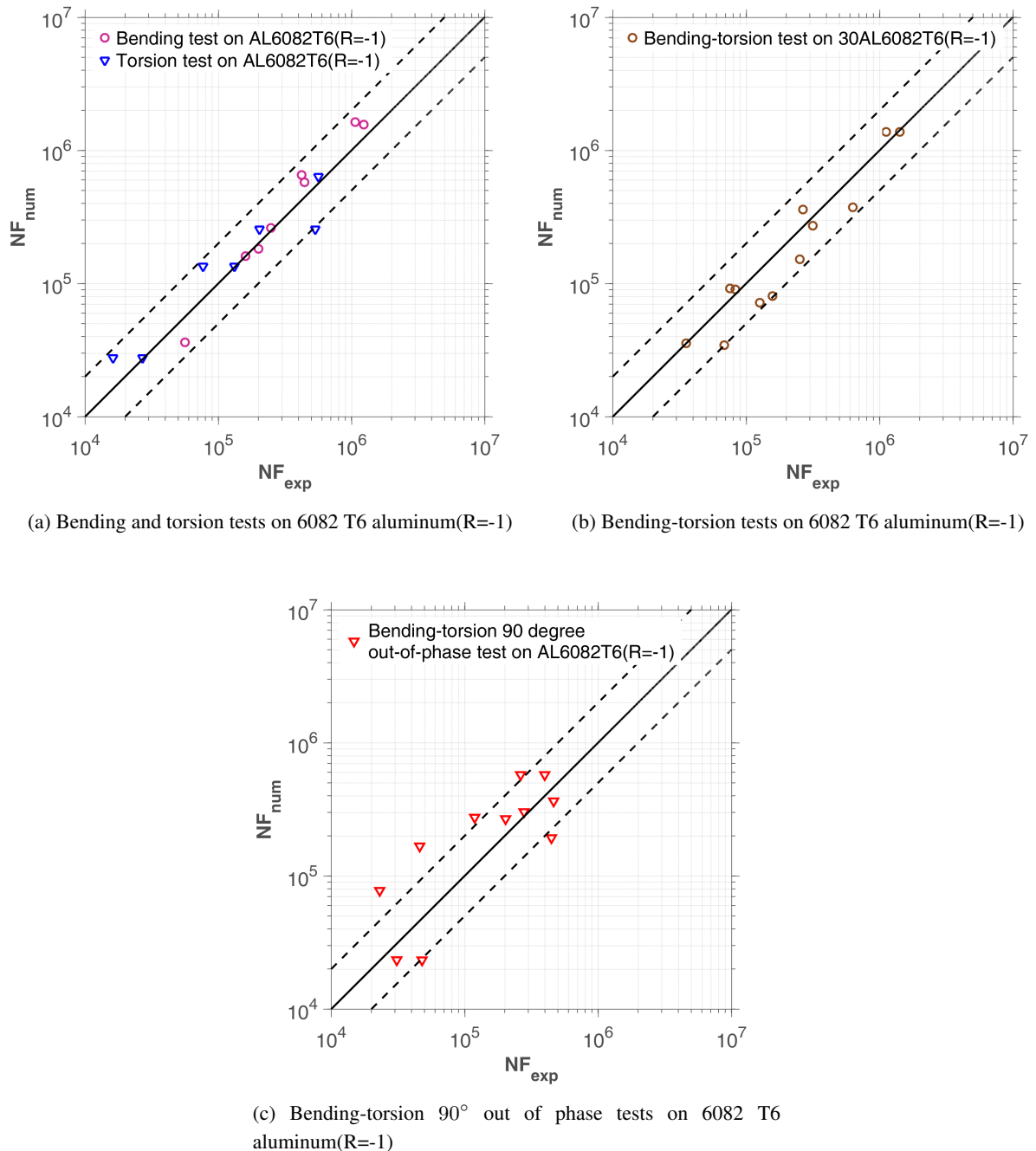


Figure 6.9 – Calibration on 6082 T6 aluminum ([Susmel and Petrone \[2003\]](#)). Comparison between experimental results and our model used with coefficients given in Tab.6.11. We obtain a good correlation in bending and torsion tests. The out of phase test are not satisfactory in these batches: P32BT8, P41BT15, P36BT11.

6.3 Experimental validation of the model on 30NCD16 steel

6.3.1 Presentation of steel 30NCD16

Tests with blocks of loading from database are compared to our model predictions. The material for testing is steel 30NCD16. The mechanical characteristics relating to each lot were determined by Dubar ([DUBAR \[1992\]](#)) by effecting monotonic tensile test batch. He eventually define “average material” one who has characteristics listed in [Tab.6.12](#):

$\sigma_{y0.02\%}$ [MPa]	$\sigma_{y0.2\%}$ [MPa]	σ_u [MPa]	σ_{-1} [MPa]	τ_{-1} [MPa]	E [GPa]
895	1080	1200	690	428	191

Table 6.12 – Mechanical and dynamic characteristics of 30NCD16 steel [DUBAR \[1992\]](#)

6.3.2 Fatigue tests performed by Dubar on steel 30 NCD 16

Tests carried out under simple bending and torsional stresses are grouped together in [Tab.6.13](#) and [6.14](#).

Bending Tests (R=-1)	N [Cycles]	$\sigma_{x,m}$ [MPa]	$\sigma_{x,a}$ [MPa]
1	51000	0	820
2	80000	0	795
3	90000	0	790
4	95000	0	785
5	100000	0	780
6	120000	0	765
7	140000	0	752
8	200000	0	725
9	210000	0	720
10	230000	0	715
11	250000	0	708

Table 6.13 – 30NCD16 steel fully reversed bending tests [DUBAR \[1992\]](#)

The results of combined bending-torsion tests in phase with or without mean stress $\sigma_{x,m}$ are given in the [Tab.6.14](#) and [Tab.6.15](#):

6.3.3 Identification of model parameters for steel 30 NCD 16

The identification of the parameters consists in minimizing the relative difference between the experimental lifetimes and calculated ones for purely alternating bending tests (R = -1). Following the identification strategy of section [5.9](#), it is clearly indicated in Figure [6.10a](#) by obtaining a good correlation between these different lifetimes

Torsion Tests (R=-1)	N [Cycles]	$\tau_{xy,a}$ [MPa]
16	51000	527
17	80000	505
18	90000	500
19	95000	497
20	100000	495
21	120000	482
22	140000	470
23	200000	450
24	210000	446
25	230000	445
26	250000	440

Table 6.14 – 30NCD16 steel fully reversed torsion tests ([DUBAR \[1992\]](#))

Bending Tests	N [Cycles]	$\sigma_{x,m}$ [MPa]	$\sigma_{x,a}$ [MPa]	$\tau_{xy,a}$ [MPa]
27	80000	0	600	335
28	200000	0	548	306
29	120000	290	0	460
30	120000	450	0	460
31	250000	450	0	430
32	95000	450	490	285
33	120000	290	500	290

Table 6.15 – 30NCD16 steel bending-torsion tests ([DUBAR \[1992\]](#))

β	λ_+	λ_-	W_0	a	f
5.3	0.55	0	4.97E8 Pa	0.4	1.1

Table 6.16 – Parameter identification of 30NCD16 steel

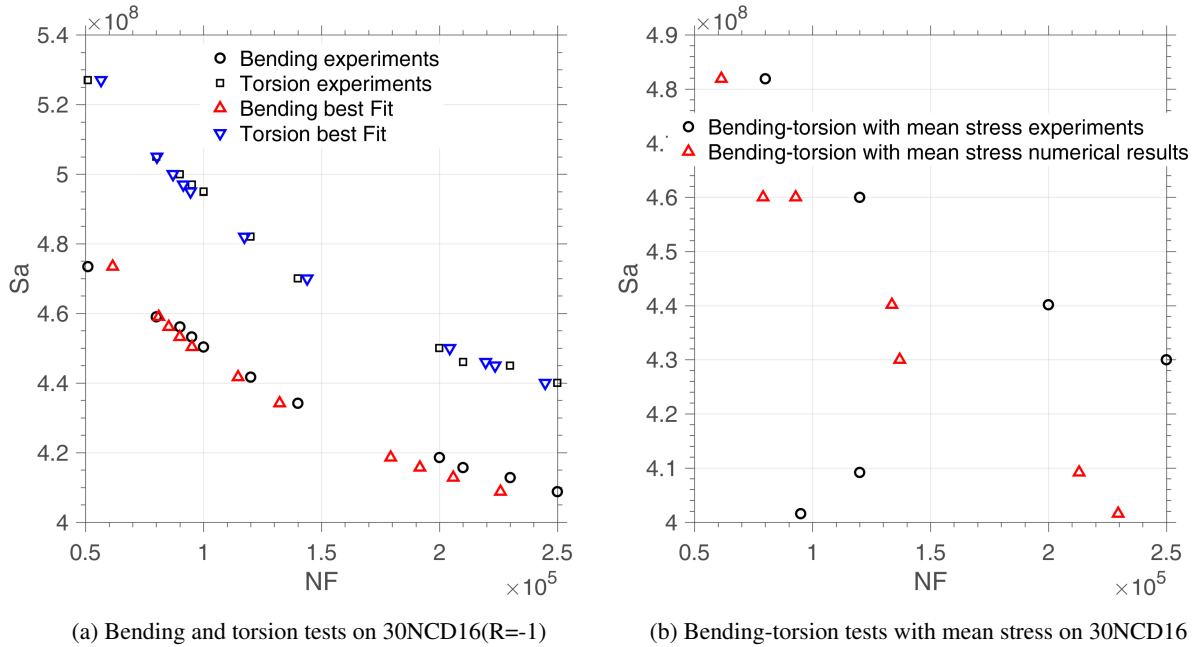


Figure 6.10 – Calibration on 30NCD16 (DUBAR [1992]). We can observe that the bending-torsion experimental values are largely dispersed

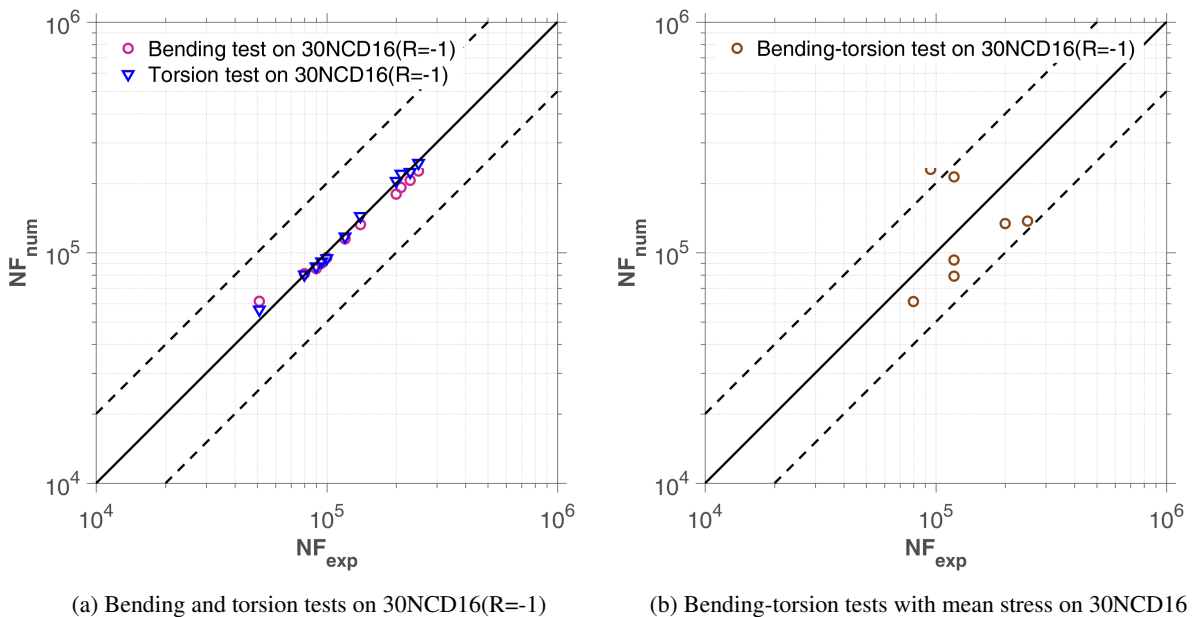


Figure 6.11 – Calibration on 30NCD16 (DUBAR [1992]). In figure (c) test 29 (same N_F with test 30 but with smaller $\sigma_{x,m}$) and test 32 (2-D with large mean stress) from Tab.6.15 are more dispersed. The numerical tests are carried out using the coefficients of Tab.6.16

6.4 Experimental validation of the model on SM45C steel

6.4.1 Presentation of steel SM45C

This is a structural steel widespread use for the crankshafts and the structural components. The chemical composition and mechanical properties of this material is given in Tab. 6.17 and Tab. 6.18.

C	Mn	P	S	Si	Ni	Cr	Cu
0.42	0.73	0.02	0.012	0.28	0.14	0.18	0.13

Table 6.17 – Chemical composition of SM45C steel

σ_y [MPa]	σ_u [MPa]	E [GPa]	G [GPa]	ν	A
638	824	213	82.5	0.29	22

Table 6.18 – Mechanical and dynamic characteristics of SM45C steel

E: Young's modulus,

G: Shear modulus,

ν : Poisson ratio,

A: Elongation at break.

6.4.2 Fatigue tests performed by Dubar on steel SM45C

Preliminary fatigue tests in purely alternating torsion and purely alternating flexion were performed by [Lee \[2013\]](#). These two types of tests were carried out with test pieces of the same geometric shape. In addition, the author had performed moderate stress bending fatigue tests to study its effect on the lifetime of SM45C steel. All uniaxial fatigue tests performed by [Lee \[2013\]](#) are illustrated in Figure 6.12. This figure shows a reduction in bending life of SM45C steel in the presence of a positive mean stress. Crack initiation was detected when the stiffness of the specimen or specimen used was reduced by 10%.

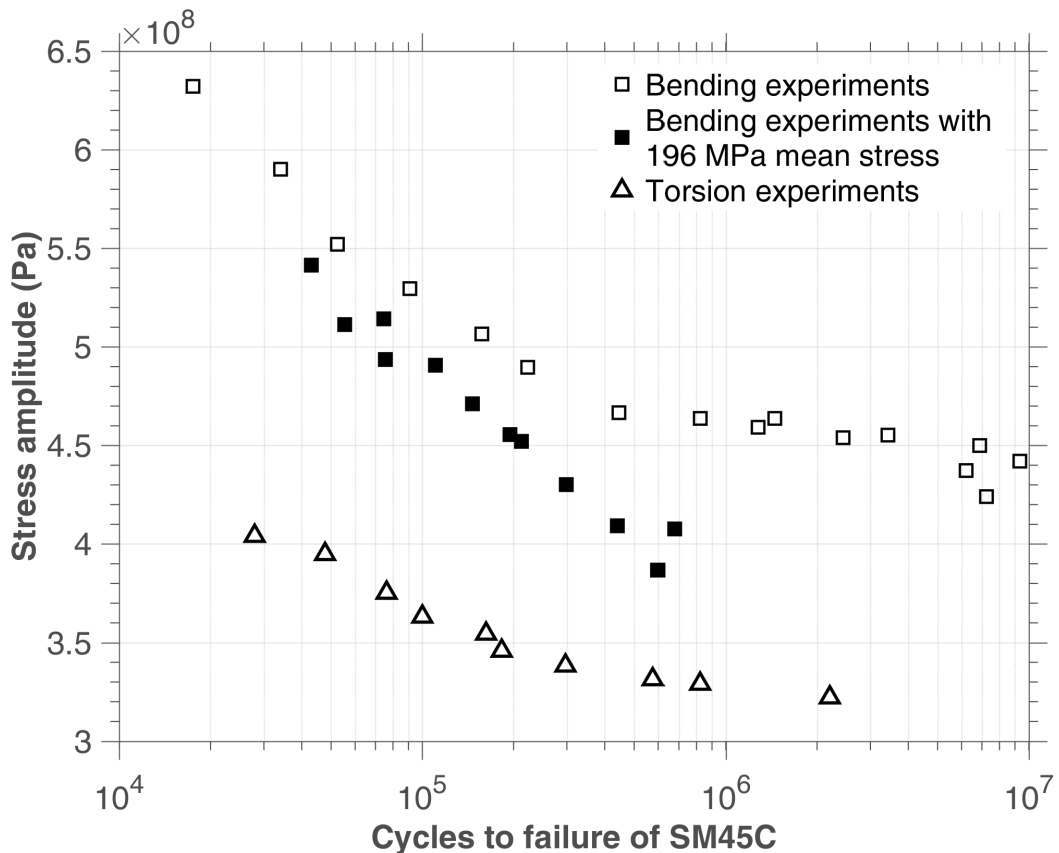


Figure 6.12 – Fatigue curves on SM45C steel by [Lee \[2013\]](#)

Preliminary fatigue tests were carried out under fully reversed bending and torsion separately.

Bending Tests		N	$\sigma_{x,a}$	$\sigma_{x,m}$
R=-1		[Cycles]	[MPa]	[MPa]
1		17520	632.1	0
2		33991	590.1	0
3		52427	552.0	0
4		91077	529.5	0
5		156882	506.5	0
6		222261	489.8	0
7		446115	466.7	0
8		822487	463.8	0
9		1279414	459.2	0
10		1453321	463.8	0
11		2440360	454.0	0
12		3428115	455.2	0
13		6880791	450.0	0
14		6213809	437.3	0
15		9342857	441.9	0
16		7240667	424.1	0
1		43043	541.5	196
2		55523	511.5	196
3		74725	514.4	196
4		75362	493.6	196
5		110407	490.7	196
6		146090	471.1	196
7		194951	455.5	196
8		212218	452.0	196
9		297990	430.1	196
10		440286	409.3	196
11		678727	407.6	196
12		597603	386.8	196

Table 6.19 – SM45C steel fully reversed bending tests(extracted from [Lee \[2013\]](#))

Torsion Tests		N	$\tau_{xy,a}$	$\sigma_{x,m}$
R=-1		[Cycles]	[MPa]	[MPa]
1		27957	404.1	0
2		47749	394.9	0
3		76194	375.3	0
4		100000	363.1	0
5		162305	354.5	0
6		182807	345.8	0
7		296705	338.3	0
8		575636	331.4	0
9		822487	329.1	0
10		2203806	322.2	0

Table 6.20 – SM45 steel fully reversed torsion tests(extracted from [Lee \[2013\]](#))

Group	N [Cycles]	τ_a [MPa]	σ_a [MPa]	σ_m [MPa]
A	29.9E3	282	449	0
	35.7E3	334	354	0
	50E3	223	485	0
	73.8E3	309	357	0
	106E3	217	449	0
	106E3	285	370	0
	112E3	199	449	0
	131E3	194	457	0
	333E3	252	354	0
B	431E3	154	437	0
	53E3	215	441	196
	59.2E3	309	286	196
	70.1E3	155	464	196
	86.3E3	136	473	196
	89.9E3	334	173	196
	92.1E3	209	403	196
	102E3	177	437	196
	135E3	321	167	196
	351E3	179	357	196
	394E3	274	182	196

Table 6.21 – Effect of mean bending stress on out-of-phase(90°) fatigue of SM45C steel (Lee [2013])

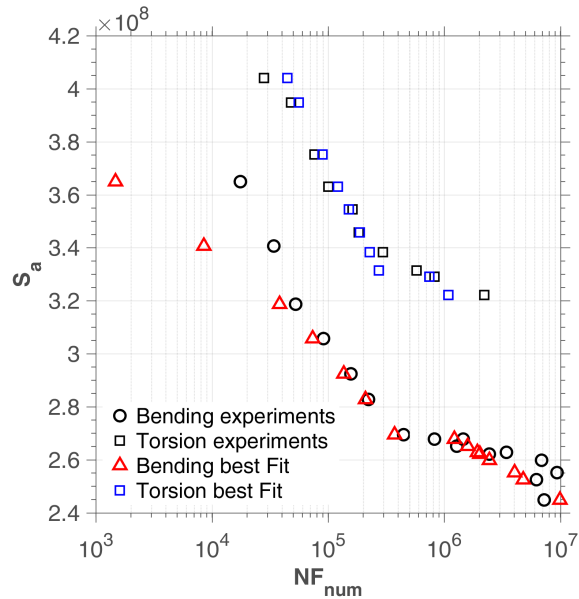
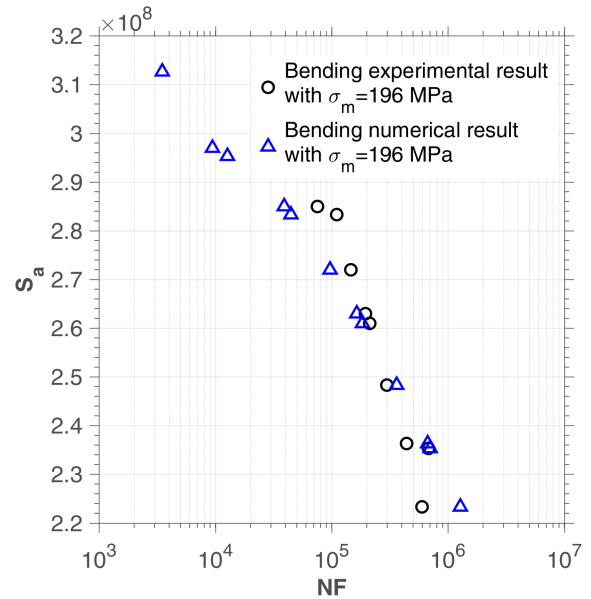
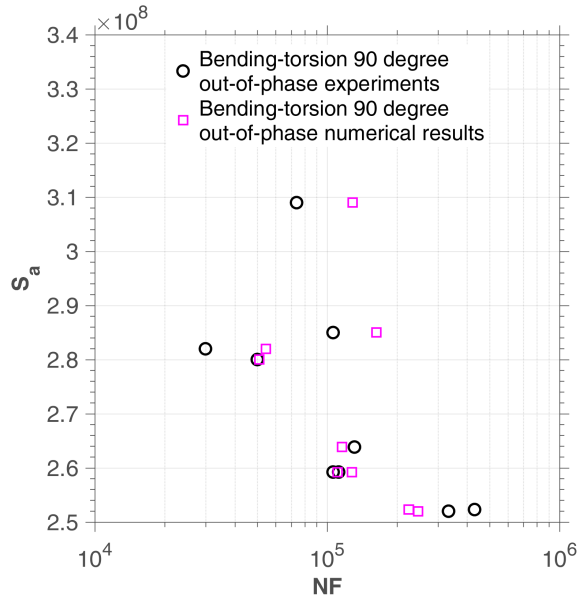
6.4.3 Identification of model parameters for steel SM45C

We use the same identification strategy as described in Section 5.9. The fitted curve using experimental data in Tab.6.21 and data with mean stress effect is shown in Figure 6.14b. The tests on SM45C steel have illustrated that the mean bending stress has an influence on both uniaxial and multiaxial fatigue life.

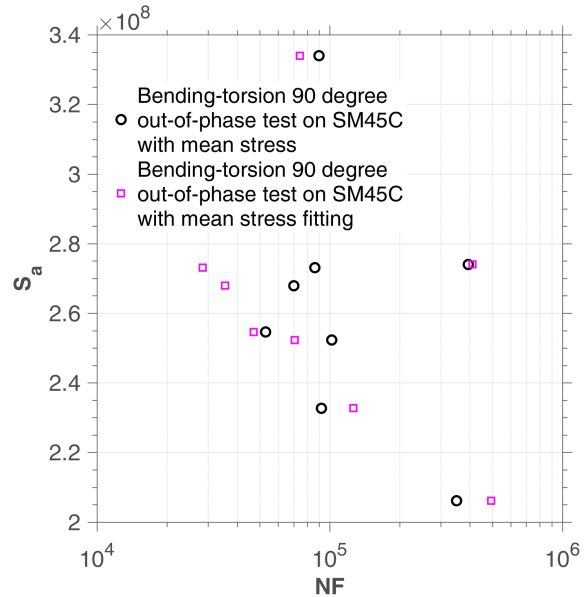
Although the uniaxial experimental data we extracted from Lee's curve (Lee [2013]) of SM45C steel are slightly dispersed, we can find our model quite satisfactory in the case of SM45C steel. As for multiaxial 90 degree out of phase, fully reversed bending-torsion fatigue tests, our model is able to evaluate the cycles to failure.

$\beta(LCF/HCF)$	λ_+	λ_-	$W_0(LCF/HCF)$	a	f
6/15.8	1.4	0	2.6E8/5.6E5 Pa	0.1	1.1

Table 6.22 – Parameter identification of SM45C steel

(a) Bending and torsion test on SM45C steel($R=-1$)(b) Bending test with mean stress on SM45C steel ($\sigma_m = 196$ MPa)

(c) Bending-torsion 90 degree out-of-phase tests on SM45C steel



(d) Bending-torsion 90 degree out-of-phase tests with mean stress on SM45C steel

Figure 6.13 – Calibration on SM45C

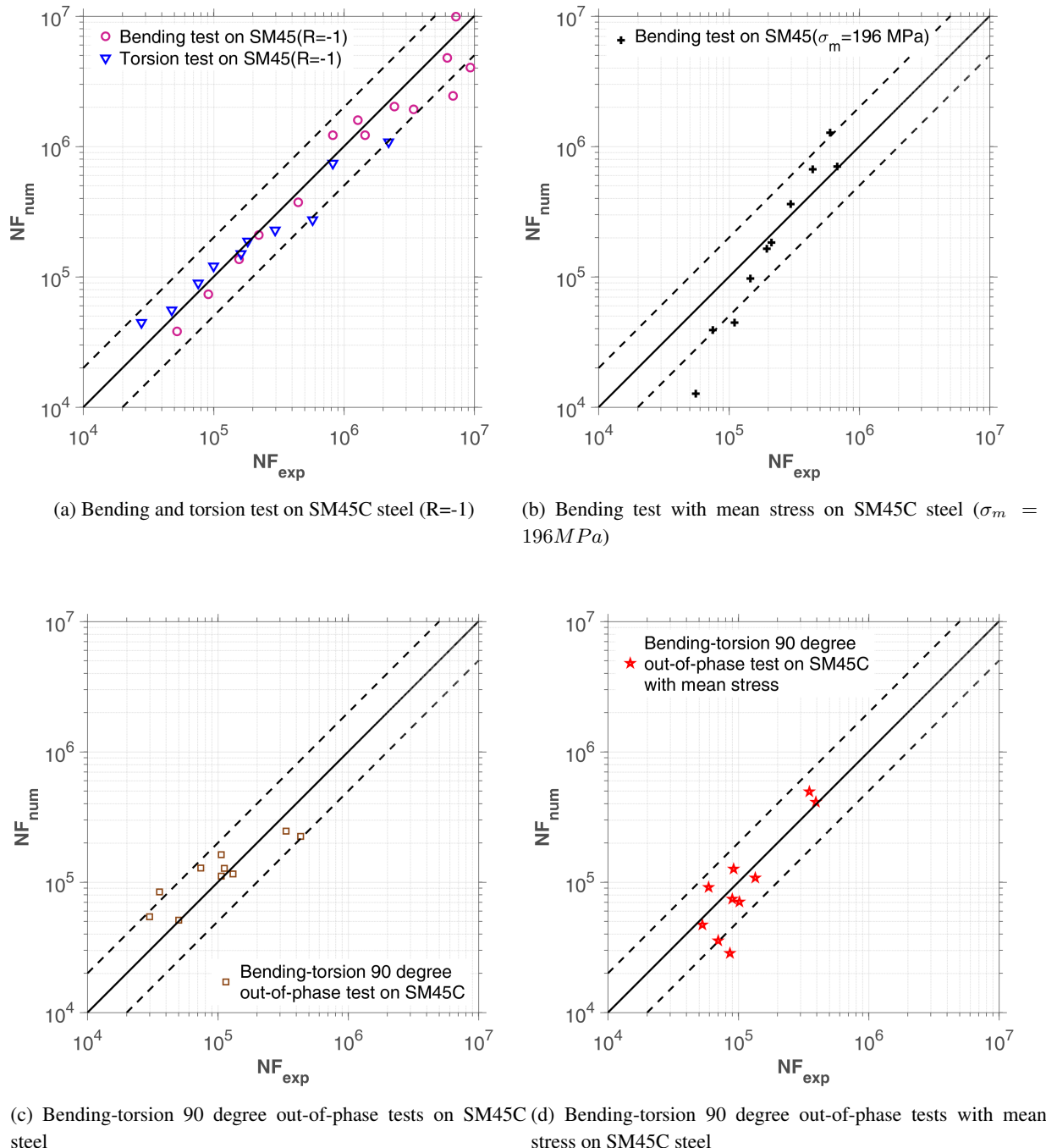


Figure 6.14 – Calibration on SM45C. The numerical tests are carried out using the coefficients of Tab.6.22

6.5 Experimental validation of the model on 10 HNAP steel

6.5.1 Presentation of the material

Fatigue tests were performed on the HNAP steel. It is a very low carbon steel which resembles the 10 CN 6. In Tab.6.23, its chemical composition is given: The mechanical properties of this steel

C	Mn	Si	P	S	Cr	Cu	Ni	Fe
0.12%	0.71%	0.41%	0.08%	0.03%	0.81%	0.30%	0.50%	the rest

Table 6.23 – Chemical composition of 10 HNAP steel, data from [Bedkowski \[1994\]](#)

are given in Tab.6.24:

$Re_{0.2\%}$	R_m	A	ν	E
418 MPa	566 Mpa	32%	0.29	215 GPa

Table 6.24 – Mechanical characteristics of steel 10 HNAP, data from [Bedkowski \[1994\]](#)

where

- $Re_{0.2\%}$: elastic limit at 0.2% of plastic deformation,
- R_m : maximum tensile strength,
- A : elongation at break,
- ν : Poisson's coefficient,
- E : Young's modulus.

6.5.2 Description of fatigue tests on 10 HNAP steel

The Macha team performed a large number of fatigue tests on the HNAP steel. Thus, it performed not only simple tensile compression and torsion tests ($R = -1$) in order to establish the corresponding Wöhler curves but also tests under variable loading on cylindrical specimens of the same material ([ACHTELIC \[1994\]](#)). [VIDAL](#) carried out tensile tests on this material for various mean stress values. It has established the Wöhler curve in repeated traction in order to validate on this steel the method of Robert whose use requires three Wöhler curves in symmetrical alternating traction, symmetrical alternating torsion and repetitive traction.

Wöhler curve in tension-compression

The model chosen by Macha and recovered by [Jabbado \[2006\]](#) for the tensile-compression Wöhler curve is that of Basquin:

$$\ln N = 68.3619.82 \ln (\sigma_{-1}), \quad (6.5.1)$$

Wöhler curve in symmetrical alternating torsion

The symmetric alternating torsion Wöhler curve was recovered by [Jabbado \[2006\]](#) using following equation:

$$\ln N = 21.550.0385 \tau_{-1}. \quad (6.5.2)$$

Tensile fatigue tests for various mean stress values

[VIDAL](#) carried out tensile tests on HNAP steel for various values of mean stress. The results are summarized in Tab.6.25. They allowed us to plot the Wöhler curves for different values of the mean stress σ_m .

N_F	$\Sigma_{xx,a}$	σ_m	$\Sigma_{xx,a}$	σ_m	$\Sigma_{xx,a}$	σ_m	$\Sigma_{xx,a}$	σ_m
1.00E+05	311.30	75	224.42	150	257.98	225	251.82	300
2.00E+05	289.36	75	208.40	150	242.47	225	224.42	300
3.00E+05	276.53	75	197.03	150	233.40	225	208.40	300
4.00E+05	267.43	75	188.21	150	226.96	225	197.03	300
5.00E+05	260.37	75	181.00	150	221.97	225	188.21	300
6.00E+05	254.60	75	174.91	150	217.89	225	181.00	300
7.00E+05	249.72	75	169.63	150	214.44	225	174.91	300
8.00E+05	245.49	75	164.97	150	211.46	225	169.63	300
9.00E+05	241.77	75	160.81	150	208.82	225	164.97	300
1.00E+06	238.43	75	233.29	150	206.47	225	160.81	300

Table 6.25 – Experimental results of tensile tests for various values of σ_m , data from VIDAL

Fatigue testing under variable loading

Random multiaxial loading fatigue tests were performed on cylindrical HNAP steel specimens (ACHTELIC [1994]). The load considered is proportional and results from a combination of bending and torsion. The random signal is stationary and has a normal distribution as a probability distribution. Tests of this type have been analyzed and simulated by Carpinteri et al. (Carpinteri et al. [2003]). They were provided to us in the form of tests carried out on the HNAP steel for two values of the angle α' : $\alpha' = \pi/8$ and $\alpha' = \pi/4$. α' is the angle made by the resultant moment M with the bending moment M_B (see Figure 6.15). The angle is kept constant during each individual test.

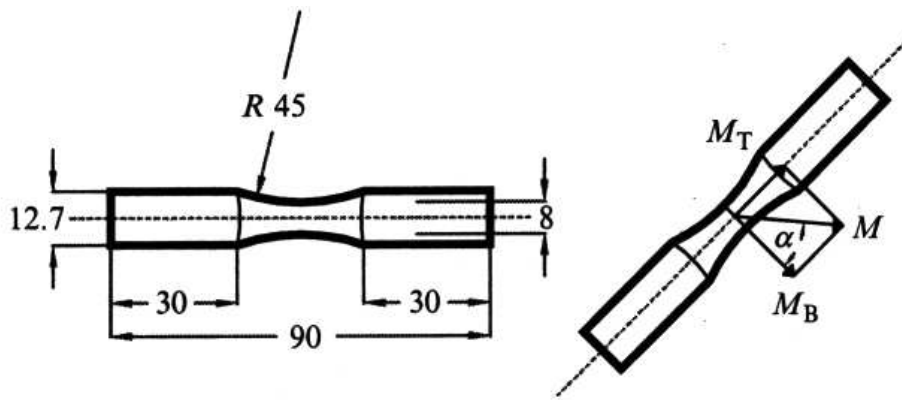


Figure 6.15 – Bending-torsion fatigue tests on cylindrical specimens (Carpinteri et al. [2003])

The stationary random loading sequence contains 49152 values recorded by a time interval of 0.00375 seconds (frequency = 266.67 Hz). It is shown in Figure 6.16. Its total duration is 184.32 seconds. This sequence is multiplied by load coefficients corresponding to bending $f(\sigma_{xx})$ and torsion $f(\tau_{xy})$ in order to obtain random multiaxial loading sequences. As the signal is stationary, the breaking life is determined in terms of number of sequences with break N_{Sq} . Knowing N_{Sq} and the total time in seconds of the sequence studied, it is easy to express the lifetime of the piece in seconds. The results of fatigue tests under variable loads are summarized in Tab.6.26 and Tab.6.27 as a function of angle α' and ratio r ; $r = f(\tau_{xy})/f(\sigma_{xx})$.

1st type of tests: $\alpha' = \pi/8$ and $r = f(\tau_{xy})/f(\sigma_{xx}) = 0.2$.

2nd type of tests: $\alpha' = \pi/4$ and $r = f(\tau_{xy})/f(\sigma_{xx}) = 0.5$.

In Figure 6.17, an example of a random multiaxial loading sequence is given.

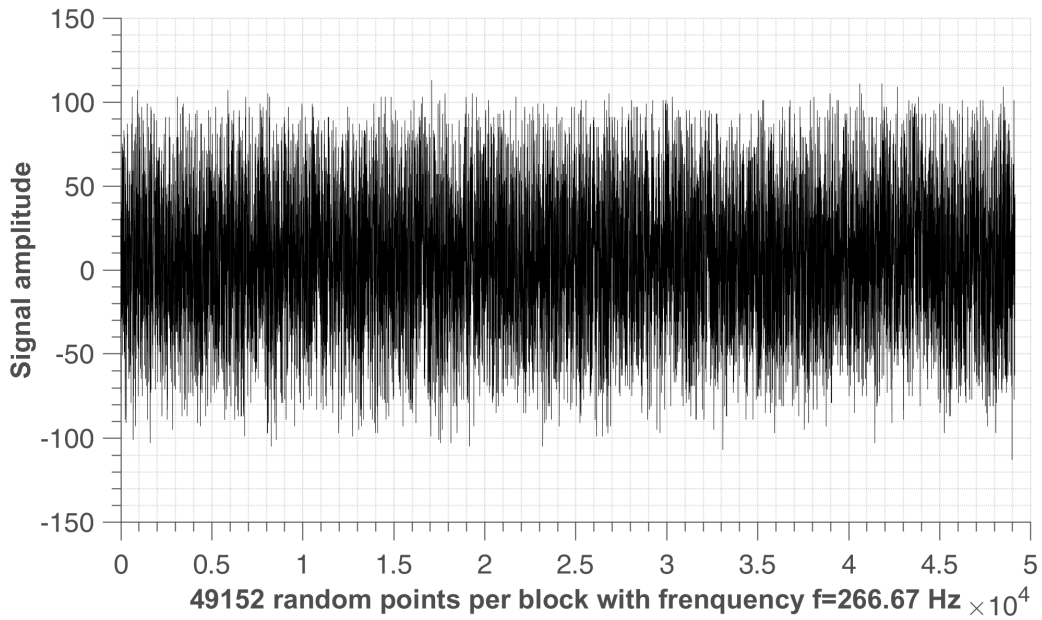


Figure 6.16 – Bending-torsion fatigue tests on cylindrical specimens (Carpinteri et al. [2003])

N^o	$f(\sigma_{xx})$	$f(\tau_{xy})$	r	$T_{exp}(s)$
1	5.7084	1.1822	0.2	16843.2
2	5.2917	1.0959	0.2	17780.1
3	4.8337	1.0010	0.2	24416.5
4	5.2674	1.0909	0.2	24858.2
5	5.4534	1.1294	0.2	26518.3
6	5.2002	1.0769	0.2	36162.3
7	4.7944	0.9929	0.2	47600.4
8	4.3862	0.9084	0.2	57993.9
9	4.6241	0.9576	0.2	60428
10	4.0194	0.8324	0.2	73373.3
11	4.0127	0.8310	0.2	87609.1
12	4.2292	0.8758	0.2	89185.2
13	3.9213	0.8121	0.2	106900
14	3.7731	0.7814	0.2	117358
15	4.1148	0.8521	0.2	118902
16	3.6150	0.7486	0.2	132448
17	3.3135	0.6862	0.2	170571
18	4.1298	0.8553	0.2	178215
19	3.4761	0.7199	0.2	225288
20	3.3430	0.6923	0.2	352635
21	3.0135	0.6241	0.2	355720

Table 6.26 – Fatigue results under variable loads for $\alpha' = \pi/8$ and $r = f(\tau_{xy})/f(\sigma_{xx}) = 0.2$

6.5.3 Identification of model parameters of 10HNAP steel

As the previous tests, we identify the slope β in pure torsion tests without the mean stress effect. Then fit λ_+ and W_0 with bending tests($R = -1$). The parameters of the HNAP steel model can be

N^o	$f(\sigma_{xx})$	$f(\tau_{xy})$	r	$T_{exp}(s)$
1	4.2519	2.126	0.5	15379.4
2	4.0567	2.0284	0.5	21465.7
3	3.8982	1.9491	0.5	25350.4
4	3.7823	1.8912	0.5	45949
5	3.5963	1.7982	0.5	62434.8
6	3.4497	1.7249	0.5	75225.7
7	2.9423	1.4712	0.5	115009
8	2.8814	1.4407	0.5	136794
9	2.3299	1.165	0.5	203365
10	2.8399	1.42	0.5	221370
11	2.8493	1.4247	0.5	244757
12	2.2542	1.1271	0.5	251723
13	2.3651	1.1826	0.5	288080
14	2.4215	1.2108	0.5	405444

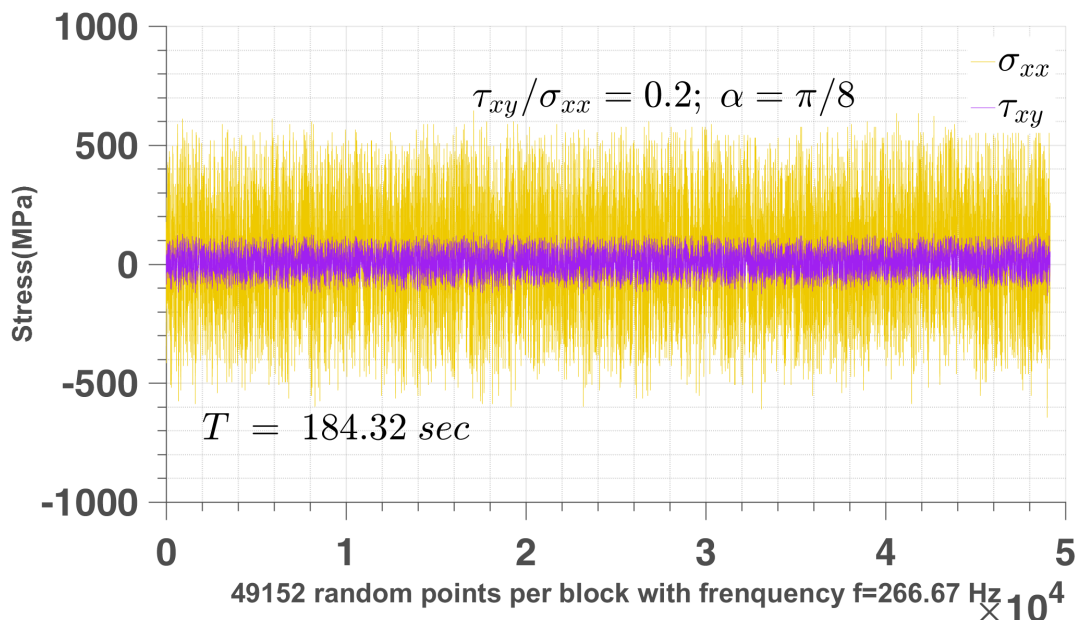
Table 6.27 – Fatigue results under variable loads for $\alpha' = \pi/4$ and $r = f(\tau_{xy})/f(\sigma_{xx}) = 0.5$ 

Figure 6.17 – Multiaxial random loading sequence

identified by referring to Tab.6.28. They are grouped in Tab.6.28:

β	λ_+	λ_-	W_0	a	f
5.3	1.7	0	3.22E7 Pa	0.01	1.1

Table 6.28 – Model parameters for 10HNAP steel

The constant amplitude loading tests corresponds to number of cycles to failure in the range of $1E5 \sim 1E6$. However, in random loading case, the total reversals to failure are $2E6 \sim 5E7$ (calculated from Tab.6.26 and 6.27). These two cases belongs to different mechanisms, so their sensitivity of sequence effect and mean stress effect can be different as shown in Tab.6.28 and 6.29.

β	λ_+	λ_-	W_0	a	f
5.3	0.3	0	2.2E8 Pa	0.001	1.1

Table 6.29 – Model parameters for 10HNAP steel (random loading)

6.5.4 Simulation of fatigue tests performed on 10HNAP steel

The constant amplitude unidimensional tests data are show in Tab.6.30 and 6.31.

N^o	N_F	$\Sigma_{xx,a}$
1	1.00E+05	326.69
2	2.00E+05	304.42
3	3.00E+05	292.11
4	4.00E+05	283.68
5	5.00E+05	277.30
6	6.00E+05	272.20
7	7.00E+05	267.96
8	8.00E+05	264.34
9	9.00E+05	261.19
10	1.00E+06	258.41

Table 6.30 – Constant amplitude bending tests performed on 10HNAP steel, data from [VIDAL](#)

N^o	N_F	$\Sigma_{xy,a}$
1	1.00E+05	260.70
2	2.00E+05	242.70
3	3.00E+05	232.17
4	4.00E+05	224.70
5	5.00E+05	218.90
6	6.00E+05	214.16
7	7.00E+05	210.16
8	8.00E+05	206.69
9	9.00E+05	203.63
10	1.00E+06	200.90

Table 6.31 – Constant amplitude torsion tests performed on 10HNAP steel, data from [VIDAL](#)

After determining the parameters of the 10HNAP steel model for each of the batches tested, the number of priming cycles can be obtained by directly applying equation (5.7.15) for the proportional periodic loads of constant amplitude and for multiaxial loadings of variable amplitude.

In Figure 6.22 and Figure 6.23, we give the prediction results of the torsion tests used to identify β and W_0 of the model, then we use the bending with various mean stress to get the parameter λ_+ ($\lambda_- = 0$).

The prediction results of the tensile tests for various values of the mean stress σ_m are summarized in Figure 6.23. These results correlate well with the experimental lifetimes.

The tests of multiaxial loadings of variable amplitude are plotted in Figure 6.24 and Figure 6.25 as a function of the angle α_M and the ratio r . In these figures, the prediction results of the proposed model and that presented by [Carpinteri et al. \[2003\]](#). For the first type of tests ($\alpha_M = \pi/8$ and $r =$

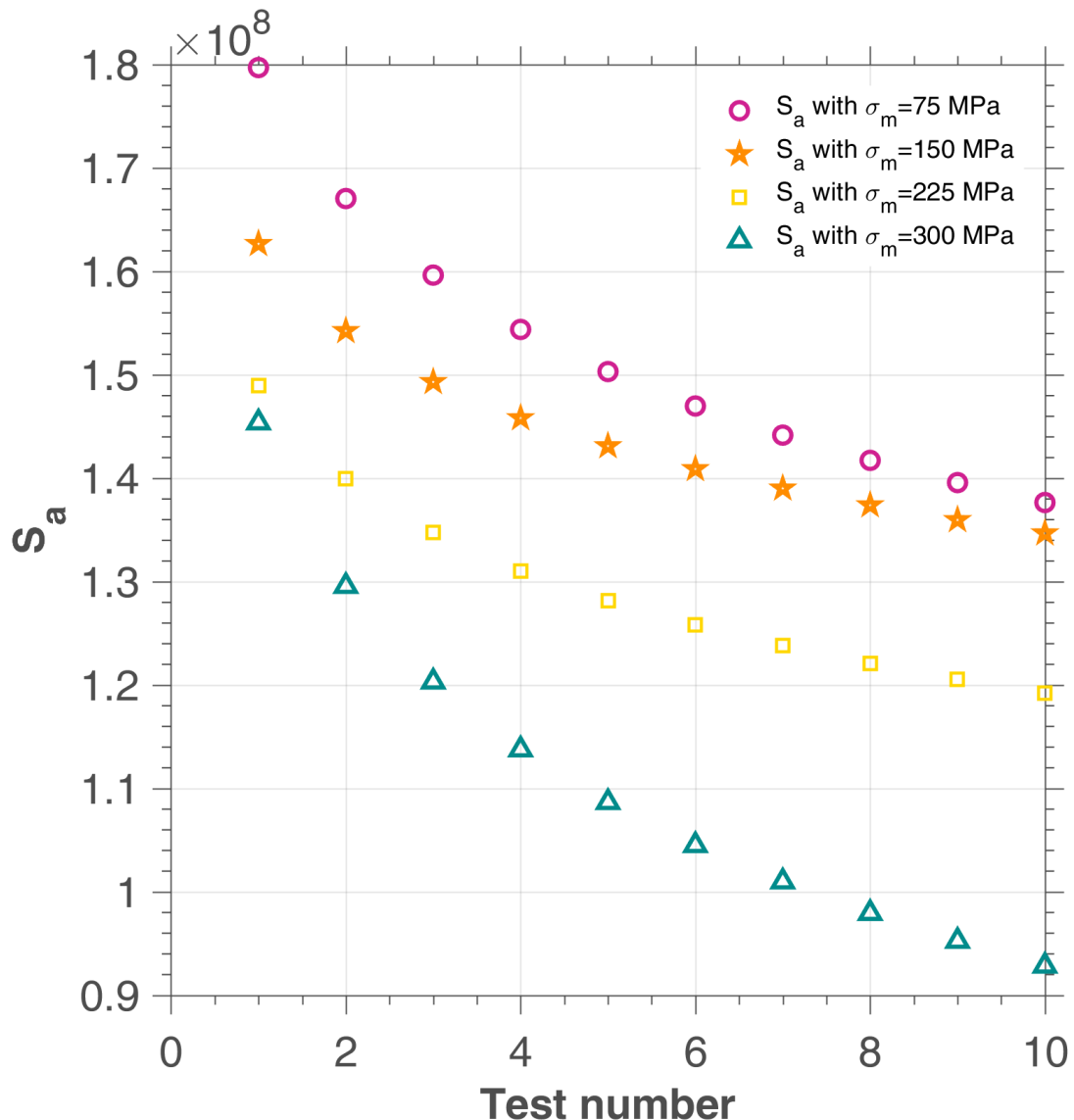


Figure 6.18 – S_a of bending tests with mean stress on 10HNAP

0.2), and the second type of tests ($\alpha_M = \pi/4$ and $r = 0.5$), the predictions of [Carpinteri et al. \[2003\]](#) are both good.

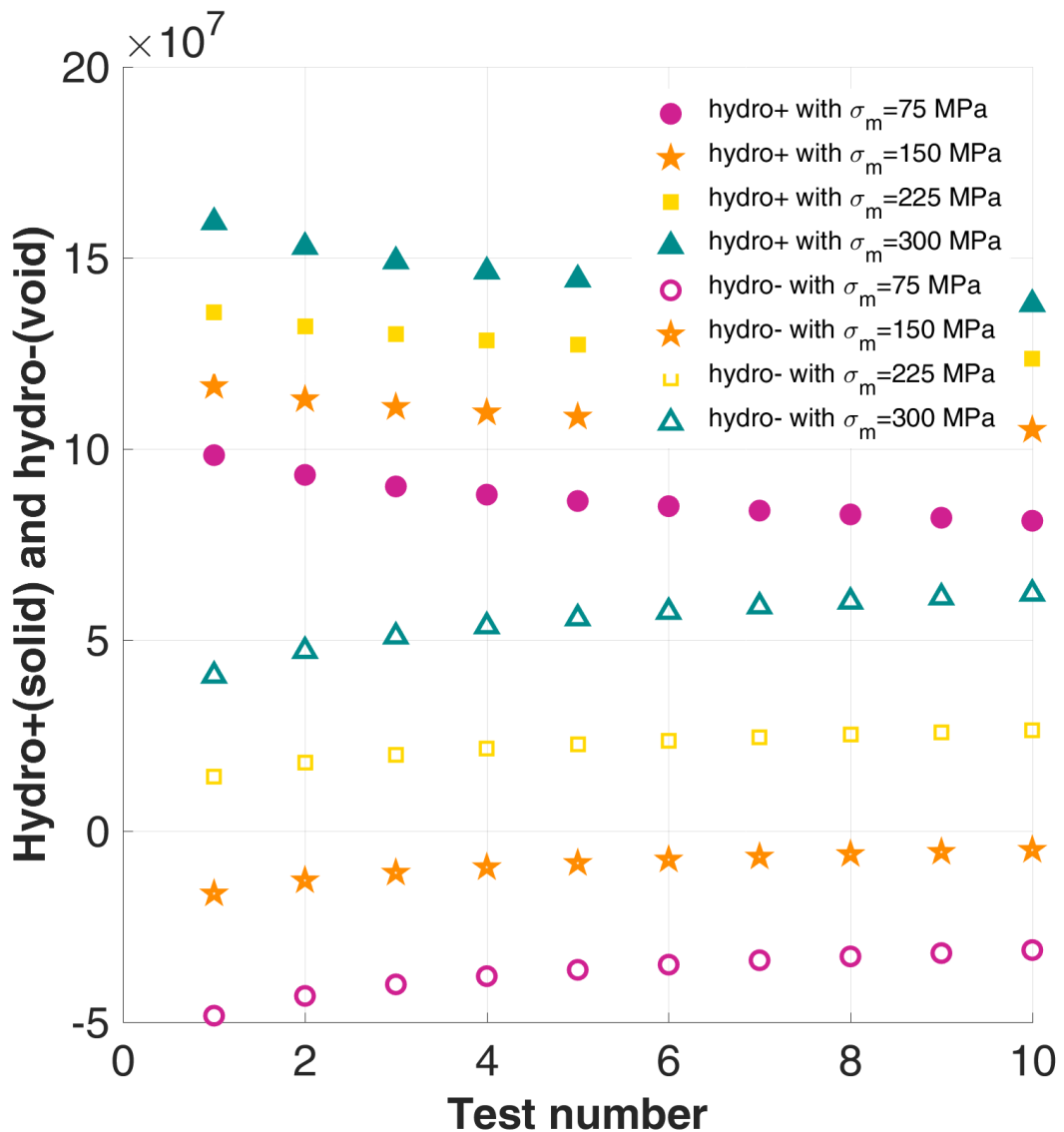


Figure 6.19 – $Hydro_{+-}$ of bending tests with mean stress on 10HNAP

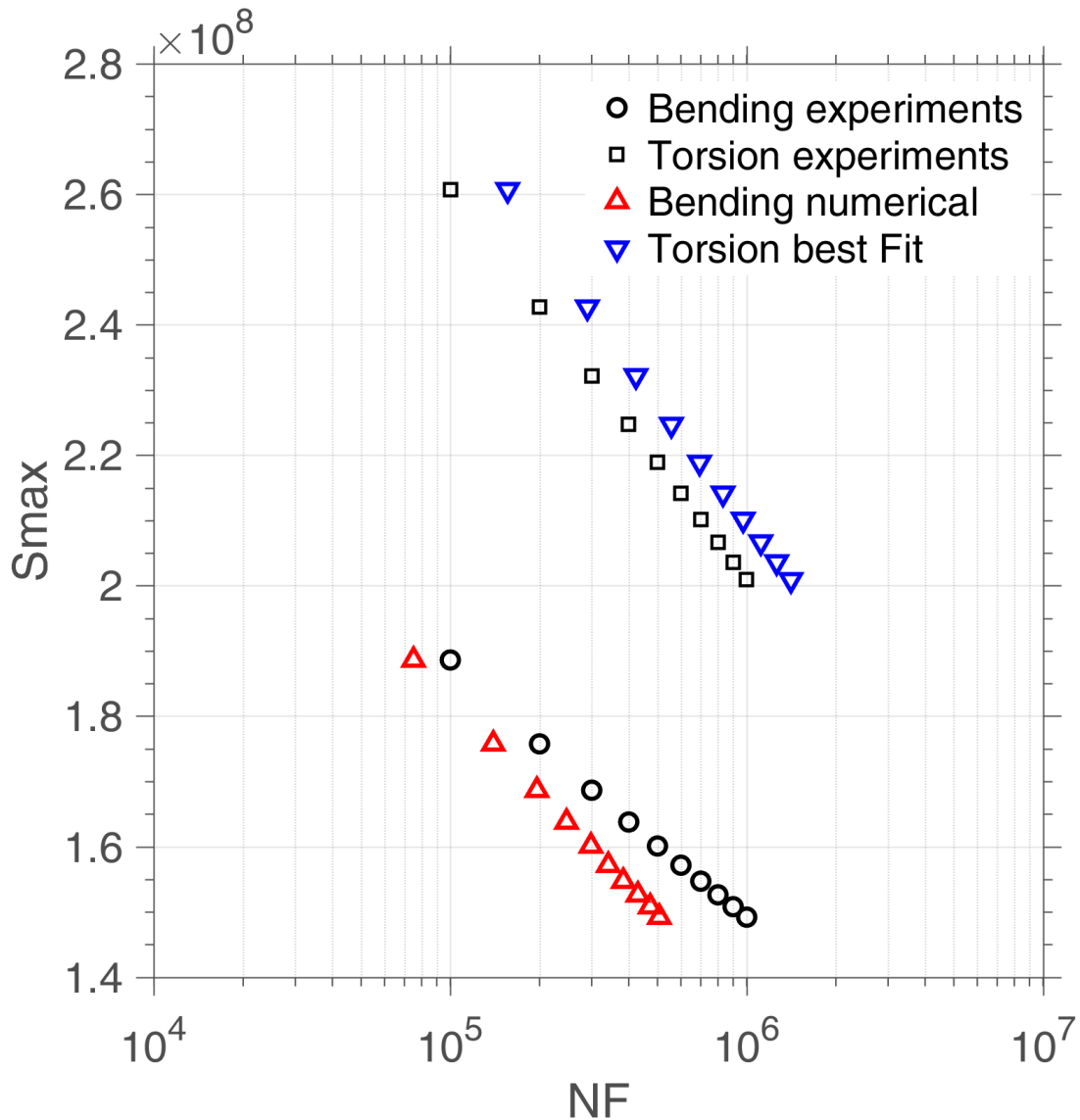


Figure 6.20 – Bending and torsion test on 10HNAP steel($R=-1$). Data are presented in Tab.6.30 and 6.31. The torsion best fit and the bending numerical results(optimal time step of method 2 deduced in Chapter 5) are obtained with the coefficients of Tab.6.28

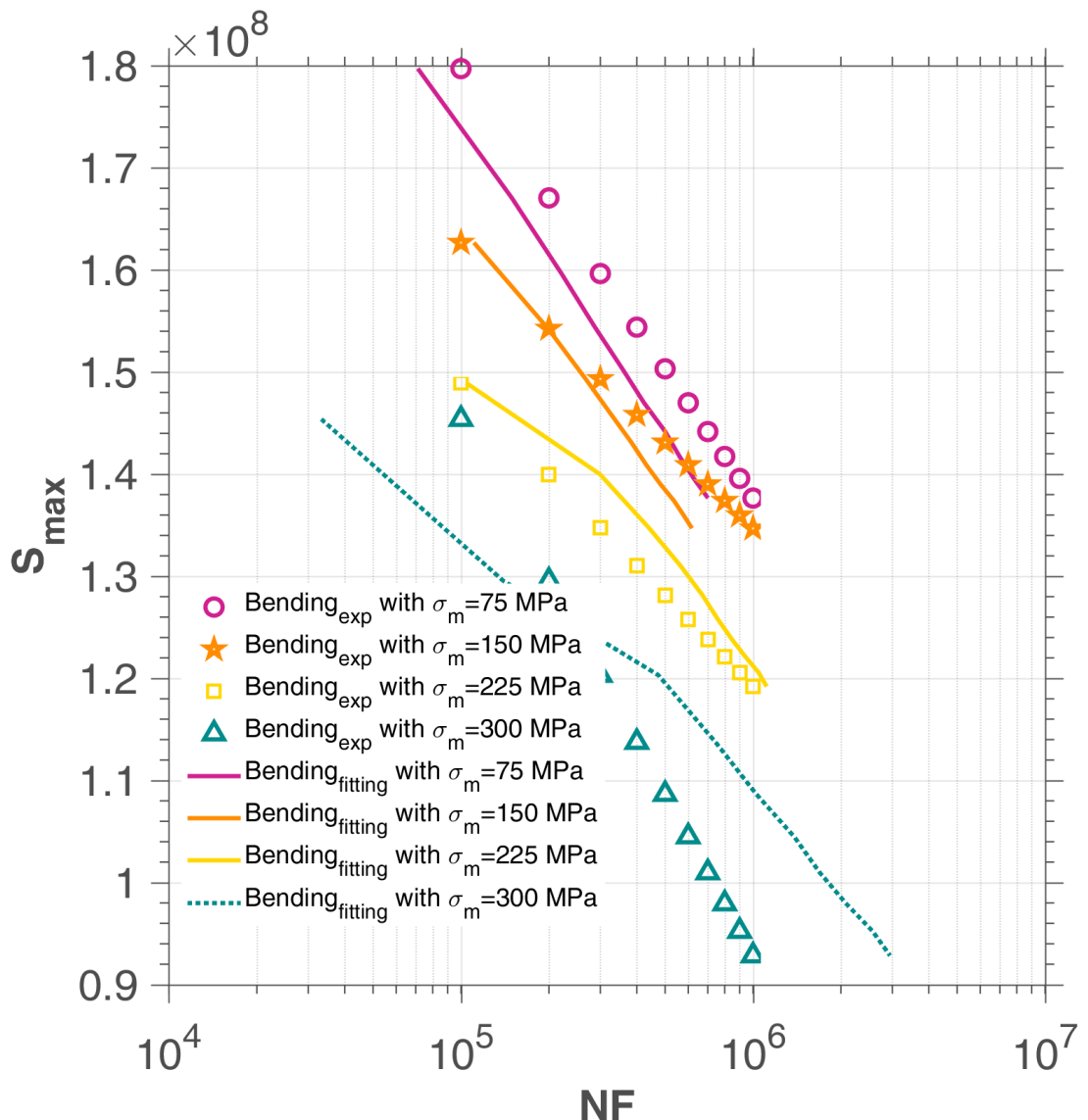


Figure 6.21 – Wöhler tensile curves for various mean stress values. Data are presented in Tab.6.25 and results are obtained with the coefficients of Tab.6.28

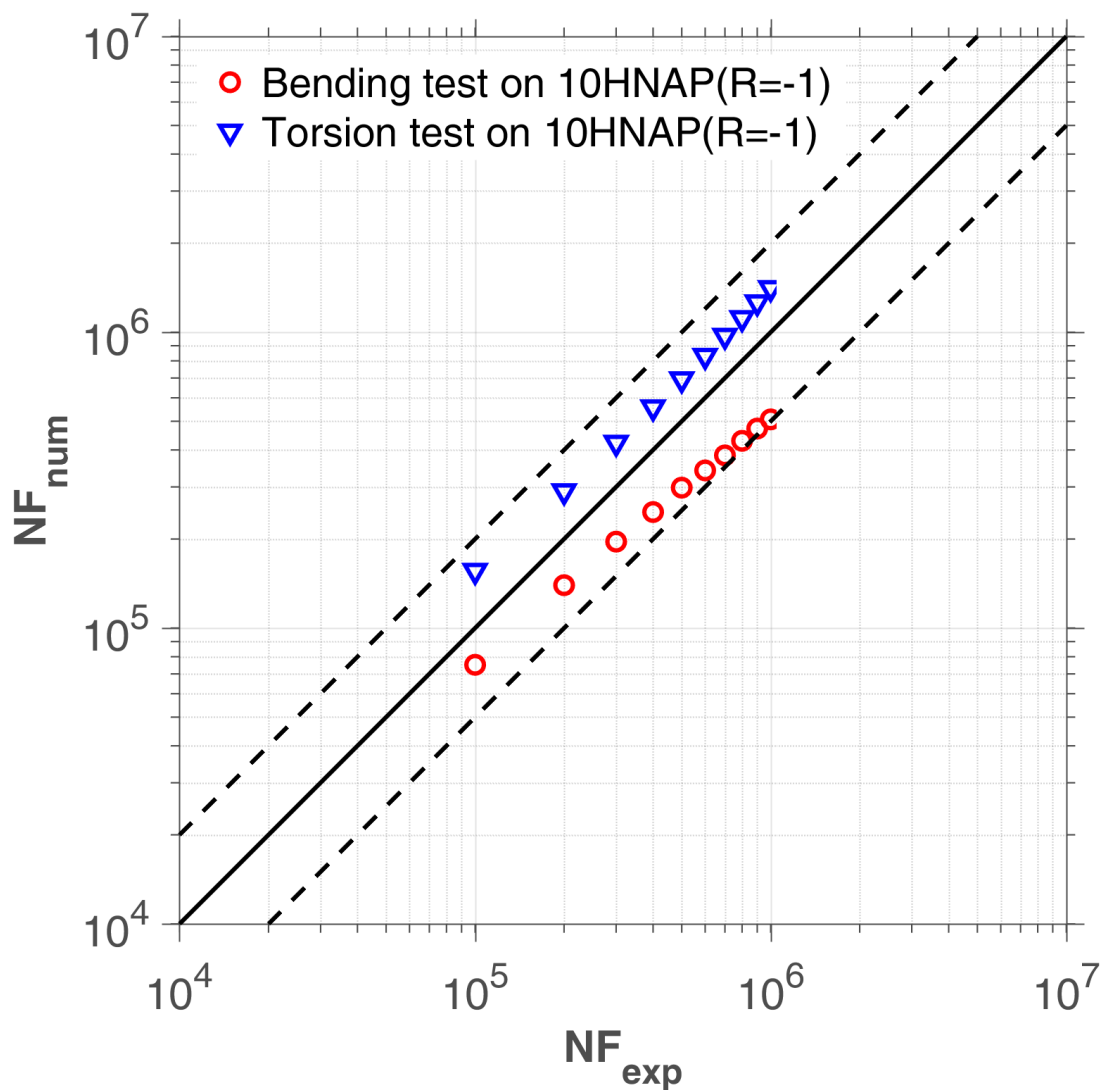


Figure 6.22 – Calibration on 10HNAP steel, bending and torsion tests on 10HNAP($R=-1$). Data are presented in Tab.6.30 and 6.31 and results obtained with the coefficients of Tab.6.28

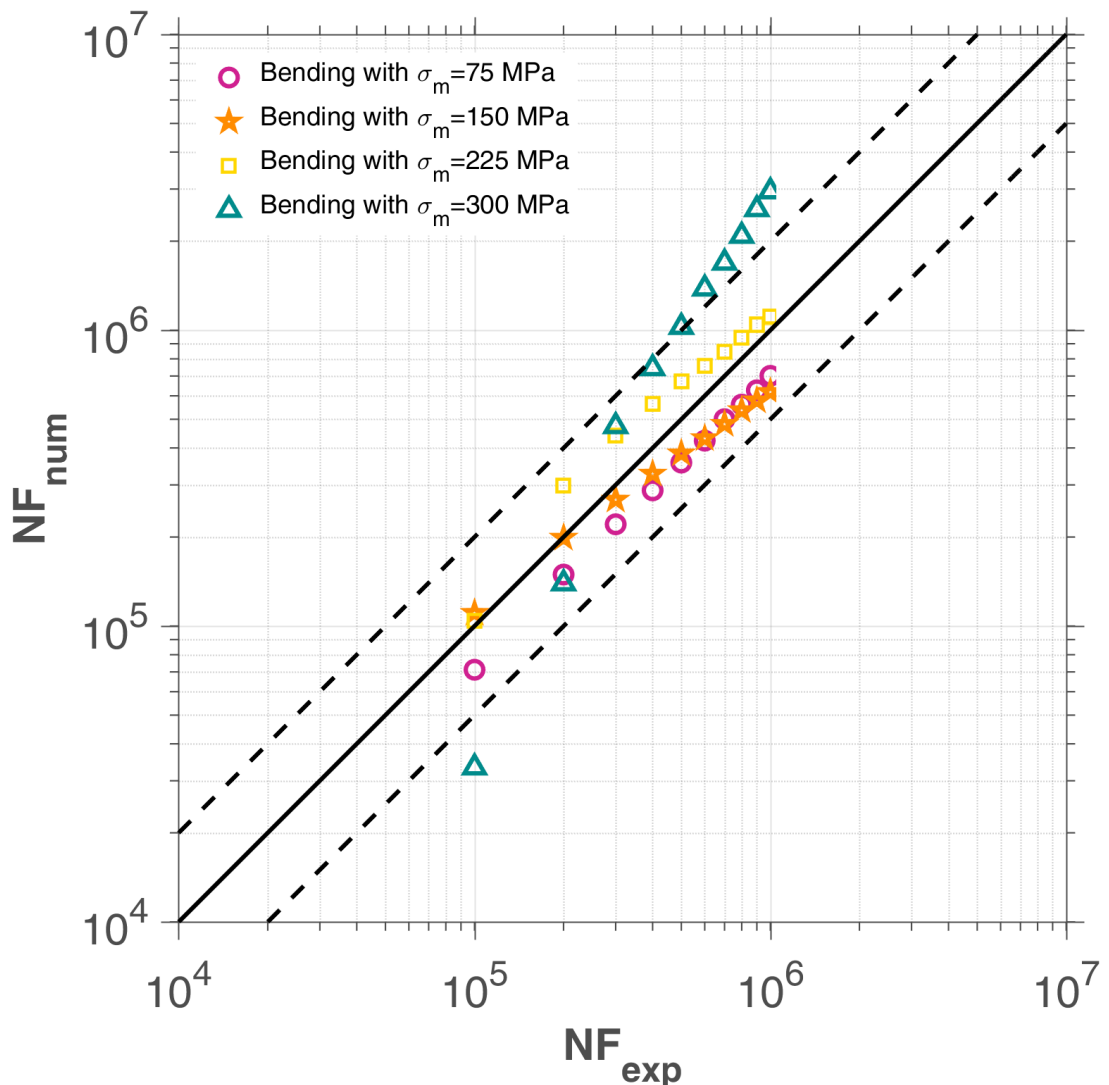


Figure 6.23 – Calibration on 10HNAP steel, bending tests with various mean stress on 10HNAP, data from Tab.6.25 and results obtained with the coefficients of Tab.6.28. For the case of $\sigma_m = 300$ MPa, the macroscopic maximum stress is greater than yield limit, which does not match our assumption that the material stays in elastic regime macroscopically (section 5.4.1).

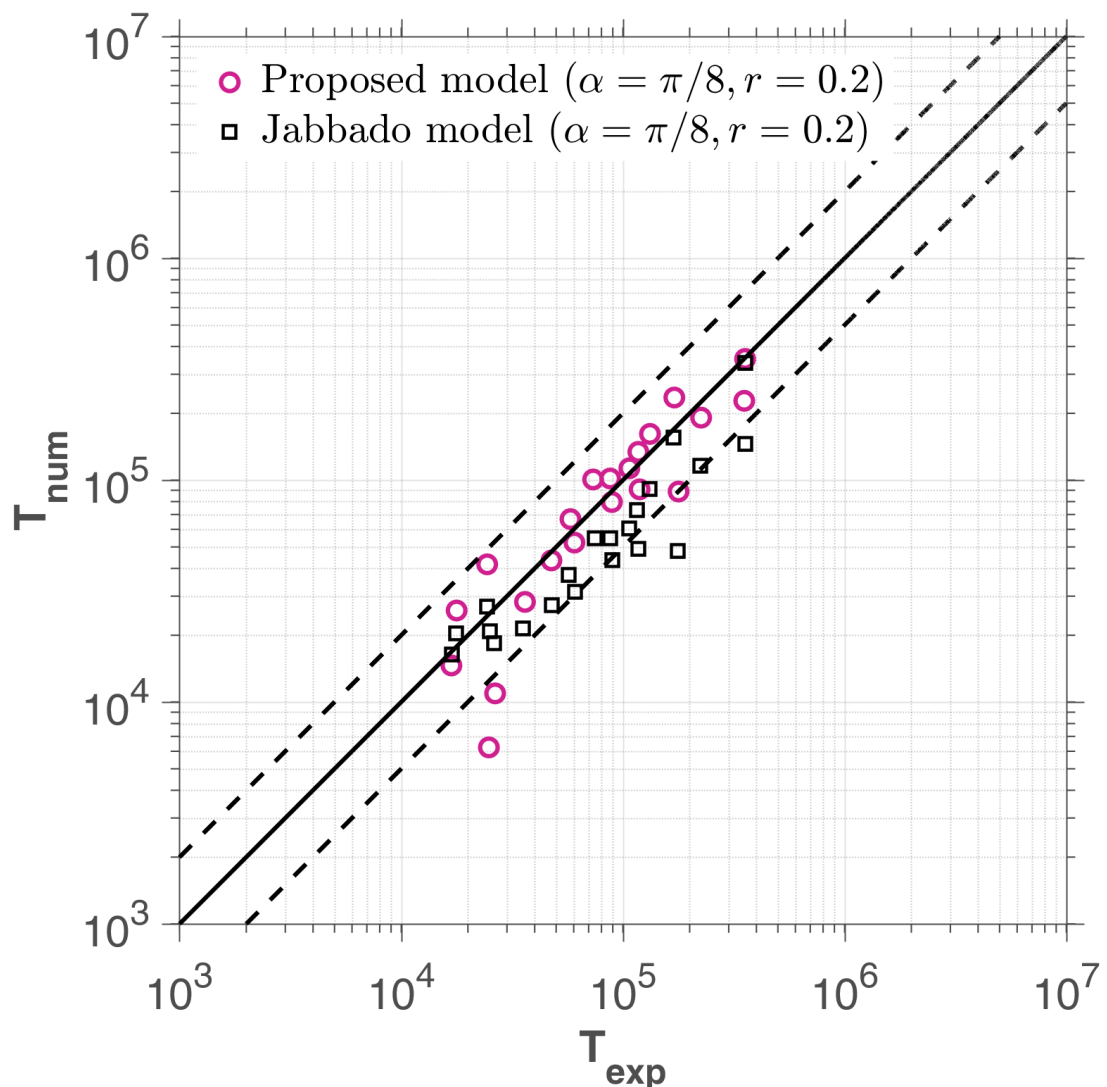


Figure 6.24 – Random bending-torsion 2D tests on 10HNAP, data from Tab.6.26 and [Jabbado \[2006\]](#). Results are obtained with the coefficients of Tab.6.29 ($\alpha_M = \pi/8$ and $r = 0.2$)

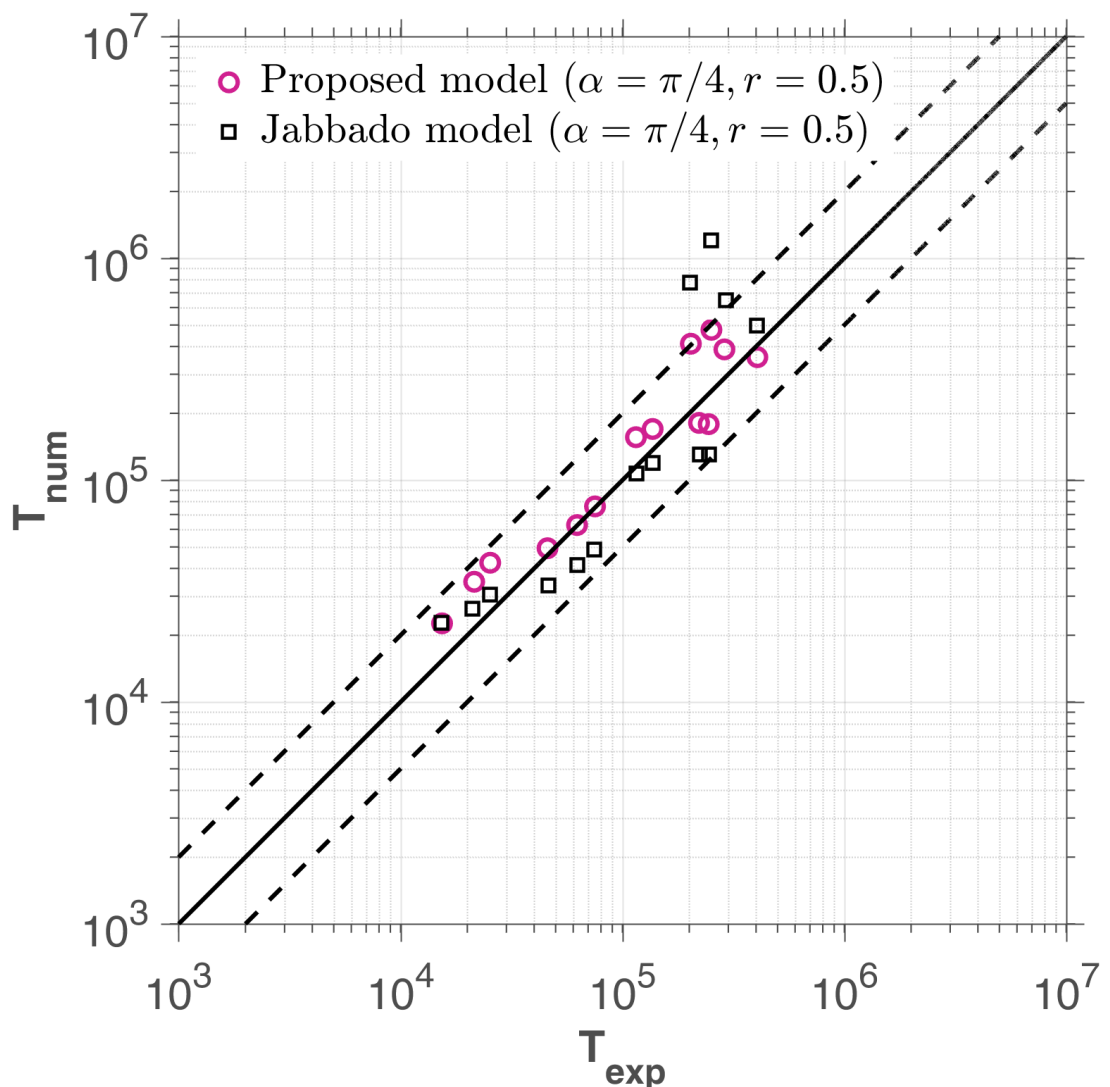


Figure 6.25 – Random bending-torsion 2D tests on 10HNAP, data from Tab.6.27 and Jabbado [2006]. Results are obtained with the coefficients of Tab.6.29 ($\alpha_M = \pi/4$ and $r = 0.5$)

6.6 Conclusions

We work on the stress tensor directly in 3D analysis in stead of using the multidimensional equivalent stress. The strategy can be made more complex by introducing a local space averaging process in the calculation of the local damage, and by taking more general plastic flows. The energy based fatigue approach takes into account impurities and hardness in the material and is applicable to any type of micro plasticity law and multiaxial load geometry. The time implicit strategy gets rid of cycle counting which is hardly applicable to complex loading, big fluctuation is magnified which reflects the real situation.

There are several advantages and drawbacks of our proposed model. The time implicit method does not take the unit of cycle so as to avoid cycle counting and relevant methods such as rain-flow filter. The possibility to handle different S-N curves corresponding to various materials and load conditions via changing the parameters. We also have the random loading suitability with nonlinear damage accumulation. The drawback is this strategy requires a scale by scale analysis which can be complicated for very high cycle fatigue. However, as introduced above, we can use the optimal time step method to calculate precisely the representative loading history sequence and use scalar integration for the rest of fatigue life. In this way the numerical cost can be dramatically reduced without losing the precision.

Since our method is based on the Dang Van paradigm, to deal with mean stress effect and multiaxial loads we only have the parameter λ_{+-} , which is insufficient to fit the experiments. In fact, our microplasticity model is probably too crude to handle situations where there is a clear strain path effect.

Also, we need more experimental data and comparison with other results from the literature.

7

General conclusions

Contents

Appendices	161
.1 DETAILED EXPLOITATION	161
.2 MATLAB CODE LISTING	165

This study was devoted to the development of a phenomenological and deterministic model of lifetime prediction of structures working in limited endurance under multiaxial stresses of variable amplitude without resorting to the counting of cycles. Special attention is paid to the model so that it can be applied to a wide variety of metallic materials and easy to use in design offices.

We develop a streamlined formulation of gradient multiaxial fatigue criteria extending the classical HCF criteria. The objective is to model the "size", surface gradient and loading effects by taking into account just the dominant gradient effect. Basing on some experimental observations, and departing from classical fatigue criteria, new class of criteria with stress gradient terms entering not only in the normal stress but also in the shear stress amplitude, are proposed. Such a formulation allows the new criteria to capture the "size" and gradient effects, and to cover a large range of loading mode (traction, bending, shearing). These new criteria are then generalized to multiaxial cases to capture both well-known phenomena "Smaller is Stronger" and "Higher Gradient is Stronger" and thus can reproduce fatigue experimental data even at small scale. Extensions of some classical fatigue limit criteria such Crossland and Dang Van are done as illustrations. The proposed criteria shown a good agreement with a number of experiments from the literature.

Our work consisted firstly of describing the methods of calculation of life in limited endurance (finite lifetime regime). We have classified these methods according to the type of stress (uniaxial or multiaxial), the nature of the signal (with constant amplitude or variable amplitude) and whether or not to adopt a cycle counting. It was found that the mesoscopic approach, initiated by Dang Van ([Dang Van et al. \[1986\]](#)) and developed later by Papadopoulos ([Papadopoulos \[2001\]](#)), gives a physical interpretation of polycyclic fatigue damage. Papadopoulos ([Papadopoulos \[2001\]](#)), Morel ([Morel \[1998\]](#)) and Zarka-Karaouni ([De Vasconcellos \[2013\]](#)) used it and chose cumulated mesoscopic plastic deformation as a variable of damage. The authors assumed that the break occurs when this variable reaches a critical value.

To construct the predictive model of lifetime, we adopted the mesoscopic approach (or macro-

meso approach) and used in part the ideas proposed by Papadopoulos and Morel. Indeed, we considered the mesoscopic plasticity induced energy accumulated on the stabilized cycle as variable of the damage. However, unlike the authors, the rupture is not linked to a critical value of the cumulated mesoscopic plastic deformation ϵ_s^{pc} , it is defined by a stochastic distribution of weak points which will undergo strong plastic yielding, which contribute to energy dissipation and cause damage, without affecting the overall macroscopic stress. Moreover, the criterion of plasticity at the mesoscopic scale is different. Indeed, the nucleation of microcracks and cracks is a complex phenomenon involving not only plasticity, but also the creation and growth of voids. Although the metallic plasticity is generally independent of the hydrostatic pressure, the growth of the voids depends on the hydrostatic pressure. For this purpose, we have chosen an elastoplastic model with linear kinematic hardening with a mesoscopic elastic limit dependent on the hydrostatic pressure to account for this influence.

A first approach using mesoscopic plastic deformation with a non-zero mean stress and a method of direct calculation of the mesoscopic stabilized cycle is formulated. The difficulty of obtaining an explicit formula for the simple mesoscopic plastic deformation of the stabilized cycle makes the procedure for identifying the parameters of the model complicated.

In limited endurance, the mesoscopic lifetime criterion was defined for the affine cyclic loads of constant amplitude as a power relation between the stress intensity on the stabilized cycle and the number of cycles at the crack initiation. This criterion was used to identify model parameters using simple loads. An extension of this law to consider the repeated multiaxial loading sequences of variable amplitude is done via a damage factor D depending on energy dissipation and certain parameters characteristic of the material and the loading. Failure is assumed when $D = 1$.

The dissipated energy to failure per defect W_0 is directly related to the fatigue life scaling. Weakening scales distribution exponent β controls the distribution of weakening scales leading to defining the slope of S-N curve. β also takes into account the major damage effect mentioned above. λ is the hydrostatic pressure sensitivity of the elastoplastic material on the mesoscopic scale. a controls the speed of non-linear damage accumulation. The identification of these parameters involves two steps:

1. Application of the method to the uniaxial case to get 1D best fit (in bending and in torsion): this mainly leads to the identification of β , which will be used later in an optimization problem.
2. Identification of all parameters of the model by solving a least-square optimization problem (previously obtained relationships): this is to minimize the error between the simulated curve and the experimental Wöhler curve of a test.

The procedure for identifying model parameters requires knowledge of a Wöhler curve (ideally in symmetrical alternate bending) and mean stress effect on fatigue life.

To validate the model, we simulated fatigue tests from the literature and carried out on smooth specimens of four materials (aluminum Al 6082 T6, steel 30NCD16, steel SM45C and steel 10 HNAP) under multiaxial loadings of constant and variable amplitudes.

A good correlation of the model prediction results with the experimental results was obtained for the proportional loads used, either at constant amplitude or at variable amplitude. The results of prediction are worse for tests carried out on aluminum Al 6082 T6 under non-proportional loads of constant amplitude.

In addition, the model has been applied to study the fatigue strength of AW-6106 T6 aluminum carried out by CETIM (Centre Technique des Industries Mécaniques) under two constant and random signals. The results showed that, in the absence of major damage effect, the life time prediction of the material under random loading is worse.

The most immediate prospects are validation of the model for different out-of-phase or non-proportional paths. Its application to other industrial structures with a comparison with experimental results is essential for its use in design offices.

Acknowledgments

We are grateful for the financial and technical support of Chaire PSA.

References

- K Dang Van. *Introduction to Fatigue Analysis in Mechanical Design by the Multiscale Approach*, pages 57–88. Springer Vienna, Vienna, 1999. ISBN 978-3-7091-2474-1. doi: 10.1007/978-3-7091-2474-1_2. URL https://doi.org/10.1007/978-3-7091-2474-1_2.
- IV Papadopoulos. *Fatigue limit of metals under multiaxial stress conditions: the microscopic approach*. Joint Research Centre, ISEI, 1993.
- Tadeusz Łagoda, Ewald Macha, and Włodzimierz Bedkowski. A critical plane approach based on energy concepts: application to biaxial random tension-compression high-cycle fatigue regime. *International Journal of Fatigue*, 21(5):431–443, 1999.
- Imade Koutiri. *Effet des fortes contraintes hydrostatiques sur la tenue en fatigue des matériaux métalliques*. PhD thesis, Arts et Métiers ParisTech, 2011.
- F. Morel. A critical plane approach for life prediction of high cycle fatigue under multiaxial variable amplitude loading. *International Journal of Fatigue*, 22(2):101 – 119, 2000. ISSN 0142-1123. doi: [http://dx.doi.org/10.1016/S0142-1123\(99\)00118-8](http://dx.doi.org/10.1016/S0142-1123(99)00118-8). URL <http://www.sciencedirect.com/science/article/pii/S0142112399001188>.
- R. G. Pogoretskii. Effect of test piece length on the fatigue strength of steel in air. *Soviet materials science : a transl. of Fiziko-khimicheskaya mehanika materialov / Academy of Sciences of the Ukrainian SSR*, 1(1):63–66, 1966. ISSN 1573-885X. doi: 10.1007/BF00714989. URL <http://dx.doi.org/10.1007/BF00714989>.
- Bastien Weber. *Fatigue multiaxiale des structures industrielles sous chargement quelconque*. PhD thesis, Lyon, INSA, 1999.
- Ioannis V. Papadopoulos and Vassilis P. Panoskaltsis. Invariant formulation of a gradient dependent multiaxial high-cycle fatigue criterion. *Engineering Fracture Mechanics*, 55(4):513 – 528, 1996. ISSN 0013-7944. doi: [http://dx.doi.org/10.1016/S0013-7944\(96\)00047-1](http://dx.doi.org/10.1016/S0013-7944(96)00047-1). URL <http://www.sciencedirect.com/science/article/pii/S0013794496000471>.
- Charles Massonnet. Le dimensionnement des pièces de machines soumises à la fatigue : contribution expérimentale à l'étude de l'effet de l'échelle et des entailles. *Revue Universelle des Mines*, 9: 203–222, 1955.
- H.F. Moore and D. Morkovin. Third progress report on the effect of size of specimen on fatigue strength of three types of steel. *ASTM (American Society for Testing and Materials International)*, (44):137–158, 1944.
- William Nichols Findley, JJ Coleman, and BC Hanley. *Theory for Combined Bending and Torsion Fatigue with Data for SAE4340 Steel*. Division of Engineering, Brown University, 1956.

- Luca Susmel and Nicola Petrone. Multiaxial fatigue life estimations for 6082-t6 cylindrical specimens under in-phase and out-of-phase biaxial loadings. *European Structural Integrity Society*, 31:83–104, 2003.
- Yuhui Huang, Shan-Tung Tu, and Fu-Zhen Xuan. Pit to crack transition behavior in proportional and non-proportional multiaxial corrosion fatigue of 304 stainless steel. *Engineering Fracture Mechanics*, 184(Supplement C):259 – 272, 2017. ISSN 0013-7944. doi: <https://doi.org/10.1016/j.engfracmech.2017.08.019>. URL <http://www.sciencedirect.com/science/article/pii/S0013794417306653>.
- Multiaxial strain-life technical background. <https://www.efatigue.com/multiaxial/background/strainlife.html>.
- L DUBAR. Fatigue multiaxiale des aciers - passage de lendurance à lendurance limitée -prise en compte des accidents géométriques. *Thèse de Doctorat, Ecole Nationale Supérieure d'Arts et Métiers, Talence, France.*, 1992.
- Soon-Bok Lee. Out-of-phase combined bending and torsion fatigue of steels. *ICBMFF2*, 2013.
- Andrea Carpinteri, Andrea Spagnoli, and Sabrina Vantadoni. A multiaxial fatigue criterion for random loading. *Fatigue & Fracture of Engineering Materials & Structures*, 26(6):515–522, 2003.
- Mohamad Jabbado. *High-Cycle Fatigue of Metallic Structures : Lifetime Duration under Variable Loadings*. Theses, Ecole Polytechnique X, March 2006. URL <https://pastel.archives-ouvertes.fr/pastel-00002116>.
- Włodzimierz Bedkowski. Determination of the critical plane and effort criterion in fatigue life evaluation for materials under multiaxial random loading. experimental verification based on fatigue tests of cruciform specimens. page s.435447, 1994.
- E. VIDAL. Prévision de la durée de vie en fatigue multiaxiale sous sollicitations d'amplitude variable à laide dun critère global.
- Robert Stone. Fatigue life estimates using goodman diagrams. *Retrieved August*, 17:2012, 2012.
- Christian Rudolf Sohar. *Lifetime controlling defects in tool steels*. Springer Science & Business Media, 2011.
- Bernard Crossland. Effect of large hydrostatic pressures on the torsional fatigue strength of an alloy steel. In *Proc. Int. Conf. on Fatigue of Metals*, volume 138. Institution of Mechanical Engineers London, 1956.
- G Sines. Behavior of metals under complex static and alternating stresses. *Metal fatigue*, 1:145–169, 1959.
- F Morel. A fatigue life prediction method based on a mesoscopic approach in constant amplitude multiaxial loading. *Fatigue and Fracture of Engineering Materials and Structures*, 21(3):241–256, 1998. ISSN 1460-2695. doi: 10.1046/j.1460-2695.1998.00452.x. URL <http://dx.doi.org/10.1046/j.1460-2695.1998.00452.x>.
- Huyen Nguyen Thi Thu. *Effet des hétérogénéités microstructurales sur le comportement en fatigue multiaxiale à grand nombre de cycles: application à l'usinage assisté laser*. PhD thesis, Arts et Métiers ParisTech, 2008.

- Nghiem Dang Van. The khmu in viet nam. *Vietnamese studies*, 36(2):62–140, 1973.
- JD Findley. Behavior output under chained fixed-ratio requirements in a 24-hour experimental space. In *Journal of the Experimental Analysis of Behavior*, volume 2, pages 258–258. SOC EXP ANALYSIS BEHAVIOR INC INDIANA UNIV DEPT PSYCHOLOGY, BLOOMINGTON, IN 47405, 1959a.
- J Liu and H Zenner. Berechnung der dauerschwingfestigkeit bei mehrachsiger beanspruchungsteil 1. *Materialwissenschaft und Werkstofftechnik*, 24(7):240–249, 1993.
- Ioannis V. Papadopoulos, Piermaria Davoli, Carlo Gorla, Mauro Filippini, and Andrea Bernasconi. A comparative study of multiaxial high-cycle fatigue criteria for metals. *International Journal of Fatigue*, 19(3):219 – 235, 1997. ISSN 0142-1123. doi: [http://dx.doi.org/10.1016/S0142-1123\(96\)00064-3](http://dx.doi.org/10.1016/S0142-1123(96)00064-3). URL <http://www.sciencedirect.com/science/article/pii/S0142112396000643>.
- K Dang Van, G Cailletaud, JF Flavenot, A Le Douaron, and HP Lieurade. Criterion for high-cycle fatigue failure under multiaxial loading. In *ICBMFF2*, 1986.
- P Ballard, K Dang Van, A Deperrois, and YV Papadopoulos. High cycle fatigue and a finite element analysis. *Fatigue & Fracture of Engineering Materials & Structures*, 18(3):397–411, 1995.
- Ioannis V Papadopoulos. Long life fatigue under multiaxial loading. *International Journal of Fatigue*, 23(10):839–849, 2001.
- E Macha and CM Sonsino. Energy criteria of multiaxial fatigue failure. *Fatigue and Fracture of Engineering Materials and Structures*, 22(12):1053–1070, 1999.
- Fernand Ellyin. A criterion for fatigue under multiaxial states of stress. *Mechanics Research Communications*, 1(4):219–224, 1974.
- Mark F Lefebvre. Cognitive distortion and cognitive errors in depressed psychiatric and low back pain patients. *Journal of consulting and clinical psychology*, 49(4):517, 1981.
- F Ellyin, K Golos, and Z Xia. In-phase and out-of-phase multiaxial fatigue. *ASME J. Eng. Mater. Technol*, 113:112, 1991.
- C Froustey, S Lasserre, and L Dubar. Validité des critères de fatigue multiaxiale à lendurance en flexion-torsion. pages Mat–Tech 92, IITT–International, France, 79–85, 1992.
- Thierry Palin-Luc. *Fatigue multiaxiale d'une fonte GS sous sollicitations combinées d'amplitude variable*. PhD thesis, 1996.
- Alexis Banvillet. Prévision de durée de vie en fatigue multiaxiale sous chargements réels: vers des essais accélérés. *These de Doctorat*, 2001.
- JL Chaboche and PM Lesne. A non-linear continuous fatigue damage model. *Fatigue & fracture of engineering materials & structures*, 11(1):1–17, 1988a.
- Thierry Palin-Luc and Serge Lasserre. An energy based criterion for high cycle multiaxial fatigue. *European Journal of Mechanics-A/Solids*, 17(2):237–251, 1998.
- Jérôme Benabes. *Approche énergétique non locale du calcul de durée de vie de structures en fatigue multiaxiale sous chargements d'amplitude variable: application à une roue de train ferroviaire*. PhD thesis, Arts et Métiers ParisTech, 2006.

- Fernand Ellyin. *Fatigue damage, crack growth and life prediction*. Springer Science & Business Media, 2012.
- Alexis Banville, Thierry Palin-Luc, and Serge Lasserre. A volumetric energy based high cycle multiaxial fatigue criterion. *International Journal of Fatigue*, 25(8):755–769, 2003a.
- NE Dowling. Fatigue life prediction for complex load versus time histories. *Journal of Engineering Materials and Technology*, 105(3):206–214, 1983.
- J Lemaitre, JP Sermage, and R Desmorat. A two scale damage concept applied to fatigue. *International Journal of fracture*, 97(1):67–81, 1999.
- J Lemaitre and Jean Louis Chaboche. Mécanique des matériaux solides. 1985.
- Laurent Flacelière. *Contribution a la modélisation du dommage en fatigue multiaxiale dun acier C36: confrontation à l'expérience*. PhD thesis, Poitiers, 2004.
- Vincent Monchiet. *Contributions à la modélisation micromécanique de l'endommagement et de la fatigue des métaux ductiles*. PhD thesis, Lille 1, 2006.
- Arthur L Gurson et al. Continuum theory of ductile rupture by void nucleation and growth: Part iyield criteria and flow rules for porous ductile media. *Journal of engineering materials and technology*, 99(1):2–15, 1977.
- J-B Leblond, G Perrin, and J Devaux. An improved gurson-type model for hardenable ductile metals. *European journal of mechanics. A. Solids*, 14(4):499–527, 1995.
- U Essmann and H Mughrabi. Annihilation of dislocations during tensile and cyclic deformation and limits of dislocation densities. *Philosophical Magazine A*, 40(6):731–756, 1979.
- E Charkaluk, A Constantinescu, H Maïtournam, and K Dang Van. Revisiting the dang van criterion. *Procedia Engineering*, 1(1):143–146, 2009.
- E Charkaluk and A Constantinescu. Approche dissipative en fatigue: influence de la contrainte moyenne en fatigue polycyclique. In *Proceedings National MECAMAT Symposium*, 2007.
- Ma Zepeng, Patrick Le Tallec, and Habibou Maitournam. Multi-axial fatigue criteria with length scale and gradient effects. *Procedia Engineering*, 133:60–71, 2015.
- John B Wachtman, W Roger Cannon, and M John Matthewson. *Mechanical properties of ceramics*. John Wiley & Sons, 2009.
- Subra Suresh. *Fatigue of materials*. Cambridge university press, 1998.
- Duy-Hao Luu, MH Maitournam, and QS Nguyen. Formulation of gradient multiaxial fatigue criteria. *International Journal of Fatigue*, 61:170–183, 2014.
- R. Amargier, S. Fouvry, L. Chambon, C. Schwob, and C. Poupon. Stress gradient effect on crack initiation in fretting using a multiaxial fatigue framework. *International Journal of Fatigue*, 32(12):1904 – 1912, 2010. ISSN 0142-1123. doi: <http://dx.doi.org/10.1016/j.ijfatigue.2010.06.004>. URL <http://www.sciencedirect.com/science/article/pii/S0142112310001404>.
- Mahaman Habibou Maitournam, Ky Dang Van, and Jean-François Flavenot. Fatigue design of notched components with stress gradients and cyclic plasticity. *Advanced Engineering Materials*, 11(9):750–754, 2009.

- David Taylor. *The theory of critical distances: a new perspective in fracture mechanics*. Elsevier, 2010.
- J.A. Araújo, L. Susmel, D. Taylor, J.C.T. Ferro, and E.N. Mamiya. On the use of the theory of critical distances and the modified wöhler curve method to estimate fretting fatigue strength of cylindrical contacts. *International Journal of Fatigue*, 29(1):95 – 107, 2007. ISSN 0142-1123. doi: <http://dx.doi.org/10.1016/j.ijfatigue.2006.02.041>. URL <http://www.sciencedirect.com/science/article/pii/S0142112306000776>.
- JF Flavenot and N Skalli. Lépaisseur de couche critique ou une nouvelle approche du calcul en fatigue des structures soumises à des sollicitations multiaxiales. *Mec. Mater. Electr*, 397:15–25, 1983.
- T Palin-Luc. Stress gradient and size effects in multiaxial fatigue. *Materials Week (Munich, Germany)*, 2000.
- A. Banville, T. Palin-Luc, and S. Lasserre. A volumetric energy based high cycle multiaxial fatigue criterion. *International Journal of Fatigue*, 25(8):755 – 769, 2003b. ISSN 0142-1123. doi: [http://dx.doi.org/10.1016/S0142-1123\(03\)00048-3](http://dx.doi.org/10.1016/S0142-1123(03)00048-3). URL <http://www.sciencedirect.com/science/article/pii/S0142112303000483>.
- Charles Massonnet. The effect of size, shape and grain size on the fatigue strength of medium carbon steel. *ASTM (American Society for Testing and Materials Int)*, pages 954–78, 1956.
- R. Ferré, S. Fouvry, B. Berthel, and J.-A. Ruiz-Sabariego. Stress gradient effect on the crack nucleation process of a tibal4v titanium alloy under fretting loading: Comparison between non-local fatigue approaches. *International Journal of Fatigue*, 54:56 – 67, 2013. ISSN 0142-1123. doi: <https://doi.org/10.1016/j.ijfatigue.2013.03.005>. URL <http://www.sciencedirect.com/science/article/pii/S0142112313000844>.
- Jean Lemaitre and Jean-Louis Chaboche. *Mechanics of solid materials*. Cambridge university press, 1990.
- J. L. Chaboche and P. M. Lesne. A non-linear continuous fatigue damage model. *Fatigue , Fracture of Engineering Materials , Structures*, 11(1):1–17, 1988b. ISSN 1460-2695. doi: 10.1111/j.1460-2695.1988.tb01216.x. URL <http://dx.doi.org/10.1111/j.1460-2695.1988.tb01216.x>.
- Lu Xi and Zheng Songlin. Strengthening of transmission gear under low-amplitude loads. *Materials Science and Engineering: A*, 488(1):55–63, 2008.
- Lu Xi and Zheng Songlin. Strengthening and damaging under low-amplitude loads below the fatigue limit. *International Journal of Fatigue*, 31(2):341–345, 2009a.
- Lu Xi and Zheng Songlin. Changes in mechanical properties of vehicle components after strengthening under low-amplitude loads below the fatigue limit. *Fatigue & Fracture of Engineering Materials & Structures*, 32(10):847–855, 2009b.
- GM Sinclair. An investigation of the coaxing effect in fatigue of metals. Technical report, DTIC Document, 1952.
- Masaki Nakajima, Jae Woong Jung, Yoshihiko Uematsu, and Keiro Tokaji. Coaxing effect in stainless steels and high-strength steels. *Key Engineering Materials*, 345:235–238, 2007.

ASTM. Standard practices for cycle fatigue counting in fatigue analysis. *Designation E 1049-85, vol. 03.01 of Metal Test Methods and Analytical procedure.*, pages 836–848, 1985.

W.M. Findley. *Engng. Industry*, 81(4):301, 1959b.

Ernst Melan. Zur plastizität des räumlichen kontinuums. *Archive of Applied Mechanics*, 9(2):116–126, 1938.

Richard M Christensen. Yield functions, damage states, and intrinsic strength. *Mathematics and Mechanics of Solids*, 5(3):285–300, 2000.

M.H. Maitournam, C. Krebs, and A. Galtier. A multiscale fatigue life model for complex cyclic multiaxial loading. *International Journal of Fatigue*, 33(2):232 – 240, 2011. ISSN 0142-1123. doi: <http://dx.doi.org/10.1016/j.ijfatigue.2010.08.017>. URL <http://www.sciencedirect.com/science/article/pii/S0142112310001933>.

Stefano Bosia and Andrei Constantinescu. Fast time-scale average for a mesoscopic high cycle fatigue criterion. *International Journal of Fatigue*, 45:39 – 47, 2012. ISSN 0142-1123. doi: <http://dx.doi.org/10.1016/j.ijfatigue.2012.06.015>. URL <http://www.sciencedirect.com/science/article/pii/S0142112312002162>.

Ma Zepeng. Structures under multiaxial fatigue taking consideration of gradients of the constraints with time and space variation, 2017.

Legendre Gauss Quadrature weights and nodes. <https://www.mathworks.com/matlabcentral/fileexchange/4540-legendre-gauss-quadrature-weights-and-nodes>. Accessed: 2004-05-11.

BEDKOWSKY-W. GRZELAK J. MACHA E. ACHTELIC, H. Fatigue life of 10hnap steel under synchronous random bending and torsion. page 421434, 1994.

Davi Silva De Vasconcellos. *Comportement en fatigue avant et après impact de composites tissés chanvre/époxy*. PhD thesis, ISAE-ENSMA Ecole Nationale Supérieure de Mécanique et d'Aérotechnique-Poitiers, 2013.

Appendices

1 DETAILED EXPLOITATION

*
* A DETAILED DESCRIPTION OF ANALYTICAL EXPLOITATION ON UNIAXIAL CYCLE
*

Phase 1: The deviatoric stress amplitude increases from σ_y/s to S_a .

The material is in local plastic regime, then $\dot{\varepsilon}^p > 0$ and $\dot{\sigma} - \dot{b} = 0 \Rightarrow \dot{\Sigma} - \frac{E}{1+\nu}\dot{\varepsilon}^p = \frac{kE}{E-k}\dot{\varepsilon}^p \Rightarrow$

$$\dot{\varepsilon}^p = \frac{(E-k)(1+\nu)}{E(E+k\nu)}\dot{\Sigma}.$$

$$\Rightarrow \dot{\varepsilon}^p \text{ varies from 0 to } \frac{(E-k)(1+\nu)(S_a - \sigma_y/s)}{E(E+k\nu)}.$$

From Taylor-Lin scale transition model:

$$\dot{\sigma} = \dot{\Sigma} - \frac{E}{1+\nu}\dot{\varepsilon}_p = \dot{\Sigma} - \frac{E-k}{E+\nu k}\dot{\Sigma} = \frac{k(1+\nu)}{E+\nu k}\dot{\Sigma}.$$

$$\Rightarrow \sigma \text{ varies from } \sigma_y/s \text{ to } \sigma_y/s + \frac{k(1+\nu)(S_a - \sigma_y/s)}{E+\nu k}.$$

$$\dot{b} = \dot{\Sigma} - \frac{E}{1+\nu}\dot{\varepsilon}_p = \dot{\Sigma} - \frac{E-k}{E+\nu k}\dot{\Sigma} = \frac{k(1+\nu)}{E+\nu k}\dot{\Sigma}.$$

$$\Rightarrow b \text{ varies from 0 to } \frac{k(1+\nu)(S_a - \sigma_y/s)}{E+\nu k}.$$

So the energy dissipation rate is:

$$(\sigma - b)\dot{\varepsilon}^p = \frac{\sigma_y}{s}\dot{\varepsilon}^p = \frac{\sigma_y}{s}\frac{(E-k)(1+\nu)}{E(E+k\nu)}\dot{\Sigma}.$$

The energy dissipation is:

$$(\sigma - b)\Delta\varepsilon^p = \frac{\sigma_y}{s}\frac{(E-k)(1+\nu)(S_a - \sigma_y/s)}{E(E+k\nu)}.$$

Phase 2: The deviatoric stress amplitude decreases from S_a to $S_a - 2\sigma_y/s$.

The material is in local elastic regime, then $\dot{\varepsilon}^p = 0$ and $\dot{\sigma} - \dot{b} = 0 \Rightarrow$

$$\dot{b} = 0, \dot{\sigma} = \dot{\Sigma} - \frac{E}{1+\nu}\dot{\varepsilon}_p = \dot{\Sigma}.$$

$$\sigma \text{ varies from } \sigma_y/s + \frac{k(1+\nu)(S_a - \sigma_y/s)}{E+\nu k} \text{ to } -\sigma_y/s + \frac{k(1+\nu)(S_a - \sigma_y/s)}{E+\nu k}.$$

$\sigma - b$ varies from σ_y/s to $-\sigma_y/s$.

The energy dissipation rate is:

$$(\sigma - b)\dot{\varepsilon}^p = 0.$$

Phase 3: The deviatoric stress amplitude decreases from $S_a - 2\sigma_y/s$ to $-S_a$.

The material is in local plastic regime, then $\dot{\varepsilon}^p > 0$ and $\dot{\sigma} - \dot{b} = 0 \Rightarrow$

$$\dot{\varepsilon}^p = \frac{(E-k)(1+\nu)}{E(E+k\nu)}\dot{\Sigma}$$

as opposite to phase 1 for $\dot{\Sigma} < 0$.

$$\Rightarrow \dot{\varepsilon}^p \text{ varies from } \frac{(E - k)(1 + \nu)(S_a - \sigma_y/s)}{E(E + k\nu)} \text{ to } \frac{(E - k)(1 + \nu)(S_a - \sigma_y/s - S_a - (S_a - 2\sigma_y/s))}{E(E + k\nu)} = -\frac{(E - k)(1 + \nu)(S_a - \sigma_y/s)}{E(E + k\nu)}.$$

From Taylor-Lin scale transition model:

$$\dot{\sigma} = \dot{\Sigma} - \frac{E}{1 + \nu} \dot{\varepsilon}_p = \dot{\Sigma} - \frac{E - k}{E + \nu k} \dot{\Sigma} = \frac{k(1 + \nu)}{E + \nu k} \dot{\Sigma}.$$

$$\Rightarrow \sigma \text{ varies from } -\sigma_y/s + \frac{k(1 + \nu)(S_a - \sigma_y/s)}{E + \nu k} \text{ to } -\sigma_y/s - \frac{k(1 + \nu)(S_a - \sigma_y/s)}{E + \nu k}.$$

$$\dot{b} = \dot{\Sigma} - \frac{E}{1 + \nu} \dot{\varepsilon}_p = \dot{\Sigma} - \frac{E - k}{E + \nu k} \dot{\Sigma} = \frac{k(1 + \nu)}{E + \nu k} \dot{\Sigma}.$$

$$\Rightarrow b \text{ varies from } \frac{k(1 + \nu)(S_a - \sigma_y/s)}{E + \nu k} \text{ to } -\frac{k(1 + \nu)(S_a - \sigma_y/s)}{E + \nu k}.$$

So the energy dissipation rate is:

$$(\sigma - b) \dot{\varepsilon}^p = -\frac{\sigma_y}{s} \dot{\varepsilon}^p = -\frac{\sigma_y}{s} \frac{(E - k)(1 + \nu)}{E(E + k\nu)} \dot{\Sigma}.$$

The energy dissipation is:

$$(\sigma - b) \Delta \dot{\varepsilon}^p = -\frac{\sigma_y}{s} \frac{(E - k)(1 + \nu)(-2S_a + 2\sigma_y/s)}{E(E + k\nu)} = \frac{2\sigma_y}{s} \frac{(E - k)(1 + \nu)(S_a - \sigma_y/s)}{E(E + k\nu)}.$$

Phase 4: The deviatoric stress amplitude increases from $-S_a$ to $-S_a + 2\sigma_y/s$.

The material is in local elastic regime, then $\dot{\varepsilon}^p = 0$ and $\dot{\sigma} - \dot{b} = 0 \Rightarrow$

$$\dot{b} = 0, \dot{\sigma} = \dot{\Sigma} - \frac{E}{1 + \nu} \dot{\varepsilon}_p = \dot{\Sigma}.$$

$$\sigma \text{ varies from } -\sigma_y/s - \frac{k(1 + \nu)(S_a - \sigma_y/s)}{E + \nu k} \text{ to } \sigma_y/s - \frac{k(1 + \nu)(S_a - \sigma_y/s)}{E + \nu k}.$$

$\sigma - b$ varies from $-\sigma_y/s$ to σ_y/s .

So the energy dissipation rate is:

$$(\sigma - b) \dot{\varepsilon}^p = 0.$$

Phase 5: The deviatoric stress amplitude increases from $-S_a + 2\sigma_y/s$ to σ_y/s .

The material is in local plastic regime, then $\dot{\varepsilon}^p > 0$ and $\dot{\sigma} - \dot{b} = 0 \Rightarrow$

$$\dot{\varepsilon}^p = \frac{(E - k)(1 + \nu)}{E(E + k\nu)} \dot{\Sigma}$$

as in phase 1.

$$\Rightarrow \dot{\varepsilon}^p \text{ varies from } -\frac{(E - k)(1 + \nu)(S_a - \sigma_y/s)}{E(E + k\nu)} \text{ to } 0.$$

$$\dot{\sigma} = \dot{\Sigma} - \frac{E}{1 + \nu} \dot{\varepsilon}_p = \dot{\Sigma} - \frac{E - k}{E + \nu k} \dot{\Sigma} = \frac{k(1 + \nu)}{E + \nu k} \dot{\Sigma}.$$

$$\Rightarrow \sigma \text{ varies from } \sigma_y/s - \frac{k(1 + \nu)(S_a - \sigma_y/s)}{E + \nu k} \text{ to } \sigma_y/s.$$

$$\dot{b} = \dot{\Sigma} - \frac{E}{1+\nu} \dot{\varepsilon}_p = \dot{\Sigma} - \frac{E-k}{E+\nu k} \dot{\Sigma} = \frac{k(1+\nu)}{E+\nu k} \dot{\Sigma}.$$

$$\Rightarrow b \text{ varies from } -\frac{k(1+\nu)(S_a - \sigma_y/s)}{E+\nu k} \text{ to } 0.$$

So the energy dissipation rate is:

$$(\sigma - b) \dot{\varepsilon}^p = \frac{\sigma_y}{s} \dot{\varepsilon}^p = \frac{\sigma_y}{s} \frac{(E-k)(1+\nu)}{E(E+k\nu)} \dot{\Sigma}.$$

The energy dissipation is:

$$(\sigma - b) \Delta \varepsilon^p = \frac{\sigma_y}{s} \frac{(E-k)(1+\nu)(S_a - \sigma_y/s)}{E(E+k\nu)}.$$

From the three phase analysis in local plastic regime, the dissipated energy is like $dW(\text{phase1}) = \frac{1}{2} dW(\text{phase3}) = dW(\text{phase5})$ and the dissipation rate is like $d\dot{W}(\text{phase1}) = d\dot{W}(\text{phase3}) = d\dot{W}(\text{phase5})$.

$$d\dot{W} = \frac{(E-k)(1+\nu)}{E(E+\nu k)} \left(\frac{\sigma_y}{s} \right) \left| \text{dev} \dot{\Sigma} \right| \quad (1.1)$$

*

* MULTI-DIMENSIONAL PLASTIC AND ELASTIC REGIME ANALYSIS

*

Detailed calculation from Eq.(5.7.5) to Eq.(5.7.9):

At a certain scale s_i , after elimination of $\dot{\underline{\underline{\varepsilon}}}^p$, there are

$$\dot{\underline{\underline{S}}} - \dot{\underline{\underline{b}}} = dev\dot{\underline{\underline{\Sigma}}} - E\xi \left(\frac{1}{1+\nu} + \frac{k}{E-k} \right) \frac{\underline{\underline{S}} - \underline{\underline{b}}}{\|\underline{\underline{S}} - \underline{\underline{b}}\|}.$$

If we are at yield limit at $(t+dt)$, we get on the other hand:

$$\begin{aligned} (\underline{\underline{S}} - \underline{\underline{b}})(t+dt) &= (\underline{\underline{S}} - \underline{\underline{b}})(t) + (\dot{\underline{\underline{S}}} - \dot{\underline{\underline{b}}}) dt, \\ \|\underline{\underline{S}} - \underline{\underline{b}}\| &= (\sigma_y - \lambda\sigma_H)/s_i. \end{aligned} \quad (1.2)$$

Replacing $(\dot{\underline{\underline{S}}} - \dot{\underline{\underline{b}}})$ in the integration by its expression we get:

$$(\underline{\underline{S}} - \underline{\underline{b}})(t+dt) = (\underline{\underline{S}} - \underline{\underline{b}})(t) + dev\dot{\underline{\underline{\Sigma}}}dt - E\xi dt \left(\frac{1}{1+\nu} + \frac{k}{E-k} \right) \frac{(\underline{\underline{S}} - \underline{\underline{b}})(t+dt)}{\|\underline{\underline{S}} - \underline{\underline{b}}\|(t+dt)} \quad (1.3)$$

Putting all terms with $(\underline{\underline{S}} - \underline{\underline{b}})(t+dt)$ on the left hand side, we get:

$$(\underline{\underline{S}} - \underline{\underline{b}})(t+dt)(1+\eta) = (\underline{\underline{S}} - \underline{\underline{b}})(t) + dev\dot{\underline{\underline{\Sigma}}}dt = (\underline{\underline{S}} - \underline{\underline{b}})_{trial}(t+dt) \quad (1.4)$$

with

$$\eta = \frac{E\xi dt}{\|\underline{\underline{S}} - \underline{\underline{b}}\|(t+dt)} \left(\frac{1}{1+\nu} + \frac{k}{E-k} \right). \quad (1.5)$$

To see whether the structure is in elastic or plastic regime at each time step, we use $(\underline{\underline{S}} - \underline{\underline{b}})_{trial}(t+dt)$ to compare with the yield stress at the same scale s_i , thus to give a value to $(\underline{\underline{S}} - \underline{\underline{b}})(t+dt)$.

Since $(\underline{\underline{S}} - \underline{\underline{b}})(t+dt)$ is in the same direction as $(\underline{\underline{S}} - \underline{\underline{b}})_{trial}(t+dt)$, we have

$$(\underline{\underline{S}} - \underline{\underline{b}})(t+dt) = (\sigma_y - \lambda\sigma_H)/s \frac{(\underline{\underline{S}} - \underline{\underline{b}})_{trial}(t+dt)}{\|\underline{\underline{S}} - \underline{\underline{b}}\|_{trial}(t+dt)} \quad (1.6)$$

We now compare Eq.(1.4) and Eq.(1.6), the only solution is to have:

$$1 + \eta = \frac{\|\underline{\underline{S}} - \underline{\underline{b}}\|_{trial}}{(\sigma_y - \lambda\sigma_H)/s} \quad (1.7)$$

that is:

$$\eta = \frac{\|\underline{\underline{S}} - \underline{\underline{b}}\|_{trial}}{(\sigma_y - \lambda\sigma_H)/s} - 1 \quad (1.8)$$

which is positive in plastic regime.

```
*****
* TRANSITION FROM SPHERICAL TO CARTESIAN COORDINATE SYSTEM
* (TO GENERATE 3D STRESS TENSOR FROM PSA DATA)
* ****
```

$$\begin{aligned}
\underline{\underline{\Sigma}} &= \frac{F_z}{A} \underline{e}_1 \otimes \underline{e}_1 + c_x \frac{F_x}{A} \underline{e}_\alpha \otimes \underline{e}_\alpha + c_y \frac{F_y}{A} \underline{e}_\beta \otimes \underline{e}_\beta \\
&= \frac{F_z}{A} \underline{e}_1 \otimes \underline{e}_1 + c_x \frac{F_x}{A} (\cos\theta_x \underline{e}_1 + \sin\theta_x \cos\varphi_x \underline{e}_2 + \sin\theta_x \sin\varphi_x \underline{e}_3) \otimes \\
&\quad (\cos\theta_x \underline{e}_1 + \sin\theta_x \cos\varphi_x \underline{e}_2 + \sin\theta_x \sin\varphi_x \underline{e}_3) \\
&\quad + c_y \frac{F_y}{A} (\cos\theta_y \underline{e}_1 + \sin\theta_y \cos\varphi_y \underline{e}_2 + \sin\theta_y \sin\varphi_y \underline{e}_3) \otimes (\cos\theta_y \underline{e}_1 + \sin\theta_y \cos\varphi_y \underline{e}_2 + \sin\theta_y \sin\varphi_y \underline{e}_3) \\
&= \left(\frac{F_z}{A} + c_x \frac{F_x}{A} \cos^2\theta_x + c_y \frac{F_y}{A} \cos^2\theta_y \right) \underline{e}_1 \otimes \underline{e}_1 \\
&\quad + \left(c_x \frac{F_x}{A} \cos\theta_x \sin\theta_x \cos\varphi_x + c_y \frac{F_y}{A} \cos\theta_y \sin\theta_y \cos\varphi_y \right) (\underline{e}_1 \otimes \underline{e}_2 + \underline{e}_2 \otimes \underline{e}_1) \\
&\quad + \left(c_x \frac{F_x}{A} \cos\theta_x \sin\theta_x \sin\varphi_x + c_y \frac{F_y}{A} \cos\theta_y \sin\theta_y \sin\varphi_y \right) (\underline{e}_1 \otimes \underline{e}_3 + \underline{e}_3 \otimes \underline{e}_1) \\
&\quad + \left(c_x \frac{F_x}{A} \sin^2\theta_x \cos^2\varphi_x + c_y \frac{F_y}{A} \sin^2\theta_y \cos^2\varphi_y \right) \underline{e}_2 \otimes \underline{e}_2 \\
&\quad + \left(c_x \frac{F_x}{A} \sin^2\theta_x \cos\varphi_x \sin\varphi_x + c_y \frac{F_y}{A} \sin^2\theta_y \cos\varphi_y \sin\varphi_y \right) (\underline{e}_2 \otimes \underline{e}_3 + \underline{e}_3 \otimes \underline{e}_2) \\
&\quad + \left(c_x \frac{F_x}{A} \sin^2\theta_x \sin^2\varphi_x + c_y \frac{F_y}{A} \sin^2\theta_y \sin^2\varphi_y \right) \underline{e}_3 \otimes \underline{e}_3
\end{aligned} \tag{1.9}$$

.2 MATLAB CODE LISTING

```

1 ****
2 *
3 * MATLAB code to integrate all scales using optimal time step strategy
4 *
5 ****
6 hydro(n+1)=1/3*trace(tensor);
7 if hydro(n+1)>=0
8 yield(n+1)=y-lamplus(end)*hydro(n+1); %yield stress at time step n+1
9 else
10 yield(n+1)=y-lamminus(end)*hydro(n+1);
11 end
12 scentre=[2*sigm/3 0 0 ; ...
13 0 -sigm/3 0 ; ...
14 0 0 -sigm/3];
15 devn=tensor-hydro(n+1)*eye(3)-scentre;
16 dev11g=devn(1,1); dev12g=devn(1,2); dev13g=devn(1,3);
17 dev21g=devn(2,1); dev22g=devn(2,2); dev23g=devn(2,3);
18 dev31g=devn(3,1); dev32g=devn(3,2); dev33g=devn(3,3);
19 Smax(n+1)=1/sqrt(2).*norm(devn,'fro');
20
21 trial11=bsxfun(@plus,Sb11,(dev11g-dev11)); trial12=bsxfun(@plus,Sb12,(dev12g-dev12)); trial13=bsxfun(@plus,Sb13,(dev13g-dev13));
22 trial21=bsxfun(@plus,Sb21,(dev21g-dev21)); trial22=bsxfun(@plus,Sb22,(dev22g-dev22)); trial23=bsxfun(@plus,Sb23,(dev23g-dev23));
23 trial31=bsxfun(@plus,Sb31,(dev31g-dev31)); trial32=bsxfun(@plus,Sb32,(dev32g-dev32)); trial33=bsxfun(@plus,Sb33,(dev33g-dev33));
24
25 trialtensor=[trial11; trial12; trial13; trial21; trial22; trial23; trial31;
26 ; trial32; trial33];
27 Smaxtrial=1/sqrt(2).*sqrt(sum(trialtensor.^2));
28 eta=bsxfun(@minus,bsxfun(@times,Smaxtrial/yield(n+1),s),1); %1*64
29 eta(eta<0)=0;
30
31 Sb11=bsxfun(@rdivide,trial11,bsxfun(@plus,eta,1));Sb12=bsxfun(@rdivide,
32 trial12,bsxfun(@plus,eta,1));Sb13=bsxfun(@rdivide,trial13,bsxfun(@plus,
33 ,eta,1));
34 Sb21=bsxfun(@rdivide,trial21,bsxfun(@plus,eta,1));Sb22=bsxfun(@rdivide,
35 trial22,bsxfun(@plus,eta,1));Sb23=bsxfun(@rdivide,trial23,bsxfun(@plus,
36 ,eta,1));
37 Sb31=bsxfun(@rdivide,trial31,bsxfun(@plus,eta,1));Sb32=bsxfun(@rdivide,
38 trial32,bsxfun(@plus,eta,1));Sb33=bsxfun(@rdivide,trial33,bsxfun(@plus,
39 ,eta,1));
40 Sbtensor=[Sb11; Sb12; Sb13; Sb21; Sb22; Sb23;Sb31; Sb32; Sb33];
41 normSb=1/sqrt(2).*sqrt(sum(Sbtensor.^2));
42
43 Ws=(bsxfun(@minus,Smaxtrial,bsxfun(@rdivide,yield(n+1),s))<=0).*...
44 (0)+...
45 (bsxfun(@minus,Smaxtrial,bsxfun(@rdivide,yield(n+1),s))>0).*...
46 (((E-k)*(1+nu)*(2*E*(E+k*nu))^-1*bsxfun(@times,weight,bsxfun(@rdivide,
47 bsxfun(@times,bsxfun(@minus,Smaxtrial,bsxfun(@rdivide,yield(n+1),s)),
48 yield(n+1)),s)));
49 W= sum(Ws);
50 W_accumulate(n+1)=W_accumulate(n)+W;

```

```

42 | sequence=((Smax(n+1)*yield(n+1)^-1)*(1-Smax(n+1)*yield(n+1)^-1)^-1)^fb ;
43 | sequence(sequence<0)=0;
44 | alp(n+1)=1-a*sequence;
45 |
46 |
47 | if n+1>(cycles-1)*stepnumber% last cycle after adaptation
48 | alp_ref(1)=alp(n);
49 | n_ref(1)=n;
50 | W_ref(1)=W;
51 | if abs(alp(n+1)-alp_ref(g))>delta_alp %——giving scalar value to
52 |     iteration after the addaptation cycle(decrease time step)
53 | alp_ref(g+1)=alp(n+1);
54 | n_ref(g+1)=n+1;
55 | W_ref(g+1)=W_accumulate(n+1)-W_accumulate(n_ref(g));
56 | g=g+1;
57 | end
58 | end

```

Titre : Une nouvelle stratégie pour l'analyse de la fatigue sous chargements multiaxiaux variables

Mots clés : fatigue à grand nombre de cycles ; énergie dissipée ; approche multi-échelle ; plasticité ; fatigue à gradient ; cumul non-linéaire de dommage

Résumé : L'objet de ce travail est de proposer une approche multi-échelle de la fatigue fondée sur l'énergie, et susceptible d'estimer les durées de vie associées à des chargements multidimensionnels variables. Le fondement de la démarche consiste à supposer que l'énergie dissipée à petite échelle régit le comportement à la fatigue. À chaque point matériel, est associée une distribution stochastique de points faibles qui sont susceptibles de plastifier et de contribuer à la dissipation d'énergie sans affecter des contraintes macroscopiques globales. Ceci revient à adopter le paradigme de Dang Van en fatigue polycyclique. La structure est supposée élastique (ou adaptée) à l'échelle macroscopique. De plus, on adopte à l'échelle mésoscopique un comportement élastoplastique avec une dépendance de la fonction de charge plastique non seulement de la partie déviatorique des contraintes, mais aussi de la partie hydrostatique. On considère également un écrouissage cinématique linéaire sous l'hypothèse d'une plasticité associée. Au lieu d'utiliser le nombre de cycles comme variable incrémentale, le concept d'évolution temporelle du chargement est adopté pour un suivi précis de l'historique du chargement réel. L'effet de la contrainte moyenne est pris en compte dans la fonction de charge mésoscopique ; une loi de cumul non linéaire de dommage est également considérée dans le modèle. La durée de vie à la fatigue est ensuite déterminée à l'aide d'une loi de phénoménologique fondée sur la dissipation d'énergie mésoscopique issue du cycle d'accommodation plastique. La première partie du travail a porté sur une proposition d'un modèle de fatigue à gradient de mise en oeuvre plus simple que les précédents modèles.

Title: A new strategy for fatigue analysis in presence of general multiaxial time varying loadings

Keywords: High cycle fatigue; dissipated energy; multiscale approach; plasticity ; gradient fatigue; non-linear damage accumulation

Abstract: The aim of this work is to propose a multi-scale approach to energy-based fatigue, which can estimate lifetimes associated with variable multidimensional loading. The foundation of the approach is to assume that the energy dissipated on a small scale governs the fatigue behavior. Each material point is associated to a stochastic distribution of weak points that are likely to plasticize and contribute to the dissipation of energy without affecting global macroscopic stresses. This amounts to adopting Dang Van's paradigm of high cycle fatigue. The structure is supposed to be elastic (or adapted) on a macroscopic scale. In addition, we adopt on the mesoscopic scale an elastoplastic behavior with a dependence of the plastic load function not only of the deviatoric part of the stresses, but also of the hydrostatic part. Linear kinematic hardening is also considered under the assumption of an associated plasticity. Instead of using the number of cycles as an incremental variable, the concept of temporal evolution of the load is adopted for a precise follow-up of the history of the actual loading. The effect of mean stress is taken into account in the mesoscopic yield function; a law of nonlinear accumulation of damage is also considered in the model. Fatigue life is then determined using a phenomenological law based on mesoscopic energy dissipation from the plastic accommodative cycle. The first part of the work focused on a proposal for a fatigue model with a simpler implementation gradient than the previous models.